,,,,,

University of Southampton Research Repository

Thesis: Davide Sarpa (2025) "Simulations of rheological properties of lubricants under operational conditions", University of Southampton, Faculty of Engineering and Physical Sciences, School of Chemistry PhD Thesis

Data: Davide Sarpa (2025) Simulations of rheological properties of lubricants under operational conditions.

University of Southampton

Faculty of Engineering and Physical Sciences
School of Chemistry

Simulations of rheological properties of lubricants under operational conditions

by

Davide Sarpa
Msc.
ORCiD: 0000-0003-3651-9050

A thesis for the degree of
Doctor of Philosophy

30th January 2025

University of Southampton

Abstract

Faculty of Engineering and Physical Sciences
School of Chemistry

Doctor of Philosophy

Simulations of rheological properties of lubricants under operational conditions

by Davide Sarpa

Understanding the microscopic behaviour of lubricants and their additives under operational conditions is critical to developing new lubricants and improving existing ones. Tribology researchers have been applying a quite diverse range of experimental techniques, that, while providing excellent insights into the macroscopic rheological properties of such systems, are not able to capture the microscopic behaviour fully, or they are limited in the range of conditions they can test. In this context, computational techniques have come forward as a tool to investigate microscopic and macroscopic behaviour at scales and conditions which are very difficult to access or probe experimentally. This thesis focuses on various computational techniques such as equilibrium molecular dynamics, non-equilibrium molecular dynamics and density functional theory to tackle a range of important technical and industrial problems in the field of rheology.

In particular, we start by investigating a set of 11 ideal mixtures of two industrially relevant synthetic esters via equilibrium and non-equilibrium molecular dynamics and compare the temperature dependence of static and dynamic properties of these systems against experimental values. We showed that computational methods can reproduce the experimental trends as well as provide a workflow that can be applied to a wide range of lubricants.

Next, we moved to non-equilibrium molecular dynamics simulations of a more complex set of non-ideal mixtures of three hydrocarbons to investigate the pressure dependence up to 4 GPa, a range which is hard to reach experimentally. We compared our simulated densities and viscosities against known and commonly employed empirical equations and we showed that we can obtain reliable estimates of the densities and viscosities, while also highlighting the limitations of current models at extreme conditions. We further moved towards even more realistic systems by confining a hydrocarbon-based lubricant between two iron oxide slabs as the interactions at the surface–lubricant interface is relevant in a range of technological applications. We employed non-equilibrium molecular dynamics simulations with reactive and non-reactive force fields to assess the effect of confinement on rheological properties. We showed that by increasing the film thickness we approach the viscosity value of the bulk fluid and that, at the conditions studied, no reactions are happening at the lubricant-surface interface.

Finally, we shifted our focus to the interactions between additives and hematite surfaces as they are widely present in a variety of industrial applications. Particularly we focus on the adsorption of Zinc dialkyldithiophosphates as it is the first step that leads to the formation of protective films (tribofilms) which are key in the anti-wear property of this class of lubricant additives. We investigated the changes in electronic structures and geometry that could increase the reactivity towards possible decomposition pathways.

The work presented in this thesis shows the applicability of computational techniques in studying the rheological properties of lubricants and related systems. The techniques

described here showed that it is possible to accurately describe realistic systems at operating conditions and beyond experimental limitations. In future, this could aid the design of new lubricants or additives as well as improving existing ones.

Contents

List of Figures

List of Tables

Definitions and Abbreviations

MD	Molecular dynamics
EMD	Equilibrium molecular dynamics
NEMD	Non-equilibrium molecular dynamics
DFT	Density functional theory
η	Dynamic viscosity
$\dot{\gamma}$	Shear rate
v	Velocity
ρ	Density
ν	Kinematic viscosity
μ	Coefficient of friction
P	Contact load
s	Entrainment speed
EHL	Elastohydrodynamic lubrication
ZDDPs	Zinc dialkyldithiophosphates
SATA	Stress-augmented thermal activation
k	Rate constant
A	Pre-exponential factor,
ΔU_{act}	Activation energy
k_B	Boltmann's constant
T	Temperature
ΔV_{act}	Activation energy corresponding to the shear stress
τ	Shear stress
σ	Normal stress
$\Delta\Omega_{\text{act}}$	Activation energy corresponding to the normal stress
NVT	Canonical Ensemble
NPT	Isothermal-isobaric ensemble
NPH	Isoenthalpic–isobaric ensemble
μVE	Grand Canonical ensemble
$\mathcal{H}$	Hamiltonian
PBC	Periodic boundary conditions
m	Mass
F	Force

a	Acceleration
$\mathcal{U}$	Potential energy
$\mathcal{L}$	Lagrangian
$\mathcal{K}$	Kinetic energy
p	Momentum
j	Vector in the phase space
r	Position
V	Volume
κ	Gaussian width
k_r	Bond force constant
k_θ	Angle force constant
$k_{\phi,n}$	Torsional force constant
q	Charge
f	Frictional term
g	Degrees of freedom
G	Gaussian
$\mathcal{C}$	Time correlation function
c	Normalised correlation function
ϵ_0	Dielectric constant in vacuum
ϵ_s	Dielectric constant of the medium
Q	Thermal inertia
L	Box dimension
∇v	Streaming velocity
ψ	Wavefunction
$\hat{}$	Operator
∇^2	Laplacian
P_b	probability
DEHS	Di-2-ethyl-hexyl sebacate
DEHA	Di-2-ethyl-hexyl adipate
HEX	Hexadecane
BB	Butylbenzene
BC	Bicyclohexyl
RDF	Radial distribution function
MSD	Mean Square Displacement

Declaration of Authorship

I declare that this thesis and the work presented in it is my own and has been generated by me as the result of my own original research.

I confirm that:

1. This work was done wholly or mainly while in candidature for a research degree at this University;
2. Where any part of this thesis has previously been submitted for a degree or any other qualification at this University or any other institution, this has been clearly stated;
3. Where I have consulted the published work of others, this is always clearly attributed;
4. Where I have quoted from the work of others, the source is always given. With the exception of such quotations, this thesis is entirely my own work;
5. I have acknowledged all main sources of help;
6. Where the thesis is based on work done by myself jointly with others, I have made clear exactly what was done by others and what I have contributed myself;
7. None of this work has been published before submission

Signed: Davide Sarpa Date: 30th January 2025.

Acknowledgements

Someone once said that every journey comes to an end, I would like to know who that person was, but I don't. Luckily though, I know who made this journey possible and somewhat bearable as, you probably know, getting a PhD is a challenge to one's mental health.

Without further ado, I would like to thank my supervisor Chris-Kriton Skylaris for his support throughout these four years and my industrial supervisors and collaborators at Schaeffler. I also thank David O'Regan for his extensive help with strongly correlated materials. A special thanks to Dimitrios Mathas, who helped me get on track with this PhD project and helped me move my first steps in the field of tribology simulations.

In four years I have had the pleasure of meeting fantastic housemates and it would be unfair not to mention them. Thanks to Davide and Domenico for being a second family, especially during COVID times. Thanks to Michael for our Sunday walks in the common discussing science, gym and life. Thanks to Rebecca for driving me around and showing me there is so much more in the UK than Southampton.

I would like to thank the members of the Skylaris group, Arihant, Jacek, Gabriel, Loukas, Apostolos, Catriona, and Lennart for the insightful scientific discussions and the enjoyable conversations beyond work.

Special thanks to Nabeel for making the office a lovely place and being the most British person I've ever met. You will be a great consultant but probably an even better politician.

Thanks to Tom, the smartest of us all and someone who managed to complain even more than I do. I thought that was impossible, but you succeeded. I'm sure you'll achieve great things in life, and I hope you find a place without airplanes waking you up.

A big thanks to Julian Holland, my first friend in the UK. I don't think I would have survived British food and weather without you. Thank you for being an amazing friend and for your support during those self-imposed hard times. I'm sure we'll see each other soon, as destiny is calling me, and I must open my eager eyes.

Finally, thanks to Brad, the golden boy of computational chemistry. You're a wonderful person, very funny, and incredibly smart—though perhaps not quite smart enough to make the Lithium slab converge! As an RSC poster award winner, I have no doubt your scientific achievements will be groundbreaking, as long as they don't involve electrochemistry.

To keep my sanity (almost) intact, I owe a huge thanks to the countless nights spent gaming, and to the people who made them memorable: Andrei, Dally, Mike, Beppe, Bonaz, Macchi, Detto, Coach, Il Forbidden Quinto, Jari, Med, Almo, and Tia. Backseating like a pro since 2020.

A special thanks go to Alessandra for being an amazing friend and our many lunchtime calls, which often made me a little late, but were always worth it.

Thank you to Gloria, who supported me throughout my PhD and beyond. If I'm the clown, you're the entire circus. The only person who could even make my mom jealous.

Thank you to my friends. Claudia, Nico, Ginger, Robi, Giulia, Cesa, Sam D., Sam. M, Denis, Isa, Marilisa, Chicco. After living abroad for five years, every time I came home, it felt like nothing had changed, and that made all the difference in the world.

Thank you, Giada. If I could write a second PhD thesis, it would be entirely about our friendship and the profound impact you've had on my life. For the past ten years, you've been my best friend and I truly don't think I'd be standing here today without you. Words aren't even necessary; you know, and I know. That's all that matters.

Last but not least, I want to thank my family. Your unconditional love has always been my greatest source of strength, and for that, I am forever grateful.

A chi ha dato tutto con la piena consapevolezza di non essere abbastanza

Part I

Introduction and Background

Chapter 1

Introduction

In a world where machines are widely spread and their usage is essential to our daily life, lubricants play a fundamental role as a tool to increase efficiency and reduce machine degradation. These capabilities have led to an increase in their worldwide demand that, as shown in Figure 1.1, has been going on since 2009.

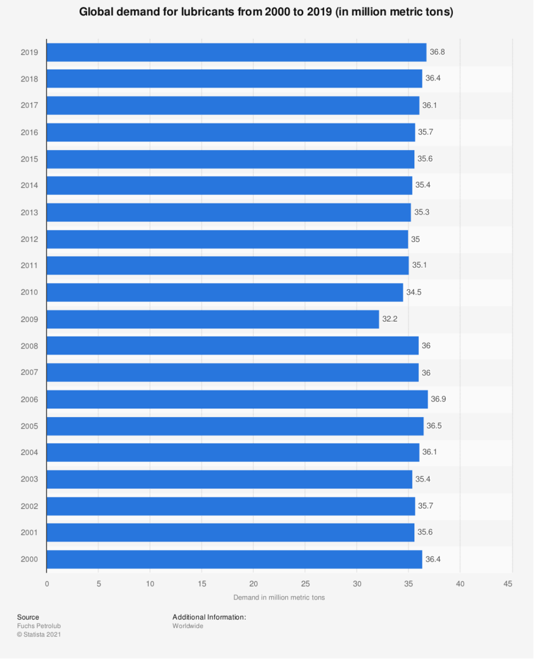

FIGURE 1.1: Lubricants worldwide demand, [1]

The development and modification of lubricants is an active area of research in tribology. Scientists are focused on enhancing the performance of lubricants across a wide range of operating conditions. The primary purpose of a lubricant is to reduce friction between surfaces, which can be influenced by factors like temperature, pressure, surface speed, material type, and the composition of the lubricant. Over the years lubricant formulations have become more complex reaching a state where the lubricants are not made of a single molecule anymore but a mixture of different molecules, additives, and, in some cases, solvents. Most techniques used to obtain lubricant formulations are based on empirical approaches which are not able to capture the atomistic behaviour of the lubricant, but being able to know and understand how lubricants, additives and surfaces interact microscopically is crucial in the development of better formulation since it could lead to accurate prediction of lubricant properties as well as to reduce the number and cost of empirical experiments.

In the past 40 years, computer simulations have become powerful and widely used techniques that allow us to gain insights that, for various reasons, can not be obtained by experiments. In particular molecular dynamics simulations (MD) and density functional theory (DFT) calculations provide the ability to obtain key information regarding the macroscopic behaviour of lubricants such as viscosity via statistical mechanical analysis of microscopic interactions and accurate quantum mechanical description of interactions between molecules and surfaces.

This thesis aims to deepen the understanding of the atomistic interactions between lubricants, additives, and surfaces through the use of advanced computer simulation techniques, including equilibrium molecular dynamics (EMD), non-equilibrium molecular dynamics (NEMD), and linear-scaling density functional theory (DFT). The primary objective is to develop a robust computational workflow and approach capable of analyzing diverse systems, ranging from idealized models to complex, realistic scenarios. These investigations provide insights into how molecular interactions evolve under varying conditions, such as non-ideal mixtures, high pressures, and confined environments.

The structure of the thesis is as follows:

Part I introduces the fundamental concepts of lubricants, additives, and surfaces, along with a comprehensive literature review of the current state of computer simulation techniques in studying lubricant systems. This section provides the necessary background to contextualize the research objectives and methods.

Part II outlines the methodologies employed throughout the work. It delves into the principles and applications of EMD, NEMD, and DFT techniques, explaining how these computational methods are adapted to address different system complexities.

Part III presents the main findings, structured to reflect the increasing complexity of the studied systems:

- Chapter 5 explores idealized lubricant systems, establishing a baseline for understanding fundamental interactions under simplified conditions.

- Chapter 6 investigates non-ideal mixtures at high pressures using molecular dynamics simulations, uncovering how molecular interactions are influenced by the presence of complex mixtures and extreme conditions.
- Chapter 7 examines confined systems, where molecular behavior is constrained by physical boundaries, such as surfaces or interfaces. These studies reveal how confinement impacts lubrication properties.
- Chapter 8 focuses on the interactions between zinc dialkyldithiophosphate (ZDDP)—a widely used class of anti-wear additives—and three different hematite surfaces. Using density functional theory, this chapter provides insights into the molecular-level interactions and adsorption mechanisms of ZDDP on hematite. This work represents the first study to investigate these interactions in such detail, marking a significant contribution to the understanding of additive-surface chemistry.

Finally, the thesis concludes with a synthesis of the findings, discussing their implications for lubricant design and performance optimization. Potential avenues for future research are also proposed, particularly in extending the computational approaches to other systems and conditions.

Chapter 2

Background

2.1 Lubricants

Lubricants are complex formulations usually made of 95% of base oil to reduce the surface wear and to obtain the desired value for the friction and 5% of additive that is added to the lubricants for many different reasons, see section 2.2. Base oils used in lubricants can be either biological or non-biological. Biological oils are primarily needed in industries where contamination must be minimized, such as food and pharmaceuticals. Non-biological oils are typically categorized into two main types: mineral oils and synthetic oils, which are the most commonly used lubricants. Mineral oils, derived from petroleum, are the most widely used across various applications. They are made from complex formulations containing more than 30 different molecules. While mineral oils are inexpensive, their molecular complexity makes it difficult to develop new lubricants or enhance their performance without relying on trial and error. Synthetic oils, in contrast, are more expensive and are designed to perform in extreme conditions such as high or low temperatures, high oxidation environments, or under high pressure. Synthetic oils have simpler compositions, which depend on the specific molecules used. The three main categories of synthetic lubricants are hydrocarbon-based, silicon-based, and organohalogen-based [2].

The most important lubricant property is viscosity. There are two types of viscosity in tribology: dynamic and kinematic viscosity. Dynamic viscosity η is defined as:

$$\dot{\gamma} = \eta \frac{\partial v}{\partial y} \tag{2.1}$$

where $\dot{\gamma}$ is the applied shear rate, v is the velocity in the x direction and η is the dynamic viscosity.

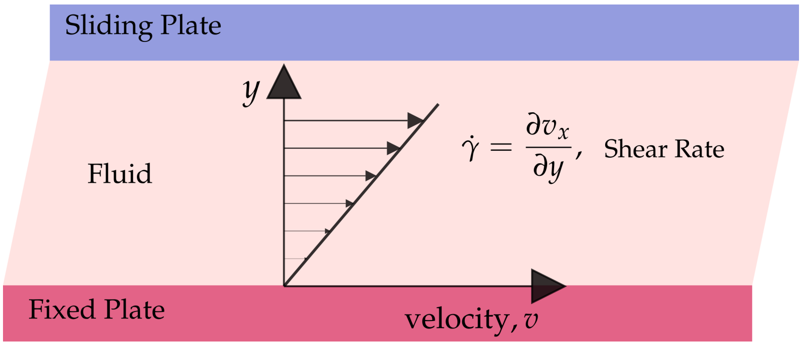

FIGURE 2.1: Schematic representation of liquid flow between a fixed and a sliding plate (Couette flow)

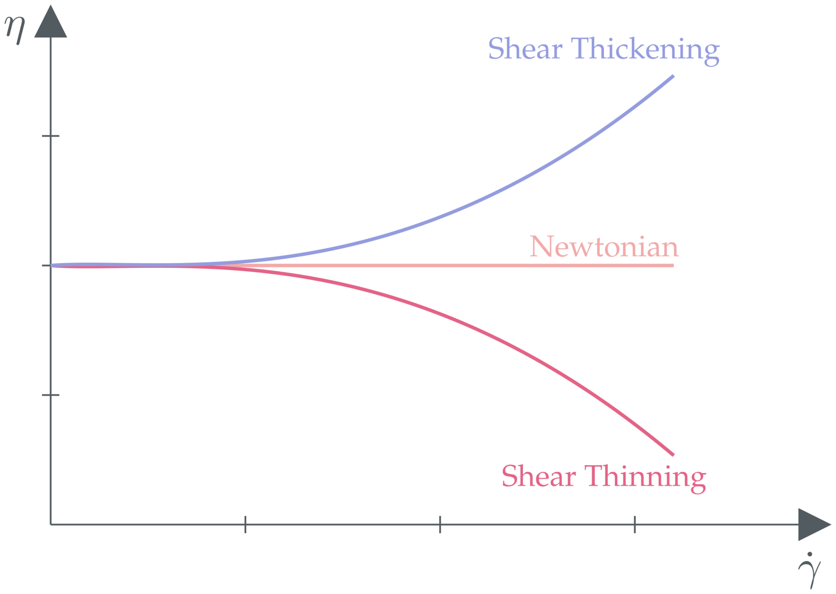

FIGURE 2.2: Viscosity vs Shear rate schematic representation of Newtonian and non-Newtonian behaviours

Kinematic viscosity is defined as

$$\nu = \frac{\eta}{\rho} \tag{2.2}$$

where ρ is the liquid density. Liquid viscosity depends among other things on pressure, temperature and shear rate. An increase in temperature usually leads to a decrease in viscosity while an increase in pressure increases the viscosity. The applied shear rate is responsible for the shift from Newtonian regime to non-Newtonian behaviour. Newtonian liquids are characterized by a constant viscosity value for applied shear rate while non-Newtonian behaviour can show quite different behaviour of dynamic viscosity over the range of applied shear rates. The two most important behaviours are the shear-thinning and shear-thickening, the first relates to the thinning of the liquid as the shear rate increases leading to a reduced viscosity; the latter is related to the thickening of the liquid as the shear rate increases leading to an increase in viscosity.

In this complex range of properties and composition, computational studies can help us get insights into how friction reduction works. Many studies have been published over the last 30 years on homogeneous bulk systems and confined simulations using both EMD and NEMD on a range of different lubricants such as hydrocarbons [3–6], ionic lubricants [7, 8], polyols [9], aqueous copolymers [10] and many more. Lubricants have been studied using EMD [11, 12] and NEMD [13, 14] testing different classical force field [15, 16] as well as reactive ones [17, 18]. Temperature and pressure dependencies were also investigated by various authors [4, 6, 9, 12], best practices were developed [19] as well as different approaches regarding the evaluation of viscosity in both EMD and NEMD [20, 21].

2.1.1 Lubrication regime

Lubricants reduce the friction between two sliding surfaces, where friction is defined as the force resisting the relative motion of the sliding surfaces and in fluid-lubricated systems, it depends on the fluid viscosity, contact load and lubricant entrainment speed, the latter is the speed of fluid transport across an interface of two surfaces. This relationship is described by the Stribeck Curve:

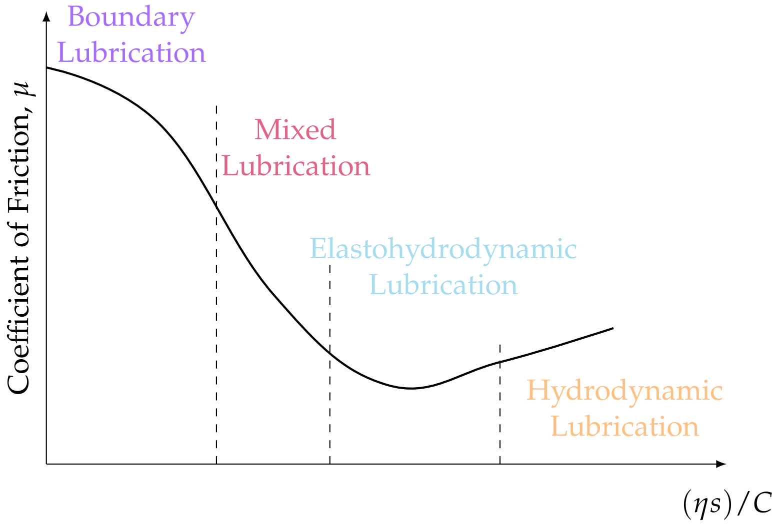

FIGURE 2.3: Stribeck curve showing the four lubrication regimes.

where η is the lubricant viscosity, s is the entrainment speed and C is the contact load. There are four lubrication regimes: boundary, mixed, elastohydrodynamic and hydrodynamic.

2.1.1.1 Boundary lubrication

Boundary lubrication is the regime where there is direct contact between the two sliding surfaces. This happens at low speed or very high load leading to high friction and wearing of the two surfaces. To reduce the wear it is necessary to choose a lubricant with appropriate viscosity, it should be viscous enough to force the separation of the two surfaces but very viscous fluid increases the operational temperature and presents higher energy loss. Another approach to reduce the wear is to introduce anti-wear additives such as ZDDP, these molecules generate a protective sacrificial film which will wear down during the boundary regime protecting the surfaces.

2.1.1.2 Mixed lubrication

Increasing the sliding speed creates a lubricant film between the surfaces hence moving away from the boundary regime and reaching the so-called mixed lubrication. In this regime, there is still some direct contact of the two surfaces at the asperities but the overall friction is greatly reduced. Increasing the film thickness by, for example, changing the lubricant or further increasing the sliding speed move the systems from mixed to elastohydrodynamic or hydrodynamic regimes.

2.1.1.3 Elastohydrodynamic lubrication

Elastohydrodynamic Lubrication (EHL) regime occurs where very high contact pressure causes elastic deformations of the surfaces and can be found in rolling element bearings, gear teeth and cam contacts. As the lubricant enters the contact zone between surfaces due to the presence of asperities, the lubricant experiences a sharp rise in pressure. This high pressure in turn significantly increases the lubricant's viscosity and load-holding ability. This load will slightly deform the surfaces but they return to their normal form as the rotation continues entering the hydrodynamic regime.

2.1.1.4 Hydrodynamic lubrication

This lubrication regime occurs when a full lubricant film is present between the two surfaces and there is no elastic deformation due to high load. The choice of lubricant is essential as it is necessary to maintain this regime under various operational conditions as deviation from this regime could cause the presence of direct contact between surfaces and hence wear down the machinery.

2.2 Additives

Additives make up 5% of the lubricant composition and they are usually organic or organometallic molecules which are added to the formulation to:

- reduce surface wear;
- increase lubrication under various operational conditions;
- increase lubricants stability;
- control of contamination;

The most important role is to reduce wear and enhance lubrication properties, There are three main groups of additives: adsorption additives, anti-wear additives, and extreme-pressure additives.

Adsorption additives are usually known as friction modifiers which are in most cases fatty acids or derivatives which are adsorbed on the surface through the polar part of the molecules creating a film. Extreme-pressure additives work by reacting with surfaces in a sort of corrosion process which requires control of concentration and thermodynamic properties, some of the most common extreme-pressure additives are dibenzylsulphide, chlorinated paraffin oils and mercaptobenzothiazole. Anti-wear additives are chemisorbed on the surfaces, the chemisorption allows the possibility of increasing operational temperature. the most common class of anti-wear additive are zinc dialkyldithiophosphates (ZDDPs) which also have antioxidant properties. ZDDPs limit the wear by forming a thick protective layer consisting primarily of amorphous or crystalline zinc phosphate. The label "R" refers to an alkyl group. Alkyl groups do not affect the structure of ZDDPs but they influence the solubility, stability and reactivity of ZDDPs and hence their applicability. The antiwear activity and reactivity depend on the alkyl group as follows:

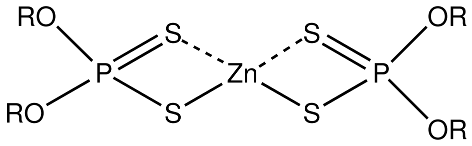

FIGURE 2.4: Zinc dialkyldithiophosphate (ZDDP)

Secondary Alkyl > Primary Alkyl > Aryl

Alkyl groups affect the lubrication regime. Branched hydrocarbons, for example, tend to give higher elastohydrodynamic friction than linear chain ones since they are not able to easily slide past one another during shear.

2.2.1 Tribofilm

Tribofilms are largely made of amorphous-crystalline phosphate with metal cations (Fe and Zn). The phosphate contains predominantly ortho and pyro-phosphate close to

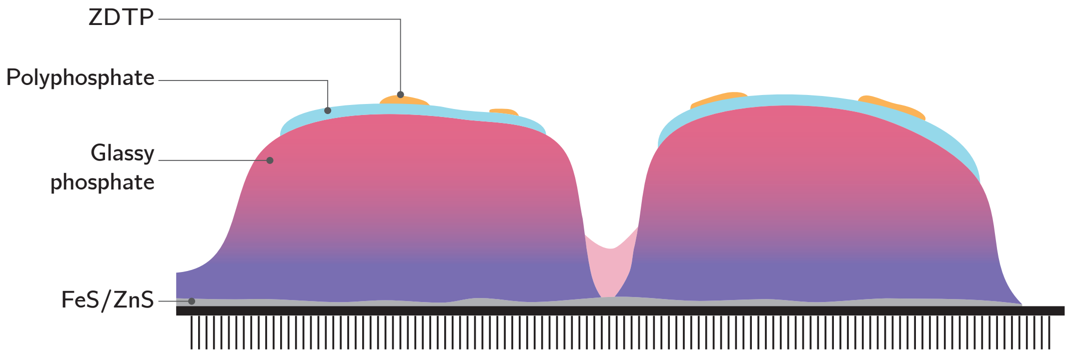

FIGURE 2.5: ZDDP tribofilm pad-like structure

the substrate but longer polyphosphate at the top. The top of the film also contains sulphides and sulphates. The film is also chemisorbed to the surface via the formation of a Fe/ZnS layer. Macroscopically they form pad-like structures as shown below

A mathematical model to describe the growth rate of the tribofilm has been developed and called the stress-augmented thermal activation (SATA) model. One version of the model is based on an extended form of the Eyring model that takes into account the effects of both compressive stress and shear stress;

$$k = A \exp\left(-\frac{\Delta U_{\text{act}} - \tau \Delta V_{\text{act}} + \sigma \Delta \Omega_{\text{act}}}{k_B T}\right) \tag{2.3}$$

where k is the rate constant, A is the pre-exponential factor, ΔU_{act} is the activation energy, k_B is Boltmann's constant, T is the temperature, ΔV_{act} is the activation energy corresponding to the shear stress,τ, and $\Delta\Omega_{\text{act}}$ is the activation energy corresponding to the normal stress, σ. The normal stress will inhibit bond stretching and breaking by forcing the atoms to be close to each other which can also promote bond formation by confinement.

2.3 Surface

So far we have discussed lubricants and additives but, another fundamental part of real-life applications is the material they have to work on, the most studied include iron, iron oxides, aluminium, steel and titanium using both experimental and computational approaches [22–27]. This thesis will focus on hematite (α-Fe_2O_3).

Hematite is a blood-red iron oxide with formula α-Fe_2O_3 with a boiling point of 1350 °C it belongs to the hexagonal crystal family, in particular, it is a Ditrigonal scalenohedral with a $R\bar{3}C$ space group, sharing the same structure as corundum. The primitive rhombohedral cell contains two formula units with lattice parameters a,b,c where a = b = c = 5.0356 Å. The hexagonal conventional cell contains six formula units with lattice parameters a,b,c where a = b = 5.0356 Å and c = 13.7489 Å. Its structure is an hpc anion stacking of O^{2-} along the [001] direction, with Fe^{3+} occupying 2/3 of the interstitial octahedral positions, featuring two different Fe-O distances of 1.98 Å and 2.09 Å [28, 29]. Its unique properties make it a subject of extensive study for a wide range of applications, including as a catalyst, photoanode, solar cell and gas sensors [30]. Hematite is particularly relevant in industrial applications involving steel under various operational conditions [29]. Chemically, hematite is a charge transfer insulator. The top of the valence band is dominated by O 2p states and Fe 3d states, while the bottom of the conduction band is filled with empty Fe 3d states, resulting in a band gap of 1.9 to 2.2 eV. The Fe atoms are in a d5 high spin configuration with experimental magnetic moments ranging from 4.0 to 4.6 μ_B [31].

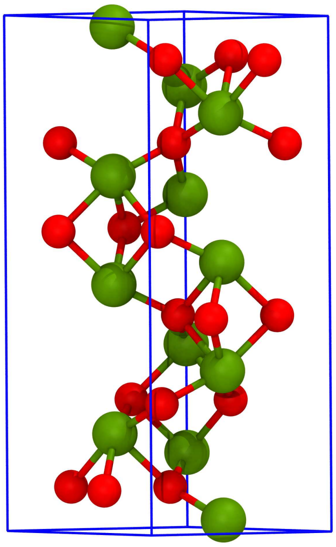

FIGURE 2.6: Hematite unit cell

Under ambient conditions, hematite is the most stable phase of iron oxide with an antiferromagnetic configuration below the Néel temperature of 955 K. There are three possible antiferromagnetic configurations in the primitive cell. If we orient the cell along the [111] direction these configurations can be described as $++--$, $+--+$ and $+-+-$. The $+--+$ is known to be the lowest in energy according to electronic structure calculations [32]. It is important to note that above 263 K, hematite undergoes a Morin transition where the magnetic moments lie in the (111) basal plane [33]. The calculations presented here will be run at 0 K and hence the antiparallel $+--+$ configuration aligned with the [111] direction will be used as the appropriate configuration in all the simulations. For each material, there are numerous possible surfaces indicated by the Miller indices *h*,*k*,*l* each one with different chemical and physical behaviour due to these differences it is important to understand which surface is the most common in real-life applications you are interested in and this is of uttermost importance for lubricants and additives because it has a direct impact on lubrication regimes as well as possible stability of both surface and lubricant formulation. Our work focuses on the stable and technologically important [001] surface.

Different terminations are possible for the [001] surface: the double iron termination Fe-Fe-O_3, the single iron termination Fe-O_3-Fe and the oxygen termination O_3-Fe-Fe [34, 35].

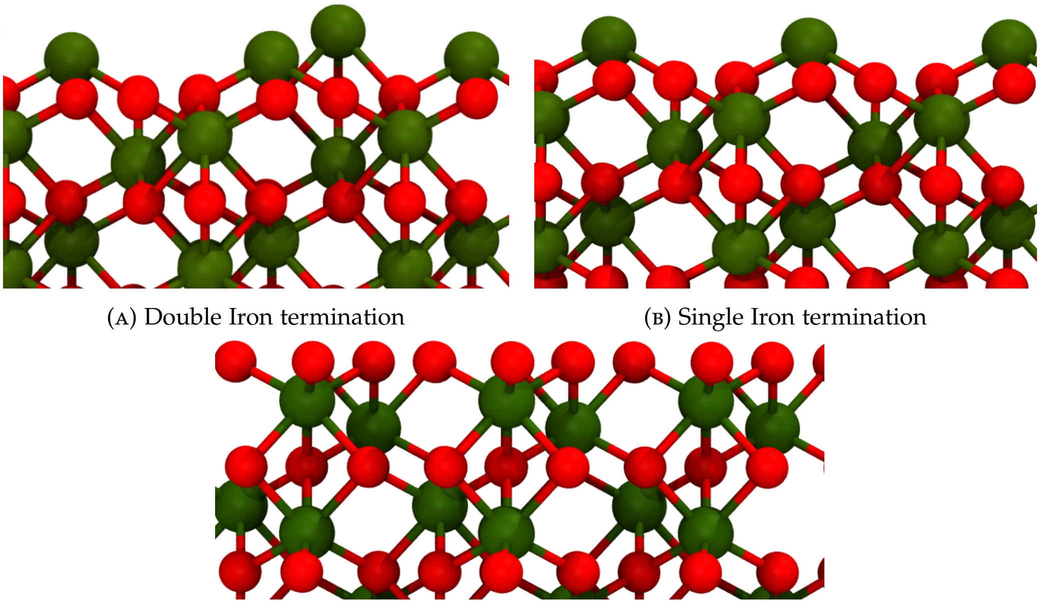
(A) Double Iron termination

(B) Single Iron termination

(C) Oxygen termination

FIGURE 2.7: Different [001] surface terminations for Hematite Fe (Dark Green) O (red)

2.4 Computer simulations

Molecular dynamics is a well-suited technique to study tribology and rheology problems at the microscopic scale providing useful insights into the chemical and physical behaviour of such complex systems. In the last 40 years EMD and NEMD have been carried out by different researchers on both bulk homogeneous and confined inhomogeneous systems.

2.4.1 Lubricant simulations

Bulk simulations mainly investigate the lubricants' behaviour and dynamic viscosity over a range of different shear rates $\dot{\gamma}$, temperature and pressure; early simulations were mostly based on small molecules using EMD. In 1973 Ashurst et al. published the first application of both EMD and NEMD to predict shear viscosity on an Argon system [36]; following the work of Ashurst computer simulations were employed as a predictive tool on a range of system such as dense soft-sphere [37], Lennard-jones [38] and with the increased computational power interested shifted towards more realistic lubricant systems such as n-alkanes, Allen et al. [39] showed how the density is affected mainly by intermolecular interactions while the torsional part of the force field and its coupling to the translational degrees of freedom affect the viscosity. They also show that this coupling increases with the chain length and that the time needed for the Green-Kubo integral to convergence can be roughly estimated by the rotational relaxation time which increases with chain length which was also confirmed by other authors [40, 41]. The effect of molecular architecture has been investigated by Kioupis et al. [42, 43] where they showed that the temperature dependence of the viscosity is reduced as the degree of branching is lowered due to lowering of energy barriers for inter-molecular orientations and that branched molecules show increased traction at higher pressure than linear alkanes. The effect of temperature, pressure and other thermodynamic properties on viscosity have been studied by various researchers [4, 6, 11, 12, 44–46]. In recent years novel techniques and approach to quantify viscosity and reduce uncertainty have developed to limit the short-comings of the Green-Kubo approach such as the high uncertainty or the need to run long simulations for the integral to converge, McCabe et al. [47] suggested a scaling approach to viscosity calculations, Kondratyuk et al. proposed a diffusion based approach to viscosity [3], Zhang et al. proposed a time decomposition method using different EMD trajectories and a fit involving the standard deviation [20]. Finally, best practices as well as investigation on the nature of the uncertainties have been developed [19, 48, 49].

NEMD was also employed in bulk simulations for a range of different lubricants such as linear or branched alkanes [50] [51], simulations were also compared to continuum mechanics techniques [52] and possible differences between confined and bulk system were also investigated [53]. Lacks et al. showed that if the simulations sample a phase space local minima this could lead to having a lower or higher shear rate than expected and that an average over multiple trajectories could provide a simple yet powerful methodology to assess this problem [54], studies on longer and lubricant-like molecules have been carried out by various researchers including possible branching effects [55–57]. The predictive power of NEMD has been tested on different types of systems including glass, polyethers, ionic liquids, polyol and bio-lubricants [8, 9, 58–61]. Thermodynamic properties and effects of temperature and pressure have been investigated on different systems [12, 62–64]. Liu et al. studied the correlation between shear thinning and radius of gyration [65] while Santank et al. suggested an automatic shear rate sample technique to perform NEMD [21]. More recent work involved the use of computer-aided MD and machine-learning in the evaluation of transport properties [66, 67].

Confining fluids between surfaces is the natural extension of lubricant simulations as they approach a more realistic environment. For example, Jiang et al. investigated the structural and rheological properties of confined n-decane between two Au(111) surfaces in contact with its bulk under constant normal loads or constant heights [68]. Benjamin Rotenberg investigated via EMD the fluid viscosity and diffusion-osmotic mobility of fluids under confinement and compared it with NEMD results [69]. Ewen et al. focused on the behaviour of n-alkanes confined and sheared between iron oxide surfaces via NEMD up to 1.5 GPa[13]. Maginn et al. compared EMD, NEMD and boundary-driven MD techniques for studying transport in microporous materials [70], Dini et al. investigated the traction and nonequilibrium phase behaviour of confined sheared liquids at high pressure [71]. Yonghao Zhang focused, among other properties, on the shear viscosity and thermal conductivity of confined van der Waals fluids [72].

Many more studies involving a variety of conditions, lubricants and surfaces are available in the literature [73–82] and numerous detailed review are available on the use of MD in tribology simulations and the reader should refer to these for more information on the field [14, 83, 84].

2.4.2 Additive simulations

Numerous studies have been carried out on different kinds of additives such as OFM by Shi et al. [85], by Ewen et al. regarding the OFM in NEMD simulations [14, 86]. Many studies have been also published regarding ZDDP including reviews by Barnes et al. [87] or by Spikes [88], additional work has been done towards understanding the mechanism of how ZDDP works [89, 90] and on the effect of pressure and temperature [91].

Computer simulations have always been of interest for additives and, in particular, for ZDDP since not much is known about the atomistic reason for such properties. Various computational modelling methods have been applied ranging from classical MD simulations [85, 92–95], *ab initio* quantum mechanical calculations [96, 97] and hybrid quantum chemical and MD approach [96], the last one is computationally very expensive and most of the works have been done using a less accurate but faster method known as tight binding DFT [90, 98–100].

Berro et al. [94] performed an EMD simulation of a solution containing hexadecane as base oil and 5% ZDDP as additive confined between two hematite slabs. They employed the OPLS-AA force field with united atoms and Lennard-Jones parameters plus a Coulombic term for the interaction between molecules and surfaces. They employed different harmonic terms for the slab as well as different roughness and they studied the influence of different interfacial phenomena on friction and slip.

Martin et al. [90] employed experimental, HSAB theory, classical MD and tight-binding MD to investigate the antiwear properties of ZDDP. In particular, they focus on calculating the friction coefficient between an iron surface/iron oxide surface and zinc phosphate layer, they showed that zinc thiophosphate clearly reacts chemically with the iron oxide and the corresponding friction coefficient is high as well as adhesion of the tribofilm on the substrate (migration of Fe and O atoms in the zinc thiophosphate). They then moved to investigate the digestion of iron oxide particles by the phosphate layer.

Similar work has been carried out by Onodera et al. [98].

Peeters et al. [101] employed DFT calculations and Ab-initio MD to investigate the energies of possible fragments generated by ZDDP decompositions, adsorption energies of ZDDP and some of the fragments on top of different materials such as Al(001) and Mg(0001). They showed that the weakest bonds are the ones involving Zn and S and that ZDDP physisorbed before decomposing.

Xue et al. [102] investigated by DFT calculations the structural features of various ZDDP monomers, the thermal decomposition of ZDDP monomers and their dimers, and the hydrolysis of alkaline tetranuclear zinc molecules with various alkyl and aryl substituents. They suggest that both alkyl and aryl substituents have very little effect on the geometric parameters of their core structures but have a significant effect on the thermal decomposition of ZDDP monomers.

They also suggested that for full-alkyl substituted ZDDP molecules, the main decomposition manner is the homolysis of the Zn–S bond, leading to DPP radicals. Whereas, the PAO bond homolysis giving alkoxy radicals is favoured for aryl-substituted ZDDPs.

Onodera et al. [103] investigated the influence of a nanometer scale film structure of a tribofilm generated from zinc dialkyldithiophosphate (ZDDP) anti-wear additive on its mechanical properties using a combined MD and finite element (FE) method. They showed that there is a significant inter-diffusion of iron and zinc atoms.

Mosey et al. [104] focused on the nnimolecular decomposition and isomerization mechanism of ZDDP using DFT calculations. In particular, they focused on intramolecular alkyl group transfer and olefin reactions, they investigated the effect of different substituents including Hydrogen. They showed that in the alkyl-substituted systems, the alkyl group transfer occurs through an asynchronous concerted mechanism where the C-O bond is significantly dissociated before the C-S bond has undergone substantial formation. It was also found that olefin elimination occurred through a concerted process involving the transfer of a hydrogen atom from one of the alkyl groups in the ZDDP molecule to an adjacent sulfur atom. The results showed that straight-chained primary alkyl ZDDPs, produced precursors to the antiwear films through alkyl group transfer reactions. Secondary alkyl ZDDPs decomposed through olefin elimination reactions producing H_2S gas.

Mosey et al. [105] employed Ab-Initio MD to study the general chemical behaviour of ZDDP, its isomers and olefin elimination. They found that Zn-O bonds dissociate at a much faster rate than Zn-S. This bond-breaking may aid in the formation of tribofilm and it is dependent upon the rate of the isomerization through an O/S exchange mechanism.

Benini et al. [106] studied the adsorption and dissociation of ZDDPs on oxidised ferrous surfaces.

2.4.3 Hematite simulations

Authors have investigated the electronic structure of bulk hematite employing different methods such as GW-BSE [107, 108], DFT and DFT+U [109–114]. A range functionals have been tested including LDA [115], GGA functionals such as PBE [116] or PW91 [115], hybrids as the HSE functional [113, 116] or B3LYP [115] and more recently, the meta-GGA SCAN functional [31].

Hematite surfaces have been the focus of numerous studies, ranging from pure phases of different cuts such as the (1100), (1000), and (0001) surfaces to mixed termination or biphase surfaces [34, 35, 117–122]. Lad et al. used a force field approach [117], Liao and coworkers tested various GW approximations [107], Alvarez-Ramirez tested various functional using both plane wave and localized basis set [115]. Hematite in presence of H_2O, H_2, O_2 was investigated by Souvi and coworkers [123], Rohrbach et al. used DFT to understand the influence of strong electronic correlations [124], and many more studies regarding thermodynamic stability, interface interactions with lubricants, additives and water have been carried out by various authors [13, 98, 125–128].

The (0001) surface, according to both experimental and theoretical works is one of the most thermodynamically stable surfaces of Hematite [129, 130]. Different terminations of the (0001) hematite facet are possible: the double Fe termination (Fe-Fe-O3), the single Fe termination (Fe-O3-Fe), the oxygen termination (O3-Fe-Fe), and the ferryl termination (O=Fe-O3-R). The dominant termination of the (0001) direction is a matter of discussion, it depends on the chemical environment and the O chemical potential. A recent study using the SCAN functional suggests that the Fe-O3-Fe and O3-Fe-Fe terminations are dominant [31]. Under operational conditions in lubricant experiments, another surface termination is reported to be present [113, 119]: the hydroxylated termination, known as the HO-Fe-Fe termination. Therefore, we decided to focus our study on three surfaces, as they are reported to be present and stable under experimental conditions with lubricants: the Fe-O3-Fe, O3-Fe-Fe and the HO-Fe-Fe termination.

Part II

Simulation Techniques

Chapter 3

Molecular Dynamics

3.1 Classical Mechanics

In 1687 Newton published his *Philosphiæ Naturalis Principia Mathematica* [131] from which we know that

$$\mathbf{F} = m\mathbf{a} \tag{3.1}$$

if the mass does not depend on time then

$$\mathbf{F} = m\frac{\mathrm{d}^2\mathbf{r}}{\mathrm{d}t^2} \tag{3.2}$$

this equation can be applied to any system of N particles and they surprisingly well describe many macroscopic and dynamic properties [132]. It can be inferred that every system can be described by positions and velocities following the Newtonian equation of motion, the whole possible set of values of positions and velocities is called *phase space* and each point in the phase space is called a *microstate*. If the forces are conservative,

$$\mathbf{F} = -\nabla U \tag{3.3}$$

It is possible to re-formulate Newtonian equations of motion in terms of generalised velocities and positions. The new formulation is called Lagrange mechanics and the associated equations of motions known as *Euler-Lagrange* equations of motion are

$$\frac{\mathrm{d}}{\mathrm{d}t}\left(\frac{\partial\mathcal{L}}{\partial\dot{\mathbf{r}}}\right) - \frac{\partial\mathcal{L}}{\partial\mathbf{r}} = 0 \tag{3.4}$$

where the $\mathcal{L}$ is the Lagrangian and defined as

$$\mathcal{L} = K - U \tag{3.5}$$

K and U are respectively the kinetic energy and the potential energy of the system expressed in terms of velocities and positions as in Newtonian mechanics. Lagrangian mechanics is powerful due to being able to describe systems for any arbitrary coordinate system. Another formulation of mechanics is possible, this time in terms of position and momenta instead of velocities and it can be derived from Lagrangian mechanics using Legendre transforms. This new formulation is called Hamiltonian mechanics and it is the formulation we will be using throughout this thesis. The Hamiltonian is defined as the Legendre transform of the Lagrangian as

$$\mathcal{H} = \sum_{i=1}^{N} \frac{\mathbf{p}_i^2}{2m_i} + U \tag{3.6}$$

the Hamiltonian description works in terms of any arbitrary coordinate system as the Lagrangian. The main difference is that Hamilton's mechanics describes systems in terms of momenta and not velocities with a set of 6N first-order differential equations while the Lagrangian equations of motion are a set of 3N second-order differential equations. The energy of the system is given by

$$E = K + U \tag{3.7}$$

where K is the kinetic energy term and U is the potential energy term. Hamilton's equations of motion describe the trajectory of a system and conserve the total Hamiltonian and hence the total energy

$$\frac{\mathrm{d}\mathcal{H}}{\mathrm{d}t} = 0 \tag{3.8}$$

Another important property of Hamilton's equations of motion is the phase space incompressibility, if we define j as a vector in the phase space then

$$\nabla_j \dot{\mathbf{j}} = 0 \tag{3.9}$$

It is possible to show that due to the space phase incompressibility, the phase space volume and the ensemble distribution function are conserved. The ensemble distribution function is a quantitative description of how the systems in an ensemble are distributed in the phase space at any point in time, where an ensemble is a subset of all the possible phase space microstates that contain only those microstates that are consistent with a given set of macroscopic observables.

In MD, there are different possible ensembles where some thermodynamic properties are held constant. The possible ensembles are:

- Microcanonical or NVE, where the number of particles (N), the volume (V) and the total energy (E) are held constant

- Canonical or NVT, where the number of particles (N), the volume (V) and the temperature (T) are held constant
- Grand canonical or μVE, where the chemical potential (μ), the volume (V) and temperature (T) are held constant
- Isothermal–isobaric or NPT, where the number of particles (N), the pressure (P) and the temperature (T) are held constant
- Isoenthalpic–isobaric or NPH, where the number of particles (N), the pressure (P) and the enthalpy (H) are held constant

3.2 Equilibrium Molecular dynamics

MD is a simulation technique used to solve Newton's equations of motion for a collection of particles, it was first done for a hard sphere system by Alder in 1957 [133]. Approximations are needed when simulating real systems due to requiring time or memory outside our current capabilities even on modern supercomputers and that is a problem occurring even for the smallest of real-life systems.

The most common method to reduce the number of particles but still obtain a bulk macroscopic behaviour is called periodic boundary conditions (PBC). Particles are surrounded by a box which is then replicated in N dimensions depending if you are interested in a bulk, a slab or a wire system and when one of the particles leaves the central box it gets replaced by its image from one of the neighbouring cells 3.1. In this way, calculations are performed on a single simulation box which heavily reduces the computational cost, using PBC raise issues such as inducing a non-physical symmetry to the system, finite size effect, radial distribution function for dense liquid is found to be not isotropic and various others but for the majority of systems the approximations due to the PBC is negligible [132, 134].

In order to solve the equations of motion it is necessary to know the forces between the particles, many analytical forms for these forces have been developed since the beginning of MD. These functions are called force fields and their general form is :

$$\mathcal{U}_{\text{total}} = \mathcal{U}_{\text{bonded}} + \mathcal{U}_{\text{non-bonded}} \tag{3.10}$$

Force fields are divided into classes based on the type of terms included, class I force fields contain the least amount of terms but they still prove to be of use for most applications and they are computationally less expensive than other classes of force fields. The bonded terms in a class I force fields have the following form.

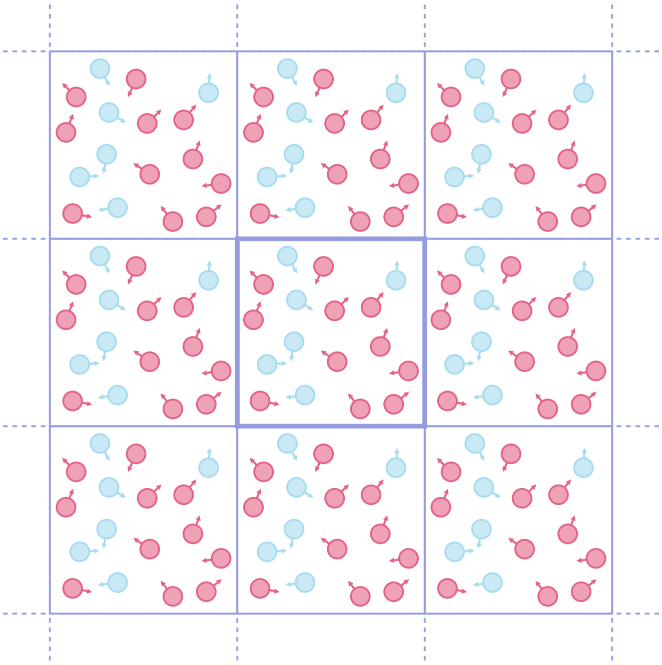

FIGURE 3.1: Schematic representation of a 2d periodic boundary conditions. Particles leaving the boxes have their image entering from the other side

Bond stretching

$$\mathcal{U}_{\text{stretching}} = \sum_{\text{bonds}} \frac{1}{2} k_r (r_{ij} - r_0)^2 \tag{3.11}$$

where k_r is the force constant and the term $(r_{ij} - r_0)^2$ is the bond stretching term in the harmonic approximation. Classes II force field add anharmonic terms to the bond stretching.

Angle Bending

$$\mathcal{U}_{\text{bending}} = \sum_{\text{angles}} \frac{1}{2} k_\theta (\theta_{ijk} - \theta_0)^2 \tag{3.12}$$

where k_θ is the force constant and the term $(\theta_{ijk} - \theta_0)^2$ is the angle bending term in the harmonic approximation. Classes II force field add anharmonic terms to the angle stretching.

Torsion

$$\mathcal{U}_{\text{torsions}} = \sum_{\text{torsions}} \sum_{n} k_{\phi,n} \left[\cos(n\phi_{ijkl} + \delta_n) + 1 \right] \tag{3.13}$$

where $k_{\phi,n}$ is the force constant, n is the multiplicity, i.e. the number of minima, ϕ_{ijkl} represent the current torsional angle and δ_n is the phase term. The total bonded term for a class I force field is given by

$$V_{\text{bonded}} = V_{\text{stretching}} + V_{\text{bending}} + V_{\text{torsions}} \tag{3.14}$$

the non-bonded terms are divided in

$$\mathcal{U}_{\text{non-bonded}} = V_{\text{electrostatic}} + \mathcal{U}_{\text{van der Waals}} \tag{3.15}$$

these terms are the most computationally expensive in the force field and they are usually made of a Coulomb term and a Lennard-Jones-like potential.

$$\mathcal{U}_{\text{non-bonded}} = \sum_i \sum_{j>i} \frac{q_i q_j}{4\pi\epsilon_0 r_{ij}} + \sum_i \sum_{j>i} \frac{A_{ij}}{r_{ij}^{12}} - \frac{B_{ij}}{r_{ij}^{6}} \tag{3.16}$$

The three or more body terms are usually included as an effective potential. In computing these properties for each of the particles we refer to the minimum image convention where only interactions between each molecule and the closest periodic image of its neighbours are considered, a pictorial representation can be seen in Fig 3.2. For the short-range part (Van der Waals) to increase the computational efficiency we introduce a cutoff (r_{cut}), outside of which the potential is set to 0 and then the rest of the interaction is usually added via corrections.

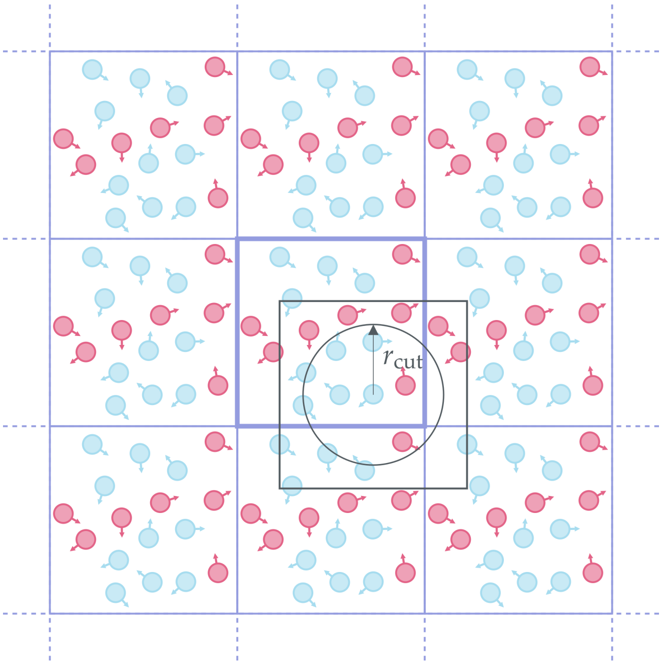

FIGURE 3.2: Minimum image convention and cutoff radius r_{cut}

Due to the divergences of the correction added to the cutoff if the potential decays slower than r^{-3}, the long-range part is calculated using different approaches and one of the most common is the Ewald summation.

3.2.1 Ewald summation

Ewald summation [135] is a technique to compute the long-range interactions. The potential derived by all the atoms in the box and their periodic images, can be written as:

$$\mathcal{U} = \frac{1}{2}\sum_{\mathrm{n}} \left(\sum_{i=1}^{\mathrm{N}} \sum_{j=1}^{\mathrm{N}} q_i q_j \left| \mathrm{r}_{ij} + \mathrm{nL} \right|^{-1} \right) \tag{3.17}$$

where q_i, q_j are the charges of particle i and particle j which can be considered as points. The sum over $\mathrm{n} = (n_x, n_y, n_z)$ is over all triplets of integer. For a cubic box, nL represents the centre of each box in the periodic array. An important point is that we omit $i = j$ for $n = 0$ as we do not want to compute the interactions of an atom with itself. For long-range potentials, this sum is conditionally convergent. It means it depends on the order in which we add up the terms. We sum in order of their proximity to the central box.

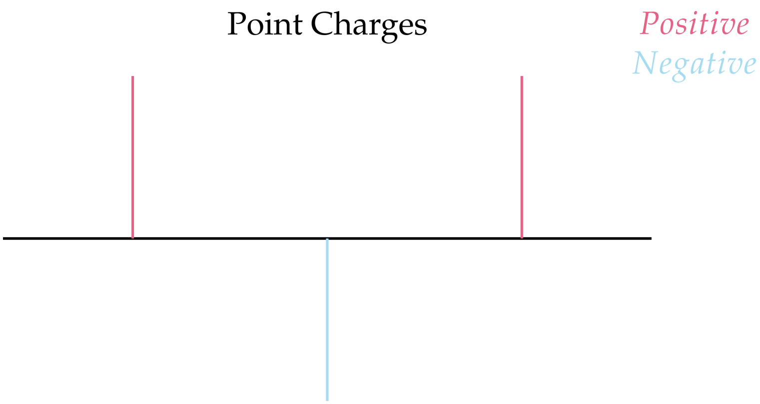

FIGURE 3.3: each atom can be considered as a point charge

In the Ewald method, each point charge is surrounded by a charge distribution of equal magnitude and opposite sign in real space and a neutralizing distribution opposite in sign and equal in magnitude to the real one in reciprocal space. Fig. 3.3 provides a visual representation of the spatial distribution of the point charges of the system. They are represented as vertical lines along a horizontal axis denoting position r. Positive charges are shown in red, while negative charges are shown in blue. The distributions are taken to be Gaussian for convenience

$$G_i^q(\mathbf{r}) = q_i \kappa^3 \exp\left(-\kappa^2 \mathbf{r}^2\right) / \pi^{3/2} \tag{3.18}$$

where κ determines the width of the distribution and r is the position relative to the centre of the distribution as shown in Fig 3.4. This extra distribution acts to screen the interaction between neighbouring charges. The screened interactions are now short-ranged and the total screened potential is calculated by summing over all the molecules in the central box and all their images in the real space.

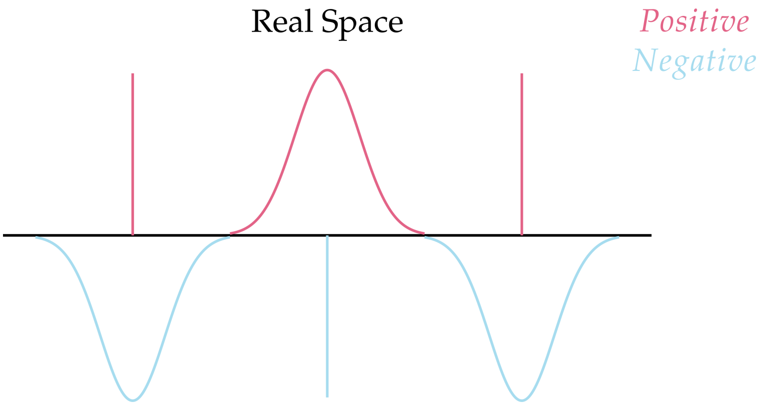

FIGURE 3.4: Real part of the Ewald sum, point charges and screening distribution

The cancelling distribution, shown in Fig 3.5, reduces the overall potential to that due to the original set of charges. The cancelling distribution is summed in reciprocal space. In other words, the Fourier transforms of the cancelling distribution are added, and the total is transformed back into real space. In the particle-particle particle-mesh PPPM algorithm [136] which is used in all simulations of this thesis the charge density is interpolated onto a mesh in the simulation box which can be then solved by the use of the Fast Fourier Transform(FFT).

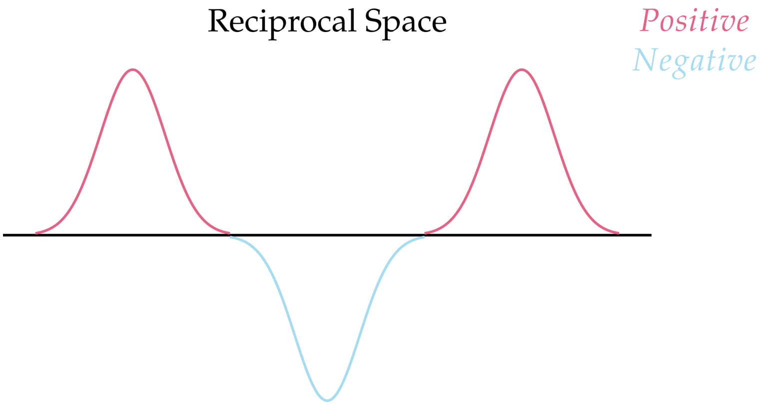

FIGURE 3.5: Reciprocal part of the Ewald sum, point charges and screening distribution

There is an additional correction which is to remove the self-interaction between the distribution, so the final result is

$$\begin{aligned}\mathcal{U}^{qq}\left(\epsilon_s=1\right) = \frac{1}{2}\sum_{i=1}^{N}\sum_{j=1}^{N} q_i q_j \Bigg(&\sum_{|\mathrm{m}|=0}^{\infty} \frac{\operatorname{erfc}\left(\kappa\left|\mathrm{r}_{ij}+L\ \mathrm{m}\right|\right)}{\left|\mathrm{r}_{ij}+L\ \mathrm{m}\right|} \\ &+ \left(1/\pi L^3\right)\sum_{\mathrm{k}\neq 0}\left(4\pi^2/k^2\right)\exp\left(-k^2/4\kappa^2\right)\exp\left(-\mathrm{ik}\cdot\mathrm{r}_{ij}\right)\Bigg) \\ &- \left(\kappa/\pi^{1/2}\right)\sum_{i=1}^{N} q_i^2 + \left(2\pi/3L^3\right)\left|\sum_{i=1}^{N} q_i \mathbf{r}_i\right|^2 \end{aligned} \tag{3.19}$$

Here $\mathrm{erfc}(x)$ is the complementary error function

$$\mathrm{erfc}(x) = \left(\frac{2}{\pi^{1/2}}\right)\int_x^{\infty} \exp\left(-t^2\right) \mathrm{d}t \tag{3.20}$$

which falls to zero with increasing x. If κ is large the distribution of charge is sharp and it is necessary to include many terms in the k-space, the only term in real space is $m = 0$, which is the minimum image convention. Ewald requires the system to be neutral so it is necessary to include an additional term in the presence of a charged system.

$$\mathcal{U}_{\text{charged}} = -\frac{\pi}{2L^3\kappa^2}\left|\sum_{i=1}^{N} q_i\right|^2 \tag{3.21}$$

3.2.2 Velocity Verlet

Newton's equations are ordinary differential equations and one of the ways to solve them is to resort to the finite-difference method. The idea behind the finite-difference method is to solve the equation step-by-step by calculating the positions and velocities of the particles that made up the system at time $t + \delta t$ by knowing the positions, and velocities at time t. The most common and known algorithm that implements this method is the Velocity Verlet which is a modification of the original Verlet algorithm [134, 137]. The algorithm proceeds as follows:

1. calculate the acceleration at time t from the forces between particles at time t

$$\mathbf{a}_i(t) = \frac{\sum_j^N \mathbf{F}_{ij}}{m} \tag{3.22}$$

2. calculate the velocity at time $t + \frac{1}{2}\delta t$ from the velocity at time t and acceleration at time t

$$\mathbf{v}_i\left(t + \frac{1}{2}\delta t\right) = \mathbf{v}_i(t) + \frac{1}{2}\delta t \mathbf{a}_i(t) \tag{3.23}$$

3. calculate position at time $t + \delta t$ from the position at time t and velocity at time $t + \frac{1}{2}\delta t$

$$\mathbf{r}_i(t + \delta t) = \mathbf{r}_i(t) + \delta t \mathbf{v}_i\left(t + \frac{1}{2}\delta t\right) \tag{3.24}$$

4. Calculate the velocity at time $t + \delta t$ from the velocity at time $t + \frac{1}{2}\delta t$ and acceleration at time $t + \delta t$

$$\mathbf{v}_i(t + \delta t) = \mathbf{v}_i\left(t + \frac{1}{2}\delta t\right) + \frac{1}{2}\delta t \mathbf{a}_i(t + \delta t) \tag{3.25}$$

The Verlet algorithm is exactly time-reversible, conserves linear momentum and has excellent energy-conserving properties and it is one of the most used algorithms in MD.

3.2.3 Thermostats and Barostat

In order to maintain a constant temperature(NPT, NVT, μVT) throughout the simulations it is necessary to introduce a thermostat. Various approaches are possible ranging from stochastic like Langevin, Dissipative particle dynamics (DPD) and Andersen [138–140] or deterministic such as Gaussian velocity rescaling or Berendsen proportional time-rescaling [141]. One of the most used thermostats is the Nosé-Hoover [142, 143] which adds a single degree of freedom to the equation of motion. The equations of motion are

$$\begin{aligned} \dot{\mathbf{r}} &= \frac{\mathbf{p}}{m}, \qquad \dot{\mathbf{p}} = \mathbf{F} - (\mathbf{p}_f/Q)\mathbf{p} \\ \dot{f} &= \mathbf{p}_f/Q, \quad \dot{\mathbf{p}}_f = \mathbf{p}\cdot\mathbf{p}/m - gk_bT \end{aligned} \tag{3.26}$$

where Q is the thermal inertia of the thermal bath with which the system is in contact. g is the number of degrees of freedom and $\dot{\eta}$ can be seen as a frictional term which controls the temperature and p_n is the associated momentum to the additional degree of freedom. The equations are not Hamiltonian but they conserve phase space volume and an energy-like variable. They are also non-ergodic which means they are not able to sample the whole phase space variable, it is usually common to fix this problem by applying a chain of thermostats.

Barostats are necessary to maintain a constant pressure during the simulations, many algorithms have been developed from the simpler volume rescaling such as Berendsen [141] or Andersen[140] to more complex one as the Martyna-Tuckerman-Tobias-Klein [144] or Nosé- Hoover [142, 143] in which the volume is scaled with an additional degree of freedom in a similar manner as the Nosé-Hoover thermostat.

In this thesis, Nosé-Hoover thermostat and barostat were used for both EMD and NEMD

3.2.4 Viscosity and Autocorrelation Functions

MD allow us to study the microscopic behaviour of a system from which, via statistical mechanics analysis, it is possible to predict macroscopic properties. In particular, time correlation functions are of enormous importance in evaluating transport coefficients such as shear viscosity.

The time correlation function of two properties $\mathcal{A}$ and $\mathcal{B}$ is defined as :

$$\mathcal{C}_{\mathcal{AB}}(t) = \langle \delta\mathcal{A}(t)\delta\mathcal{B}(0)\rangle_{\text{ensemble}} \tag{3.27}$$

where the subscript ensemble refers to the value being an ensemble average. It is more common to work with the normalized correlation functions:

$$c_{\mathcal{AB}}(t) = \frac{\mathcal{C}_{\mathcal{AB}}(t)}{\mathcal{C}_{\mathcal{AB}}(0)} \tag{3.28}$$

If $\mathcal{A}$ $\mathcal{B}$ are the same property the correlation function is called autocorrelation function.

Time correlation functions describe how long it takes for the property at time t to "forget" its initial state and this time, called correlation time τ, is obtained by a time integral from 0 to $t = \infty$; this integral can be linked via linear response theory to macroscopic transport coefficients.

Out of all the transport coefficients possible to compute using MD, shear viscosity is of main interest for lubricant simulations, it is defined as a function of the pressure tensor

$$\eta = \frac{V}{k_{\mathrm{B}}T}\int_0^{\infty} dt \langle \mathcal{P}_{\alpha\beta}(t)\mathcal{P}_{\alpha\beta}(0)\rangle \tag{3.29}$$

where V is the volume, T is the temperature, k_{B}, and $P_{\alpha\beta}$ are the off-diagonal terms in the pressure tensor. Equation 3.29 is an example of the Green-Kubo equations.

EMD and Green-Kubo formalism allow us to predict shear viscosity for molecular fluids, this method requires long simulations time due to the intrinsic limitation on the integral convergence which is achieved only when the correlation function has decayed to 0. These limitations can be overcome by resorting to NEMD

3.3 Non-equilibrium Molecular Dynamics

NEMD is a simulation technique in which a perturbation is applied to the system and it more closely represents the real world and it is most suitable for computing transport coefficients. The equations of motion obtained by applying which applies a streaming velocity by introducing a fictitious external field in the Hamiltonian are called the SLLOD equations of motions [145]:

$$\begin{aligned}\dot{\mathbf{r}}_i &= \frac{\mathbf{p}_i}{m_i} + \mathbf{r}_i \cdot \nabla v \\ \dot{\mathbf{p}}_i &= \mathbf{F}_i - \mathbf{p}_i \cdot \nabla v\end{aligned} \tag{3.30}$$

where ∇v is the streaming velocity; in lubricants simulations we are mainly interested in planar shear flow for which the streaming velocity is equal to

$$\nabla v = \begin{bmatrix} 0 & 0 & 0 \\ \dot{\gamma} & 0 & 0 \\ 0 & 0 & 0 \end{bmatrix} \tag{3.31}$$

where $\dot{\gamma} = \frac{\partial v_x}{\partial y}$ is the shear rate or the magnitude of the velocity gradient. These new equations have to be used with a set of proper periodic boundary conditions; for a planar shear rate the appropriate PBC are the Lee-Edwards periodic boundary condition or the Lagrangian-Rhomboid [146]. Shearing a system creates heat that has to be dissipated and this is achieved by the implementation of a thermostat. Many thermostats are available but we will restrain ourselves on the Nosé-Hoover thermostat as in EMD. Nosé-Hoover is widely spread but has a known deficiency for NEMD; it assumes a linear profile of the streaming velocity and considers excess thermal energy any non-linearity in the profile which enhances ordering effect such as alignment to the streaming velocity[146].

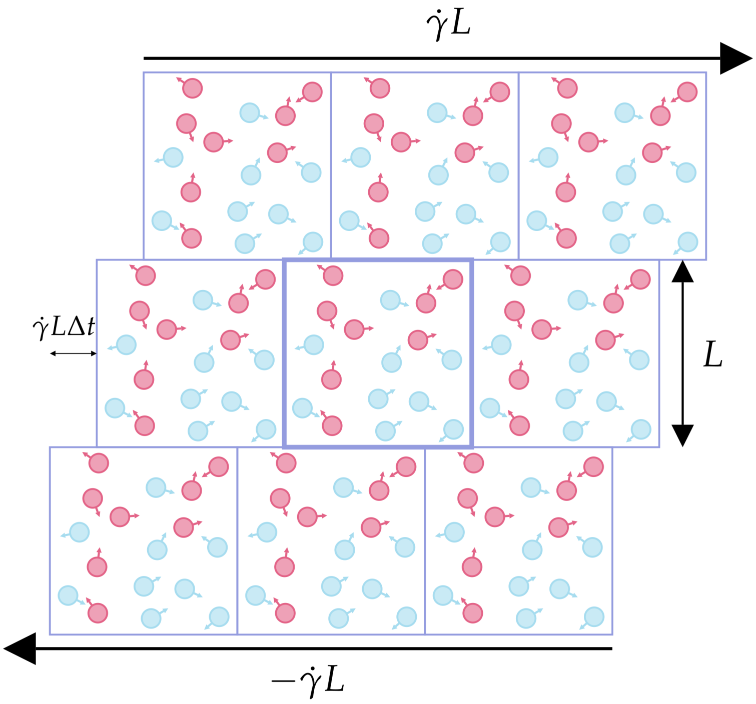

FIGURE 3.6: "sliding-brick" Lee-Edwards periodic boundary conditions

Introducing the SLLOD equations of motion allows us to properly compute and predict shear viscosity for Newtonian and non-Newtonian liquids at different shear rates[146]. For a system in a non-equilibrium steady-state viscosity can be calculated by

$$\eta(t) = -\frac{\langle P_{xy}(t) \rangle}{\dot{\gamma}} \tag{3.32}$$

which is related to eq 2.1, where $\langle P_{xy}(t) \rangle$ is the average of the off-diagonal terms of the pressure tensor.

In confined NEMD simulations the thermostat is usually only applied to the wall atoms allowing a thermal gradient to develop through the thickness of the lubricant film. Applying the thermostat directly to the confined fluid molecules has been shown to artificially influence their structure, flow and friction behaviour under shear. For example, the slip behaviour of thermostatted molecules confined between rigid walls disagrees with that observed experimentally and in simulations where only flexible wall atoms are thermostatted.

Stochastic thermostats, e.g. Langevin, are generally more popular than the Nosé-Hoover thermostat since they can remove heat more efficiently. Pressure is usually controlled by applying a constant normal force to one or both of the walls. The latter technique is usually preferable since the former has been shown to lead to unphysical behaviour in certain systems; as the force between two surfaces does not evolve smoothly with the separation distance as predicted by the van der Waals theory.

Chapter 4

Quantum Chemistry

4.1 Schrödinger's equation

In chapter 3 Newton's equations of motions were used to describe the time evolution of a system of classical particles, this is not possible in the field of quantum chemistry: Newton's equations do not work for electrons.

In 1926, Erwin Schrödinger published in a breakthrough paper the following equation[147]:

$$\hat{\mathcal{H}}\psi(\mathbf{r},t) = i\hbar\frac{\delta}{\delta t}\psi(\mathbf{r},t) \tag{4.1}$$

where $\psi(\mathbf{r},t)$ is called wavefunction and it describes the state of a system, $\hbar$ is the Plank's constant and $\hat{\mathcal{H}}$ is the Hamiltonian operator, which, for a single particle, is as follows:

$$\hat{\mathcal{H}} = \hat{\mathcal{K}} + \hat{\mathcal{U}} = -\frac{\hbar^2}{2m}\nabla^2 + \mathcal{U}(\mathbf{r},t) \tag{4.2}$$

where ∇^2 is called Laplacian and m is the particle mass.

The equation is the time-dependent Schrödinger equation and it describes the time evolution of a quantum system. If the system under investigation does not depend on time its state is called stationary state and it is a solution of the time-independent Schrödinger equation which is extensively used in quantum chemistry.

$$\hat{\mathcal{H}}\psi(\mathbf{r}) = E\psi(\mathbf{r}) \tag{4.3}$$

In quantum mechanics the state of a system is completely described by its wavefunction and its interpretation is given by Bohr and it is the so-called Copenhagen interpretation of quantum mechanics: The probability density of finding a particle at a given point is equal to the absolute value of the wave function squared.

$$P_b = |\psi(\mathbf{r}_1, \mathbf{r}_2, ..., \mathbf{r}_N)|^2 \tag{4.4}$$

since it is a probability density it has to be normalized

$$\int d\mathbf{r}_1 \int d\mathbf{r}_2 ... \int d\mathbf{r}_N |\psi(\mathbf{r}_1, \mathbf{r}_2, ..., \mathbf{r}_N)|^2 = 1 \tag{4.5}$$

The expectation value of a physical property is obtained by applying its corresponding operator to the wave function as follow :

$$\langle O \rangle = \int d\mathbf{r}_1 \int d\mathbf{r}_2 ... \int d\mathbf{r}_N \psi^*(\mathbf{r}_1, \mathbf{r}_2, ..., \mathbf{r}_N) \hat{O} \psi(\mathbf{r}_1, \mathbf{r}_2, ..., \mathbf{r}_N) \tag{4.6}$$

The Schrödinger equation is not limited to a single particle system, it can fully describe a many-body problem. For the sake of simplicity and calculations, we resort to the use of atomic units in which the fundamental constants are all set to 1. The many-body Hamiltonian is described as

$$\hat{\mathcal{H}} = -\frac{1}{2} \sum_{i=1}^{N} \nabla_i^2 - \frac{1}{2} \sum_{k=1}^{M} \nabla_k^2 - \sum_{i=1}^{N} \sum_{k=1}^{M} \frac{Z_k}{r_{ik}} + \sum_{i=1}^{N} \sum_{j>i}^{N} \frac{1}{r_{ij}} + \sum_{k=1}^{M} \sum_{l>k}^{M} \frac{Z_k Z_l}{R_{kl}} \tag{4.7}$$

the first two terms are the kinetic energy of the electrons and nuclei, the third term is the electrons-nuclei attraction, the fourth is the electron-electron repulsion and the last is the nuclei-nuclei repulsion. The Hamiltonian is quite daunting but it is possible to introduce an approximation known as the Born-Oppenheimer approximation which states that due to the mass difference between electrons and nuclei, one can decouple the electronic motion from the nuclei since electrons move much faster than nuclei when the nucleus moves the electrons instantaneously follow it, i.e. to the electrons the nuclei are fixed in space. This leads to two equations one for the electrons and one for the nuclei

$$\text{Electronic} : \hat{\mathcal{H}}_e \psi(\mathbf{r}, \mathbf{R}) = E_e \psi(\mathbf{r}, \mathbf{R}) \tag{4.8a}$$

$$\text{Nuclear} : [\hat{\mathcal{T}}_n + E_e(\mathbf{R})] \phi(\mathbf{R}) = E \phi(\mathbf{R}) \tag{4.8b}$$

where $\hat{\mathcal{H}}_e$ is given by:

$$\hat{\mathcal{H}}_e = -\frac{1}{2} \sum_{i=1}^{N} \nabla_i^2 - \sum_{i=1}^{N} \sum_{k=1}^{M} \frac{Z_k}{r_{ik}} + \sum_{i=1}^{N} \sum_{j>i}^{N} \frac{1}{r_{ij}} \tag{4.9}$$

where $E_e(R)$ means that the nuclei move inside an electron cloud generated by the electronic equation.

Born-Oppenheimer approximation decreases the complexity of the equations but due to the electron-electron repulsion it is still not possible to solve exactly the electronic equations and further approximate methods to solve the equation are necessary, the most known is called Hartree-Fock

4.2 Hartree-Fock Method

The Hartree-Fock method is a self-consistent iterative method, which means it has to be solved in an iterative way until the same set of values is found within two consecutive cycles. The main approximations in the Hartree-Fock theory are the mean-field approximation where the potential energy only depends on the positions of the particles, the wavefunction as a Slater determinant (product of spin-orbitals) and substitution of the instantaneous interaction between electrons by an average potential, i.e. the electron i interacts with the field generated by the N-1 electrons.

$$\psi_{\text{trial}}(\mathbf{x}_1, \mathbf{x}_2, ..., \mathbf{x}_N) = \frac{1}{\sqrt{N!}} |\phi_1 \phi_2 ... \phi_N\rangle \tag{4.10}$$

where ϕ_i is a spin-orbital, which is a monoelectronic wavefunction made of a spatial part and a spin part, the wavefunction has the subscript trial because in principle one does not know the exact wavefunction and the Hartree-Fock method starts by guessing one and minimize the energy by varying the wavefunction parameters.

This approach is based on the variational principle which states that the energy of a trial wavefunction is an upper-bound solution to the exact ground state energy:

$$\langle \psi_{\text{trial}} | \hat{\mathcal{H}} | \psi_{\text{trial}} \rangle \geq \langle \psi_0 | \hat{\mathcal{H}} | \psi_0 \rangle, \tag{4.11}$$

where the equal sign holds true only if the trial wavefunction is exactly the ground state wavefunction.

The Hartree-Fock method applies this principle to approximate the ground state energy. By solving the Hartree-Fock equations, the total energy is expressed as:

$$E_{\text{HF}} = \langle \psi_{\text{trial}} \mid \hat{\mathcal{H}} \mid \psi_{\text{trial}} \rangle = \sum_i^N \left\langle i \mid \hat{h}_i \mid i \right\rangle + \frac{1}{2} \sum_i^N \sum_j^N [\langle ij \mid ij \rangle - \langle ij \mid ji \rangle] \tag{4.12}$$

where

$$\left\langle i \mid \hat{h}_i \mid i \right\rangle = \int \phi_i^*(1) \left[-\frac{1}{2} \nabla_i^2 - \sum_{k=1}^M \frac{Z_k}{r_{ik}} \right] \phi_i(1) d\mathbf{r}_1 \tag{4.13a}$$

$$\langle ij \mid ij \rangle = \int \phi_i^*(1) \phi_j^*(2) \frac{1}{r_{12}} \phi_i(1) \phi_j(2) d\mathbf{r}_1 d\mathbf{r}_2 \tag{4.13b}$$

$$\langle ij \mid ji \rangle = \int \phi_i^*(1) \phi_j^*(2) \frac{1}{r_{12}} \phi_j(1) \phi_i(2) d\mathbf{r}_1 d\mathbf{r}_2 \tag{4.13c}$$

the first term is the monoelectronic term and is made by the kinetic energy of the electron and its interaction with the nuclei, the other two terms are bi-electron terms and they are called Coulomb integral and Exchange integral, the $\frac{1}{r_{12}}$ represent the distance between electron 1 and electron 2. The associated operators are $\hat{\mathcal{J}}$ e $\hat{\mathcal{K}}$.

The Hartree-Fock method retrieves 99 % of the non-relativistic energy but it is not enough to study chemical reactions between molecules. Different methods were developed to retrieve the 1 % of missing energy called correlation energy and defined as

$$E_{\mathrm{corr}} = E_{\mathrm{non-relativistic}} - E_{\mathrm{HF}} \tag{4.14}$$

4.3 DFT

In section 4.2 the energy of a system was seen to be a functional of the wavefunction $E[\psi]$, in DFT the focus is placed on the electron density: that is because for an N particles system, the external potential $v(\mathbf{r})$, the potential from the external field due to positively charged nuclei, fully determines the system Hamiltonian and hence the ground-state wavefunction and all other properties. In 1964 Hohenberg and Kohn published in Physical Review a paper that presented the theorems on which DFT was built. The first theorem states

Theorem 4.1. *$v(\mathbf{r})$ is a unique functional of $\rho(\mathbf{r})$ apart of a trivial additive constant*

Since ρ determines the number of electrons, it follows that the electron density is sufficient to fully determine the Hamiltonian.

The second theorem links the electron density and the system energy via the variational principle which allows the new formalism to be of practical applicability.

Theorem 4.2. *For a trial density $\tilde{\rho}(\mathbf{r})$ such that $\tilde{\rho}(\mathbf{r}) \geq 0$ and $\int \tilde{\rho}(\mathbf{r})d\mathbf{r} = N$*

$$E_0 \leq E_v[\tilde{\rho}(\mathbf{r})] \tag{4.15}$$

where $E_v[\tilde{\rho}(\mathbf{r})]$ is the energy functional

These theorems provide us with the theoretical framework of DFT. They define the uniqueness of the functional of the density but they do not provide a form for this functional and to carry on DFT calculations one has to guess a functional form. Many functionals over the past 60 years have been developed and it still is an active field of research. The DFT allows us to replace the $4N$ variables wavefunction with the much simpler electron density.

The total energy of a system is given by

$$E = K + V_{\mathrm{ee}} + V_{\mathrm{Ne}} \tag{4.16}$$

where the first term is the particle's kinetic energy, the second is the repulsive interaction between electrons and the last term is the attractive interaction between nuclei and electrons.

Since the energy is a functional of the density so must be the single terms

$$E[\rho] = \int \rho(\mathbf{r}) V_{\mathrm{Ne}} d\mathbf{r} + F_{\mathrm{HK}}[\rho] \tag{4.17}$$

where $F_{\mathrm{HK}}[\rho]$ is the sum of kinetic energy and interaction potential between electrons.

$$F_{HK}[\rho] = K[\rho] + V_{ee}[\rho] \tag{4.18}$$

$F_{\mathrm{HK}}[\rho]$ is called the holy grail of DFT since if one is able to know its form it would lead to the exact solution of the Schrödinger equation, unfortunately, no such thing is known and approximate forms were implemented.

4.3.1 Kohn-Sham Approach

Kohn-Sham developed the practical framework of modern DFT [148]. The exact functional form for the Hohenberg-Kohn functional for a system of interacting particles is not known, but Kohn and Sham proved that it is possible to gain a good approximation by constructing a non-interacting system which has the same electron density as the real system. For this kind of system is it possible to obtain accurate descriptions for the kinetic energy and Coulomb interaction following the same description as in the Hartree-Fock theory

$$K_{\mathrm{ni}}[\rho] = \langle \phi_{\mathrm{ni}} | \sum_{j}^{N} (-\frac{1}{2} \nabla_j^2) | \phi_{\mathrm{ni}} \rangle \tag{4.19}$$

the kinetic term in 4.19 is exact for the non-interacting particle and it is a good approximation of the kinetic energy of the interacting particle. In the same way, one can obtain the Coulomb term. The Kohn-Sham approach is to include everything unknown into a single term called *exchange-correlation energy* which contains the difference between the real kinetic energy term and the Kohn-Sham kinetic energy plus the difference between the real interaction potential between electrons and the Coulomb potential:

$$E_{\mathrm{XC}}[\rho] = (K[\rho] - K[\rho]_{\mathrm{ni}}) + (V_{\mathrm{ee}}[\rho] - J[\rho])\rangle \tag{4.20}$$

where $J[\rho]$ is the Coulomb term. The wavefunctions in 4.19 are called Kohn-Sham orbitals and they are necessary to obtain the kinetic and potential terms: how can one determine which wavefunction to use? Tje Kohn-Sham's approach is to develop a SCF scheme that closely resembles that of the Hartree-Fock theory. The final equation of the Kohn-Sham approach is as follows

$$\left[-\frac{1}{2} \nabla^2 + v_{\mathrm{eff}} \right] \psi_i = \varepsilon_i \psi_i \tag{4.21}$$

where

$$v_{\mathrm{eff}}(\mathbf{r}) = v(\mathbf{r}) + \int \frac{\rho\left(\mathbf{r}'\right)}{|\mathbf{r}-\mathbf{r}'|} d\mathbf{r}' + v_{\mathrm{xc}}(\mathbf{r}) \tag{4.22}$$

One way to approach the SCF cycle is: [149]

1. Define a non-interacting system of N particles whose ground state is a single Slater determinant ϕ_{ni} and whose density ρ_{ni} is equal to the real density ρ_0.
2. The orbitals which form the Slater determinant are the solutions of N single particle equations 4.21.
3. The energy of the interacting system is separated into the kinetic energy K_{ni} of the non-interacting system, the electron-electron Coulomb energy J and the remainder E_{XC}.
4. The orbitals are optimized via the variational principle
5. The orbitals give us the density provided we know the form of the functionals. In all real applications, however, we have to resort to approximations for the unknown functional E_{XC}.

4.3.2 Exchange-correlation functionals

The exact analytical expression for the exchange-correlation is not known and hence approximations are needed. As shown in the previous section a useful system is that of a uniform gas with a constant electron density for this system, it is possible to derive the exchange part of the functional exactly and it is possible to determine the correlation via numerical methods. This approximation is known as the local density approximation (LDA), and the exchange functional is given by,

$$E_x^{LDA} = -\frac{3}{4}\left(\frac{3}{\pi}\right)^{\frac{1}{3}} \int \rho^{\frac{4}{3}}(\mathbf{r}) d\mathbf{r}. \tag{4.23}$$

The reasoning behind this choice is that while the electronic density distribution in molecular and periodic systems is inhomogenous, if we consider a small volume inside this system they can be considered homogeneous and a good approximation comes from the uniform gas as described previously. The LDA functional is appropriate when the density varies slowly with respect to its position in space, **r**. A natural extension is to include the gradient of the density making the functional semilocal as it depends not only on **r** but also on the infinitesimal neighbourhood of **r** The general form of these functionals, known as generalized gradient approximation functionals (GGA) is

$$E_{xc}^{\mathrm{GGA}} = f(\rho(\mathbf{r}), \nabla\rho(\mathbf{r})) d\mathbf{r} \tag{4.24}$$

One of the most used GGA functional, especially in the solid state community is the Perdew-Burke-Ernzerhof (PBE) functional

$$E_x^{PBA} = \int \rho^{\frac{4}{3}}(\mathbf{r}) f(\nabla\rho(\mathbf{r})) d\mathbf{r}, \tag{4.25}$$

where f is given by,

$$f = C_\alpha + \beta\left(\frac{x^2}{1+\gamma x^2}\right), \tag{4.26}$$

and $x(\mathbf{r}) = \frac{\nabla\rho(\mathbf{r})}{\rho^{\frac{4}{3}}(\mathbf{r})}$ is a dimensionless entity. The PBE functional has no empirical parameter and is designed only to match some of the constraints an exact functional must satisfy. In the molecular DFT community, the Becke 88 (B88) functional is more common and contains empirical parameters.

One way to improve GGA functionals is to add the dependence on the second derivative and/or kinetic energy density such functionals are called meta-GGA(mGGA) and the general form is given by

$$E_{xc}^{\text{mGGA}} = f(\rho(\mathbf{r}), \nabla\rho(\mathbf{r}), \nabla^2\rho(\mathrm{r}, \tau)) d\mathbf{r} \tag{4.27}$$

mGGA performs better than GGA, but comes with additional computational cost. Another approach to improve functionals is to add exchange and/or correlation functional from the Hartree-Fock theory, this helps in alleviating some of the well-known limitations of standard DFT functionals. These are called Hybrid functionals.

4.3.3 Finite temperature DFT

Finite-temperature DFT is a theory that was developed in order to deal with metals by introducing fractional occupancies. In metallic systems or in systems with very low band gaps the SCF shows numerical instabilities due to states swapping occupancies from one iteration to the other. This is called level-crossing and hinders the convergence of your self-consistent cycle. This is caused by the binary nature of the occupancies that must be either 0 or 1, by relaxing this constraint you can improve the convergence of your calculations. The occupancies are usually determined by introducing a function that smears the occupancies around the Fermi level. In Ensemble DFT proposed by Mermin [150] each of the conclusions of Hohenberg and Kohn for the ground state has their counterpart in thermal equilibrium, To show this, Mermin constructed a grand potential functional of the density

$$\Omega[\rho] = \hat{\mathcal{H}}[\rho] - T\hat{S}[\rho] - \mu\hat{N} \tag{4.28}$$

whose minimum is the equilibrium grand potential

$$\Omega = \Omega\left[\rho_0\right] = -\frac{1}{\beta}\ln \mathrm{Tr}\, \mathrm{e}^{-\beta(\dot{H}-T\hat{S}-\mu\dot{N})} \tag{4.29}$$

where $\hat{\rho}_0$ is the grand canonical density matrix

$$\hat{\rho}_0 = \frac{\mathrm{e}^{-\beta(\dot{H}-T\hat{S}-\mu\tilde{N})}}{\mathrm{Tr}\, \mathrm{e}^{-\beta(\dot{H}-\mu T\hat{S}\tilde{N})}}. \tag{4.30}$$

where the entropic term is

$$S[\{f_i\}] = -k\sum_i [f_i \ln f_i + (1-f_i)\ln(1-f_i)] \tag{4.31}$$

where f_i are occupancies and the density is computed (in the KS regime) by

$$n(\mathbf{r}) = \sum_i^{\frac{N}{2}} f(\epsilon_i)\psi_i(\mathbf{r})\psi_i^*(\mathbf{r}), \tag{4.32}$$

The Mermin theorem leads to the fact that not only the energy but also the entropy is a functional of the equilibrium density. The equilibrium thermal ensemble of Mermin at fixed chemical potential (Grand Canonical Ensemble) allows the fluctuations of the number of electrons around the average number so it also follows that there must be discontinuities in the derivative of the energy with respect to the number at integer occupations or, in the case of solids, for filled bands. This means that it can deal with metallic systems where the fractional occupancies are not solvable with conventional DFT

4.3.4 Plane waves

In both Hartree-Fock theory and DFT, the trial wavefunction is typically expanded in a basis set. This basis can be either localized or extended. Localized basis functions, such as Gaussian functions, are confined to specific regions of space, making them suitable for molecular systems. On the other hand, extended basis functions, such as plane waves, are delocalized and periodic, making them ideal for periodic systems like crystals.

The periodic nature of plane waves matches the periodicity of the unit cell, simplifying calculations for crystalline systems compared to using localized basis functions. The most important theorem regarding periodic systems is the Bloch theorem which states that wavefunctions can be written as a product of a plane wave and a function with the same periodicity as the cell.

$$\psi_{n\mathbf{k}}(\mathbf{r}) = \mathrm{e}^{i\mathbf{k}\cdot\mathbf{r}}u_{n\mathbf{k}}(\mathbf{r}) \tag{4.33}$$

where $\mathbf{k}$ is a wavevector and

$$u_{n\mathbf{k}}(\mathbf{r}+\mathbf{R}) = u_{n\mathbf{k}}(\mathbf{r}). \tag{4.34}$$

note that the previous equations imply that

$$\psi_{n\mathbf{k}}(\mathbf{r}+\mathbf{R}) = \mathrm{e}^{i\mathbf{k}\cdot\mathbf{r}}\psi_{n\mathbf{k}}(\mathbf{r}). \tag{4.35}$$

Practically, the periodic function $u_{n,\mathbf{k}}(\mathbf{r})$ is decomposed into a Fourier series,

$$u_{n,\mathbf{k}}(\mathbf{r}) = \sum_{\mathbf{G}} c_{n\mathbf{k}} e^{i\mathbf{G}\cdot\mathbf{r}}, \tag{4.36}$$

where the G vectors are defined by the basis of the reciprocal lattice of your system. A Fourier series contains infinite terms, in practical calculations we define a kinetic energy cutoff which in turn limits the amount of term in the sum. The kinetic energy cutoff is defined as

$$E_{\mathrm{cut}} = \frac{|\mathbf{G}_{\mathrm{max}}|^2}{2} \tag{4.37}$$

Bloch theorem transformed an infinite system problem, i.e. an orbital for each electron, to study only the electrons in the unit cell. The price is that the solutions become a function of the reciprocal space vector $\mathbf{k}$. The $\mathbf{k}$ appears as a parameter in the equation similar to the nuclear positions in molecular Hartree-Fock theory. The solutions are continuous as a function of $\mathbf{k}$.

4.3.5 Pseudopotentials

The fundamental idea of a "pseudopotential" is to reduce the cost of calculations by substituting the core electrons which are not important to chemical reactions by an effective potential. This approach not only reduces the computational cost but also allows to introduce corrections to relativistic effects which are more important for core electrons. In most cases, the loss in accuracy is not enough to justify the cost of fully considering all the electrons explicitly. To generate the potentials in molecular DFT Gaussian functions are used and since Gaussians are continuous there is no fixed distance to characterize the extent of the core potential and the quality of the pseudopotential is dependent on the number of electrons considered.

When plane waves are used as the basis set, the size of the basis is determined by the energy cutoff. However, the nuclear potential's singularity and the strongly localized core electrons cannot be accurately described within a practical energy cutoff. To address this, pseudopotentials are employed to smooth out the nuclear charges. Typically, pseudopotentials are defined by a core radius, within which the potential is replaced by analytical functions, such as Bessel functions. The pseudo-wave function and its first and second derivatives are required to match those of the reference wave function at the core radius. The smaller the core radius the more accurate is the calculation but also the more expensive. There are many different kinds of pseudopotentials but only the norm-conserving and Projector Augmented (PAW) waves are briefly described here. The norm-conserving pseudopotentials proposed by Hamann, Schlüter and Chiang require that the integral of the square of the reference and pseudo-wave from 0 to the core radius agrees, resulting into conservation of the wave function norm.

The Projector Augmented Wave (PAW) wave function is written as a valence term expanded in a plane wave basis plus a contribution from the region within the core radius of each nucleus, evaluated on a grid. The contribution from a core region is expanded as a difference between two sets of densities, one arising from the (all-electron) atomic orbitals, the other from a set of nodeless pseudo-atomic orbitals, i.e. this term allows the wave function within the core region to adjust for different environments.

4.3.6 Onetep

DFT scales cubically with the number of electrons $\mathcal{O}(N^3)$. In order to address this problem linear-scaling approaches have been developed. In particular, throughout this thesis, the approach used in the ONETEP software is used[151, 152].

ONETEP implements a set of atom-centred orbitals which are localised and non-orthogonal as:

$$\phi_\alpha(\mathbf{r}) = \sum_i \psi_i(\mathbf{r}) M_{i\alpha} \text{ and } \psi_i(\mathbf{r}) = \sum_\alpha \phi_\alpha(\mathbf{r}) M_i^\alpha \tag{4.38}$$

where ψ_i are the KS orbitals and M_i^α and $M_{i\alpha}$ are unitary matrices that map KS into the new basis and vice-versa. In the new basis, the Hamiltonian and overlap matrices become sparse allowing us to obtain linear-scaling behaviour by avoiding dense matrices diagonalisation.

The orbitals used are non-orthogonal generalised Wannier functions (NGWFs) which are expanded in a set of periodic sinc (psinc) basis functions

$$\phi_\alpha(\mathbf{r}) = \sum_k D_k(\mathbf{r}) c_{k,\alpha} \tag{4.39}$$

where k is the index that defines the grid point in the simulation cell and $C_{k,\alpha}$ is the expansion coefficient and D_k represents the psinc function.

By specifying a cut-off radius, r_c, for which $\rho(\mathbf{r}, \mathbf{r}') = 0$ beyond $|\mathbf{r} - \mathbf{r}| > r_c$ we localise NGWFs so that we do not calculate any interactions of points far apart from each other.

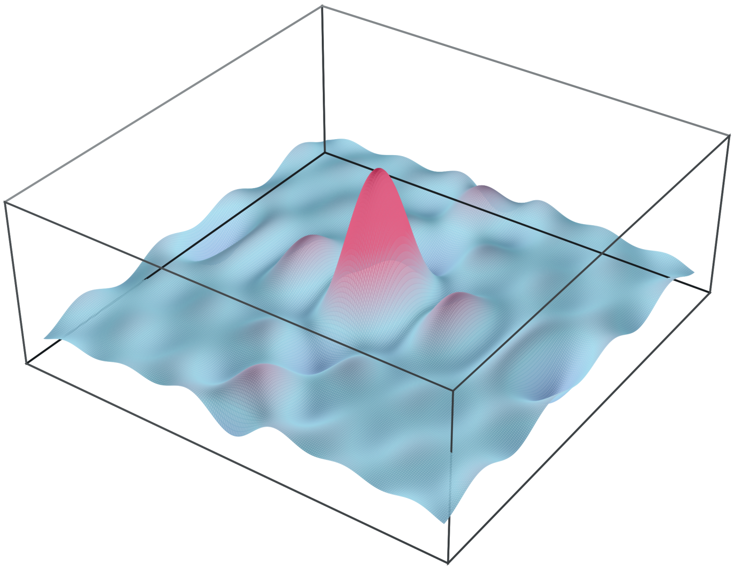

FIGURE 4.1: Psinc function

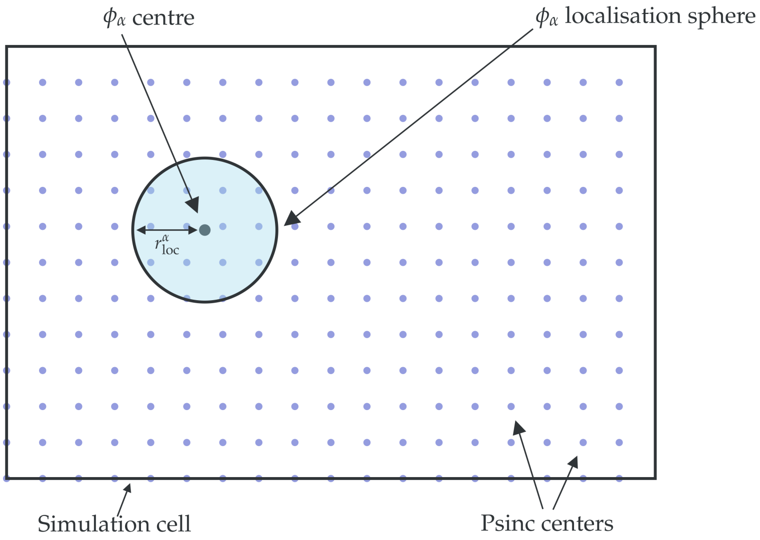

FIGURE 4.2: Localization on the $\phi_\alpha(\mathbf{r})$ function in real space. From the regular grid of psinc functions $D_k(\mathbf{r})$, only the ones within its localization sphere are allowed to contribute to $\phi_\alpha(\mathbf{r})$.

The density matrix in terms of the new orbital is

$$\rho\left(\mathbf{r},\mathbf{r}'\right) = \phi_\alpha(\mathbf{r}) K^{\alpha\beta} \phi^*_\beta\left(\mathbf{r}'\right) \tag{4.40}$$

where $K^{\alpha\beta}$ is the density kernel, which is the representation of the density matrix in the basis of the localized orbitals

$$K^{\alpha\beta} = \sum_n M^\alpha{}_i f_i M_i^{\dagger\beta}, \tag{4.41}$$

where f_i represents the occupancy of state i.

Localised basis, such as Gaussian or numerical atomic orbitals, are usually predetermined and there is usually no systematic way to improve the quality of the basis. A way to overcome this limitation is to optimise both the basis and the density kernel via a double-loop approach. Removing the constraints on the basis allows for more variational freedom while retaining the small number of basis typical when using localised basis. Finally, by tuning the cut-off radius and the spacing of the psinc grid, it is possible to improve the quality of the calculations.

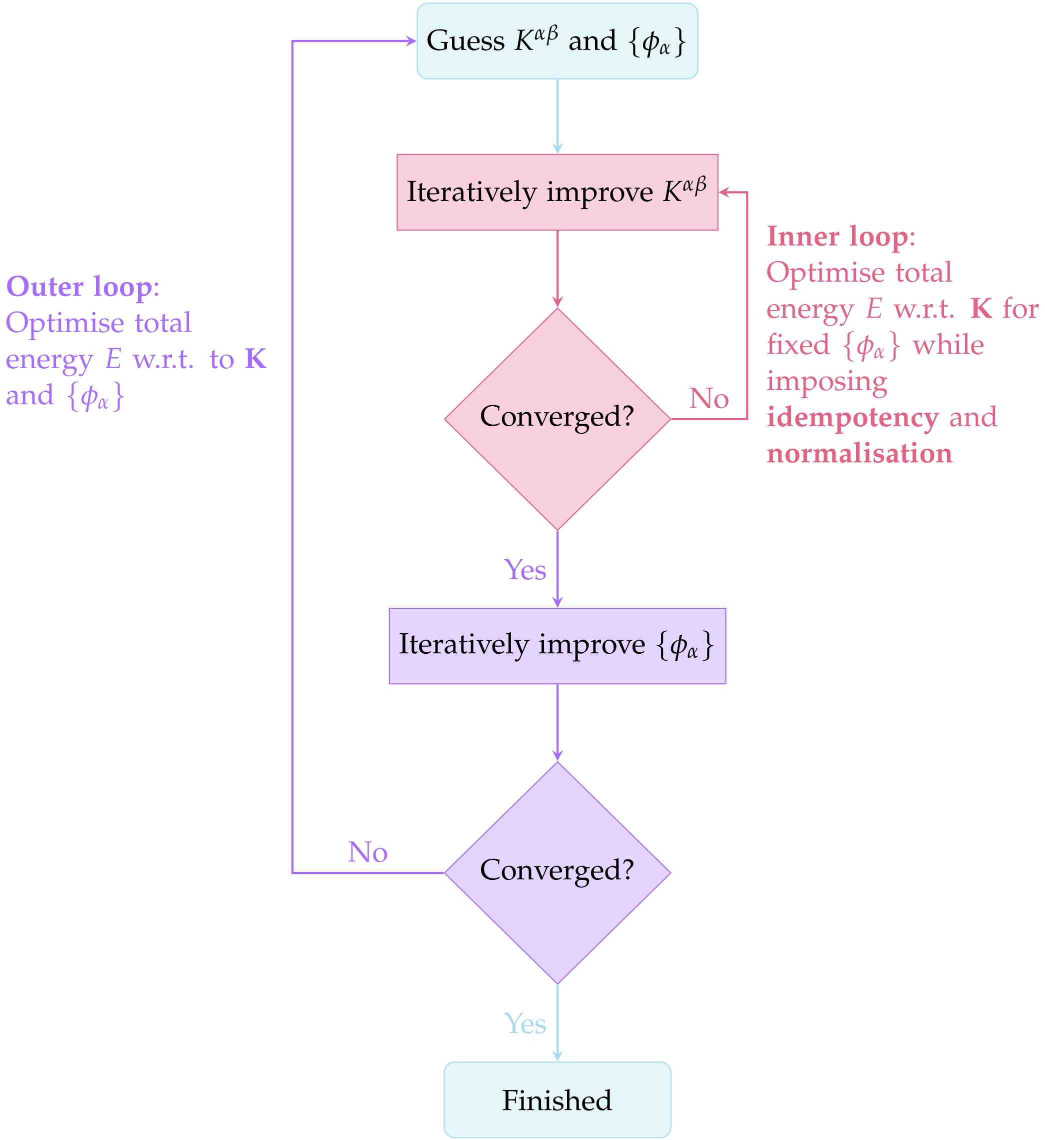

FIGURE 4.3: Onetep double loop, inner loop optimises the total energy at fixed NGWFs imposing idempotency. Outer loop optimises total energy with respect to both density kernel and NGWFs

4.3.7 DFT+U

DFT+U is an extension to DFT based on the Hubbard model[153], it is used to improve the description of the so-called strongly correlated materials which consist of transition metals and their oxides as well as lanthanoid oxide materials, organometallic molecules and more. These materials are characterised by localised orbitals or bands and conventional exchange-correlation functional as LDA, GGA, and meta-GGA are not able, sometimes, to capture their physics correctly

Typically, they tend to favour high-spin ground states and/or metallic states and to underestimate local magnetic moments and the band gap. These failures stem from the inability of the approximate xc functionals to satisfy the flat-plane condition, which combines two constraints that the exact functional must meet: piecewise linearity with respect to electron number and the spin constancy constraint.

In DFT+U, the idea is to describe the strongly correlated electronic states using the Hubbard model by projecting the Kohn-Sham orbitals onto a localised basis, while the rest of the valence electrons are treated at the standard DFT level.

The general form for the total energy in DFT+U is given by:

$$E_{\mathrm{DFT+U}}[\rho(\mathbf{r})] = E_{\mathrm{DFT}}[\rho(\mathbf{r})] + E_{\mathrm{Hub}}\left[\{n_i\}\right] - E_{\mathrm{dc}}\left[\{n_i\}\right] \tag{4.42}$$

In the above $E_{\mathrm{DFT}}[\rho(r)]$ is the energy at the standard DFT level, $E_{\mathrm{Hub}}\left[\{n_i\}\right]$ is the Hubbard correction and the last term $E_{dc}\left[\{n_i\}\right]$ is a double-counting correction for that contribution already included in the LDA term.

The DFT+U correction term is usually thought of as an explicit mean-field treatment of the exchange-correlation energy contributed by the correlated sites There are many variants of the DFT+U method, the flavour implemented in ONETEP is the basis-set independent, rotationally invariant quadratic penalty functional of Cococcioni[154] defined by the additive energy correction.

$$E_{\mathrm{DFT+U}}\left[n^{(I)(\sigma)}\right] = \sum_{I\sigma} \frac{U^{(I)}}{2} \mathrm{Tr}\left[n^{(I)(\sigma)}\left(1 - n^{(I)(\sigma)}\right)\right] \tag{4.43}$$

Here, U is an estimate of the scalar screened density-density Coulomb repulsion between localised orbitals. The occupancy matrix of the correlated atomic site I, for spin channel σ, is defined, in the case of orthonormal projector functions $\{|\varphi_m^{(I)}\rangle\}$, and density-matrix $\hat{\rho}^{(\sigma)}$, by

$$n_{mm'}^{(I)(\sigma)} = \langle \varphi_m^{(I)} | \hat{\rho}^{(\sigma)} | \varphi_{m'}^{(I)} \rangle \tag{4.44}$$

The DFT+U method forces the on-site occupancy matrix to be idempotent. This means that the DFT+ U method penalises non-integer occupancy of these orbitals, tending to fill states with occupancy greater than 0.5 or occupancy less than 0.5, as can be seen from the expression for the DFT+U potential.

$$\hat{V}^{(\sigma)}_{\text{DFT+U}} = \sum_I U^{(I)} |\varphi^{(I)}_m\rangle \left(\frac{1}{2}\delta_{mm'} - n^{(I)(\sigma)}_{mm'}\right) \langle\varphi^{(I)}_{m'}| \tag{4.45}$$

The DFT+U term may be considered as a correction which cancels the contribution to the energy due to the spurious self-interaction of a partially occupied orbital. In this case, the U parameter is the curvature of the total energy with respect to the occupancy of the correlated manifold. The U parameter can be computed empirically or from linear-response theory (among other methods such as constrained DFT) according to the prescription given in [155]. Standard DFT+U only deals with like-spin electrons, a corrective term to include J for anti-parallel spin is described in and is given by

$$E_J[n^\sigma] = \sum_I \frac{J^I}{2} \mathrm{Tr}[n^{I\sigma} n^{I-\sigma}] \tag{4.46}$$

The inclusion of this term leads to the so-called DFT+U+J method

4.3.7.1 Linear Response

The basic idea is to compare the response of the system to a perturbation in the DFT and in the DFT+U frameworks. We start by defining the response function χ, which describes how the occupation of localised orbitals changes with respect to a shift in the potential acting on these orbitals: The linear response method determines the Hubbard U parameter by comparing the response of the system to a perturbation in standard DFT and DFT+U frameworks. We define the response function χ as:

$$\chi = \frac{dn^{I\sigma}}{d\alpha} \tag{4.47}$$

where n is the occupation matrix of the localised orbitals and α is a potential shift applied to these orbitals. We compute two response functions:

- χ_0: the bare Kohn-Sham (KS) response (U)
- χ: the interacting response (with U)

These are related by:

$$U = \chi^{-1} - \chi_0^{-1} \tag{4.48}$$

which allows us to compute U. In practice, we compute χ_0 and χ by applying a small perturbation α to the system:

$$\chi_0 \approx \frac{\Delta n}{\Delta \alpha} \text{(computed without U)} \tag{4.49}$$

$$\chi \approx \frac{\Delta n}{\Delta \alpha} \text{ (computed with a trial U)} \tag{4.50}$$

The perturbation is applied by shifting the potential of the localised orbitals:

$$V_{\text{ext}}^{p} = V_{\text{ext}} + \alpha \sum_{m,m'} |\varphi_{m'}^{(I)}\rangle\langle\varphi_{m}^{(I)}| \tag{4.51}$$

We then iterate until self-consistency is achieved. This is done in a supercell as the perturbation should not interact with its periodic images. This is the conventional linear response but it poses practical problems: The response χ_0 is usually computed via the first iteration of the Kohn-Sham equations during a self-consistent field (SCF) calculation; that is, the response is to be measured following the initial charge redistribution introduced by the perturbation but before the Kohn-Sham potential is updated. This approach is impractical to implement in codes that use a direct-minimization procedure of the total energy with respect to the density, Kohn-Sham orbitals, or density matrix.

Another approach to computing U and J is known as the minimum tracking method.

4.3.7.2 Minimum Tracking response

The minimum tracking method is based on a reformulation of the response matrices based on the ground state density of the perturbed system. We can identify the interacting and noninteracting response matrices as:

$$\chi_{IJ} = \frac{dn^{I}}{dv_{\text{ext}}^{J}} \tag{4.52}$$

$$(\chi_0)_{IJ} = \left[\frac{dn}{dv_{\text{KS}}}\left(\frac{dv_{\text{KS}}}{dv_{\text{ext}}}\right)^{-1}\right]_{IJ} \tag{4.53}$$

This allows us to work around the practical issues from the conventional linear response. This approach can also be extended to include the J exchange term In practice this is done by modifying the perturbation by including an additional term (spin-splitting):

$$V_{\text{ext}}^{p} = V_{\text{ext}} + \beta \sum_{m,m'} |\varphi_{m'}^{(I\uparrow)}\rangle\langle\varphi_{m}^{(I\uparrow)}| - |\varphi_{m'}^{(I\downarrow)}\rangle\langle\varphi_{m}^{(I\downarrow)}| \tag{4.54}$$

This approach will be used to compute U and J in chapter 8.

Part III

Results and Conclusions

Chapter 5

Ideal Mixtures

The work presented in this chapter has been published with the same figures in the *journal of physical chemistry B* [156].

5.1 Introduction

Lubricants play a crucial role in reducing machine degradation and improving efficiency by minimizing friction between surfaces. While lubricants can be categorized as biological or non-biological, our focus lies on the latter, specifically synthetic oils. These lubricants are designed to perform under extreme conditions, such as high temperatures and pressures, making them ideal subjects for studying operational behaviours.

The development of lubricants has traditionally relied on trial-and-error methods due to the complexity of their formulations. However, this approach limits our understanding of their atomistic behaviour and our ability to predict crucial properties like viscosity. To address these limitations, MD simulations have emerged as a powerful tool for predicting both static and dynamic properties of lubricants, offering valuable insights into their chemical and physical behaviours under various conditions.

Our research focuses on a model system consisting of an ideal mixture of two synthetic esters: Di-2-ethyl-hexyl sebacate (DEHS) and Di-2-ethyl-hexyl adipate (DEHA). This choice of an ideal mixture allows us to study a more realistic yet simple system compared to previous works that often focused on single-component lubricants or mixtures of linear and branched alkanes or fatty acids. To the best of our knowledge, this work represents the first MD simulation of ester mixtures in the context of lubricant research.

The primary goal of the work presented in this chapter is to establish a reliable workflow for predicting the viscosity of ester mixtures under operational conditions. By combining experimental measurements with both NEMD and EMD simulations, we aim to provide a comprehensive understanding of how composition, temperature, and pressure affect the behaviour of these lubricant mixtures. Our study evaluates densities and viscosities across a range of compositions, from pure DEHS to pure DEHA in 10% increments, creating a total of 11 distinct mixtures.

We examine these properties at three different temperatures (293 K, 343 K, and 393 K) to simulate various operational conditions. This approach allows us to validate our simulation methods against experimental data and explore the predictive power of MD simulations for complex lubricant systems. By focusing on an ideal mixture of synthetic esters, we bridge the gap between simplified model systems and more complex, industrially relevant lubricants. This research not only contributes to the fundamental understanding of lubricant behaviour at the molecular level but also paves the way for more efficient design and optimization of future ester-based lubricants for high-performance applications.

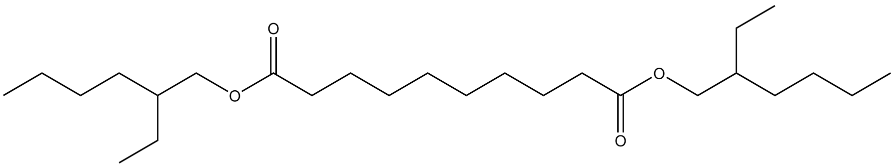

(A) Di-2-ethyl-hexyl sebacate (DEHS)

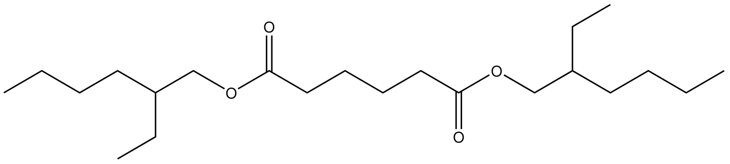

(B) Di-2-ethyl-hexyl adipate (DEHA)

FIGURE 5.1: Structures of two esters, sebacate (top) and adipate (bottom), studied in this work

In section 5.2 methodology, computational and experimental procedures are explained, in section 5.3 main results and their discussion are presented and in section 5.4 conclusions are presented.

5.2 Methodology

We employed both EMD and NEMD simulations in which system size, long-range cutoff, timestep and simulation length were investigated via trial and error process. The shear rate was chosen to provide a high signal-to-noise ratio but still lower than the critical shear rate $\dot{\gamma}_c$, which is the shear rate at which the system behaviour changes from Newtonian to non-Newtonian. This was done by running pure sebacate and adipate simulations at different shear rates and then fitting the values using the Powell-Eyring model.

$$\eta(\dot{\gamma}) = (\eta_N - \eta_\infty)\frac{\sinh^{-1}(\tau\dot{\gamma})}{\tau\dot{\gamma}} + \eta_\infty \tag{5.1}$$

where η_N is the newtonian viscosity, η_∞ is the viscosity at infinite shear rate, τ relaxation time.

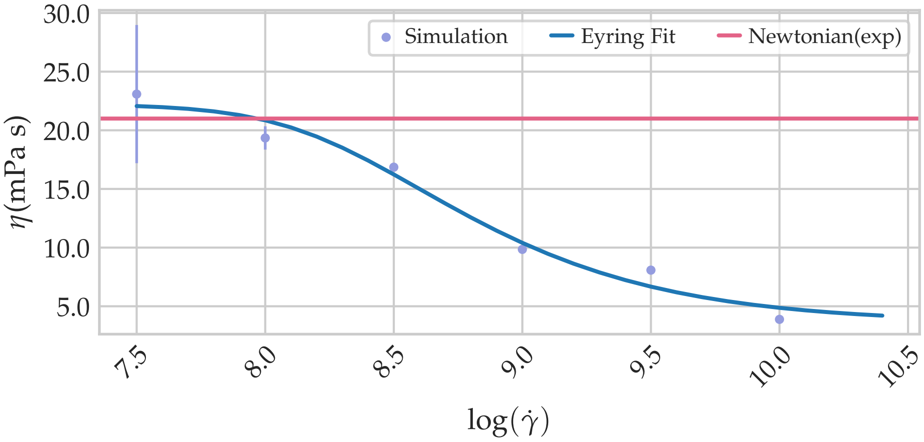

FIGURE 5.2: Sebacate room pressure and temperature viscosity values at different shear rates, Newtonian behaviour taken from experiments

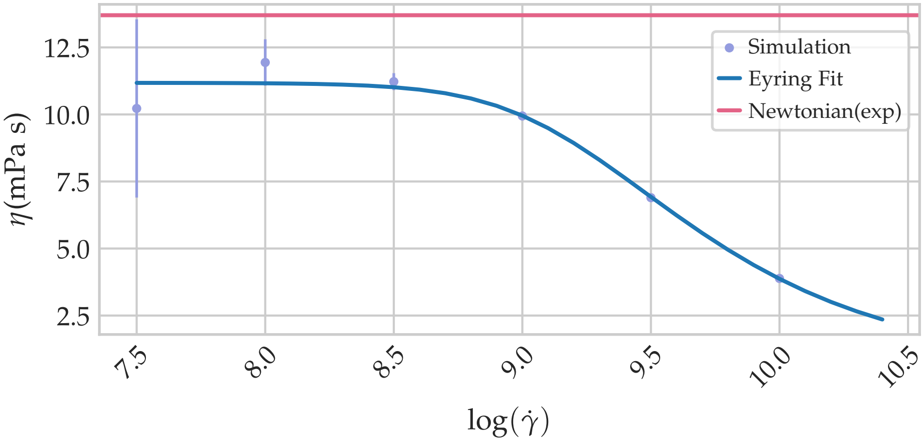

FIGURE 5.3: Adipate room pressure and temperature viscosity values at different shear rates, Newtonian behaviour taken from experiments

Considering the high standard deviation at a $\log(\dot{\gamma}) = 7.5$ it would be safe to assume that running simulations at $\log(\dot{\gamma}) = 8.0$ should be appropriate enough due to the behaviour of the system being Newtonian or quasi-Newtonian and the higher signal-to-noise ratio.

TABLE 5.1: Sebacate and adipate shear rate test simulations at room pressure and temperature, viscosity values in mPa s

$\log(\dot{\gamma})$	**Sebacate**	**Adipate**
7.5	23.09 ± 5.89	10.22 ± 3.32
8.0	19.35 ± 0.99	11.94 ± 0.86
8.5	16.85 ± 0.22	11.22 ± 0.31
9.0	9.85 ± 0.06	9.94 ± 0.17
9.5	8.08 ± 0.0079	6.89 ± 0.03
10	3.88 ± 0.0073	3.88 ± 0.004

5.2.1 Computational details

5.2.1.1 System Setting

A set of 11 mixtures with different concentrations of DEHS and DEHA were prepared using Packmol[157] to generate starting configurations which were then used by Moltemplate[158] to generate the files necessary to run the simulations using the MD software LAMMPS[159].

Each system consists of ≈ 12000 atoms (the numbers of DEHS and DEHA molecules per mixture are available in Table A.1 from Appendix A), and the force field employed throughout this work is the L-OPLS-AA[160] with a long-range cutoff of 12 Å. The reciprocal space part is solved using the PPPM algorithm[136] with a relative error in forces of 1×10^{-4}. All systems were run using 1 fs as timestep.

5.2.1.2 Equilibration

Each system first underwent a minimization step with energy and force thresholds of $1 \times 10^{-5}\,\mathrm{kcal\,mol^{-1}}$ and $1 \times 10^{-7}\,\mathrm{kcal\,mol^{-1}\,Å^{-1}}$ respectively, then went through 5 ns NVT run with a temperature damping parameter of 100 fs to reach the target temperature of 293 K or 343 K or 393 K. A 20 ns NPT run was performed to allow the system to relax its volume and reach the target pressure of 1 atm. Another 5 ns NPT simulation was also run and the average density was calculated. The system was then scaled to match the average density as in [9] then the systems were allowed to relax with another 5 ns NVT simulation. This was the starting point for both EMD and NEMD following different workflows.

5.2.1.3 EMD simulations

For the EMD only the system at 393 K was studied and the system underwent a 5 ns NVT simulation, at the end of which five configurations of positions and velocities were saved 50 fs apart from each other. These 5 different data files were used to run the EMD production runs which consisted of 80 ns NVT run, the autocorrelation and viscosity were calculated on the fly via fixes available in LAMMPS as an average of 3 off-diagonal pressure tensor values, P_{xy},P_{yz},P_{xz}. The viscosity reported is the 5 trajectories average.

5.2.1.4 NEMD simulations

The system was sheared for 10 ns using an NVT/sllod run with a shear rate of $1 \times 10^8\,\mathrm{s}^{-1}$, at the end of which five configurations of positions and velocities were saved 50 fs apart from each other. These data files will be used as a starting point for the production run, generating in total 5 different trajectories per mixture where the final viscosity will be the average of the trajectory viscosities Fig.5.4a. The production run consists of 40 ns using a NVT/sllod run with a shear rate of $1 \times 10^8\,\mathrm{s}^{-1}$. The viscosity for each trajectory was calculated using the last 35 ns. The velocity profile was checked to be linear for all trajectories as expected from bulk shear rate lubricant simulations.

5.2.2 Experimental procedure

The dynamic viscosities and the densities of DEHS and DEHA mixtures were measured by using an Anton Paar Stabinger viscometer, Stabinger SVM 3001, with autosampler XSample 530.

Stabinger viscosity measurement principle is based on a floating cylinder in test fluid which is centred by a rotating force. This is tracked in terms of speed and torque as viscosity indicators by a magnetic field and retarder, avoiding any bearing friction. Density is captured by the principle of a bending oscillator. The measurements could be done in an effective range from 0.2 mm^2/s up to 30000 mm^2/s.

The shear rate is part of the measurement principle and depends on the measured viscosity, hence it could not be pre-selected. Shear rate value in experimental measurements is at most in the range of $1000\,\mathrm{s}^{-1}$. This could be considered as low shear compared to bearing applications, but the value is comparable to measuring methods such as Ubbelohde for example. DEHS and DEHA samples were blended in 10% steps from 100% DEHS up to 100% DEHA. The measurements were done under normal pressures and covered three temperatures 293 K, 343 K and 393 K for every mixture. The densities and viscosities reported are an average of 2 and 3 different measurements respectively.

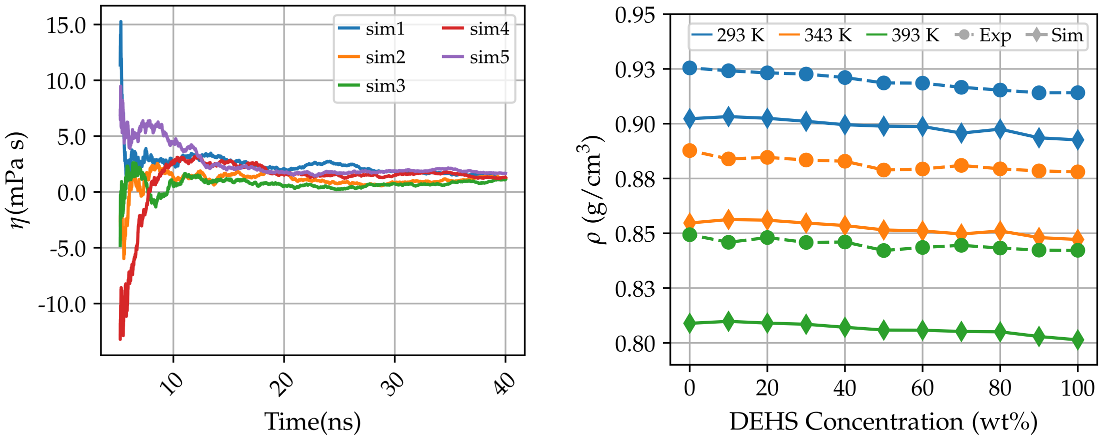

(A)

(B)

FIGURE 5.4: Viscosity values from 5 different trajectories for the 10% DEHS 90% DEHA mixture at 343 K (left), Experimental and Simulated densities (right) in g cm^{-3} as a function of DEHS concentration(wt%) at 293 K, 343 K and 393 K. Circles experimental data, diamonds simulated data.

5.3 Results and Discussion

5.3.1 Experimental results

Table 5.2 reports the measured densities in g cm^{-3} and measured viscosities in mPa s at 293 K, 343 K and 393 K. All measurements were obtained at atmospheric pressure.

TABLE 5.2: Experimental densities, ρ, in g cm^{-3} and dynamic viscosities, η, in mPa s at 293 K, 343 K and 393 K for the 11 mixtures studied.

Mixture (wt%)	Density (293 K)	Density (343 K)	Density (393 K)	Viscosity (293 K)	Viscosity (343 K)	Viscosity (393 K)
100% dehs 0% deha	0.9141	0.8779	0.8421	21.53	4.86	2.08
90% dehs 10% deha	0.9141	0.8781	0.8418	21.14	4.82	2.07
80% dehs 20% deha	0.9153	0.8791	0.8429	20.22	4.66	2.01
70% dehs 30% deha	0.9166	0.8813	0.8446	19.35	4.33	1.91
60% dehs 40% deha	0.9185	0.8813	0.8461	18.10	4.31	1.83
50% dehs 50% deha	0.9186	0.8825	0.8471	17.70	4.12	1.76
40% dehs 60% deha	0.9211	0.8838	0.8468	16.36	3.96	1.75
30% dehs 70% deha	0.9226	0.8847	0.8474	15.46	3.82	1.70
20% dehs 80% deha	0.9232	0.8857	0.8484	14.97	3.68	1.64
10% dehs 90% deha	0.9241	0.8868	0.8492	14.41	3.54	1.59
0% dehs 100% deha	0.9254	0.8877	0.8488	13.72	3.43	1.54

The simulated and experimental densities for the mixtures were plotted in Fig.5.4b, as a function of DEHS concentration. The densities decrease as the temperature increases as expected.

Fig. 5.5 plots the measured viscosities as a function of DEHS concentration at 293 K (Fig.5.5a), 343 K (Fig.5.5b) and 393 K (Fig.5.5c). We decided to fit the viscosities data to a linear function:

$$y = Ax + B \tag{5.2}$$

where x is the concentration by weight of DEHS in the mixtures. The viscosities change linearly with the mixture composition at all temperatures. The B values correspond to the viscosities of pure DEHA and the A corresponds to the slopes of the fit.

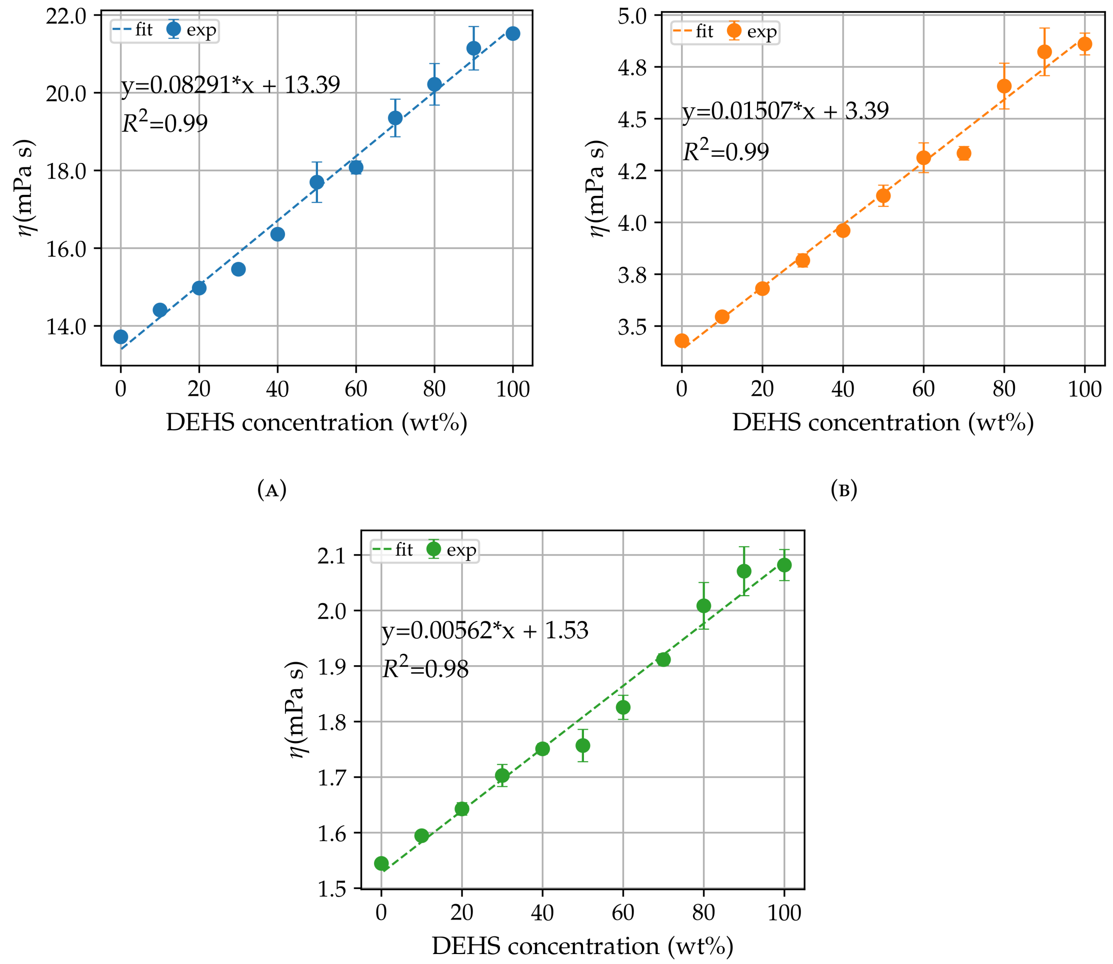

(A)

(B)

(C)

FIGURE 5.5: Experimental data and linear fit as a function of DEHS concentration at 293 K (top left, blue), 343 K(top right, orange), 393 K(bottom, green).

The standard deviation for the viscosity measurements are reported as percentages of the mean and are on average 1.25% for the systems at 293 K, 1.04% at 343 K and 1.08% at 393 K.

5.3.2 Simulation results

5.3.2.1 NEMD

We performed NEMD simulations on three different temperatures to be compared to experimental results; Density values are reported in Table 5.3 while viscosities are shown in Table 5.4.

The viscosities reported are trajectory average (Fig. 5.4a) and the standard deviation reflects the spread of those trajectories. The number of trajectories used to calculate the average was selected by looking at the individual trajectories to check if any of them were trapped in local minima, a region of lower or higher viscosity than expected [54].

TABLE 5.3: Densities ρ, in g cm^{-3} obtained from NEMD 40 ns simulations with a shear rate of $1 \times 10^8\,\mathrm{s}^{-1}$ at 293 K, 343 K and 393 K for the 11 mixtures studied.

Mixture	293 K	343 K	393 K
100% DEHS	0.8926	0.8472	0.8014
90% DEHS 10% DEHA	0.8936	0.8480	0.8029
80% DEHS 20% DEHA	0.8975	0.8511	0.8050
70% DEHS 30% DEHA	0.8957	0.8497	0.8052
60% DEHS 40% DEHA	0.8987	0.8511	0.8058
50% DEHS 50% DEHA	0.8989	0.8515	0.8058
40% DEHS 60% DEHA	0.8995	0.8535	0.8071
30% DEHS 70% DEHA	0.9011	0.8547	0.8085
20% DEHS 80% DEHA	0.9025	0.8510	0.8090
10% DEHS 90% DEHA	0.9032	0.8563	0.8098
100% DEHA	0.9023	0.8547	0.8089

In Fig. 5.4 we plot (right) both the simulated and experimental densities as a function of DEHS concentration. The simulated densities show, for all temperatures, a decreasing trend in values. At 293 K simulated densities are on average lower than experimental ones by 2.13%, at 343 K by 3.11% and at 393 K by 4.3 %. L-OPLS-AA underestimates densities for all temperatures. The simulations get less accurate as the temperature increases which is in agreement with another similar study [9].

Simulation viscosities were compared to the experimental measurements and all values are, on average, lower than their respective experimental viscosities by 17.4% and no higher than 25% which is in agreement with values from a study on a closely related polyol system at different pressure and temperature [9]. We applied the same fitting function to the simulated values and the linear behaviour is obtained only in the simulation at 293 K with a $R^2 = 0.95$, the slope is comparable to the experimental but the viscosities are on average underpredicted by 2 mPa s. The situation gets worse for the simulations at 343 K with $R^2 = 0.12$ and 393 K with $R^2 = 0.45$. Increasing the temperature from 293 K (Fig.5.6a) to 343 K (Fig.5.6b) and 393 K (Fig.5.6b) decreases the viscosity exponentially but the spread between trajectories does not decrease. This could lead to problems with the detection of possible linear or non-linear relations in viscosity simulations at high temperatures or, more generally, this could be the case for low viscosity lubricants.

The underprediction of viscosities could be linked to the force field limitations or the use of a profile-biased thermostat which assumes a velocity linear profile[146].

TABLE 5.4: Viscosities η, in mPa s obtained from NEMD 40 ns simulations with a shear rate of $1 \times 10^8\,\mathrm{s}^{-1}$ at 293 K, 343 K and 393 K for the 11 mixtures studied. Standard deviations reflect the spread of the trajectories.

Mixture	293 K	343 K	393 K
100% dehs 0% deha	19.35 ± 1.00(5.2%)	3.78 ± 0.89(23.5%)	2.07 ± 0.38(18.4%)
90% dehs 10% deha	17.30 ± 0.91(5.3%)	3.94 ± 0.24(6.0%)	1.40 ± 0.36(26.7%)
80% dehs 20% deha	16.86 ± 2.43(14.4%)	3.57 ± 0.61(17.1%)	1.48 ± 0.36(24.3%)
70% dehs 30% deha	15.38 ± 2.0(13.0%)	2.74 ± 0.85(31.0%)	1.51 ± 0.62(41.0%)
60% dehs 40% deha	15.18 ± 1.08(7.1%)	2.71 ± 0.53(19.6%)	1.55 ± 0.30(19.3%)
50% dehs 50% deha	14.53 ± 1.29(8.87%)	2.80 ± 0.84(30.0%)	1.44 ± 0.35(24.3%)
40% dehs 60% deha	13.71 ± 1.47(10.7%)	3.72 ± 0.74(19.9%)	1.67 ± 0.38(22.7%)
30% dehs 70% deha	13.33 ± 1.13(8.48%)	3.68 ± 0.22(6.0%)	1.14 ± 0.36(31.6%)
20% dehs 80% deha	12.89 ± 0.80(6.2%)	2.79 ± 0.53(18.9%)	1.37 ± 0.34(24.8%)
10% dehs 90% deha	12.11 ± 1.59(13.1%)	3.11 ± 0.4213.5%)	1.25 ± 0.44(35.2%)
0% deha 100% deha	11.90 ± 0.5(4.2%)	3.24 ± 0.67(20.8%)	1.26 ± 0.29(23.0%)

To decrease the spread of the trajectories at 393 K we decided to run new EMD and NEMD simulations for up to 120 ns starting with three mixtures: 100% DEHA, 100% DEHS and 50% DEHS 50% DEHA due to being the end and the middle point of the line plot and providing guidance whether running for a longer time would decrease the spread.

Table 5.5 shows that increasing the simulation length decreases the spread between trajectories for both NEMD and EMD and it shows that NEMD seems to be less precise than EMD.

TABLE 5.5: Experimental and EMD and NEMD simulations viscosities in mPa s as trajectory average for 3 mixtures at 393 K. Simulations are reported for two different simulations length 80 ns and 120 ns. Viscosities.

Mixture	Exp	EMD (80 ns)	NEMD (80 ns)	EMD (120 ns)	NEMD (120 ns)
100% dehs	2.05	1.41 ± 0.1	1.24 ± 0.34	1.46 ± 0.08	1.33 ± 0.13
50% deha 50% dehs	1.79	1.23 ± 0.15	1.62 ± 0.45	1.24 ± 0.09	1.54 ± 0.24
100% deha	1.54	1.19 ± 0.08	1.11 ± 0.25	1.16 ± 0.11	1.14 ± 0.22

The error or spread for NEMD at 120 ns is higher than EMD and it is still higher or at least comparable to the EMD at 80 ns. We decided to run EMD on the rest of the

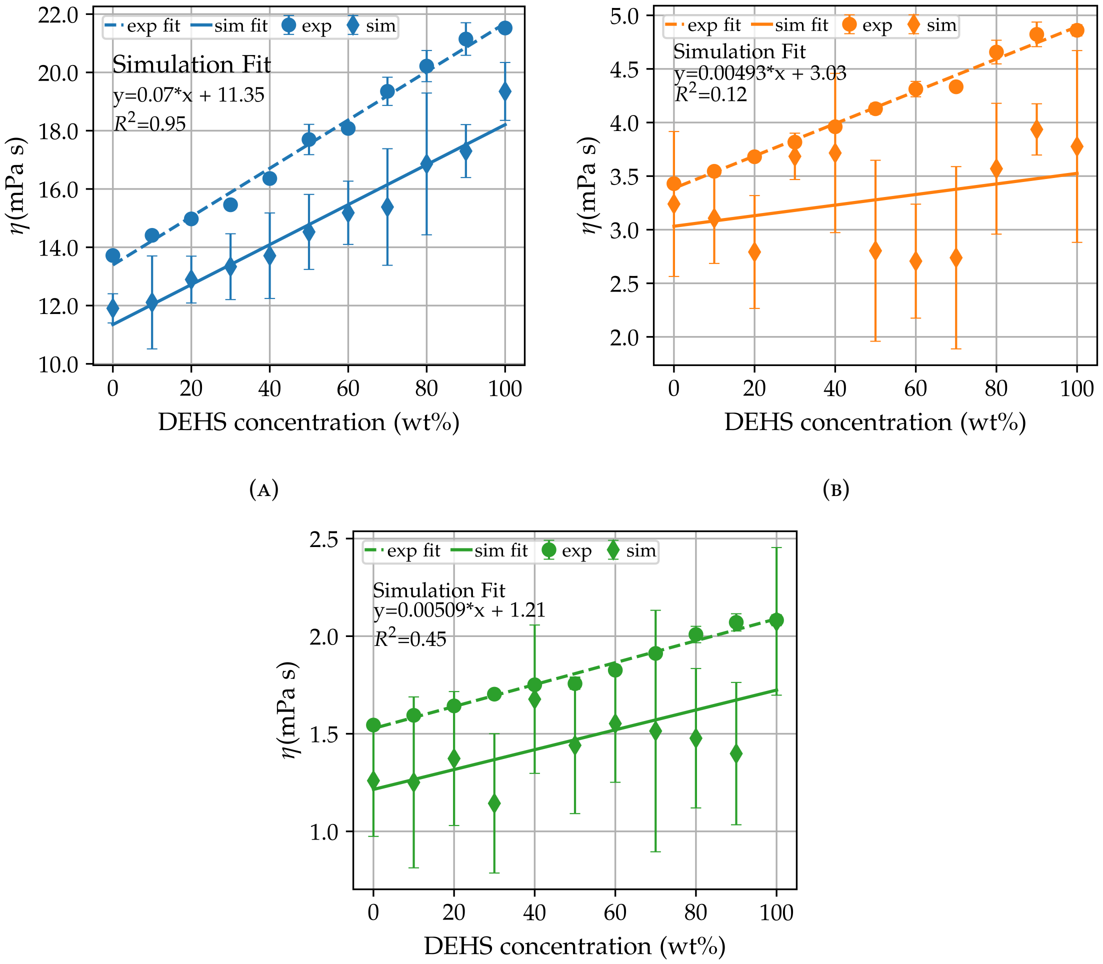

(A) (B)

(C)

FIGURE 5.6: Simulation and Experimental fit for three temperatures 293 K, 343 K and 393 K. Dashed lines and circles refer to experimental fit and values, and full lines and diamonds refer to simulated values.

mixtures at 393 K for 80 ns as it appears to be a good trade-off between computational cost and precision. Fig. 5.7 shows the line fit for the EMD simulations, the linearity is more robust compared to the NEMD, with $R^2 = 0.88$ for EMD against $R^2 = 0.45$ for NEMD, which shows that the spread of trajectories played a big role in the noisier NEMD simulations and consequently in the linear fit. EMD can predict the linear trend qualitatively, but the slope and intercept are still off from the experiments.

We have run NEMD and EMD simulations for 11 different mixtures of esters at three different temperatures and compared them against experiments. We were able to retrieve between 99% and 75% of the experimental values but the general viscosity trend was retrieved only for the lowest temperature due to the high spread between trajectories. We then compared EMD and NEMD for three mixtures to reduce the spread and EMD proved to be more precise, as it is able to reproduce, at least qualitatively, the linear behaviour at high temperature. This could be related to the low viscosity values.

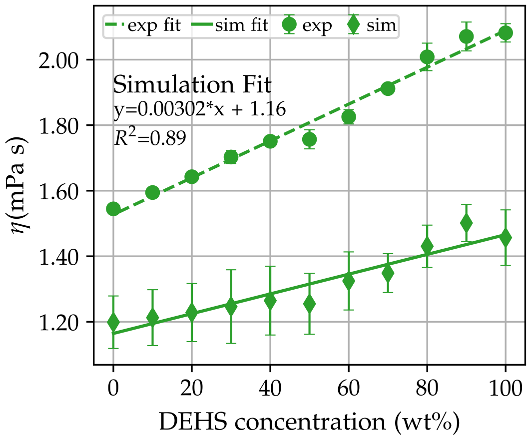

FIGURE 5.7: EMD simulations and experimental fit for mixtures at 393 K Dashed lines and circles refer to experimental fit and values, full line and diamond refer to simulated values.

In our study, the difference in viscosity between mixtures with a 10% increase of DEHS is, on average, 0.05 mPa s. This difference would require the methods and force field to be able to predict viscosities with a resolution of < 0.05 mPa s to provide a quantitative description via a linear fit. All the raw viscosity and density data are provided in the Appendix A.

5.3.3 Radial Distribution function

The observed linearity in the viscosity plot (Fig. 5.6) could be caused by the molecules having a similar structure, giving the liquid the properties of an ideal mixture. We can check this hypothesis by plotting a radial distribution function (rdf) between DEHS-DEHS, DEHA-DEHA and DEHS-DEHA. If the mixture is ideal, then we would expect the rdf plots to be similar. Fig. 7 shows the non-equilibrium all-atom rdfs for the 50% DEHS 50% DEHA mixture at 393 K. As expected, we observe that the DEHS-DEHS, DEHA-DEHA and DEHS-DEHA rdfs are very similar. We can therefore conclude that linear viscosity behaviour is caused by the formation of an ideal mixture. We have been underestimating the viscosity of this mixture A possible cause of this under-prediction would be a high shear rate that causes the fluid to transition to non-Newtonian behaviour, specifically the so-called shear-thinning behaviour where the viscosity decreases as the shear rate increases. Bernardino and Ribeiro[161]showed that, for 1-ethyl-3-methylimidazolium based ionic liquid, a small change between the rdf of the NEMD simulation compared to the EMD is shear influenced and their fluid is in a shear-thinning region. Fig. 6 shows the all-atom rdf for 50% DEHS 50% DEHA at 393 K for both NEMD and EMD where we observe perfect agreement. This allows us to assess the Newtonian regime of the NEMD simulation.

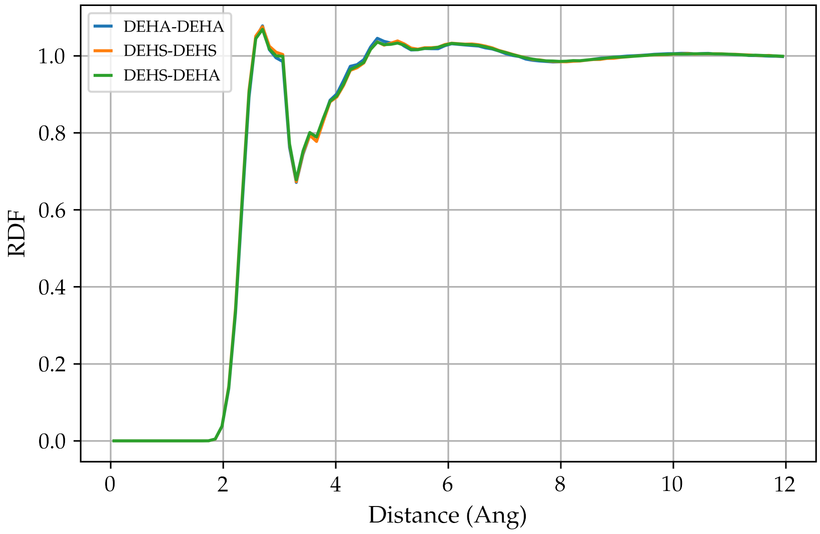

FIGURE 5.8: All atom to all-atom Radial distribution function for DEHS-DEHS, DEHA-DEHA and DEHS-DEHA at 393 K

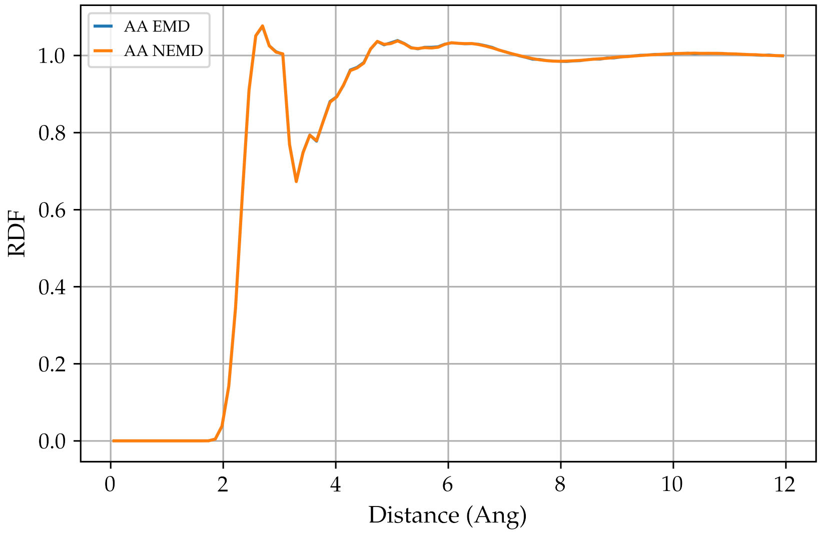

FIGURE 5.9: All atom to all-atom radial distribution functions for 50% dehs 50% deha simulation for both EMD and NEMD

5.4 Conclusions

We performed experiments and NEMD 40 ns simulations on 11 different mixtures of two synthetic diesters at 293 K and 343 K with a shear rate of $1 \times 10^8\,\mathrm{s}^{-1}$ and EMD and NEMD simulations at 393 K for up to 120 ns. We employed a 5 trajectory average to avoid a skewed viscosity in case the system is stuck in local minima. We showed that the experimental viscosities of mixtures follow a linear trend for all temperatures, but only the simulations at 293 K were able to show the same linear trend via NEMD while simulations at 343 K and 393 K did not show a trend. To solve this issue we ran

NEMD and EMD simulations at 393 K and the latter was able to achieve a low enough spread which led to the prediction of the expected linear trend, at a qualitative level. This is probably due to the small differences in viscosity between the mixtures, as such accuracy is beyond what can be obtained via MD and force fields. Viscosity values were overall underpredicted but were able to retrieve between 99% and 75% of the experimental value, the underestimation of viscosity could be caused by limitations of the force field or in the use of profile-biased thermostats which assume a linear velocity profile. Possible solutions to both underestimation and the possibility of reproducing experimental trends would be to include viscosity during the force field parameterisation and to employ configurational thermostats, but these developments are not available in commonly used simulation packages. In conclusion, NEMD simulations, EMD simulations using L-OPLS-AA and employing a 5 trajectory average predicted viscosity between 99% and 75% of experimental values. We expect that this work will serve as a basis for future simulations of mixtures of industrially relevant ester-based lubricants at different temperatures.

Chapter 6

Non-ideal mixtures

6.1 Introduction

In the previous chapter, we focused on an ideal mixture of two synthetic esters, while synthetic lubricants are developed to address specific issues or to work under extreme conditions they come at an extra cost compared to mineral oils derived from petroleum and hence they are not as commonly used as mineral oils. Mineral oils consist of complex formulations of tens or hundreds of different molecules, which pose significant challenges for researchers and engineers attempting to develop new lubricants or enhance the performance of existing ones [162]. Consequently, the development process often presents a trial-and-error component. Many industrial applications of mineral oils involve high-pressure regimes up to 5 GPa [163] and understanding how lubricant mobility and viscosity are affected by these high pressures could inform the direction of lubricant development.

Computational methods have proven particularly valuable in investigating the rheological properties of lubricants in high-pressure regimes. Researchers explored various aspects of lubricant behaviour under extreme conditions. Ewen et al. compared different force fields up to 202.7 MPa[15]. Galvani Cunha et al. investigated the pressure-viscosity relationship for 2,2,4-trimethylhexane up to 1000 MPa[62]. Kadupitiya et al. employed a novel approach combining NEMD with machine learning to elucidate the transition between Newtonian and non-Newtonian regimes[67]. The impact of molecular structure on lubricant properties has also been a focus of MD studies. Kioupis et al. examined the effect of molecular architecture on the high-pressure rheological properties of poly-α-olefins, providing insights into structure-property relationships[42]. Kondratyuk et al. contributed to the understanding of multi-component systems by probing the high-pressure behaviour of a binary alkane mixture, revealing important deviations between ideal and non-ideal mixtures[164]. Li et al. conducted a comparative analysis of EMD and NEMD for PEC6 lubricants across a pressure range of 0.1 to 1 GPa[165]. Similarly, Lin and coworkers demonstrated the predictive power of NEMD for a polyol system under various temperatures and pressures, further validating the utility of these computational methods[9].

Building upon the work showed in the previous chapter on the temperature effects in an ideal mixture of two synthetic esters [156] and upon our group's previous work on the pressure effect on a model system of PAO2[12], we now extend our investigation to the high-pressure behaviour of two ternary non-ideal hydrocarbon mixtures. These mixtures serve as model systems representative of the more complex mineral oil lubricants. To our knowledge, this study represents the first MD simulation of ternary mixtures at extremely high pressures, up to 4 GPa. Our objectives are twofold: to establish a robust workflow for simulating ternary mixtures under high-pressure conditions and to elucidate the pressure dependence of viscosity and mobility. We anticipate that these findings will contribute valuable insights to the design of future lubricants. Our investigation employs NEMD simulations to evaluate several properties: mean square displacements, radial distribution functions, densities, and viscosities. We conducted simulations across three temperatures (313 K, 343 K, and 393 K) and four pressures (0.5 GPa, 1 GPa, 2 GPa, and 4 GPa). Two distinct mixtures were studied, differing in their relative compositions:

- Mixture 1: 65% hexadecane, 5% butylbenzene, and 30% bicyclohexyl
- Mixture 2: 65% hexadecane, 30% butylbenzene, and 5% bicyclohexyl

the choice of using NEMD instead of the Green-Kubo approach via EMD relies on the fact that at very high pressure the relaxation time for the off-diagonal pressure tensor autocorrelation function needed to obtain a converged integral is prohibitively long, preventing us from obtaining a viscosity value in a reasonable amount of time. We compare our simulation results with experimental data at room pressure to validate our approach and the force field parameters. Fig. 6.1 illustrates the molecular structures of the three components used in our ternary mixtures.

In section 6.2 computational and experimental procedures are explained, in section 5.3 results are presented and discussed and in section 5.4 conclusions are presented.

6.2 Computational and experimental details

6.2.1 System Setting

The simulations were run using the LAMMPS[159] software, the starting configurations were generated using Packmol[157] and Moltemplate[158].

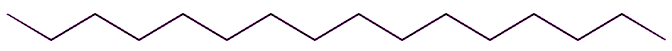

(A) Hexadecane molecular structure (HEX)

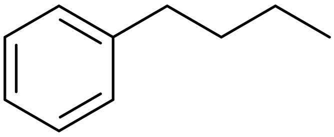

(B) Butylbenzene molecular structure (BB)

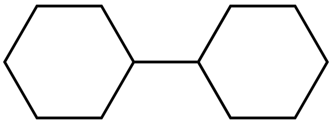

(C) Bicyclehexyl molecular structure (BC)

FIGURE 6.1: The three components present in the two mixtures

Each mixture consists of $\approx$ 12000 atoms (the numbers of HEX, BB and BC molecules per mixture are available in the Appendix, Table B.1). The L-OPLS-AA[160] force-field with a long-range cutoff of 12 Å was used throughout this study with a timestep of 1 fs. The temperature and pressure were held constant by employing the Nosé-Hoover thermostat and barostat, respectively.The temperature damping parameter was set to 100 timesteps, while the pressure damping parameter was set to 1000 timesteps.

6.2.2 Equilibration

Each mixture first underwent a minimization step with energy and force thresholds of $1 \times 10^{-5}\,\mathrm{kcal\,mol^{-1}}$ and $1 \times 10^{-7}\,\mathrm{kcal\,mol^{-1}\,\mathring{A}^{-1}}$ respectively, then went through 5 ns NVT run with a temperature damping parameter of 100 fs to reach the target temperature of 313 K, 343 K or 393 K. The NVT run was followd by a 25 ns NPT run to reach the target pressure of 0.5 GPa,1 GPa,2 GPa or 4 GPa. The average density was calculated using the last 5 ns, each mixture was then scaled to match the average density as in [9]. Finally, each system was allowed to relax with another 5 ns NVT simulation. The mixtures were then sheared for 10 ns at the end of which five configurations of positions and velocities were saved 50 fs apart from each other. These served as starting points for generating 5 trajectories used to compute average properties.

6.2.3 Production runs

The production run consists of 120 ns shear simulation. The viscosity for each trajectory was calculated using the last 100 ns. The velocity profile was checked to be linear for all trajectories as expected from bulk shear rate lubricant simulations. All the properties reported in the study are reported as a five trajectories average.

6.3 Experimental procedure

The dynamic viscosities and the densities of the two mixtures were measured by using an Anton Paar Stabinger viscometer, Stabinger SVM 3001, with autosampler XSample 530. The shear rate is part of the measurement principle and depends on the measured viscosity, hence it could not be pre-selected. Shear rate value in experimental measurements is at most in the range of $1000\,\mathrm{s}^{-1}$.

6.4 Results and Discussion

6.4.1 Room Pressure

Room pressure simulations of the two mixtures were conducted at three distinct temperatures: 40 °C, 70 °C, and 120 °C. This approach was adopted to validate the computational method and force field against available experimental data, a crucial step before exploring the high-pressure regime where experimental data are scarce. The simulated and experimental densities and viscosity as a function of temperature for the two mixtures at room pressure are plotted in Fig. 6.2. Both properties exhibit an inverse relationship with temperature, decreasing as temperature increases. Mixture 1 consistently demonstrates higher density and viscosity than mixture 2 across all temperatures. This difference can be attributed to mixture 1's higher content of bicyclohexyl which possesses greater density and viscosity compared to butylbenzene. The density is slightly underestimated by $\approx 5\%$ for both mixture 1 and mixture 2 at all temperatures, while the viscosity is consistently underestimated for mixture 1 but not for mixture 2 where the average viscosity value from simulations underestimates the experimental value only at 40 °C. It is important to notice that the average error on the simulated viscosities for both mixtures is $\approx 15\%$ at all temperatures which is greater than for the density justifying this different behaviour for the two properties. Overall, the simulations are able to reproduce the experimental trends with reasonable accuracy. This validation at room pressure provides confidence in the computational approach, suggesting its potential applicability for predicting fluid properties under high-pressure conditions.

6.4.2 High pressure

We performed NEMD simulations at three different temperatures and four different pressures up to 4 GPa. Viscosity values are shown in Table 6.3, and density values are reported in Table 6.1. All reported values are trajectory averages.

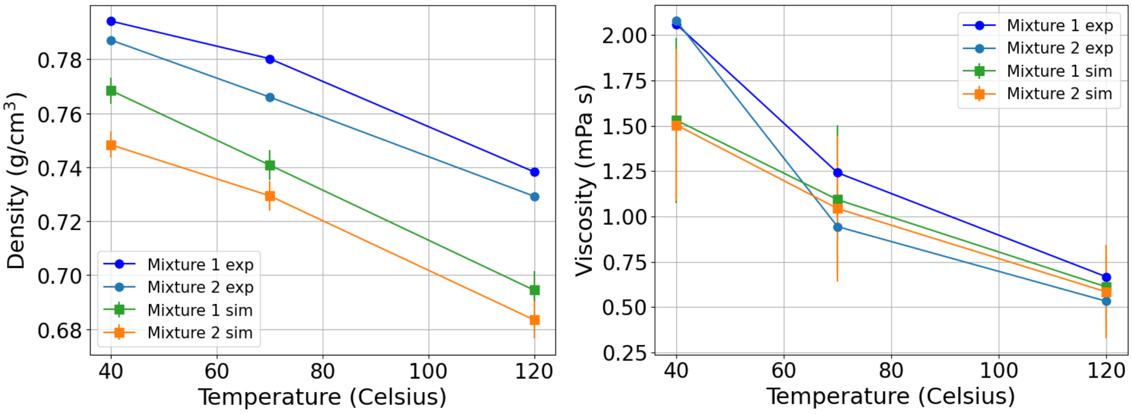

FIGURE 6.2: Experimental and simulated densities (left) in g cm^{-3} and viscosities (right) as a function of temperature. The densities are slightly underestimated at all temperatures with slightly increasing differences as the temperature rises. Viscosities on the other hand are consistently underestimated only for mixture 1, while mixture 2 is underestimated only at 40 C.

TABLE 6.1: Densities in g/cm^{-1} at 4 different pressures and 3 different temperatures. The density increases as temperature decreases and pressure increases as expected showing a non-linear behaviour. Mixture 1 is denser at room pressure but not at higher pressures compared to mixture 2. The changes in densities when increasing temperature or pressure are similar between the two mixtures.

Temperature (°C)	Pressure (GPa)	Mixture 1	Mixture 2
40	0.0001	0.768 ± 0.004	0.748 ± 0.005
70	0.0001	0.740 ± 0.005	0.729 ± 0.005
120	0.0001	0.694 ± 0.006	0.683 ± 0.007
40	0.5	0.926 ± 0.002	0.927 ± 0.002
70	0.5	0.914 ± 0.002	0.914 ± 0.002
120	0.5	0.895 ± 0.003	0.895 ± 0.003
40	1.0	0.988 ± 0.002	0.992 ± 0.002
70	1.0	0.980 ± 0.002	0.981 ± 0.002
120	1.0	0.964 ± 0.002	0.966 ± 0.002
70	2.0	1.053 ± 0.001	1.060 ± 0.001
40	2.0	1.057 ± 0.001	1.065 ± 0.001
120	2.0	1.043 ± 0.002	1.054 ± 0.002
40	4.0	1.135 ± 0.001	1.145 ± 0.001
70	4.0	1.133 ± 0.001	1.143 ± 0.001
120	4.0	1.130 ± 0.001	1.140 ± 0.001

6.4.2.1 Density

The density exhibits the expected behaviour, increasing as temperature decreases and pressure increases, with a notable non-linear trend. Interestingly, while mixture 1 is denser than mixture 2 at room pressure, their densities converge at higher pressures. This convergence may be attributed to the higher presence of butylbenzene in mixture 2, which introduces significantly different intermolecular interactions compared to the non-aromatic components. The pressure dependence of hydrocarbon density is usually

TABLE 6.2: Parameters of the Tait fit for the two mixtures. The values of ρ_0 are in g/cm^3, A is unitless and the values B are in GPa.

Temperature	ρ_0 (mix 1)	A (mix 1)	B (mix 1)	ρ_0 (mix 2)	A (mix 2)	B (mix 2)
40	0.768	0.176	0.059	0.787	0.184	0.087
70	0.741	0.179	0.045	0.766	0.189	0.077
120	0.694	0.183	0.031	0.729	0.196	0.062

described by the Tait equation

$$\frac{\rho - \rho_0}{\rho} = A \log \left(\frac{B + P}{B + P_0} \right) \tag{6.1}$$

where ρ_0 is the density at room pressure P_0, and A and B are parameters obtained through fitting. Table 6.2 presents the Tait fit parameters for both mixtures across all temperatures, while Fig 6.3a illustrates the simulated data points and the Tait fit for mixture 1 and Fig. 6.3b for mixture 2 across the three temperatures.

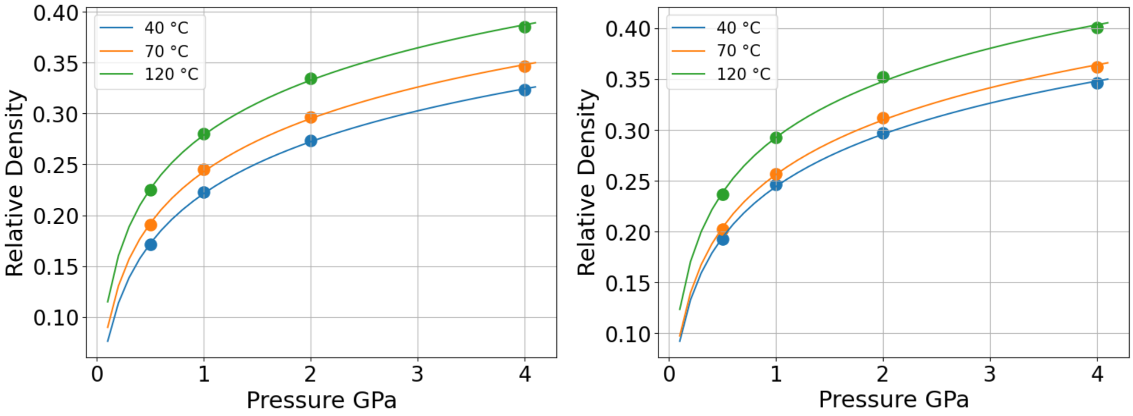

(A) Tait fit on simulated data for mixture 1 at three different temperatures.

(B) Tait fit on simulated data for mixture 2 at three different temperatures.

FIGURE 6.3: Simulated densities and Tait fits for mixture 1 (a) and mixture 2 (b)

The relative errors in the fit are for the two mixtures and across all temperatures below 10^{-4} showing an excellent agreement between the simulated data and Tait equation fit. The ρ_0 values decrease with increasing temperature for both mixtures, consistent with thermal expansion. The A parameter shows a slight increase in temperature for both mixtures, this suggests that the fluids become more compressible at higher temperatures. The B parameter decreases with increasing temperature. This indicates that the density becomes less sensitive to pressure changes at higher temperatures. Mixture 2 consistently shows higher A and B values compared to mixture 1 suggesting that is more sensitive to pressure changes. This could be related to the higher content of butylbenzene in mixture 2.

TABLE 6.3: Viscosities for the two mixtures at four different pressures and three different temperatures in mPa s.

Temperature (°C)	Pressure (GPa)	Mixture 1	Mixture 2
40	0.0001	1.53 ± 0.45	1.50 ± 0.42
70	0.0001	1.10 ± 0.41	1.04 ± 0.40
120	0.0001	0.61 ± 0.23	0.58 ± 0.26
40	0.5	275.49 ± 29.55	84.00 ± 31.67
70	0.5	61.66 ± 27.19	27.75 ± 7.99
120	0.5	21.10 ± 0.94	4.50 ± 2.23
40	1.0	5510.54 ± 341.62	1936.04 ± 136.36
70	1.0	2011.98 ± 86.50	541.78 ± 52.40
120	1.0	256.00 ± 104.50	30.07 ± 40.79
40	2.0	21969.24 ± 2756.06	17724.38 ± 215.94
70	2.0	18388.30 ± 548.44	12687.46 ± 432.84
120	2.0	8230.84 ± 551.99	3903.10 ± 45.82
40	4.0	51736.68 ± 2204.59	44044.52 ± 870.09
70	4.0	49824.12 ± 1120.88	39546.82 ± 715.14
120	4.0	40108.40 ± 1447.03	30735.64 ± 1197.98

6.4.3 Viscosity

Mixture 1 consistently exhibits higher viscosity than mixture 2 across all temperatures and pressures. This observation aligns with the composition of the mixtures, where mixture 1 contains a higher proportion of bicyclohexyl, which typically has a higher viscosity than butylbenzene. Interestingly, the viscosity of mixture 2 decreases slightly faster than that of mixture 1 at all pressures, although this difference diminishes as pressure increases. This behaviour can be attributed to the higher content of butylbenzene in mixture 2. Butylbenzene's viscosity is more sensitive to temperature changes compared to the other components, which explains the slightly different behaviour when temperature varies. The change in viscosity as a function of pressure is incredibly important in many applications but it's system-dependent and it could present very different behaviours. One of the first viscosity-pressure relations that has been proposed is the Barus equation where the viscosity increases approximately exponentially:

$$\eta = \eta_0 e^{\alpha_0 P} \tag{6.2}$$

where η_0 is the viscosity at a pressure close to room pressure, and α_0 is the pressure–viscosity coefficient. While this relationship is very simple and can be applied to a range of fluids at low-pressure and low-temperature regimes, it can not be applied to all hydrocarbons and it also fails to capture pressure-viscosity response behaviours which are known to happen at higher pressures or temperatures such as slower-than-exponential response.[164]. One of the equations employed to describe this type of response is the McEwen equation:

$$\eta = \eta_0 \left(1 + \frac{\alpha_0 P}{q-1}\right)^q \tag{6.3}$$

where η_0 is the viscosity at a pressure close to room pressure, α_0 is the pressure–viscosity coefficient and q is the McEwen exponent. Another change of behaviour from slower-than-exponential to faster-than-exponential occurs at higher pressure as it approaches the glass transition pressure. This behaviour is often described by the Paluch equation but it is not able to capture the slower-than-exponential so a hybrid model was suggested by Bair [166] called the McEwen-Paluch equation

$$\eta = \eta_0 \left(1 + \frac{\alpha_0 P}{q-1}\right)^q \exp\left(\frac{C_F P}{P_\infty - P}\right), \tag{6.4}$$

where C_F is the fragility parameter and P_∞ is a finite pressure at which relaxation times diverge at a given temperature. Given the ability of the McEwen-Paluch equation to capture both slower-than-exponential and faster-than-exponential behaviours, we chose to fit it into our simulation data. The fitted parameters are reported in SI, while Fig. 6.4a and Fig. 6.4b present the simulation data and McEwen-Paluch fit on a logarithmic scale. The plots demonstrate excellent agreement between the simulation data and the fit, both qualitatively and quantitatively, up to 2 GPa. The fit successfully captures the inflexion point in the viscosity-pressure relationship, which is a key feature of the McEwen-Paluch equation. This agreement suggests that the equation accurately describes the complex pressure-dependent viscosity behaviour of our hydrocarbon mixtures within this pressure range. However, the fit breaks down above 2 GPa, where the observed viscosity does not increase as rapidly as predicted by the McEwen-Paluch equation. This deviation is significant and warrants further discussion. The McEwen-Paluch equation assumes that viscosity continues to increase faster than exponentially across all pressure ranges. While this assumption is reasonable for a wide range of pressures, it becomes problematic at very high pressures. For hydrocarbons, it is unlikely that viscosity will continue to increase at such a rapid rate indefinitely, especially when approaching very high pressures where phase transitions to glassy states are likely to occur. The breakdown of the fit above 2 GPa could be linked to changes in the fluid structure that alter its viscosity or to phase transition to a glass-like state where viscosity increase might slow down or simply by limitations of the McEwen-Paluch model or of the force-field at very high pressures To fully understand the reasons behind this behaviour would require further investigation on possible phase transition or structural changes as well as force field limitations at very high pressure but this comprehensive investigation is beyond the scope of the current study.

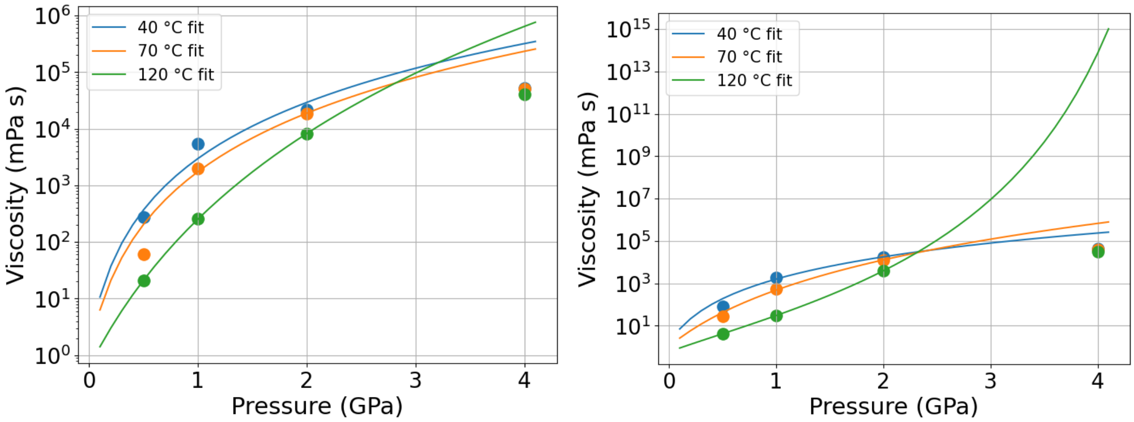

(A) McEwen-Paluch fit the simulated viscosity values for mixture 1 at three different temperatures. The circles are simulated values. The scale on the y-axis is logarithmic

(B) McEwen-Paluch fit the simulated viscosity values for mixture 2 at three different temperatures. The circles are simulated values. The scale on the y-axis is logarithmic

FIGURE 6.4: Simulated viscosities and McEwen-Paluch fits for mixture 1 (a) and mixture 2 (b)

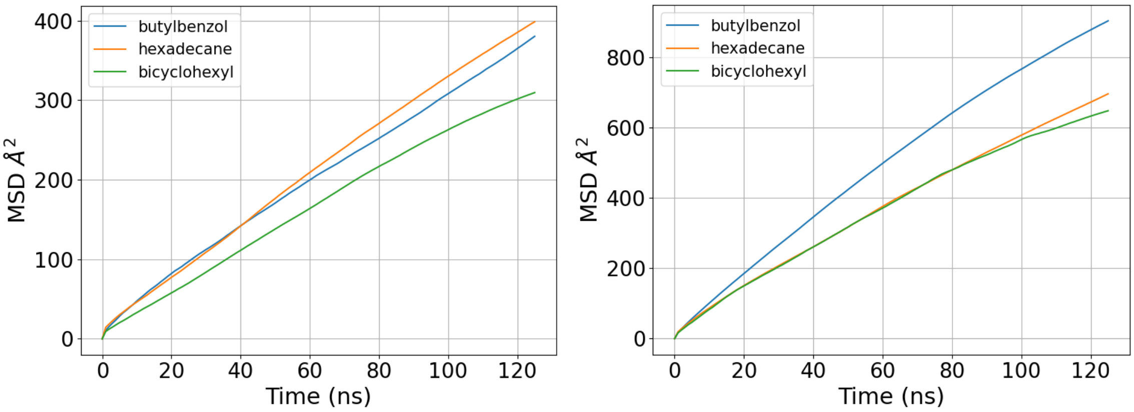

(A) Mixture 1 mean square displacement for the three components at 1 GPa and 120 °C

(B) Mixture 2 mean square displacement for the three components at 1 GPa and 120 °C.

FIGURE 6.5: Mean square displacement mixture 1 (a) and mixture 2 (b)

6.4.4 Mean Square Displacement

Fig 6.5 shows the mean square displacement (MSD) for the two mixtures at 120°C and 1 GPa, we observe that hexadecane shows the highest MSD over time, followed closely by butylbenzene, with bicyclohexyl exhibiting the lowest MSD. This suggests that in this mixture, hexadecane molecules are the most mobile, while bicyclohexyl molecules are the least mobile. Mixture 2 shows a significantly different behavior. Here, butylbenzene demonstrates the highest MSD, followed by hexadecane and bicyclohexyl which show lower MSDs. Looking at the temperature and pressure dependence we can see that on average bicyclohexyl possess the lowest MSD while the mobility of hexadecane and butylbenzene is highly affected by the conditions for both mixture 1 and mixture 2. MSD also decreases as the pressure increases as expected and increases when the temperature is increased as the molecule possesses greater kinetic energy. Butylbenzene's mobility increases in mixture 2 suggesting that its higher concentration (30% vs 5%) allows for more freedom of movement, possibly due to increased butylbenzene-butylbenzene interactions. Relating these observations to viscosity, we can infer that the higher mobility of butylbenzene in mixture 2, as indicated by its larger MSD, suggests less resistance to flow. Conversely, the more uniform and generally lower MSDs in mixture 1 imply higher viscosity, with molecules experiencing more restricted movement as can be seen from the values in Tab. 6.3 These differences highlight how the composition of these mixtures significantly affects their MD, which in turn influences macroscopic properties like viscosity. The interplay between the concentrations of different components clearly has a profound impact on the overall behaviour of the liquid mixtures.

6.4.5 Radial Distribution Function

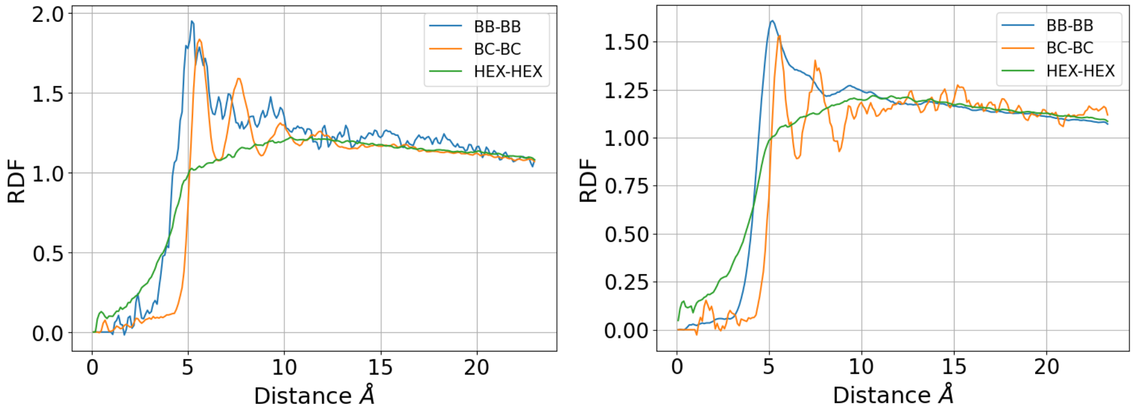

(A) Mixture 1 Radial distribution function for the three component at 1 GPa and 120 °C.

(B) Mixture 2 Radial distribution function for the three component at 1 GPa and 120 °C.

FIGURE 6.6: Radial distribution function mixture 1 (a) and mixture 2 (b)

6.4.6 Radial Distribution function

Fig. 6.6 plots the all-atom to all-atom radial distribution functions for the two mixtures at 120 °C and 1 GPa. Looking at mixture 1 we can see that the BB-BB (butylbenzene-butylbenzene) curve shows the highest and sharpest first peak, indicating strong self-association of butylbenzene molecules despite their low concentration. This suggests that butylbenzene molecules tend to cluster together,due to $\pi - \pi$ interactions. The BC-BC (bicyclohexyl-bicyclohexyl) curve also shows a prominent first peak, though slightly lower than BB-BB, indicating significant self-association of bicyclohexyl molecules. The HEX-HEX (hexadecane-hexadecane) curve has a broader, less intense first peak, suggesting a more uniform distribution of hexadecane molecules throughout the mixture resembling the RDF of a gas. In mixture 2 the BB-BB curve still shows the highest first peak, but it's less intense compared to mixture 1. This suggests that while butylbenzene molecules still associate, the higher concentration leads to more dispersed clustering. The BC-BC curve shows a similar pattern to mixture 1, but with slightly lower intensity, reflecting its reduced concentration. The HEX-HEX curve remains broadly similar to mixture 1, indicating that hexadecane's self-association is less affected by the composition change. Comparing the behaviour of RDF of the two mixtures at different conditions we can see that the BC-BC and HEX-HEX RDF show that increasing the temperature has very little effect on the distribution while pressures decrease the position of the first peak as well as increasing their value indicating a stronger clustering of molecules. The most affected distribution is the BB-BB for mixture 1 and BC-BC for mixture 2, they show a very complex behaviour where the only clear effect is that at very high pressure the height of the peaks is greater compared to the RDF at lower pressure and the position of the peaks are also at shorter distances. This seems to be related to the very small concentration of the molecules in the mixture providing a very crude RDF plot.

6.5 Conclusions

In this chapter, we conducted NEMD simulations on two distinct mixtures of three hydrocarbons at temperatures of 40 °C, 70 °C, and 120 °C, and pressures of 0.5 GPa, 1 GPa, 2 GPa, and 4 GPa. To ensure statistical reliability and avoid local minima traps, we employed a 5-trajectory averaging approach. Our simulations demonstrated both quantitative and qualitative agreement with experimental measurements at room pressure and temperature, validating our computational approach. We successfully fitted the simulated density data at higher pressures to the empirical Tait equation, providing a reliable model for density prediction under extreme conditions. For viscosity, we fit the McEwen-Paluch equation to the simulation data and found that it accurately described the pressure-viscosity relationship up to 2 GPa. Beyond this pressure, the equation broke down, predicting higher viscosities than our simulations. This deviation suggests a possible phase transition to a more glass-like state at extreme pressures. Comparing the two mixtures, we observed that mixture 1 exhibited higher density at room pressure but lower density at higher pressures compared to mixture 2 This behaviour is likely caused by the increased $\pi - \pi$ interactions in mixture 2 due to its higher butylbenzene content. Viscosity values were consistently higher for mixture 1 across all tested conditions. Analysis of mean square displacement revealed that bicyclohexyl, present in greater quantity in mixture 1, was the least mobile component. This reduced molecular mobility explains the higher viscosity observed in mixture 1. The radial distribution function analysis provided further insights into the molecular structure and interactions within each mixture, corroborating the observed macroscopic properties and helping to explain the diffusive behaviour and viscosity differences between the mixtures. Our comprehensive approach, combining density, viscosity, mean square displacement and radial distribution function analyses, offers a detailed understanding of these complex hydrocarbon mixtures under a wide range of temperatures and pressures. The breakdown of the McEwen-Paluch equation at extreme pressures opens up new questions about the behaviour of these fluids in such conditions and suggests the need for more sophisticated models. This study serves as a robust foundation for future investigations into lubricant mixtures at various temperatures and very high pressures. It demonstrates the ability of MD simulations in predicting and understanding fluid properties under extreme conditions, where experimental data are difficult to obtain. Future work could focus on developing new viscosity models for extreme pressure conditions or investigating potential phase transitions at very high pressures. These findings and methodologies have significant implications for the design and optimization of lubricants for high-pressure applications, potentially leading to improved performance in various industrial and technological sectors.

Chapter 7

Confined simulations

The work presented in this chapter has been published in *RSC Advances* [167]

7.1 Introduction

In previous chapters we have focused on ideal and non-ideal mixtures of bulk lubricants, while this is an important and active field of research, it is desirable to have a more realistic model where the liquid of interest is confined between explicitly defined walls which aim to resemble as closely as possible real-life applications under different operational conditions. This method is known as confined NEMD simulation and has been applied to various systems including Lennard-Jones particles [168], linear and branched hydrocarbon oils [53, 56, 169], esters [170], acids [171] and many more [13, 172–177]. Within the formulation of confined NEMD, there are several ways to derive the shear stress which is essential for calculating viscosity. There exist several methods to do so including the Irving-Kirkwood method (IK) [178], the method of Planes (MoP) [179], the average shear force over area [180] and the direct shear stress from average atom shear stress of lubricant atoms. In this work, we employed the direct shear method, due to its conceptual simplicity, as implemented in the LAMMPS [181] software for calculating viscosity at various operational conditions. We investigated varying pressure, the applied shear rate and the film thickness of the confined lubricant. This method calculates shear viscosity as:

$$\eta_{\alpha\beta} = \frac{\langle \tau_{\alpha\beta} \rangle}{\dot{\gamma}} \ . \tag{7.1}$$

where $\eta_{\alpha\beta}$ is the viscosity, $\langle \tau_{\alpha\beta} \rangle$ is the shear stress that is averaged over the ensemble, $\alpha\beta \equiv x, y, z$ and $\dot{\gamma}$ is the applied shear rate. In such context, the simulation box is periodic in the x and y-dimension and non-periodic in the z-dimension.

In this chapter, we explore the rheological properties of a system of 9,10-dimethyloctadecane molecules confined between two α-Fe_2O_3 (Hematite) (001) slabs. We study the effect of three different pressures (0.1, 0.5 and 1 GPa), two shear rates ($10^{7.5}$ and $10^{8.5}$ s^{-1}) and the predictive power of two force fields L-OPLS-AA and ReaxFF, the latter being a reactive force field. We present the advantages and discuss the limitations of this method. We then compare these results against bulk simulations on the same liquid published in our previous study [12], where bulk simulations were compared to experimental measurements of viscosity at pressures up to 1 GPa. Our goal is to study the impact of film thickness, shear rate and force field on the viscosity of confined lubricant compared to the bulk system.

7.2 Methods

Hematite is known to form in tribological systems of steel under various conditions. For this reason, it is chosen as a surface for our system. We have chosen 9,10-dimethyloctadecane as the model liquid due to being the main component of the industrially relevant PAO-2 lubricant. Three different systems were generated consisting of either 100, 200, or 450 9,10-dimethyloctadecane molecules between two slabs of iron oxide (2,700 molecules of α-Fe_2O_3 in total). The numbers of molecules were chosen such as they would model film thicknesses found in experiments (200 molecules) in bulk (450 molecules) and an extreme condition which is hard to obtain experimentally (100 molecules). The three molecular systems were generated by using an in-house modified version of LAMMPS_builder [182, 183].

7.2.1 Computational Details

The three systems were studied using the open-source LAMMPS software [181] via two different force fields L-OPLS-AA [184] and ReaxFF [185, 186]. Parameters for ReaxFF were taken from [187]. The L-OPLS-AA force field, which is among the most popular force fields for liquid simulations, is a bonded all-atom force field. ReaxFF force field does not consider bonds explicitly as in L-OPLS-AA force field, but instead employs a bond-order formalism in conjunction with polarisable charge descriptions to describe both reactive and non-reactive interactions between atoms. This allows ReaxFF to accurately model both covalent and electrostatic interactions for a diverse range of materials. As a result, the ReaxFF force field can be used to study chemical reactions, as bonds can form and break during a simulation, something that can not happen in bonded force fields, for example, during simulations with L-OPLS-AA.

The workflow included three distinct steps: an equilibration (reorientation) step, followed by compression and at last a shearing step. The shearing part consists of a steady state part followed by a production run.

7.2.2 L-OPLS-AA

The interactions within the fluid were modelled via L-OPLS-AA [184], while interactions between the iron oxide and fluid atoms were governed by Lennard-Jones (L-J) and electrostatic interactions (E.I). The E.I. and L-J. parameters were those developed by Savio *et al.* [188] and Berro *et al.* [94]. The α-Fe_2O_3 slabs were restrained in their crystal structure using harmonic restrains with a spring constant of 130 kcal/mol [94]. A 1 fs timestep was used during the entire workflow.

The equilibration and molecular reorientation step was achieved by an energy relaxation process, followed by a run of 8 ns in the canonical (NVT) ensemble that included a Langevin thermostat [189], which was applied to the lubricant atoms, to control the temperature at 373 K with a time constant of 0.1 ps. To allow molecular reorientation of the lubricant, the outermost layer of iron atoms of the upper and lower iron oxide slabs was kept frozen for the whole duration of the simulation.

Three independent trajectories were produced by randomizing the positions and velocities of the initial configuration. This was achieved by heating and then cooling the configuration through separate cycles. These heat-quench cycles [15] for simulations at 373 K were performed from 373 K to T = 375, 380 and 385 K, respectively, during 1 ns runs in the NVT ensemble, after which the systems were immediately quenched back to 373 K during another 1 ns run in the NVT ensemble.

The second step of the simulation included the application of external pressure (0.1, 0.5 and 1.0 GPa) at the outermost layer of iron atoms of the upper slab to compress the systems. The pressure values were chosen to be in the range of the applied pressure in bulk NEMD simulations that were used in a previous study for the same liquid [12]. This was achieved during 5-8 ns runs where the outermost bottom layer of the lower iron oxide slab was kept frozen for the whole duration of the simulation. The simulation ran for long enough until the film thickness, calculated as the distance between the two surfaaces, reached a negligible fluctuation (≤ 0.05 Å). Then, the film thickness values during the last 2 ns were used to determine the average film thickness value needed for the next step of shearing.

The third step of the simulation included the shearing stage where a shear rate was applied to the system by applying an external velocity at the top outermost layer of iron atoms while continuing to apply an external pressure. The applied shear rate was chosen so that our simulations capture the Newtonian and non-Newtonian (shear

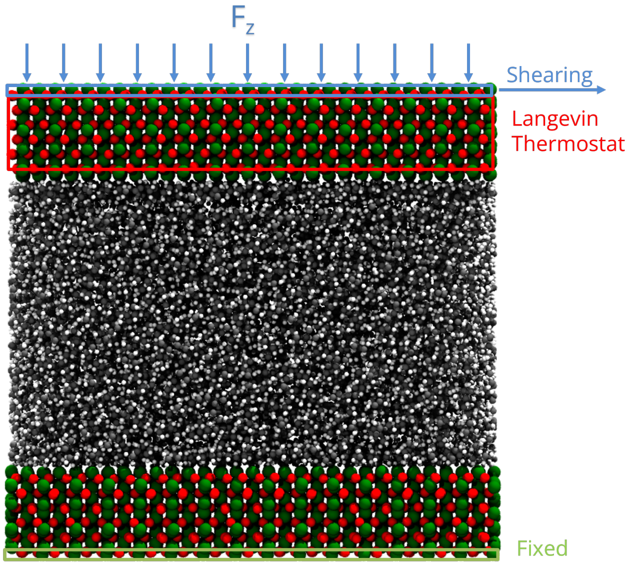

FIGURE 7.1: Illustration of the molecular snapshot of system 3 with L-OPLS-AA at 0.1 GPa and 100 °C. The red box represents the thermostatting region during the shearing stage of confined NEMD and the blue and green boxes represent the outermost iron layers at the top and bottom part of the simulation box. The upper blue box shows the area where the external force F_z is applied, while the green box at the bottom represents the fixed area of iron atoms. The carbon atoms are coloured gray, hydrogen atoms with white, oxygen atoms with red and iron atoms with green.

thinning) regions. The values were $10^{7.5}$ and $10^{8.5}$ s^{-1}, respectively. At this stage, the Langevin thermostat was applied at the inner atomic layers of the upper iron oxide slab, as this is known to be a better and more realistic approach to thermostat regions in shearing systems [174], instead of applying the thermostat to the fluids, which is known to affect their dynamics [190]. Figure 7.1 illustrates the thermostatting region during shearing. Again, the outermost bottom layer of the lower iron oxide slab was kept frozen for the whole duration of the simulation. The system was then sheared for 4 ns to ensure a steady state, followed by a production run of 8-80 ns until viscosity converged.

7.2.3 ReaxFF

The ReaxFF protocol was the same as the L-OPLS-AA, with the only difference being the duration of the simulation, as ReaxFF is more computationally expensive than L-OPLS-AA. For this reason, system 3 (case of 450 inserted molecules) was excluded from simulations. The changes were the following.

The simulation timestep was set to 0.25 fs, which has been also used before for investigating the thermal decomposition of phosphate esters on ferrous surfaces with ReaxFF [187], while the time constant of the Langevin thermostat was set to 0.01 ps. In addition, the chosen timestep value is included in the suggested timestep range of

0.1 - 0.5 fs from literature [191], which is needed to produce reliable dynamics and ensure energy conservation. The heat-quench cycles for simulations at 373 K were performed from 373 K to T = 375, 380 and 385 K, respectively. After a 0.15 ns run in the NVT ensemble, the systems were heated during a 0.025 ns run and then they were immediately quenched back to 373 K during another 0.025 ns run in the NVE ensemble. This process occurred two times to ensure molecular reorientation.

During the compression step the same pressures as the L-OPLS-AA case were applied, and the compression lasted for 5.8 - 7.75 ns where the outermost bottom layer of the lower iron oxide slab was kept frozen for the whole duration of the simulation. The simulation ran for long enough until the film thickness fluctuations were lower than 0.07 Å. The film thickness values during the last 0.5 ns were used to determine the average film thickness value needed for the next step of shearing.

During the shearing step the same shear rates as the L-OPLS-AA case were applied, and the system was sheared for 2 ns to ensure a steady state. Again, the film thickness values during the last 0.5 ns were used to determine the average film thickness value needed for the production step of shearing.

Then, the simulation continued with a production run of up to 8 ns, during which viscosity was calculated for each shear rate and trajectory. The simulations at a shear rate of $10^{7.5}$ s^{-1} were not converged after 8 ns, and due to the computational cost those systems were not run any longer and the ReaxFF results reported are related only to the systems sheared at $10^{8.5}$ s^{-1}.

7.3 Results

7.3.1 Compression stage

Figure 7.2 shows a molecular snapshot of the systems studied after successful compression at a pressure of 0.1 GPa at 100 °C by using the L-OPLS-AA force field. As can be seen from the illustrations, the atomic arrangement of the iron oxide surface is well-preserved as their bonds are described by a bonded force field. On the other hand, at the ReaxFF level at a pressure of 0.1 GPa at 100 °C, the iron oxide atoms have more freedom to move as there are no explicit bonds between atoms. Interestingly, for both force fields, we can see the of wall on liquid layering at the lubricant-surface interface, which has also been observed in other studies using different systems of surface and lubricants [174, 180].

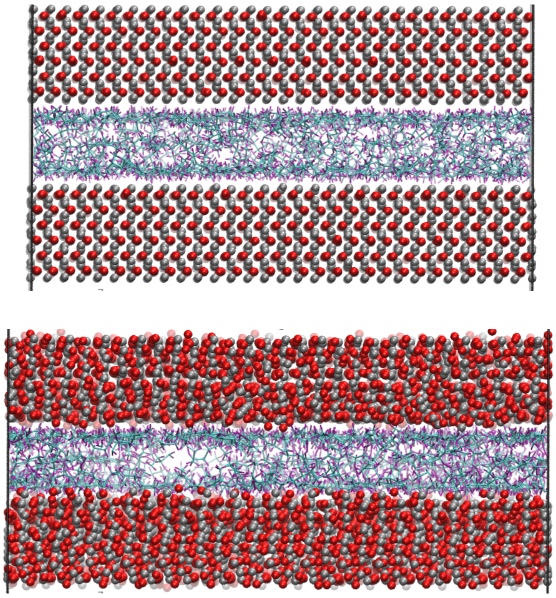

FIGURE 7.2: (a) Molecular snapshot of system 1 (100 lubricant molecules), with L-OPLS-AA at 0.1 GPa and 100 °C after the compression stage. (b) Molecular snapshot of system 1 (100 lubricant molecules), with ReaxFF at 0.1 GPa and 100 °C after the compression stage. Carbon atoms are coloured cyan, hydrogen atoms with purple, oxygen atoms with red and iron atoms with silver.

7.3.2 Density profiles

The structural analysis of the layering of the fluid due to the presence of hematite slabs, seen in the confined simulations is presented in the following Figures, quantified as density profiles. The density profiles were acquired by averaging over the last 5000 iterations (1.25 ps for ReaxFF and 5 ps for L-OPLS-AA) during the shearing production run. Figure 7.3 shows the atomic mass density profiles in the z-direction, for system 2 (200 lubricant molecules) at 0.5 GPa and a log $\dot{\gamma}$ of 8.50, by using the ReaxFF and L-OPLS-AA force fields. The term "relative gap thickness" is a dimensionless parameter that quantifies the normalized bin sizes ranging from 0 to 1, which are employed to partition and subsequently calculate density along the $z-$direction. When multiplied by the box dimension, it yields the distance in Angstrom. The oscillatory atomic mass density profile closer to the surface indicates stronger layering of the lubricant when compared to the centre of the film. These oscillations are similar to those from confined NEMD simulations of squalane [174]. Additionally, by looking at the density profile closer to the surface, stronger layering was observed in ReaxFF than L-OPLS-AA for the same conditions that were tested. Then, Figure 7.4 shows the atomic mass density profile in the z-direction, for system 3 (450 lubricant molecules) at a range of pressures (0.1 to 1.0 GPa) and a log $\dot{\gamma}$ of 8.50, by using the L-OPLS-AA force field. By comparing these density profiles, the following can be said. Firstly, by increasing the applied pressure, density oscillations become more apparent, and as expected, the overall densities increase as well. Secondly, the increase in pressure shrinks the total density profile which is equivalent to the volume contraction where the fluid is confined. Finally, the average density of the confined fluid (blue line in Figure 7.4) is in excellent agreement with the respective density of the bulk liquid simulations at 0.1 GPa, with both densities being equal to 0.79 g/ml.

Moreover, the average densities of the three systems (L-OPLS-AA case) with 100, 200 and 450 lubricant molecules at 0.5 GPa and a shear rate of $10^{8.5}$ s^{-1} were found to be equal to 0.90 ± 0.52, 0.90 ± 0.50 and 0.89 ± 0.35 g/ml, respectively. By comparing the standard deviation of these average densities for the three systems, we see that by increasing the number of lubricant molecules, the density oscillations decrease.

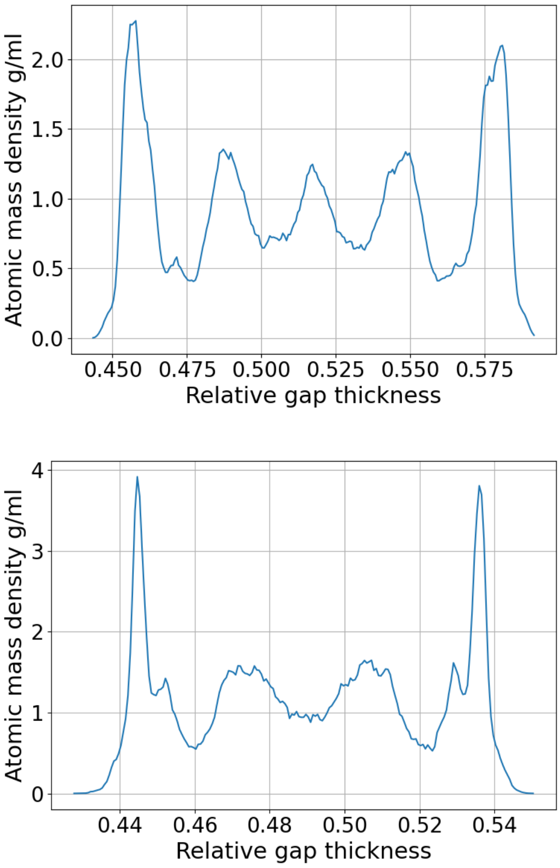

FIGURE 7.3: Atomic mass density profile of system 2 (200 lubricant molecules) at 100 °C, a log $\dot{\gamma}$ of 8.50 and a pressure of 0.5 GPa with (a) ReaxFF and (b) L-OPLS-AA.

7.3.3 Film thicknesses

Table 7.1 shows the different average film thicknesses, which were calculated before the shearing stage, with their respective standard deviation. We see that by increasing the number of confined lubricant molecules within the two iron oxide surfaces, the relative standard deviation (coefficient of variation, i.e., standard deviation divided by the mean thickness) decreases. For example, for the case of L-OPLS-AA force field at

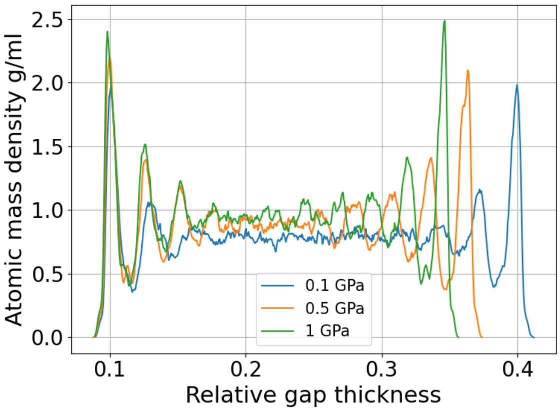

FIGURE 7.4: Atomic mass density profile of system 3 (450 lubricant molecules) with L-OPLS-AA at 100 °C, a log $\dot{\gamma}$ of 8.50 and a pressure range of 0.1 GPa, 0.5 GPa and 1.0 GPa.

TABLE 7.1: Average film thickness L-OPLS-AA (last 2 ns) and ReaxFF (last 0.5 ns) simulations

Lubricant molecules	**Film thickness(Å)**	**Force field**	***P*(GPa)**
100	13.70 ± 0.08	L-OPLS-AA	0.1
200	25.40 ± 0.12	L-OPLS-AA	0.1
450	55.93 ± 0.22	L-OPLS-AA	0.1
100	12.45 ± 0.04	ReaxFF	0.1
200	19.59 ± 0.06	ReaxFF	0.1
100	12.27 ± 0.04	L-OPLS-AA	0.5
200	22.75 ± 0.06	L-OPLS-AA	0.5
450	49.54 ± 0.09	L-OPLS-AA	0.5
100	11.06 ± 0.03	ReaxFF	0.5
200	17.91 ± 0.03	ReaxFF	0.5
100	11.44 ± 0.04	L-OPLS-AA	1.0
200	21.50 ± 0.05	L-OPLS-AA	1.0
450	46.43 ± 0.07	L-OPLS-AA	1.0
100	10.12 ± 0.02	ReaxFF	1.0
200	17.35 ± 0.03	ReaxFF	1.0

0.1 GPa, the relative standard deviations of systems 1, 2 and 3 are 0.6%, 0.5% and 0.4% respectively.

We can also see that by applying higher pressure loads at the upper outermost layer of the iron oxide slab, for a given system that has the same number of lubricant molecules and regardless of the force field used, the standard deviation of the average film thickness decreases. This can be explained by the fact that the increase in pressure leads to less freedom of movement for the lubricant molecules while overcoming repulsion forces between the lubricant and the walls.

Compared to L-OPLS-AA, ReaxFF simulations resulted in a thinner film for the same systems and conditions. This can be explained by the fact that ReaxFF allows atoms to come closer into contact with the surface (see Figure 7.2a and 7.2b). It appears that this difference is more evident at higher pressures (Table 7.1). It is also important to notice that the hematite density is better described by ReaxFF compared to the LJ potential. This is linked to the better description of the forces between atoms in the slabs in the ReaxFF compared to the simple LJ potential.

Figure 7.5 shows the compression stage during the time evolution of the simulation when using the L-OPLS-AA force field for system 3 (450 lubricant molecules). It was found that the time required to reach a fully compressed state increases with the system's size. This can be explained by the increase of repulsion forces arising from the lubricant. Increasing the pressure from 0.1 GPa to 1.0 GPa decreases the compression time from 3 ns to 1 ns.

It was also observed that the ReaxFF force field is slower than the L-OPLS-AA force field in terms of time required for reaching equilibrium during compression and overall time performance (approximately 44 times slower than L-OPLS-AA per femtosecond).

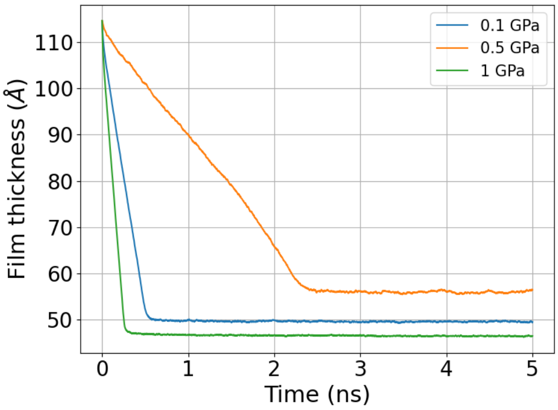

FIGURE 7.5: Film thickness of system 3 (450 lubricant molecules), with L-OPLS-AA at 100 °C during the compression stage of 5 ns. For this case, compression is slower compared to systems 1 and 2, as there are more confined lubricant molecules between the iron oxide slabs. This results in increased repulsion forces arising from the lubricant.

7.3.4 Statistical analysis of viscosity results

Table 7.2 and Table 7.3 show the viscosity results obtained from molecular simulation with the L-OPLS-AA and ReaxFF force field at 100 °C, respectively.

When we take into consideration the effect on viscosity by varying the number of confined lubricant molecules within the surfaces, it can be seen that in both force field cases, when applying the same pressure and shear rate, viscosity decreases when the number of lubricant molecules increases. This is due to an increased film thickness which allows the molecule to have more freedom but also reduces the surface

TABLE 7.2: Viscosity results of 9,10-dimethyloctadecane at 100 °C using L-OPLS-AA and comparison with bulk simulations [12]. Note that the deviation is with respect to the bulk value at the same operational conditions of temperature, pressure and shear rate. Pressure values are in GPa, viscosity in mPa s.

Molecules	$\log(\dot{\gamma})$	P	**Viscosity**	**Deviation %**	**Bulk Viscosity**
100	7.50	0.1	27.8	300	6.94
100	7.50	0.5	664	425	126
100	7.50	1.0	1.95×10^3	48	1.32×10^3
100	8.50	0.1	15.0	132	6.47
100	8.50	0.5	117	50	78.1
100	8.50	1.0	236	-13	272
200	7.50	0.1	22.3	221	6.94
200	7.50	0.5	431	241	126
200	7.50	1.0	1.56×10^3	19	1.32×10^3
200	8.50	0.1	11.4	76	6.47
200	8.50	0.5	103	33	78.1
200	8.50	1.0	223	-18	272
450	7.50	0.1	6.50	-6	6.94
450	7.50	0.5	178	41	126
450	7.50	1.0	1.31×10^3	-0.4	1.32×10^3
450	8.50	0.1	6.21	-4	6.47
450	8.50	0.5	85.9	10	78.1
450	8.50	1.0	230	-16	272

interactions. When we refer to "surface interactions", we are specifically addressing the non-bonded interactions (Lennard-Jones and electrostatic) between the surface and the lubricant molecules.

Increasing the shear rate resulted in almost all cases, in shear thinning. The only exception was the case of system 3 (L-OPLS-AA), where at a pressure of 0.1 GPa, the viscosity values for both applied shear rates were very close, as for this case, simulations were very close to the Newtonian regime, where viscosity does not depend on the applied shear rate and has a constant value.

We also studied the effect of pressure on viscosity, which increased when a higher pressure was applied externally. The ReaxFF force field predicts a higher viscosity compared to the L-OPLS-AA force field but we observe the same change in viscosity behaviour qualitatively. The deviation between the two force fields is more apparent in lower pressures. For example, at $P = 0.5$ GPa and $\dot{\gamma} = 10^{8.5}$ s^{-1} (system 2) ReaxFF overestimated viscosity by 224% compared to L-OPLS-AA, while at $P = 1.0$ GPa and $\dot{\gamma} = 10^{8.5}$ s^{-1} (system 2) ReaxFF overestimated viscosity by 172%.

We also see that by increasing the number of molecules the viscosity approaches the bulk value reported in a previous study [12]. For those interested, the overestimation of

TABLE 7.3: Viscosity results of 9,10-dimethyloctadecane at 100 °C using ReaxFF at a pressure range of 0.1 to 1.0 GPa and a $\log(\dot{\gamma}[s^{-1}])$ of 8.5. Pressure values are in GPa, Viscosity in mPas

Molecules	**System**	$\log(\dot{\gamma})$	P	**Viscosity**
100	1	8.50	0.1	294
100	1	8.50	0.5	540
100	1	8.50	1.0	764
200	2	8.50	0.1	181
200	2	8.50	0.5	335
200	2	8.50	1.0	607

viscosity compared to the experiments and the comparison with experiments regarding the Newtonian limit are discussed in [12].

The time-averaged viscosity during the shearing stage of the production run for system 3 can be seen in Figure 7.6 for the case of ReaxFF. The overall trend was that simulations at a shear rate of $10^{7.5}$ s^{-1} did not converge, compared to those at a shear rate of $10^{8.5}$ s^{-1} (orange, yellow and green lines, respectively), which converged after 1 ns. This is due to the fact that at lower shear rates, the equilibrium fluctuations become comparable with the non-equilibrium response, which results in a lower signal-to-noise ratio, as a result, we need to increase the total simulation time and the sampling interval of viscosity, which in the end is the whole duration of the simulation.

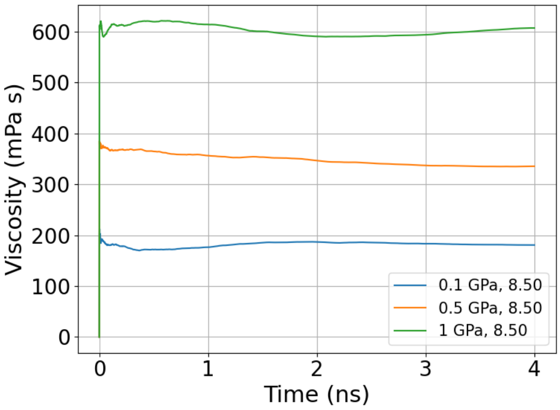

FIGURE 7.6: Average viscosity of system 2 (200 lubricant molecules), with ReaxFF at a pressure range from 0.1 to 1.0 GPa at 100 °C and at a shear rate of $10^{8.5}$ s^{-1}.

Figure 7.7 shows the behaviour of viscosity as a function of the number of lubricant molecules confined within the iron oxide surfaces, which are compared against the bulk NEMD simulations (system 4). The overall trend of viscosity, as we reach a film thickness close to the bulk simulation, is that we approach the bulk values of viscosity. This means that if the number of lubricant molecules is sufficient, confined NEMD can also give reliable viscosity results that are close to the bulk viscosity values. The only exception was the case of the highest pressure of 1.0 GPa at a high shear rate of $10^{8.5}$

s^{-1}, where all systems gave very similar results, this indicates that confinement effects are less prominent at sufficiently high shear rates that depend on the applied pressure.

In principle, one should increase the number of molecules further to assess possible oscillatory behaviour of the convergence but this is at the moment out of our computational capabilities. Nonetheless, it's worth noting that our analysis indicates a monotonic trend rather than any oscillatory behaviour in the viscosity as the number of molecules increases. While we are unable to explore larger systems due to their computational cost, the available data does not suggest any oscillatory nature in the convergence of viscosity values.

It is also important to notice that the viscosity exhibits a significant variation, changing by more than sixfold, from 1320 to 270 mPas, when the strain rate is increased tenfold, shifting from $10^{7.5}$ to $10^{8.5}$ s^{-1} at 1 GPa. Interestingly, when the number of molecules is altered, moving from 100 to 450 while keeping the strain rate constant at $10^{7.5}$ s^{-1} and at 1 GPa, the change in viscosity is comparatively modest, being less than a twofold difference, shifting from 1950 to 1310 mPas. Furthermore, we analyzed the effect of pressure on the bulk viscosity. Notably, a tenfold change in pressure, from 0.1 to 1 GPa, led to a substantial alteration in viscosity. At a strain rate of $10^{8.5}$ s^{-1}, the change amounted to approximately 40-fold, while at $10^{7.5}$ s^{-1}, it exceeded 200-fold. In contrast, when modulating confinement and the associated shift in film thickness within the range of approximately 10-50 Angstroms, we observed a notably weaker influence on viscosity compared to similar adjustments in other parameters, such as strain rate and pressure.

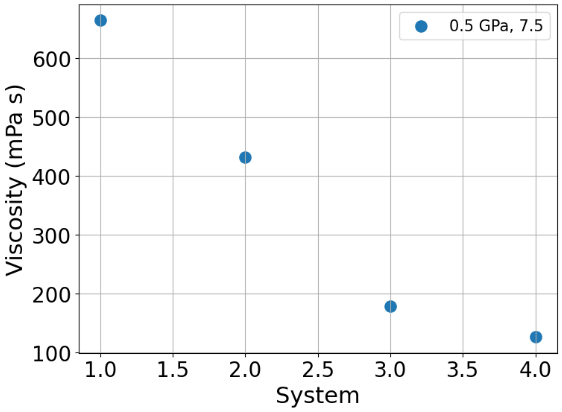

FIGURE 7.7: Viscosity results comparison between confined NEMD simulations (system 1, 2 and 3) and bulk NEMD simulations (system 4) at $P = 0.5$ GPa and $\log(\dot{\gamma}[s^{-1}]) = 7.5$, by using the L-OPLS-AA force field. As we increase the number of confined lubricant molecules we approach the bulk behaviour of viscosity. Systems 1, 2 and 3 contain 100, 200 and 450 lubricant molecules, respectively.

Comparing viscosity values in Tables 7.3 and 7.2 we observe the same behaviour with L-OPLS-AA force field qualitatively, as viscosity decreased when the number of lubricant molecules increased. L-OPLS-AA predicts viscosity values to be closer to

Simulation	R_g	λ_x	λ_y	λ_z
L-OPLS-AA 100	28,9	11.0	355.3	471.1
L-OPLS-AA 200	29.6	48.0	356.6	474.4
L-OPLS-AA 450	32.8	245.3	357.0	475.0

TABLE 7.4: Radius of gyration and gyration moments for L-OPLS-AA simulation at 0.1 GPa and at shear rate of $10^{8.5}$ s^{-1}

experiments than ReaxxFF, although the latter could be used for studying possible chemical reactions at high-pressure-temperature regimes.

7.3.5 Radius of gyration and gyration moments

To gain deeper insights into the intramolecular orientation, we analysed the behaviour of lubricant molecules. Specifically, we computed the average radius of gyration (R_g) over the last nanosecond (ns) of the simulations (Table 7.4).

As anticipated, we observed that R_g increased as the number of lubricant molecules, and consequently the film thickness, increased. This behaviour aligns with our expectations as the confinement is less strict when the number of lubricant molecules increases.

However, what truly piqued our interest was the significant role played by the λ_x component of the gyration tensor, which corresponds to the component aligned with the flow direction. Our analysis revealed that as the film thickness increased, this component made the greatest contribution to the change in R_g. In practical terms, this implies that as the lubricant film becomes thicker, the molecules within it exhibit a pronounced elongation along the direction of the flow. When we compare this observation with the viscosity values, it becomes apparent that as molecules become more elongated in the direction of the flow, their viscosity tends to decrease.

7.4 Conclusions

In this chapter, we have performed confined NEMD with two force fields (L-OPLS-AA and ReaxFF) to understand the microscopic behaviour and shear viscosity of 9,10-dimethyloctadecane molecules confined between two hematite slabs at various pressures, shear rates and film thicknesses. L-OPLS-AA is a well-established force field known for its accuracy in viscosity simulations for various classes of lubricants. However, it lacks parameters for surfaces, which are crucial for simulating industrial applications involving lubricants. In many cases, in confined L-OPLS-AA simulations surfaces are fixed and the interactions with the lubricant employ a simple Lennard-Jones (L-J) approach. ReaxFF, on the other hand, offers a unique advantage in that it treats both hematite surfaces and lubricants on equal footing. This allows it to capture more physics and chemistry at the interface, making it suitable for simulating systems with complex surface-lubricant interactions. Given its reactivity, ReaxFF has the potential to provide insights into chemical aspects of lubricant behaviour, which is essential in certain scenarios. We have shown that the film thickness affects viscosity and as we increase the number of lubricant molecules, we approach the viscosity value of the bulk fluid, that was obtained with NEMD. In particular, viscosity values were in good agreement between the two methods (NEMD and confined NEMD), when there were enough lubricant molecules confined within the walls. For example, at a shear rate of $10^{7.5}$ s^{-1} and 0.1 GPa at a film thickness of 25 Å the simulation already deviates from the bulk behaviour by 221%. The only exception that was observed was in the high pressure (1.0 GPa) - high shear rate ($10^{8.5}$ s^{-1}) regime, where the different film thicknesses had no influence on viscosity. This indicates confinement effects are less prominent at sufficiently high shear rates that depend on the applied pressure. The density profiles in the z-direction have been investigated. For both force fields, we observed the formation of a monolayer of lubricant molecules near the lubricant-surface interface. We also observed a reduction in the oscillation of the density when increasing the number of molecules. The liquid densities calculated for both force fields are in agreement with experimental data but ReaxFF predicts hematite density better than the simple LJ which is employed to describe the hematite in the case of L-OPLS-AA. We also found that the ReaxFF force field overestimates viscosity when compared to the L-OPLS-AA force field but the same change in viscosity behaviour with simulation parameters is observed qualitatively. L-OPLS-AA appears to have a better prediction of viscosities of organic lubricants under confinement compared to ReaxFF, probably due to being parameterised specifically for these types of molecules. The deviation between the two force fields was more apparent at lower pressures. For example, at $P = 0.5$ GPa and $\dot{\gamma} = 10^{8.5}$ s^{-1} (system 2 - 200 lubricant molecules) ReaxFF overestimated viscosity by 224% compared to L-OPLS-AA, while at $P = 1.0$ GPa and $\dot{\gamma} = 10^{8.5}$ s^{-1} (system 2 - 200 lubricant molecules) ReaxFF overestimated viscosity by 172%. Our findings suggest that capturing more physics and chemistry, as offered by ReaxFF, does not necessarily translate into better accuracy in describing viscosity. This phenomenon bears a resemblance to findings in biomolecular simulations, exemplified in the work of Bradshaw et al.[192] In their study, they compared the AMOEBA force field with the GAFF force field to investigate the hydration free energy of various neutral organic compounds. Interestingly, their research revealed that despite AMOEBA's departure from the pairwise additive models of electrostatics, it was only able to achieve free energy values on par with the traditional GAFF. This achievement, however, required extensive and meticulous parameter optimization. This observation raises important questions about the parametrization of force fields and the balance between complexity and simplicity. The ReaxFF force field, in our case, exhibits a notably higher level of complexity when juxtaposed with classical force fields like L-OPLS-AA.

Consequently, this heightened complexity translates into a more intricate and time-consuming parameterisation process. As the field of molecular simulations evolves, the question of how to improve force field accuracy and applicability remains. Machine learning (ML) force fields are emerging as a promising avenue, and it is indeed worth considering their potential for addressing some of the limitations associated with traditional force fields.

Our simulations provide new insights into rheological properties that can occur in concentrated contacts but are difficult to study experimentally. The simulation protocols and workflows we have developed in this work can be used to improve the understanding of lubricant behaviour at the atomic scale, providing insights into the fundamental mechanism of very thin lubricant films.

Chapter 8

Adsorption of ZDDPs on Hematite surfaces

8.1 Introduction

Additives are an essential element in lubricant composition used to optimise friction reduction and minimise surface wear across various industrial applications. This chapter focuses on a specific class of lubricant additives known as ZDDPs. The adsorption of ZDDPs on metallic surfaces is considered a critical first step in formation of anti-wear films in many of the proposed pathways [90, 193–195]. These adsorption and subsequent chemical reactions are difficult to probe experimentally, making computational techniques essential for understanding the complex interactions between ZDDPs and metallic surfaces. Despite extensive research on the interactions and reactivity of ZDDPs with surfaces like iron, iron oxides, aluminium, steel, and titanium, there remains a critical gap in understanding the electronic structure of these systems. Although binding energies and the effects of surfaces, alkyl chains, and temperature on ZDDPs decomposition pathways have been studied, the electronic structure changes remain largely unexplored. Understanding these changes is crucial for gaining insights into ZDDPs decomposition pathways. This chapter focuses on a DFT+U analysis of ZDDPs binding on three industrially relevant hematite ($\alpha - \mathrm{Fe_2O_3}$) surfaces. The goal is to understand changes in the electronic structure of both the additive and the surfaces upon binding and to provide indications of possible decomposition pathways for ZDDPs.

8.1.1 Computational Details

In this study, spin-polarised calculations were performed using the ONETEP software [196] at the PBE + D2 level with a kinetic energy cutoff of 1250 eV. Four and thirteen non-orthogonal generalized Wannier functions (NGWFs) were used for the O atoms and for the Fe atoms, respectively. The NGWFs radius was set to 11 Bohr. The DFT+U projection subspaces were constructed from the pseudoatomic orbital initial guess for the NGWFs[197] with Fe in its nominal 3+ reference state for Fe_2O_3, specifically the 3d orbitals only. Ultrasoft PBE pseudopotentials, including semi-core states for Fe, generated by the CASTEP software were used in all simulations[198].

The initial guesses for the density were generated using a superposition of densities from the aforementioned pseudoatomic calculations, with iron atoms in a 3+ configuration (3d5 4s0) and spin equal to ± 5 depending on the sub-lattice in the anti-ferromagnetic configuration, and for neutral-reference pseudoatomic oxygen however with a renormalization of its charge to a -1 state with no spin. The total spin-density was renormalised for an overall charge-neutral crystal before DFT calculations commenced.

In order to provide effective k-point sampling with explicit Γ-point sampling only and real-valued orbitals, a 4x4x1 supercell was generated from the hexagonal conventional cell, totaling 360 atoms, which were then allowed to relax in a fixed-cell simulation using the PBE functional. The values we obtained for the Fe-Fe bond distances are 3.0 Å and 3.5 Å which are reasonably close to the experimental values of 2.9 Å and 3.98 Å , and, for the Fe-O bond distances, 1.9 Å and 2.1 Å against the experimental values of 1.98 Å and 2.09 Å.

Hubbard correction was then applied to the Fe 3d states with an empirical value U_{eff} = 6.0 eV for applied calculations, a value which arrived at by comparing band gap and magnetic moments against experimental values reported in the literature. This choice was validated by direct first-principles Hubbard U and Hund's J calculations including self-consistency over the parameters. This indicates room for some relatively minor refinement in future work, as we go on to describe; however, the U_{eff} = 6.0 eV value has proved to be a reasonable approximation.

8.2 Results and Discussion

8.2.1 Hubbard parameter evaluation for bulk hematite

Approximate local and semi-local exchange-correlation functionals typically fail to capture the charge-transfer nature and band gap of hematite, as well as the correct magnetic ordering. This necessitates the use of a more general density-matrix functional such as DFT+U, noting this is not the only applicable formalism, to obtain the correct insulating character. This method requires choosing or calculating the effective U_{eff} parameter. We have tested several different values, using the 3+ configuration projectors for Fe, noting that U_{eff} = 4 eV is a low bound to the U values used in the literature for hematite[31, 121, 123, 199, 200].

Table 8.1 reports the effect of the Dudarev effective Hubbard parameter U_{eff} on selected indicators for comparison with experiments. The band gap and local moments increase monotonically with U_{eff} as expected, and in particular, the band gap exhibits two different regimes of linear increase. The rate is approximately 0.3 eV/eV from 0 eV < U_{eff} < 5 eV and 0.1 eV/eV from 6 eV < I_{eff} < 8 eV, the transition point representing the cross-over from a predominantly d-d band-gap character to a p-d one, as anticipated.

	Hubbard U in eV						
Properties	U = 0	U = 2	U = 4	U = 5	U = 6	U = 7.044	U = 7.695
Band Gap (eV)	0.96	1.65	2.32	2.61	2.81	2.94	3.00
Density-based Fe spin (μ_B)	3.13	3.32	3.44	3.48	3.52	3.56	3.58
Atomic Fe 3d spin (μ_B)	3.71	3.92	4.05	4.11	4.15	4.20	4.23
Atomic Fe 3d Occupancy (e)	6.03	5.93	5.84	5.80	5.77	5.73	5.71

TABLE 8.1: The effect of the Dudarev effective Hubbard parameter U_{eff} on the fundamental band gap, along with the spin magnetic moment per iron atom calculated from the integral of the absolute value of the spin density, divided by the number of such atoms. This is followed by representative spin atomic moments and occupancies in the same Fe^{3+} 3d pseudoatomic orbitals basis used to define DFT+U. The tensorial representation of DFT+U used, so that the projection is strictly localised. The final two columns correspond to the parameter non-self-consistently directly calculated values for U_{eff} = U - J and U, respectively (the calculated J = 0.651 eV).

The most reliable available estimate for the experimental band gap is 2.2 eV. As we can see, this is matched by simulation at approximately U_{eff} = 3.7 eV using Fe^{3+} 3d projectors for DFT+U, and over-estimated thereafter. This comparison of course neglects excitonic binding effects, phonon zero-point motion, and inevitable finite-temperature and disorder effects. By contrast, the magnetic moments only come into the experimental range of 4.0 to 4.6 μB beyond approximately the same U_{eff} value, referring to the possibly more reliable pseudoatomic orbital based estimate. This comparison made it more difficult by the partial arbitrariness of both theoretical population analysis and the experimental estimation, as well as the neglect or orbital moment contributions to the former.

We have directly calculated the Hubbard U and Hund J values using the scaled (more conventional) variety of the minimum-tracking linear response formalism described in Ref. [201]. The same supercell was used, and a single Fe atom was perturbed in reasonable isolation from its periodic images and the subspace spin-density on the same Fe atom was monitored. Based on excellent run-time convergence and good four-point linear response, this yielded U = 7.695 eV, J = 0.651 eV, and therefore U_{eff} = U - J = 7.044 eV. This was based on perturbations around the uncorrected PBE ground state, and to test the dependency of these parameters on the density, which will response to an applied U_{eff}, we re-ran this linear response procedure at input values of U_{eff} = 2 eV and 4 eV. The output U_{eff} fell with respect to the applied input U_{eff}, as expected, and with a slope of approximately -1.01 eV/eV, reflecting a truly negligible effect of consistency over U_{eff}, where a slope of -1 would indicate vanishing effect. The extrapolated self-consistent value for U_{eff} matched the non-self-consistent value, within the errors introduced by the finite set of data used, and hence we can conclude that parameter self-consistency is not a helpful complication at least within this system, underlying exchange-correlation functional, and DFT+U projection choice. The results of DFT+U (using both the parameter U_{eff} and simply U) are showin in Table 8.1 We also performed DFT+U+J using the functional described in Ref. [202] (without the minority-spin term, following established practice), and this yielded a band gap of 3.25 eV, which is too large, and a pseudoatomic Fe^{3+} 3d spin moment of 4.29 μ_B, which is close to the center of the experimental range. Ultimately, for practical calculations, we settled upon U_{eff} = 6 eV as a reasonable compromise between accuracy for the band gap and spin-density.

In parallel with our investigation, we continued to explore ways to improve the agreement with experiments regarding the bulk properties, on a first-principles basis. Using DFT+U projectors of 3d from neutral Fe pseudoatomic configuration $3d^6 4s^2$ (followed by charge renormalization to 3+ and spin renormalization to ± 5 μ_B for the spin-density initial guess) we re-ran our minimum-tracking linear response calculations for the U and J, using two different perturbations around the PBE ground state (three-point finite differences). With this population analysis at U = 0 eV, we found a somewhat lower subspace spin magnetic moment than with 3+ projectors, of 3.48 μ_B. The calculated U was approximately 1/3 lower, at 5.154 eV, and the calculated J was less affected, at 0.605 eV, giving U_{eff} = 4.549 eV. The reduction in parameters, together with a change in their effect (for a given value) due to the projector profile change, gave rise to a change in the effect of the DFT+U correction, apparently for the better. DFT+U with U_{eff} = 4.549 eV yielded a band gap of 2.22 eV, in excellent agreement with experiments, alongside a not-unreasonable local spin moment of 3.80 μ_B. The results from DFT+U with a parameter of U also gave good results, at 2.29 eV and 3.83 μ_B, while DFT+U+J gave 2.53 eV and 3.90 μ_B. Overall, charge-neutral projectors seem to give better band-gap estimates with first-principles parameters, at least given the limitations of the methodology. For completeness, we note that the 'simple' version of the minimum-tracking linear response method, which is effectively when magnetization is fixed while occupancy is varied, and vice versa, gave values of U = 10.959 (7.621) eV and J = 0.632 (0.581) eV for 3+ (0+) Fe 3d projectors. It is also worth noting the spin-resolved '1×1' U values (J is not applicable here), which were 0.892 (0.567) eV for the majority spin and 3.592 (2.964) eV for the minority spin, for 3+ (0+) Fe 3d projectors.

8.2.2 Electronic Structure of Bulk Hematite

8.2.2.1 Density of states

Hematite is a charge transfer insulator with an experimental band gap of $\approx 2.2\,\mathrm{eV}$. The top of the valence band is dominated by O 2p orbitals while the bottom of the conduction band is dominated by minority spin Fe 3d orbitals. In Fig 8.1 we report the total density of states (DOS) for both spin channels (Fig. 8.1a, the space-resolved density of states (LDOS Fig. 8.1b) and the projected density of states (PDOS 8.1c).The LDOS is based on Mulliken partitioning of the NGWFs while the PDOS is based on the projection on pseudo-atomic basis generated from the atomic solver, as explained in [197]. The total density of states for an antiferromagnetic system should be equivalent for both spin channels and this is indeed the case for the plotted density of states. The DOS for the spin minority channel has been flipped along the x-axis to facilitate comparison with the majority spin channel, hence the negative DOS value. It is also clear that the system is an insulator with a band gap of 2.65 eV which is reasonably close to the reported experimental value. In all of the DOS plots reported the Fermi energy has been shifted to 0.

The top of the valence band in the plotted projected density of states is dominated by O 2p orbitals and the bottom on the conduction band is dominated by minority spin Fe 3d orbitals. This is in agreement with the expected electronic structure of hematite. Additionally, comparing the PDOS to the LDOS in Fig 8.1b shows that most of the contribution to the top of the valence band from O and Fe is indeed coming from the O 2p orbitals and Fe 3d, while other O and Fe states, such as oxygen 2s and Iron 3p, do not contribute much.

8.2.2.2 Band gap, magnetic moment, spin and charges

In Table 8.2, the magnetic moments, charges, and spin values are reported. The magnetic moment values fall within the experimental range of 4.0 to $4.6\,\mu$B. The charges and spin values obtained from a Mulliken analysis offer further insight into the electronic structure of the crystal. Hematite exhibits characteristics intermediate between ionic and covalent bonding, which aligns with previous studies[31, 123, 199].

Understanding these electronic properties is crucial, as they significantly influence the surface chemistry and reactivity of the crystal. Our study will focus on three different surface terminations and the adsorption of ZDDP. The interaction of the molecule with each surface will be analyzed in terms of changes in magnetic moments, charge redistribution, and spin states.

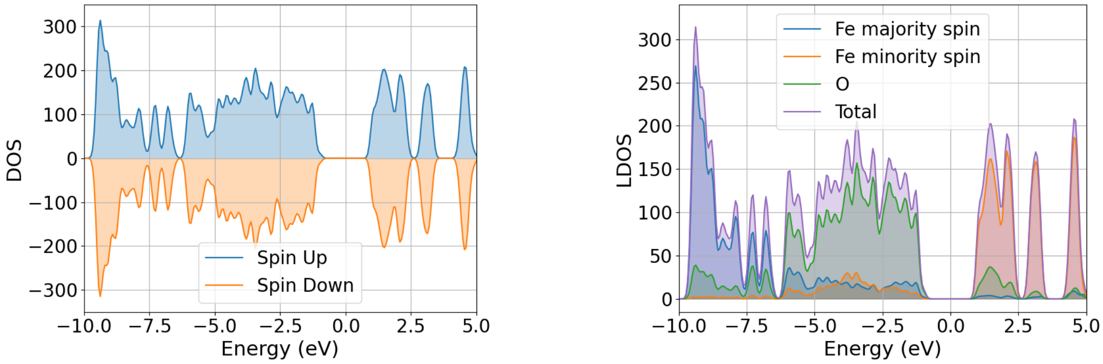

(A) Total density of states for majority spin up and spin down channels in bulk hematite, the spin down channel density of states was reflected along the x-axis to facilitate comparison. The DOS has been shifted such that the Fermi energy is at 0 eV.

(B) Local density of states for bulk hematite. The top of the valence band (around −2.5 to −2.0 eV is mainly composed of O bands with very little contribution from both the majority spin and minority spin bands of the Fe atoms. The bottom of the conduction band, on the other hand, is mainly composed of Fe minority spin empty bands with very little contribution from the O bands.

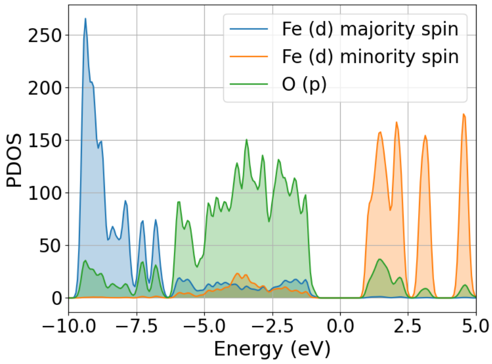

(C) Projected Density of states for bulk hematite, here we only show the contribution from Fe 3d orbitals and O 2p. This further supports the conclusion drawn from the LDOS. Specifically, the top of the valence band shows little contribution from Fe 3d bands while the minority 3d spin bands serve as the major components in the bottom of the conduction band.

FIGURE 8.1: Total DOS (a), LDOS (b) and PDOS(c) for bulk hematite.

8.2.3 Hematite Surfaces

Three different (0001) surface terminations, shown in Fig. 8.2, were investigated: The Fe-O-Fe termination (Fig. 8.2a) , the O-Fe-Fe termination (Fig. 8.2b) and the HO-Fe-Fe termination (Fig. 8.2c).

Property	Fe Up	Fe Down	O
Magnetic Moment	4.1	-4.1	0.00
Charge	1.38	1.38	-0.91
Spin	2.21	-2.21	0.00

TABLE 8.2: Magnetic moment, charge and spin in bulk hematite from the NGWFs Mulliken population analysis at the PBE + U level with a U value of 6 eV on the Fe 3d manifold. The magnetic moments are localised on the Fe atoms as expected and their values fall well within the experimental range of 4.0 to 4.6 μB, this is further supported by the spin values based on Mulliken population analysis. From the same analysis it is clear that bonding in hematite has a strong covalent character which reduces the absolute charge on both Fe and O atoms.

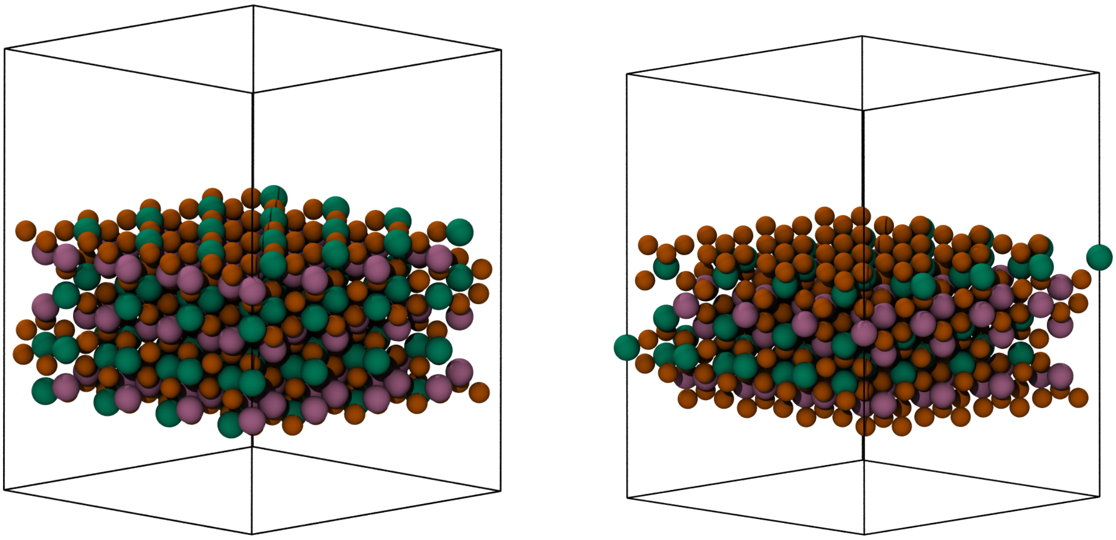

(A) Hematite (0001) Fe-O-Fe terminated slab.

(B) Hematite (0001) O-Fe-Fe terminated slab.

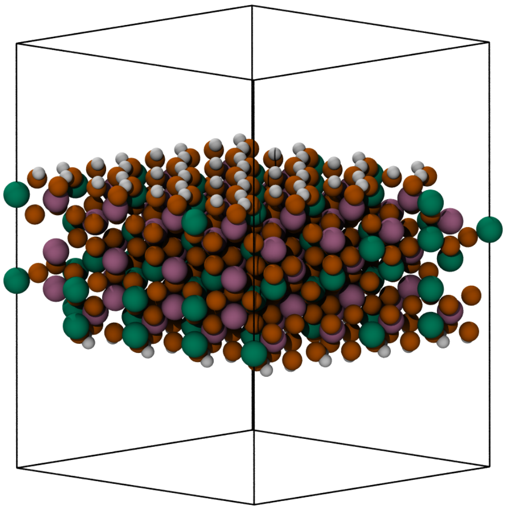

(C) Hematite (0001) HO-Fe-Fe terminated slab.

FIGURE 8.2: The three different surfaces investigated in this study, The Fe-O-Fe (a), O-Fe-Fe (b), HO-Fe-Fe (c). Green and pink atoms refer to spin up and spin down Fe atoms, white to H atoms and orange to O

8.2.3.1 Fe-O-Fe slab

The first termination we investigated is the Fe-O-Fe slab. A 15 Å layer of vacuum was added on top the surface to prevent interaction with periodic images and then the ions' positions were allowed to relax.

The values we obtained for the Fe-Fe and Fe-O bond distances remained very close to the bulk values in the middle of the slab, while at the edges, the Fe-Fe distances reduced from 3.0 Å and 3.5 Å to 2.9 Å and 3.39 Å, respectively. The Fe-O bond distances were reduced to 1.82 Å and 2 Å compared to the the bulk values. The charges and spins show the same trend, with bulk-like properties in the middle of the slab, while they differ when approaching the edges. Quantitatively, we see that the Fe atoms have average charges and spins of 1.36 e and 2.19 $\hbar$, respectively, compared to 1.38 e and 2.21 $\hbar$ in the bulk. The difference in spin also explains the slightly lower magnetic moment on the surface Fe atoms, 3.99 μB compared 4.1 μB in the bulk. This observation aligns with reported DFT studies of hematite surfaces and is expected due to the different chemical environment for atoms in the top layers caused by the presence of dangling bonds. [31, 35]

8.2.3.2 Density of states

The total density of states is shown in Fig 8.3a. Compared to the bulk DOS, the Fe-O-Fe DOS is less diffuse and shows a clear separation into three blocks of states, which is not seen in the bulk DOS. Nonetheless, the top of the valence band and bottom of the conduction bands exhibit similar characteristics to the bulk structure, i.e. the charge transfer from O 2p to iron 3d states. The slab remains antiferromagnetic with the same ordering and a band gap of 2.6 eV as in the bulk phase.

8.2.3.3 O-Fe-Fe slab

The second termination we investigated is the O-Fe-Fe slab. Following the same procedure as for the first termination, a 15 Å layer of vacuum was added on top of the surface to prevent interactions with periodic images and then the ions' positions were allowed to relax.

The slab does not undergo extensive relaxation, and the Fe-Fe and Fe-O distances remain close to the bulk phases. However, The electronic structure changes significantly: the charges and spins show very different behaviour for both Fe and O atoms. Focusing first on the atoms in the middle layers, we observe that the Fe atoms have charges and spins of 1.52 e and 2.40 $\hbar$, respectively, compared to 1.38 e and 2.21 $\hbar$ in the bulk. The O atoms show a similar behaviour, having no spin as in the bulk but a higher of

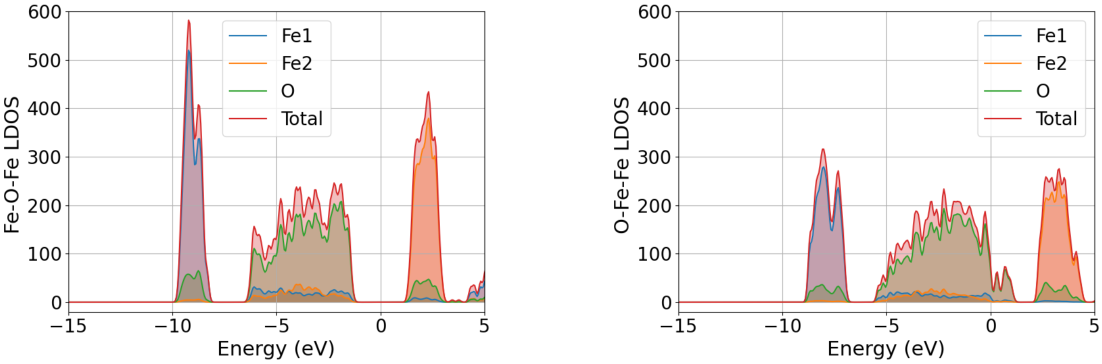

(A) Hematite (0001) Fe-O-Fe terminated slab LDOS. Comparing the LDOS with the bulk one, we notice that the band at around −10 to −8 eV is narrower and comprises more states with respect to the bulk one. The wide valence band starting at around −5 eV on the other hand does not seem to show any important changes.

(B) Hematite (0001) O-Fe-Fe terminated slab LDOS. Similar behaviour to the Fe-O-Fe slab is seen here, the band starting at around −10 eV has fewer states due to fewer Fe atoms compared to the Fe-O-Fe slab. Important to notice is the metallic behaviour, this is due to the surface O states crossing the Fermi energy.

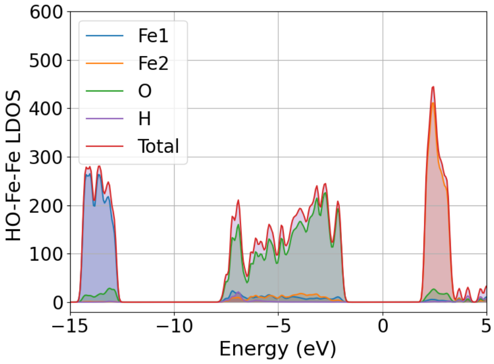

(C) Hematite (0001) HO-Fe-Fe terminated slab LDOS. The presence of the H capping the O dangling bonds has the effect of removing the metallic behaviour seen previously but also to stabilise majority spin states that now appear at −15 eV compared to −10 eV in both the bulk and the other two surfaces.

FIGURE 8.3: The three different surfaces LDOS, The Fe-O-Fe LDOS (a), O-Fe-Fe LDOS (b), HO-Fe-Fe LDOS (c).

−1.0 e compared to −0.91 e in the bulk. The surface Fe atoms, on the other hand, have a charge of 1.58 e and a spin of 2.38 $\hbar$, slightly different from the values for Fe atoms in the middle layers. The O atoms on the surface exhibit very interesting behaviour: they have a much lower charge compared to their counterparts in the middle layers or bulk system, i.e., −0.55 e for the surface atoms against −1.0 e and −0.91 e for O atoms in the middle layers and bulk hematite, respectively. Even more interesting is the fact that the surface O atoms have a small spin value of 0.46 $\hbar$, while O atoms in the middle layers and in bulk hematite are spinless. This can be understood by looking at the stoichiometry of the slab. The surface was obtained by removing the top and bottom Fe atoms layers from the Fe-O-Fe slab, generating a non-stoichiometric slab with 48 extra O, which are the surface O atoms. These changes are known to occur in transition metal oxides, and reintroducing the stoichiometry in the slab could lead to a bulk-like behaviour [203].

8.2.3.4 Density of states

The LDOS is shown in Fig 8.3b. The O-Fe-Fe LDOS has a dip at the Fermi energy, but compared to the bulk, the system exhibits metallic behaviour. This is not surprising, as it is known that metallic states can appear at the surfaces in transition metal oxides [204]. This means that, in contrast to the bulk and Fe-O-Fe slab, the O terminated slab has no band gap.

8.2.3.5 OH-Fe-Fe slab

We then investigated the OH-Fe-Fe termination, which was generated by adding H atoms to all unsaturated surface O atoms, resulting in a total of 48 H atoms. The ions' positions were then allowed to relax.

Similar to the O-Fe-Fe slab, the surface does not undergo extensive relaxation and the Fe-O and the Fe-Fe distances differ from the values in bulk hematite by only 0.03 Å on average.

The charges and spins are very similar to the bulk hematite values for both Fe and O atoms, with no significant differences between the atoms on the surface and those in the middle layers. Quantitatively, the charge and spin of Fe atoms close to the HO surface are $1.38\,e$ and $2.23\,\hbar$, respectively, those for iron atoms in the middle of the slab are $1.41\,e$ and $2.25\,\hbar$. The O atoms are spinless with a charge of $-0.93\,e$ throughout the slab, which is reasonably close to the bulk value.

Properties	Fe-O-Fe	O-Fe-Fe	OH-Fe-Fe
Magnetic moments Mid layer (μ_B)	4.10	4.51	4.15
Magnetic moments Top Layer (μ_B)	3.99	4.50	4.14
Charge on top layer O (e)	-0.82	-0.96	-0.93
Charge on top layer Fe (e)	1.36	1.54	1.38
Band Gap (eV)	2.6	0.0	2.45

TABLE 8.3: Comparison of magnetic moments, charges and band gap for all the three surfaces. The magnetic moments and charges approach the bulk values going away from the surface for the Fe-O-Fe termination. They seem to be quite constant for the HO-Fe-Fe O-Fe-Fe terminated slabs.

It appears that by saturating dangling bonds on the O atoms, the system electronically restructures and it resembles the behaviour of both bulk and Fe-O-Fe which can be seen from the magnetic moments and charges. A comparison of magnetic moments, charges and band gaps for all three surfaces is reported in Tab 8.3.

8.2.3.6 Density of states

The LDOS for the OH-Fe-Fe termination is shown in Fig. 8.3c. When compared with the LDOS for the other two surface terminations, it is evident that saturating the oxygen dangling bonds has opened up a gap, unlike the O-Fe-Fe terminated slab. This is likely due to the Fermi level pinning at the dangling bonds, a phenomenon where the presence of unsaturated bonds traps the Fermi level, impacting the electronic structure and properties of the material.

8.2.4 ZDDP Adsorption

8.2.4.1 ZDDP

The general structure of zinc dialkyldithiophosphates (ZDDPs) is depicted in Fig. 8.4. ZDDP is an inorganic compound where a central Zn atom is bonded to four alkyl-dithiophosphate groups. Previous studies have explored how different alkyl substituents affect the decomposition pathways of ZDDPs. While the type of alkyl chains influences their anti-wear activity, it does not significantly impact the binding of ZDDPs. Therefore, to save computational time, we focused on investigating ethyl-substituted ZDDPs.

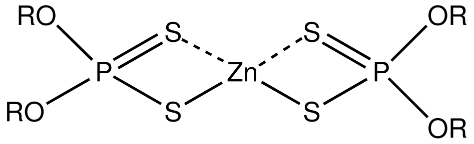

FIGURE 8.4: Zinc dialkyldithiophosphate (ZDDP).

In ZDDPs, the Zn is in a tetragonal configuration with a Zn-S bond of 2.38 Å, which is a typical length for Zn-S_4 compounds and consistent with previous computational studies [205]. The P-S bond length is 2.02 Å, the P-O bond length is 1.61 Å and S-S bond length 3.31 Å.

The angles between the atoms in the ZDDP complex are also indicative of its molecular geometry. The S-Zn-S angle is typically around 90.1°, The P-S-Zn angle is approximately 80°, the O-P-O angle is around 105.66°, and the S-P-S is around 109.6°. These values reflect the strain and steric effects within the molecule.

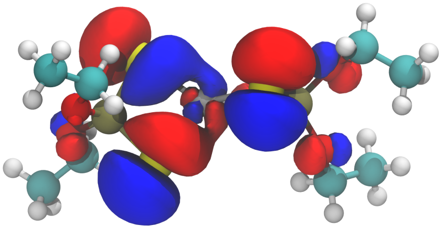

FIGURE 8.5: ZDDP highest occupied molecular orbital (HOMO), it is heavily localised on the S atoms. This suggests that the binding of ZDDP to metallic surfaces could primarily be due to the interaction between the S atoms in ZDDP and the metal atoms on the surface.

The electronic structure of ZDDPs reveals significant insights into their chemical behaviour. The Zn atom typically carries a partial positive charge due to its interaction with the more electronegative S and O atoms. Computational studies have shown that the charge on the Zn atom is approximately $0.76\,e$[205], while the S atoms have partial charges around $-0.5\,e$ each, and the O atoms exhibit partial charges of about $-0.74\,e$. These charges are consistent with the electronegativity differences and the coordination environment around the Zn centre.

Possible decomposition pathways have been suggested to occur via an O/S exchange or via the formation of phosphate moieties that can bind to surfaces. Changes in both bond lengths and bond angles upon binding could provide insights into which pathway ZDDPs are more likely to undergo. For instance, significant deviations in the P-O-Zn angle upon interaction with the surface might indicate the formation of phosphate intermediates, while changes in the S-Zn-S or O-P-O angles could suggest an O/S exchange mechanism. Monitoring changes in the charge distribution, such as an increase in the positive charge on Zn or the redistribution of charges on S and O atoms, can further elucidate the mechanistic pathways of ZDDP decomposition. Understanding these geometrical and electronic parameters is crucial for determining the chemical behaviour and stability of ZDDPs under different conditions.

8.2.4.2 ZDDP on Fe-O-Fe Slab

The binding of ZDDP on the Fe-O-Fe slab leads to various changes in both the configuration and the electronic structure. ZDDP binds with an energy of -0.84 eV and the distance to the surface, defined by the Fe-S distance, is 2.57 Å. This is slightly longer than the typical Fe-S bond found in covalent compounds of 2.35 Å. This distance indicates a weak interaction between ZDDP and the surface. Additionally, the two S atoms closer to the surface exhibit lower charges compared to the unbound molecule, with values of $-0.3\,e$ and $-0.43\,e$ versus $-0.5\,e$ in the unbound state. The Zn atom also shows a lower charge of $0.69\,e$ compared to $0.76\,e$ in the unbound molecule. The binding also slightly affects the molecular geometry: the P-S-Zn angle changes to 81.2° from 80° and the O-P-O angle decreases to 103° from 105.66°.

The LDOS shows minimal changes compared to the slab without the ZDDP molecule. This indicates that the electronic structure of the slab is not significantly perturbed by the presence of the ZDDP, suggesting that the interaction is relatively weak. This is further supported by the calculated binding energy of -0.84 eV. The modest binding energy and minimal changes in the LDOS suggest that the ZDDP is probably physisorbed rather than chemisorbed.

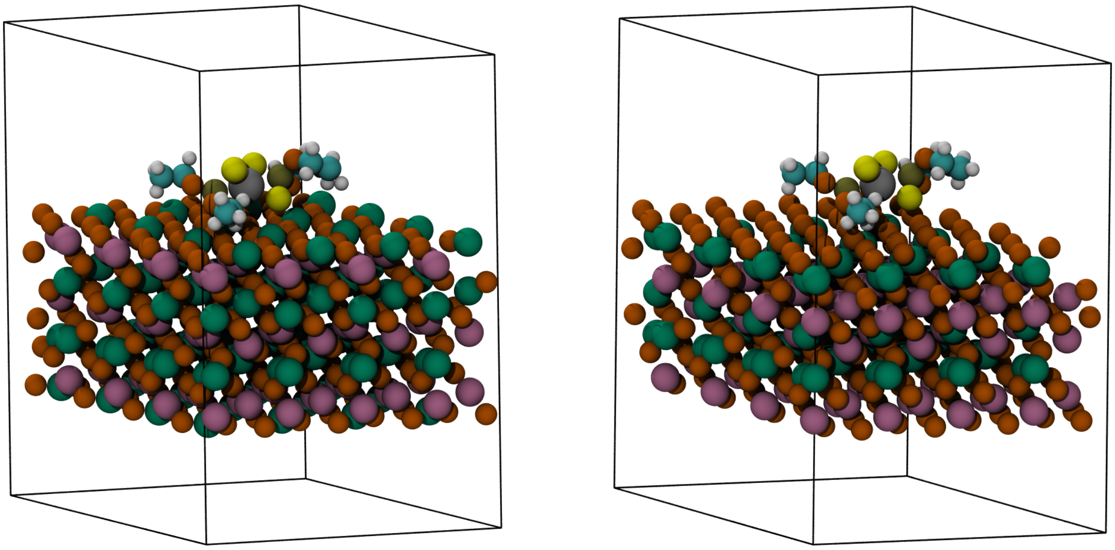

(A) ZDDP on top of Hematite (0001) Fe-O-Fe terminated slab.

(B) ZDDP on top of Hematite (0001) O-Fe-Fe terminated slab.

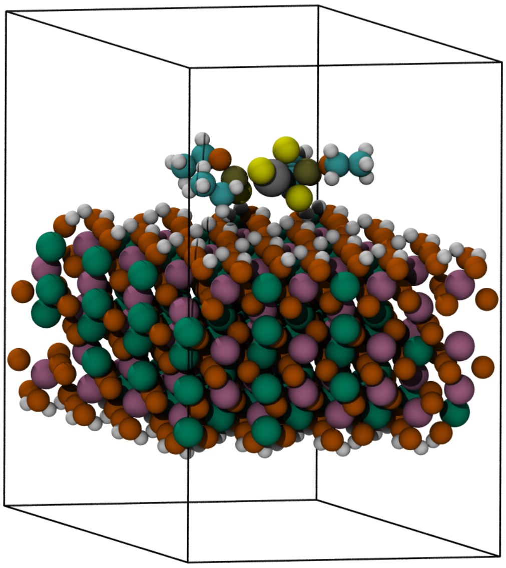

(C) ZDDP on top of Hematite (0001) HO-Fe-Fe terminated slab.

FIGURE 8.6: ZDDP on top of the three different surfaces.

8.2.4.3 ZDDP on top of O-Fe-Fe

ZDDP weakly binds to the O-Fe-Fe slab with a binding energy of -0.11 eV, this indicates that ZDDP only weakly physisorbed to the O-Fe-Fe. The distance from the surface, defined by the O-S distance, is 3.6 Å. Unlike the Fe-O-Fe slab, the electronic structure, charges, spins, and molecular angles/bond lengths of the ZDDP molecule show no significant changes upon binding to the O-Fe-Fe surface. Consequently, the LDOS remains largely unchanged compared to the clean slab without the ZDDP molecule. Overall, the interaction between ZDDP and the O-Fe-Fe slab is weak, with negligible changes to the molecule's electronic structure and geometry, reflecting a weak physisorption characteristic.

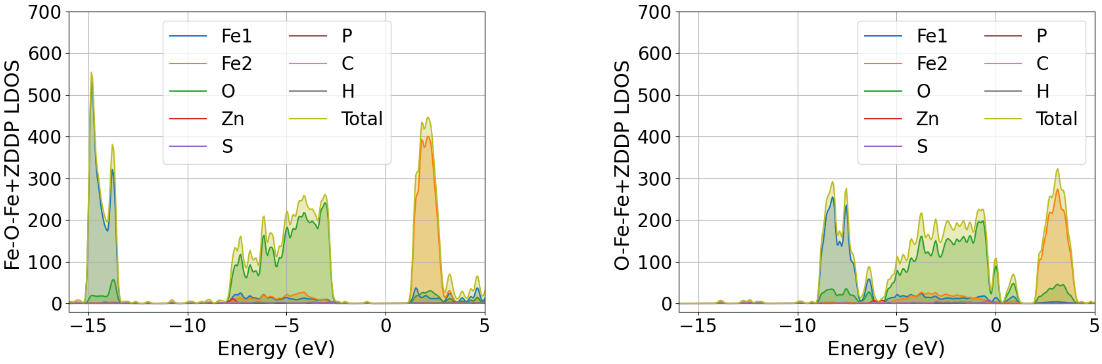

(A) ZDDP on top of Hematite (0001) Fe-O-Fe terminated slab LDOS.

(B) ZDDP on top of Hematite (0001) O-Fe-Fe terminated slab LDOS.

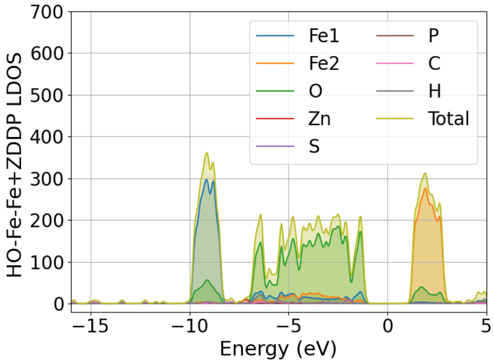

(C) ZDDP on top of Hematite (0001) HO-Fe-Fe terminated slab LDOS.

FIGURE 8.7: LDOS of ZDDP on top of three different surfaces, ZDDP on top of Fe-O-Fe LDOS (a), ZDDP on top of O-Fe-Fe LDOS (b), ZDDP on top of HO-Fe-Fe LDOS (c).

8.2.4.4 ZDDP on top of HO-Fe-Fe

When ZDDP binds to a HO-Fe-Fe slab, the interaction results in minimal conformational changes compared to its unbound state. The distance between the molecule and the slab, defined by the H-S bond, is 3.3 Å, which is relatively large, indicating a weak interaction. The ZDDP molecule shows no significant changes in its conformation or electronic structure upon binding to the HO-Fe-Fe surface. The binding energy of ZDDP to the HO-Fe-Fe slab is calculated to be -0.49 eV, which is lower than that for the Fe-O-Fe slab, further indicating a weaker interaction but higher compared to the O-Fe-Fe slab this is probably due to the excessive formal charge on the O surface atoms in the O-Fe-Fe due to the presence of dangling bonds. This weak binding energy is consistent with the large distance between the molecule and the slab, suggesting that ZDDP is only weakly physisorbed to the HO-Fe-Fe surface. The LDOS also remains largely unchanged.

8.3 Conclusions

We performed DFT+U calculations using the ONETEP software on bulk hematite and three differently terminated pristine (0001) hematite surfaces: Fe-O-Fe terminated, O-Fe-Fe terminated, and HO-Fe-Fe terminated. We also studied a zinc diethyldithiophosphate (ZDDP) molecule in the gas phase and adsorbed on the three surfaces. To achieve good agreement with experimental data and correct antiferromagnetic charge-transfer insulator behaviour, a high kinetic energy cutoff and proper initial setup of the NGWF are necessary. This setup ensures the initialization of Fe atoms to the correct high spin state, allowing DFT+U to open up a band gap. In the Fe-O-Fe slab, we observed that the top and bottom layers relax, reducing the Fe-Fe and Fe-O distances compared to the bulk. Charge, spin, and magnetic moments approach bulk values away from the surface edges. However, looking at the LDOS of the O-Fe-Fe surface, it is a metallic system due to the Fermi level being pinned at the dangling bonds, generating partially occupied surface states. For the middle layers of the O-Fe-Fe surface, Fe atoms have charges and spins of $1.52\,e$ and $2.40\,\hbar$, respectively, compared to $1.38\,e$and $2.21\,\hbar$ in the bulk. O atoms exhibit no spin as in the bulk but have a higher charge of $-1\,e$ compared to $-0.91\,e$ in the bulk. Surface Fe atoms have a charge of $1.58\,e$ and a spin of $2.38\,\hbar$, slightly different from the middle layer Fe atoms. Surface O atoms show a much lower charge of $-0.55\,e$ and a small spin value of $0.46\,\hbar$. Saturating the dangling bonds with hydrogen (HO-Fe-Fe terminated) restores the insulating behaviour, with spin and charge values similar to the bulk. Upon binding ZDDPs, we observed binding energies of -0.87 eV, -0.11 eV, and -0.49 eV for the Fe-O-Fe, O-Fe-Fe, and HO-Fe-Fe slabs, respectively. There were no significant structural changes in either the surfaces or the molecules, except for a slight decrease in the P-S-Zn and O-P-O angles in the Fe-O-Fe system. The largest changes in the electronic structure were also observed in the Fe-O-Fe slab, where charges on S and Zn atoms near the surface were lower compared to the gas phase, indicating stronger interactions. The other two terminations showed very low binding energies and minimal electronic structure changes, suggesting that the tribofilm formation might be similar for these two surfaces while we expect that the reactivity of the ZDDP on the Fe-O-Fe to be higher. As this is the first time, as far as we know, of studying ZDDP interactions with different hematite surfaces and the consequent changes in electronic structure, we anticipate that this study will serve as a solid foundation for future simulations exploring various ZDDP compounds on hematite surfaces.

Chapter 9

Conclusions

This thesis investigated the use of MD and DFT calculations for the prediction of properties of lubricants under operational conditions. The research focused on understanding the complex interactions in lubricated systems, which are crucial for reducing wear and improving performance in various applications.

We began by examining the temperature and composition dependence of ideal mixtures of two synthetic esters (DEHA and DEHS) as a simple yet realistic lubricant model. We compared EMD and NEMD with experimental measurements. The findings revealed that experimental viscosities of mixtures follow a linear trend across all temperatures. However, this trend was not always observed in NEMD simulations due to a low signal-to-noise ratio. This issue was resolved by conducting longer EMD simulations which predicted the expected linear trend qualitatively. Although EMD simulations had better precision compared to NEMD, they came with increased computational costs that could be prohibitive for certain systems. Overall, the viscosity values were underpredicted by the simulations, retrieving between 77% and 99% of the experimental values. This underestimation is attributed to limitations in the force fields used, as classical force fields are not parameterized to reproduce experimental viscosity values accurately.

We then extended the investigation to two ternary non-ideal mixtures, representing a step towards more complex lubricant systems. The study examined rheological properties at temperatures up to 120°C and pressures up to 4 GPa, which are common in industrial applications. The simulations showed good quantitative agreement with experimental measurements at room temperature and pressure, validating the computational approach. At higher temperatures and pressures, the simulated density data was successfully fitted to the empirical Tait equation, providing a reliable model for density prediction under extreme conditions. For viscosity, the McEwen-Pauluch equation accurately described the pressure-viscosity relationship up to 2 GPa. Beyond this pressure, the equation broke down, predicting higher viscosities than the simulations. This deviation suggests a possible phase transition to a more glass-like state at extreme pressures. Comparing the two mixtures, mixture 1 showed higher density at room pressure but lower density at higher pressures compared to mixture 2. This behaviour could be attributed to increased π-π interactions in mixture 2 due to higher butylbenzene content. Viscosity values were consistently higher for mixture 1 across all conditions, explained by the reduced molecular mobility of bicyclohexyl, which was present in greater quantity in mixture 1. The breakdown of the McEwen-Pauluch equation at extreme pressures raises new questions about fluid behaviour under such conditions and suggests the need for more sophisticated models.

We then decided to simulate even more realistic lubricated systems by confining 9,10-dimethyloctadecane molecules between iron-oxide slabs, as iron oxide is a common material in steel applications. Using MD simulations, we compared two force fields, L-OPLS-AA and ReaxFF, to examine the microscopic behaviour and shear viscosity under varying pressures, shear rates, and film thicknesses. We found that film thickness influences viscosity: an increase in lubricant molecules bringing the viscosity closer to the bulk fluid's value. However, higher pressure and shear rates prevented this bulk-like behaviour, even in thicker systems. Liquid densities calculated by both force fields agreed with experimental data, although ReaxFF was more accurate in predicting hematite density. Despite this, ReaxFF overestimated viscosity compared to L-OPLS-AA with respect to experimental data, though both force fields displayed similar qualitative behaviour. Our findings highlight that increased complexity in force fields, as seen with ReaxFF, does not necessarily result in better accuracy, particularly in predicting viscosity. This suggests that the trade-off between complexity and accuracy in force field parameterization is a critical factor to consider in simulations.

We showed that computer simulations employing EMD and NEMD are a powerful tool to predict rheological properties that can occur in ideal, non-ideal and confined systems under operational and non-operational conditions. We provided simulation protocols and workflows that can be used to improve the understanding of lubricant behaviour at the atomic scale and develop better lubricants.

To study the formation of protective films by additive molecules in lubricated systems, we moved beyond molecular mechanics simulations and adopted a more reactive and accurate approach using the DFT+U method within the ONETEP linear-scaling software. Our focus was on bulk hematite and three different pristine hematite (0001) surface terminations: Fe-O-Fe, O-Fe-Fe, and HO-Fe-Fe. Additionally, we investigated a zinc diethyldithiophosphate (ZDDP) molecule both in the gas phase and adsorbed on these surfaces. First, we verified that our simulations accurately reproduced known properties of bulk hematite, including its magnetic moments, band gap, antiferromagnetic behaviour, and charge-transfer insulating nature. We then found that in the Fe-O-Fe slab, the top and bottom layers relaxed, reducing the Fe-Fe and Fe-O distances relative to the bulk, while charge and magnetic moments converged to bulk values further from the surface. The O-Fe-Fe surface exhibited metallic behaviour due to surface states created by dangling bonds, with significant deviations in spin and charge values compared to the bulk. However, saturating these dangling bonds with hydrogen in the HO-Fe-Fe surface restored the insulating behaviour and produced spin and charge values similar to the bulk. We then studied the binding energies of ZDDP on the three surfaces, finding values of -0.87 eV for Fe-O-Fe, -0.11 eV for O-Fe-Fe, and -0.49 eV for HO-Fe-Fe. While there were no significant structural changes, slight adjustments in bond angles were observed in the Fe-O-Fe system. This system also showed the largest changes in electronic structure, with lower charges on sulfur and zinc atoms near the surface compared to the gas phase, indicating stronger interactions. These findings provide a basis for future simulations of ZDDP compounds on hematite surfaces.

Computational Cost Sveral high-performance computing (HPC) facilities that enabled this research. I acknowledge the use of the IRIDIS 5 High Performance Computing facility at the University of Southampton and the UK national high-performance computing service, ARCHER2. I also utilised the UK Materials and Molecular Modelling Hub for additional computational support.

Density Functional Theory (DFT) simulations, being orders of magnitude more computationally expensive than molecular dynamics methods, required approximately one month of computing time on ARCHER2 using 1204 cores. Molecular dynamics simulations, including Equilibrium Molecular Dynamics (EMD) and Non-Equilibrium Molecular Dynamics (NEMD), were comparatively less demanding. For instance, simulations using the OPLS-AA force field required about 40 hours to achieve 40 nanoseconds of simulation on 120 CPUs on IRIDIS5 and the Young HPC cluster. In contrast, simulations using the ReaxFF force field were approximately four times more computationally expensive than those employing OPLS-AA. These resources were critical in performing the extensive simulations required for this work.

9.1 Future Outlook

Computer simulations of lubricants and related systems have become indispensable tools in modern research. These simulations offer valuable insights, predict both macroscopic and microscopic properties, and help explain experimental findings. However, it is crucial to recognize that these techniques are not without limitations.

One of the primary challenges in MD simulations is the treatment of molecules as classical particles, which is a fundamental approximation. The interactions between these particles are governed by force fields, which are parameterised based on experimental data. While this approach has proven successful for many applications, its accuracy varies across different systems. Lubricant systems, in particular, present a significant challenge due to their complexity.

The parameterisation process often overlooks certain rheological properties such as viscosity, leading to less accurate predictions for these characteristics. Another critical aspect is reactivity, which is either not accounted for in common force fields or poorly represented in reactive force fields.

Researchers have often turned to quantum chemistry methods, particularly DFT. These methods offer a more accurate description of molecular interactions and can capture chemical reactions. However, they come with their own set of challenges. While theoretically more precise, they are computationally much more intensive. This computational cost severely restricts the size and duration of simulations, limiting them to a few atoms or picoseconds.

This limitation poses a significant problem for studying rheological properties, which are macroscopic in nature. Accurate predictions of these properties often require longer simulation times and larger systems to produce statistically significant results. Consequently, bridging the gap between the microscopic accuracy of quantum methods and the macroscopic nature of rheological properties remains a formidable challenge in the field.

These ongoing challenges might make one question the value of pursuing simulations for lubricant systems. However, recent advancements are providing new reasons for optimism. In recent years, new and better-parameterised force fields and exchange-correlation functionals have become available, improving the physics and chemistry of such systems. Advancements in high-performance computing resources now allow us to run simulations of greater complexity for much longer periods than previously possible. In particular, advances in GPU computing have made applications run at unprecedented speeds[206–208].

Furthermore, in the age of data, machine-learning techniques have become ubiquitous in science. This paradigm shift could potentially bridge the gap between accuracy and speed. Machine-learned force fields are often not strictly bound to traditional functional forms and can be parameterised for thousands of different species using DFT or even more accurate wave function methods such as coupled clusters. This, in turn, allows us to run simulations at a much higher level of accuracy compared to standard MD simulations, but at a fraction of the cost of explicit ab initio MD[209–213].

In this thesis, we have provided robust workflows and protocols for both MD and linear-scaling DFT to predict and gain insights into a wide range of lubricant systems. These techniques have demonstrated their power and utility in advancing our understanding of lubricant behaviour. However, this work represents only a first step, and there are numerous opportunities for further research and development.

Several key areas for future investigation include:

1. creation of new force field parameters or machine-learnt force fields specifically tailored for rheological properties of lubricated systems. This could allow the possibility of treating additives, surfaces and lubricant on equal footing,
2. develop a new model for viscosity-pressure relationship addressing the limitations of the McEwen-Pauluch equations,
3. investigate the effect of surfaces defects and roughness on the decomposition of ZDDPs,
4. investigating the dynamics of ZDDP on top of hematite under shear.

Appendix A

Ideal Mixtures

TABLE A.1: Number of molecules per mixture

Mixture	DEHS	DEHA
100% DEHS	150	0
90% DEHS	135	17
80% DEHS	121	35
70% DEHS	106	52
60% DEHS	91	70
50% DEHS	76	87
40% DEHS	61	105
30% DEHS	46	123
20% DEHS	31	141
10% DEHS	15	158
0% DEHS	0	176

TABLE A.2: Experimental densities in g/cm^3 at 293 K

Mixture	Measurement 1	Measurement 2	Measurement 3
100% DEHS	0.9141	0.9141	0.9142
90% DEHS	0.9152	0.9140	0.9142
80% DEHS	0.9163	0.9153	0.9154
70% DEHS	0.9170	0.9167	0.9165
60% DEHS	0.9153	0.9187	0.9183
50% DEHS	0.9151	0.9186	0.9186
40% DEHS	0.9194	0.9211	0.9210
30% DEHS	0.9205	0.9226	0.9227
20% DEHS	0.9213	0.9232	0.9232
10% DEHS	0.9207	0.9242	0.9241
0% DEHS	0.9253	0.9255	0.9254

TABLE A.3: Experimental densities in g/cm^3 at 343 K

Mixture	Measurement 1	Measurement 2	Measurement 3
100% DEHS	0.8782	0.8781	0.8778
90% DEHS	0.8792	0.8780	0.8782
80% DEHS	0.8800	0.8791	0.8791
70% DEHS	0.8802	0.8816	0.8811
60% DEHS	0.8754	0.8814	0.8812
50% DEHS	0.8715	0.8826	0.8825
40% DEHS	0.8810	0.8838	0.8838
30% DEHS	0.8809	0.8847	0.8847
20% DEHS	0.8824	0.8857	0.8858
10% DEHS	0.8782	0.8868	0.8868
0% DEHS	0.8878	0.8877	0.8877

TABLE A.4: Experimental densities in g/cm^3 at 393 K

Mixture	Measurement 1	Measurement 2	Measurement 3
100% DEHS	0.8425	0.84216	0.84205
90% DEHS	0.8433	0.84215	0.84148
80% DEHS	0.8441	0.84295	0.84278
70% DEHS	0.8444	0.84447	0.84467
60% DEHS	0.8385	0.84618	0.84594
50% DEHS	0.8322	0.84723	0.84697
40% DEHS	0.8444	0.84685	0.84685
30% DEHS	0.8426	0.84743	0.84743
20% DEHS	0.8473	0.84844	0.84846
10% DEHS	0.8392	0.84922	0.84925
0% DEHS	0.8505	0.84743	0.85014

TABLE A.5: Experimental viscosities in mPa · s at 293 K

Mixture	Measurement 1	Measurement 2	Measurement 3
100% DEHS	21.4	21.587	21.582
90% DEHS	20.5	21.442	21.493
80% DEHS	19.6	20.500	20.550
70% DEHS	18.8	19.545	19.707
60% DEHS	17.9	18.103	18.229
50% DEHS	17.1	17.948	18.045
40% DEHS	16.4	16.314	16.363
30% DEHS	15.6	15.358	15.415
20% DEHS	15.0	14.941	14.979
10% DEHS	14.4	14.395	14.431
0% DEHS	13.7	13.714	13.739

TABLE A.6: Experimental viscosities in mPa · s at 343 K

Sample	Measurment 1	Measurement 2	Measurement 3
100% DEHS	4.80	4.8956	4.8855
90% DEHS	4.69	4.8931	4.8844
80% DEHS	4.53	4.7253	4.7167
70% DEHS	4.37	4.3075	4.3222
60% DEHS	4.23	4.3410	4.3642
50% DEHS	4.07	4.1514	4.1640
40% DEHS	3.94	3.9736	3.9676
30% DEHS	3.78	3.8380	3.8314
20% DEHS	3.67	3.6894	3.6821
10% DEHS	3.55	3.5453	3.5389
0% DEHS	3.42	3.4364	3.4320

TABLE A.7: Experimental viscosities in mPa · s at 393 K

Mixture	Measurement 1	Measurement 2	Measurement 3
100% DEHS	2.05	2.1025	2.0930
90% DEHS	2.02	2.0993	2.0930
80% DEHS	1.96	2.0342	2.0311
70% DEHS	1.90	1.9146	1.9202
60% DEHS	1.85	1.8084	1.8185
50% DEHS	1.79	1.7356	1.7449
40% DEHS	1.74	1.7560	1.7567
30% DEHS	1.68	1.7157	1.7130
20% DEHS	1.63	1.6513	1.6468
10% DEHS	1.59	1.5980	1.5954
0% DEHA	1.54	1.5478	1.5460

TABLE A.8: NEMD Simulated viscosities in mPa · s at 393 K using a shear rate of $10^{8.0}$ s^-1

Mixture	Sim 1	Sim 2	Sim 3	Sim 4	Sim 5
100% DEHS	1.47567	1.93383	2.29641	2.61061	2.06284
90% DEHS	1.90497	1.38599	1.64744	1.2129	0.840531
80% DEHS	1.53953	1.9249	0.923076	1.74947	1.24904
70% DEHS	1.09814	1.4156	0.892657	1.49023	2.67313
60% DEHS	1.56766	0.999813	1.82259	1.54681	1.82386
50% DEHS	1.44349	2.09275	1.34165	1.05732	1.26873
40% DEHS	1.88127	1.30093	2.21765	1.19368	1.79214
30% DEHS	1.41055	0.456006	1.22551	1.43333	1.19204
20% DEHS	1.75655	1.29741	0.837279	1.73486	1.23938
10% DEHS	0.637257	1.4794	1.86702	0.886978	1.38416
0% DEHS	1.31866	1.26602	0.751429	1.32701	1.63518

TABLE A.9: EMD Simulated viscosities in mPa · s at 393 K

Mixture	Sim 1	Sim 2	Sim 3	Sim 4	Sim 5
100% DEHS	1.35681	1.37317	1.54107	1.44738	1.56535
90% DEHS	1.56489	1.44647	1.45993	1.57633	1.4598
80% DEHS	1.33518	1.45534	1.5224	1.45473	1.38451
70% DEHS	1.36545	1.33665	1.29309	1.47255	1.3753
60% DEHS	1.20986	1.31837	1.25017	1.44903	1.39569
50% DEHS	1.15665	1.42013	1.27373	1.24578	1.17834
40% DEHS	0.979914	1.51036	1.37516	1.31516	1.14249
30% DEHS	1.13143	1.25615	1.27258	1.4375	1.13405
20% DEHS	1.15201	1.23664	1.38756	1.13892	1.22566
10% DEHS	1.3194	1.21002	1.13747	1.10126	1.29524
0% DEHS	1.33386	1.23307	1.17444	1.09871	1.1533

TABLE A.10: NEMD Simulated viscosities in mPa · s at 343 K using a shear rate of $10^{8.0}$ $\mathrm{s}^{-}1$

Mixture	Sim 1	Sim 2	Sim 3	Sim 4	Sim 5
100% DEHS	5.20373	3.17659	2.55105	3.86292	4.08831
90% DEHS	3.74814	4.34317	3.7022	3.82062	4.06491
80% DEHS	3.04861	3.98753	4.11072	2.63283	4.06506
70% DEHS	3.79686	1.86459	1.61644	3.33484	3.07929
60% DEHS	2.85277	2.68636	3.62504	2.1453	2.2235
50% DEHS	1.6346	3.46118	1.94045	3.68776	3.29252
40% DEHS	3.94019	2.93982	4.12112	2.80574	4.77117
30% DEHS	3.68474	3.35464	3.88528	3.94409	3.55292
20% DEHS	3.08243	3.17085	3.33484	2.43976	1.93192
10% DEHS	2.44014	3.3542	2.97634	3.71123	3.0543
0% DEHS	2.94679	3.01567	2.24485	4.08723	3.90481

TABLE A.11: NEMD Simulated viscosities in mPa · s at 293 K using a shear rate of $10^{8.0}$ $\mathrm{s}^{-}1$

Mixture	Sim 1	Sim 2	Sim 3	Sim 4	Sim 5
100% DEHS	19.3601	19.0723	20.7817	17.7328	19.7875
90% DEHS	17.309	17.1312	18.9698	16.2492	16.8455
80% DEHS	12.7746	20.3967	16.7248	17.43	16.9771
70% DEHS	18.09	12.4066	15.7088	16.7124	13.9906
60% DEHS	15.4708	13.2387	15.0742	15.5904	16.5427
50% DEHS	16.895	14.0516	13.4636	14.8098	13.4153
40% DEHS	11.6325	15.3372	15.0181	14.2087	12.3551
30% DEHS	11.8026	12.9843	15.037	14.1295	12.7197
20% DEHS	12.8643	12.8756	13.2167	13.9933	11.5103
10% DEHS	9.06055	13.7538	12.6618	12.3689	12.6936
0% DEHS	11.3143	11.7982	12.071	12.7719	11.5679

Appendix B

Non-ideal mixtures

TABLE B.1: Number of molecules per mixture

Components	Mixture 1	Mixture 2
Hexadecane	156	156
Butylbenzene	25	150
Bicyclohexyl	105	17

TABLE B.2: Mixture 1 Diffusivity m^2/s

Temperature	Pressure	BB	HEX	BC
40	0.5	1.912e-11	2.016e-11	2.257e-11
70	0.5	1.225e-10	9.621e-11	1.009e-10
120	0.5	1.522e-10	1.342e-10	1.278e-10
40	1.0	8.340e-12	7.939e-12	5.433e-12
70	1.0	5.505e-12	8.619e-12	7.228e-12
120	1.0	2.579e-11	2.090e-11	1.350e-11
40	2.0	3.985e-12	2.065e-12	3.549e-12
70	2.0	3.078e-11	6.987e-12	6.016e-12
120	2.0	6.520e-12	6.245e-12	5.493e-12
40	4.0	4.380e-12	1.868e-12	3.009e-12
70	4.0	3.611e-12	5.729e-12	4.696e-12
120	4.0	9.297e-12	6.041e-12	4.070e-12

Table B.3: Mixture 2 Diffusivity in m^2/s

Temperature	Pressure	BB	HEX	BC
40	0.5	3.599e-11	3.113e-11	2.096e-11
70	0.5	9.985e-11	6.689e-11	3.753e-11
120	0.5	2.771e-10	2.279e-10	2.559e-10
40	1.0	6.646e-12	1.613e-11	1.288e-11
70	1.0	1.010e-11	3.007e-11	8.878e-12
120	1.0	4.271e-11	4.020e-11	2.446e-11
40	2.0	5.141e-12	4.570e-12	6.519e-12
70	2.0	5.083e-12	6.871e-12	5.433e-12
120	2.0	4.316e-11	5.081e-11	2.198e-11
40	4.0	4.934e-12	5.306e-12	3.542e-12
70	4.0	1.945e-12	4.199e-12	9.394e-13
120	4.0	5.047e-12	1.101e-11	5.616e-12

Table B.4: Density for mixture 1 in g/cm^3

Pressure GPa	40	70	120
0.0001	0.768392 ± 0.004867	0.740778 ± 0.005532	0.694408 ± 0.006983
0.5	0.926920 ± 0.002410	0.914919 ± 0.002511	0.895679 ± 0.003044
1	0.988934 ± 0.002141	0.980911 ± 0.002043	0.964426 ± 0.002323
2	1.057028 ± 0.001606	1.053392 ± 0.001688	1.043984 ± 0.002115
4 GPa	1.135570 ± 0.001346	1.133349 ± 0.001541	1.130146 ± 0.001315

Table B.5: Density for mixture 2 in g/cm^3

Pressure GPa	40	70	120
0.0001	0.748274 ± 0.005012	0.729378 ± 0.005024	0.683411 ± 0.007257
0.5	0.927001 ± 0.002410	0.914919 ± 0.002511	0.895679 ± 0.003044
1	0.992717 ± 0.002043	0.981883 ± 0.002141	0.966751 ± 0.002323
2	1.065090 ± 0.001606	1.060877 ± 0.001688	1.054842 ± 0.002115
4 GPa	1.145484 ± 0.001315	1.143773 ± 0.001346	1.140384 ± 0.001541

Table B.6: Mixture 1 experimental and simulated density in g/cm^3 and viscosity in mPa s

Temperature	Viscosity (exp)	Viscosity (sim)	Density (exp)	Density(sim)
40	2.060000	1.530502 ± 0.455252	0.794110	0.768392 ± 0.004867
70	1.241000	1.092597 ± 0.410714	0.780190	0.740778 ± 0.005532
120	0.667460	0.612032 ± 0.229520	0.738250	0.694408 ± 0.006983

Table B.7: Mixture 2 experimental and simulated density in g/cm^3 and viscosity in mPa s

Temperature	Viscosity (exp)	Viscosity (sim)	Density (exp)	Density(sim)
40	2.077801	1.504121 ± 0.416256	0.78708	0.748274 ± 0.005012
70	0.943811	1.043679 ± 0.400158	0.76596	0.729378 ± 0.005024
120	0.532850	0.584211 ± 0.257547	0.72921	0.683411 ± 0.007257

Table B.8: Mixture 1 viscosity values in mPa s

Pressure (GPa)	40 °C	70 °C	120 °C
0.0001	1.5305 ± 0.4552	1.0925 ± 0.4107	0.6120 ± 0.2295
0.5	275.4948 ± 29.5548	61.6557 ± 27.1885	21.0985 ± 0.9383
1	5510.5440 ± 341.6213	2011.9840 ± 86.4996	256.0002 ± 104.4994
2	21969.2401 ± 2756.0579	18388.3000 ± 548.4410	8230.8380 ± 551.9926
4	51736.6800 ± 2204.5945	49824.1200 ± 1120.8851	40108.4000 ± 1447.03405

Table B.9: Mixture 2 viscosity values in mPa s

Pressure (GPa)	40 °C	70 °C	120 °C
0.0001	1.5041 ± 0.4162	1.0436 ± 0.4001	0.5842 ± 0.2575
0.5	84.0048 ± 31.6703	27.7498 ± 7.9870	4.1496 ± 2.2334
1	1936.0440 ± 36.3627	541.7844 ± 2.4990	30.0707 ± 0.7890
2	17724.3800 ± 215.9362	12687.4600 ± 432.84	3903.0997 ± 5.8171
4	44044.5287 ± 91.2101	39546.8271 ± 13.6559	30735.6411 ± 983.9810

Table B.10: Parameters of the McEwen-Pauluch for mixture 1.

Temperature	α_0	q	C_F	P_∞
40	$1.85854313e+01$	$3.62546970e+00$	$1.53948472e-09$	$5.89751786e+00$
70	$1.64609705e+01$	$3.86059102e+00$	$2.31554161e-09$	$7.97027162e+00$
120	$7.75471466e+00$	$8.43912558e+00$	$5.98136607e-18$	$7.99735550e+00$

Table B.11: Parameters of the McEwen-Pauluch for mixture 2.

Temperature	α_0	q	C_F	P_∞
40	$1.40281890e+01$	$4.02433763e+00$	$1.54117709e-09$	$7.96238145e+00$
70	$8.29579527e+00$	$7.28001506e+00$	$3.64897337e-08$	$7.79923466e+00$
120	0.26851618	1.17620704	14.00874682	5.91169376

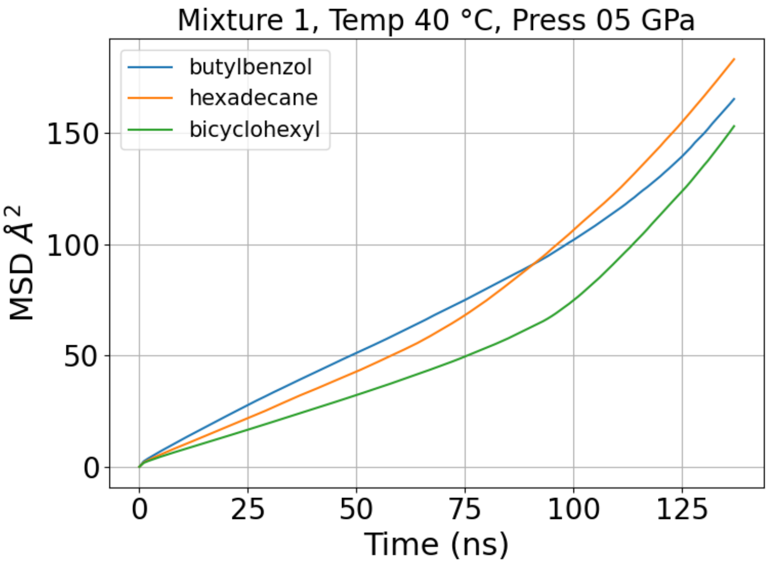

Figure B.1: Mixture 1 mean square displacement at 0.5 GPa and 40 °C

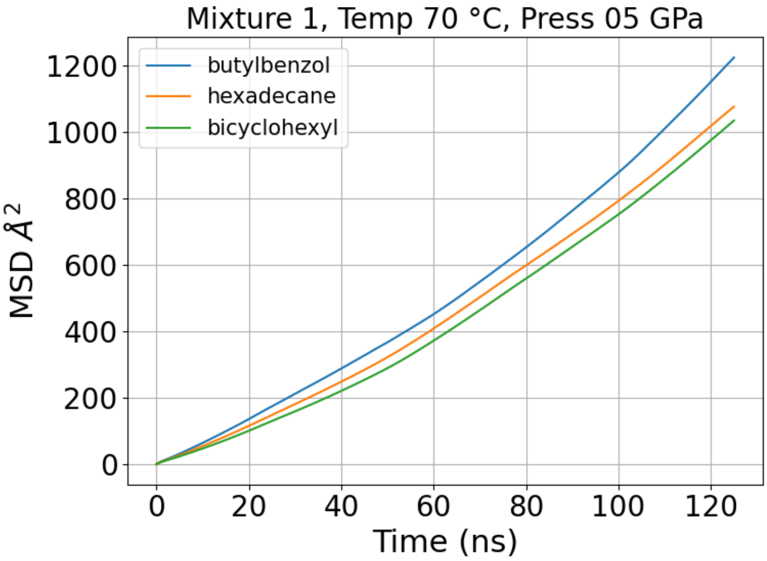

FIGURE B.2: Mixture 1 mean square displacement at 0.5 GPa and 70 °C

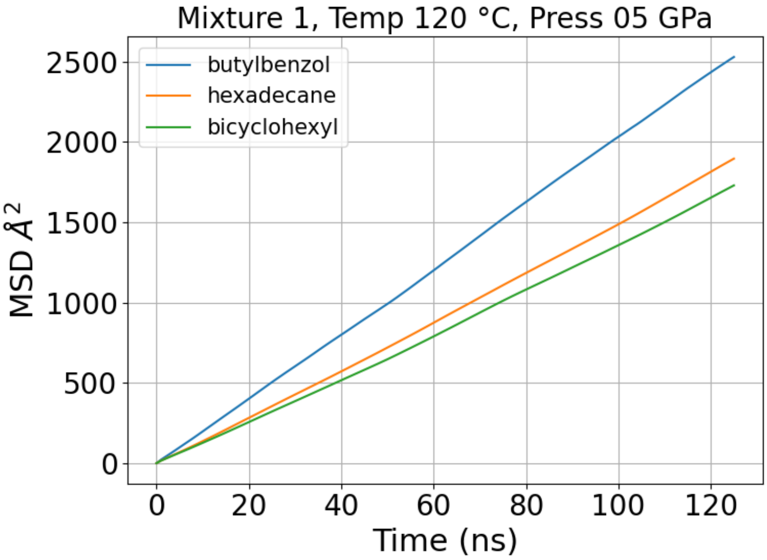

FIGURE B.3: Mixture 1 mean square displacement at 0.5 GPa and 120 °C

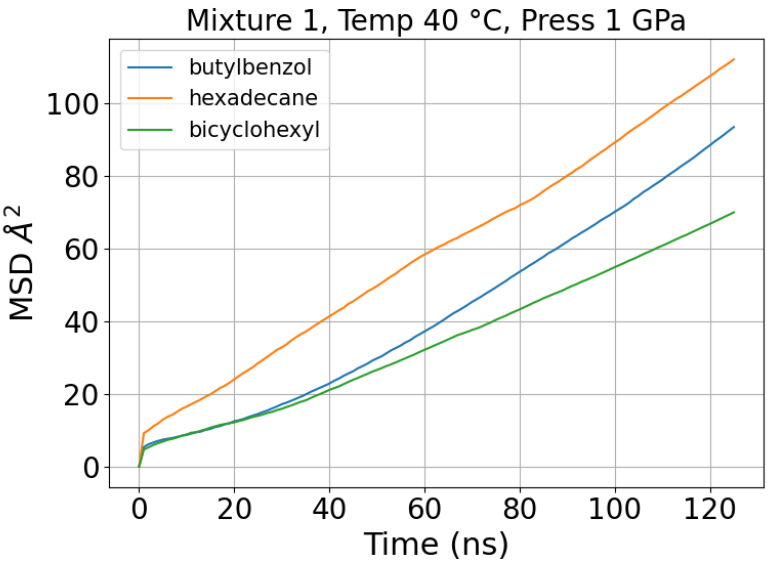

FIGURE B.4: Mixture 1 mean square displacement at 1 GPa and 40 °C

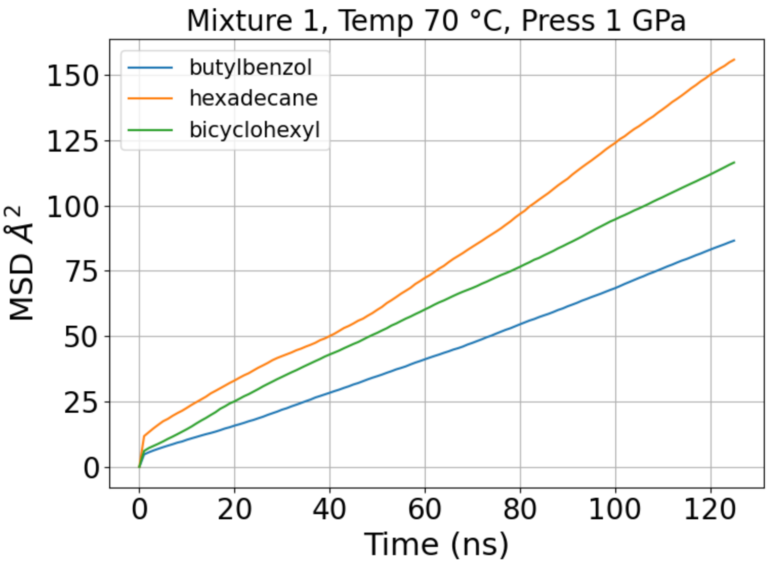

FIGURE B.5: Mixture 1 mean square displacement at 1 GPa and 70 °C

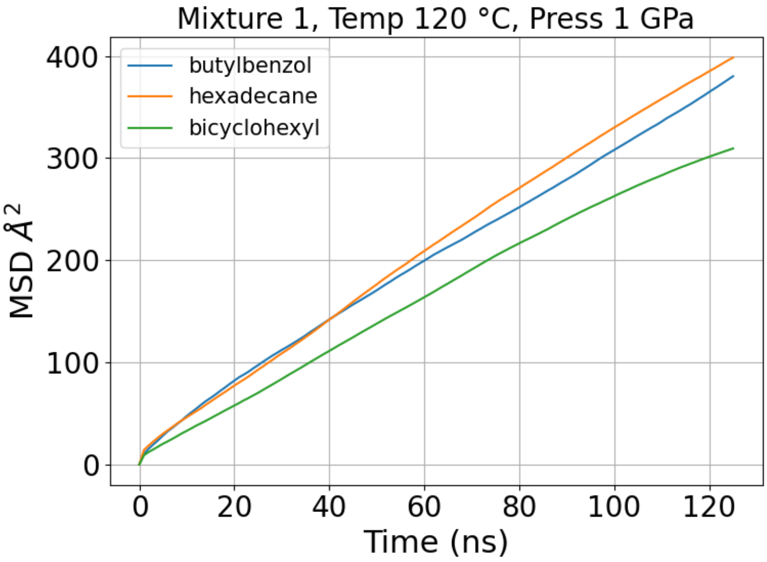

FIGURE B.6: Mixture 1 mean square displacement at 1 GPa and 120 °C

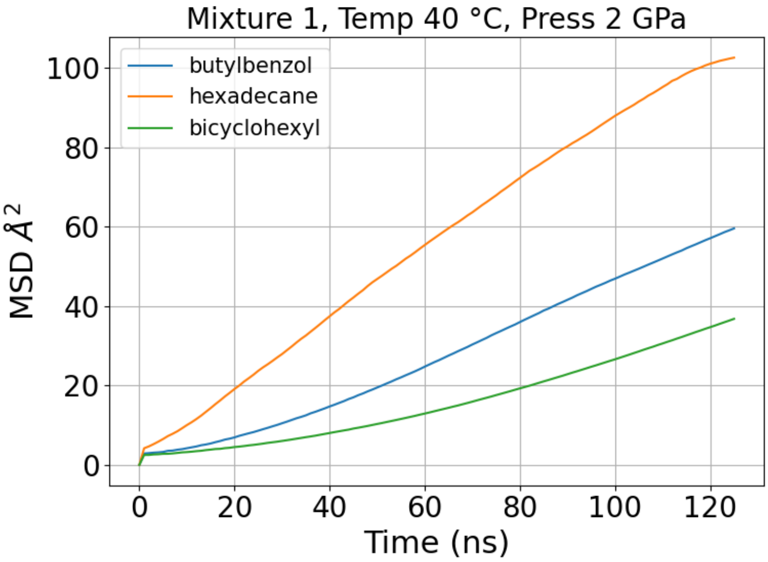

FIGURE B.7: Mixture 1 mean square displacement at 2 GPa and 40 °C

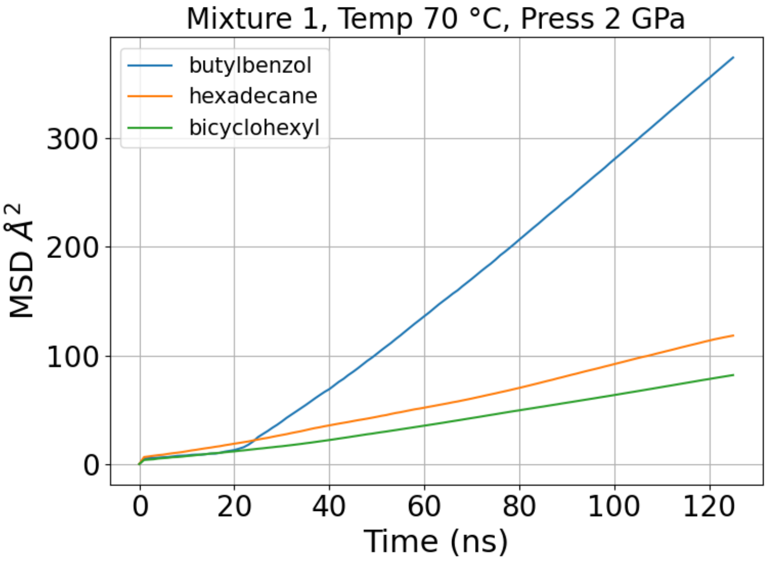

FIGURE B.8: Mixture 1 mean square displacement at 2 GPa and 70 °C

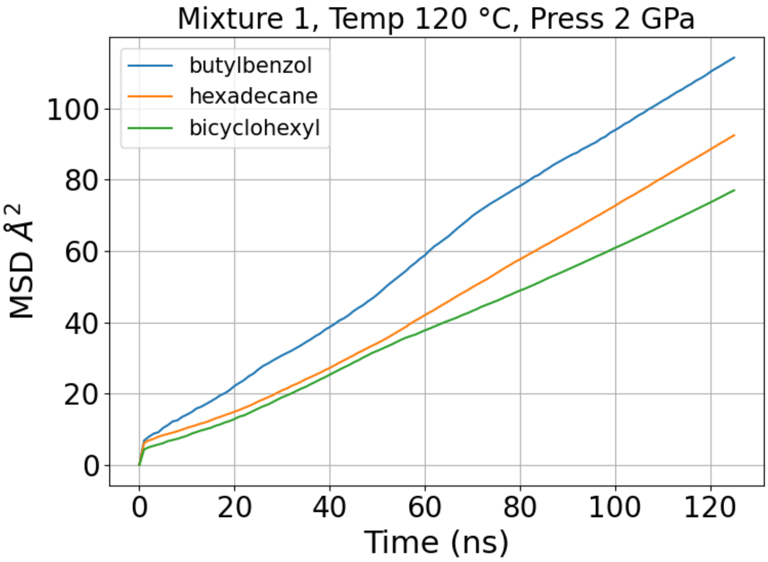

FIGURE B.9: Mixture 1 mean square displacement at 2 GPa and 120 °C

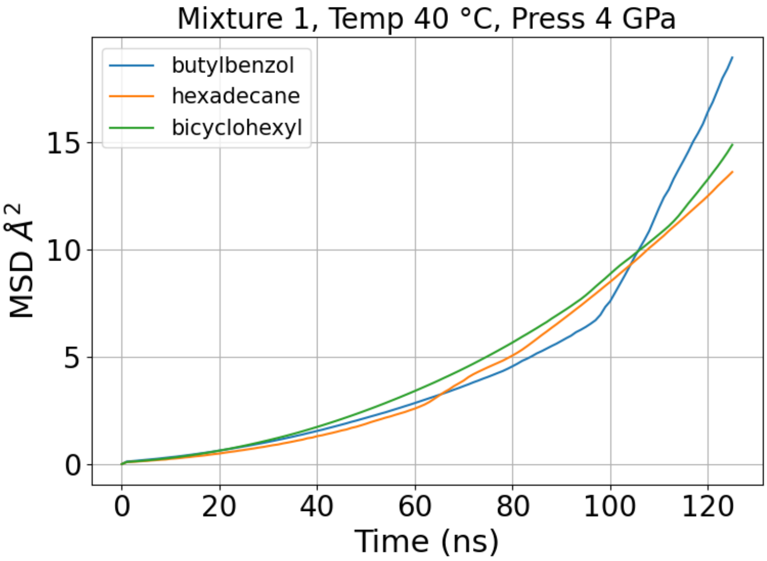

FIGURE B.10: Mixture 1 mean square displacement at 1 GPa and 40 °C

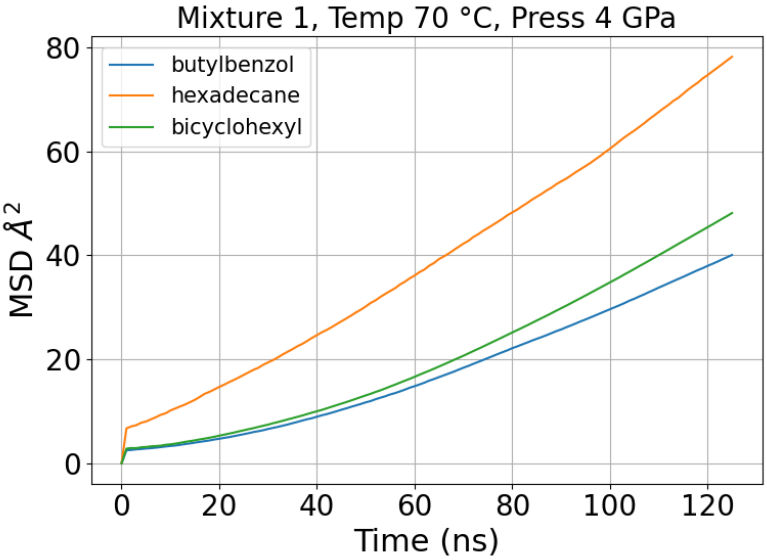

FIGURE B.11: Mixture 1 mean square displacement at 1 GPa and 70 °C

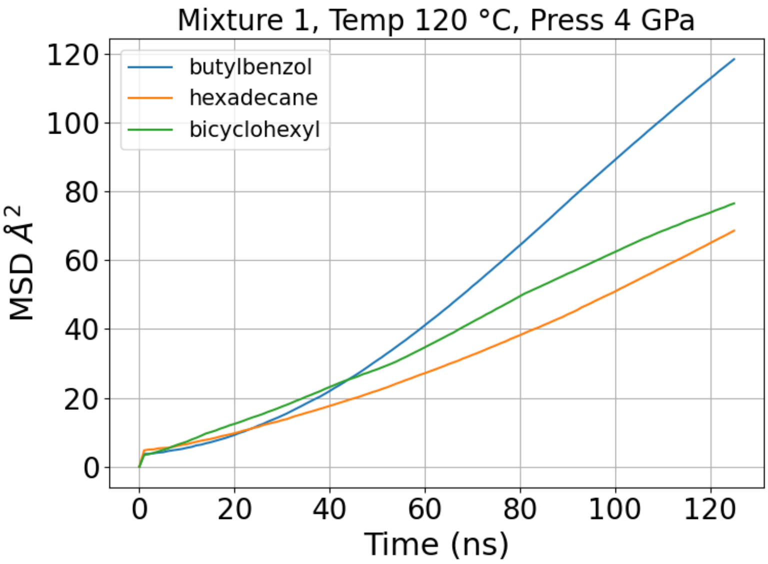

FIGURE B.12: Mixture 1 mean square displacement at 4 GPa and 120 °C

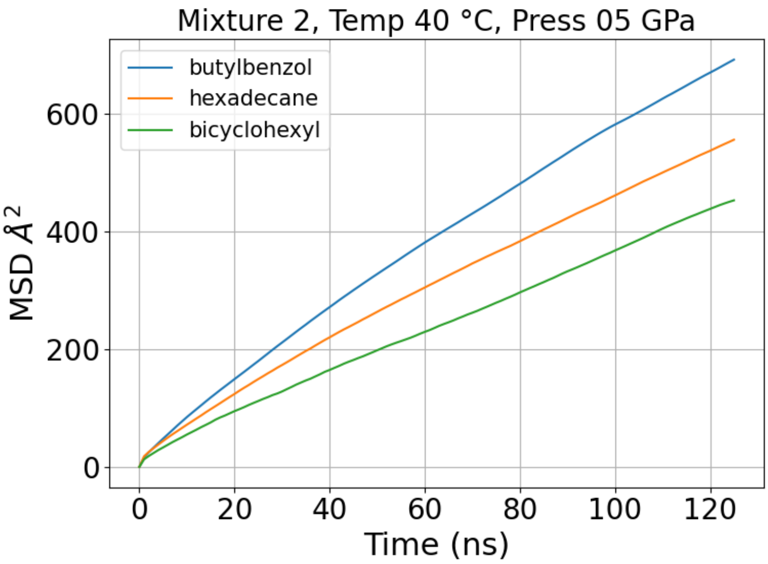

FIGURE B.13: Mixture 2 mean square displacement at 0.5 GPa and 40 °C

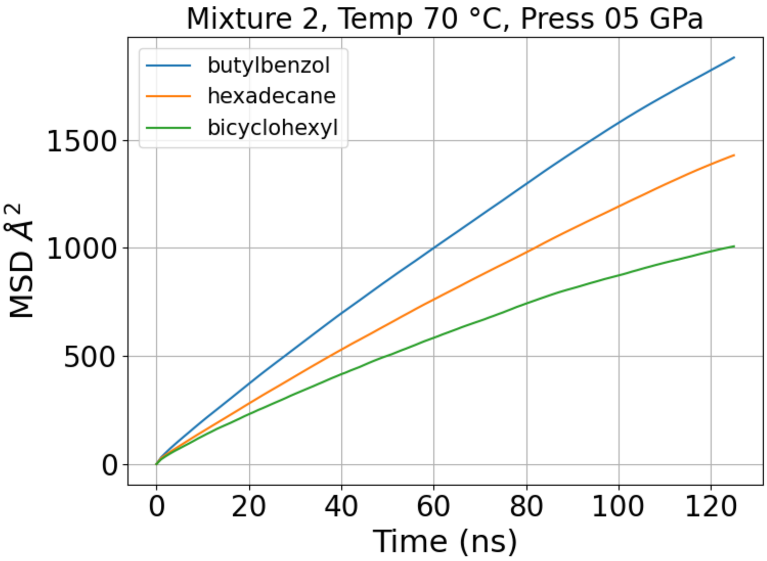

FIGURE B.14: Mixture 2 mean square displacement at 0.5 GPa and 70 °C

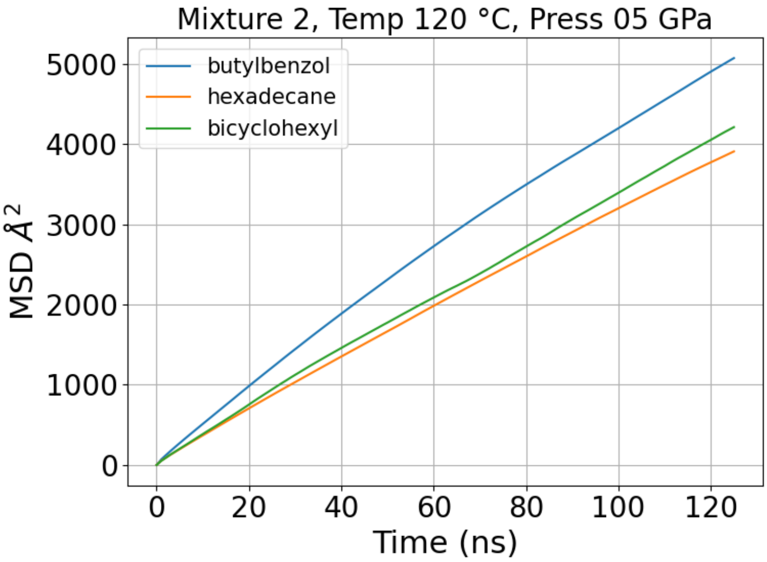

FIGURE B.15: Mixture 2 mean square displacement at 0.5 GPa and 120 °C

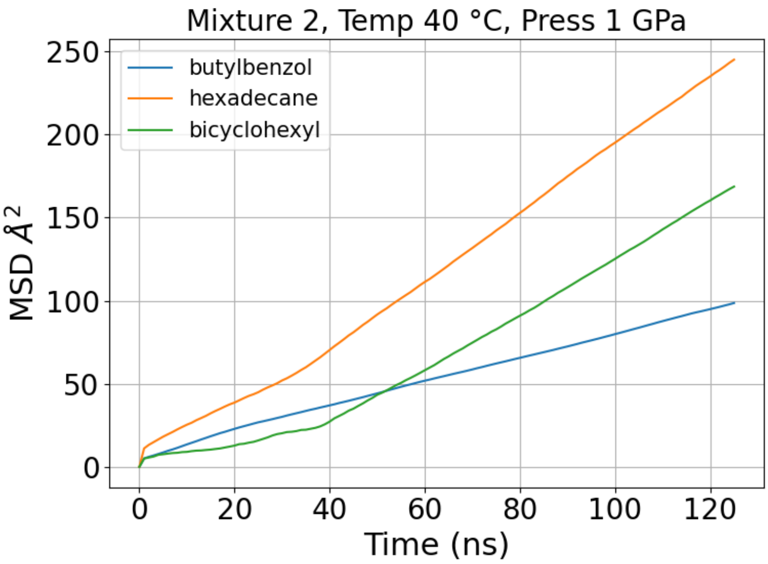

FIGURE B.16: Mixture 2 mean square displacement at 1 GPa and 40 °C

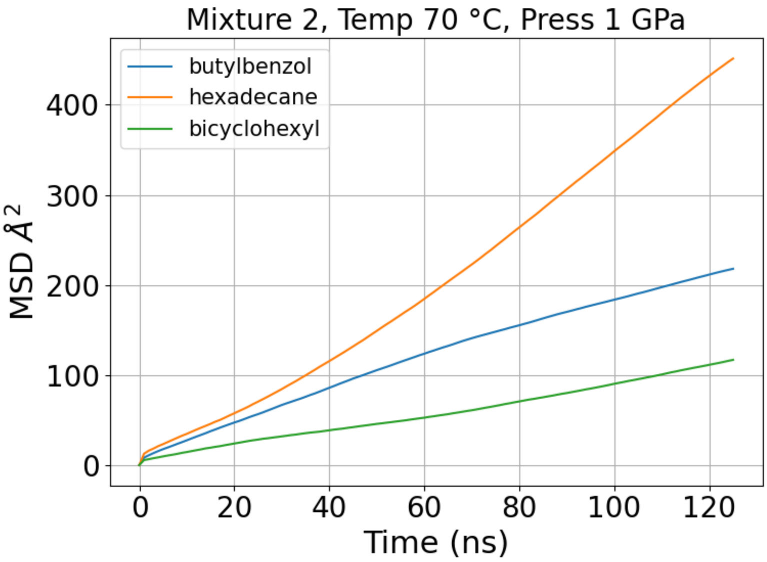

FIGURE B.17: Mixture 2 mean square displacement at 1 GPa and 70 °C

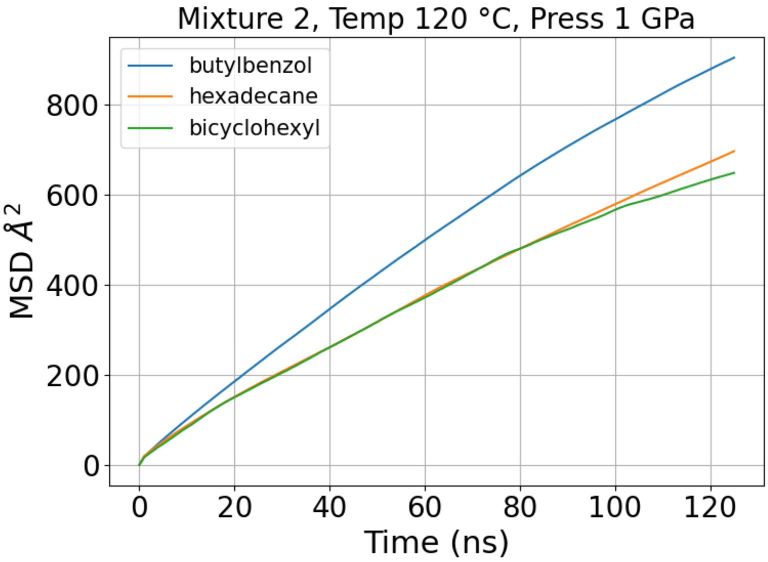

FIGURE B.18: Mixture 2 mean square displacement at 1 GPa and 120 °C

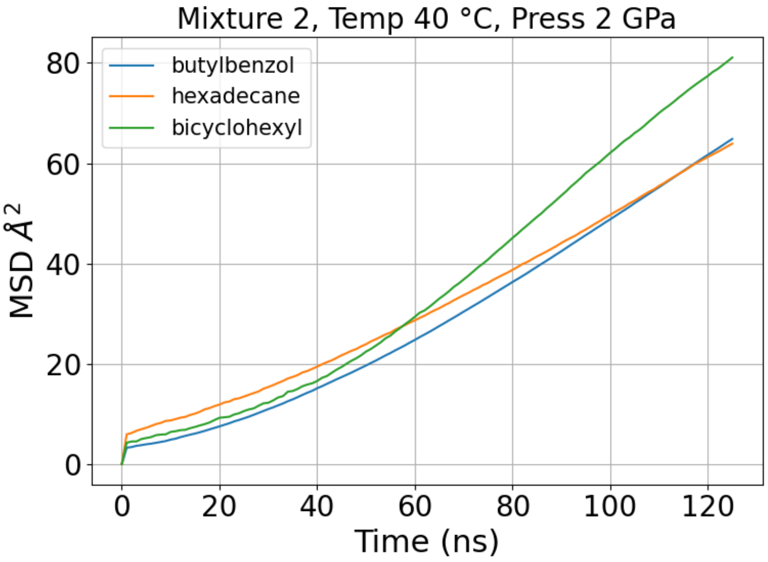

FIGURE B.19: Mixture 2 mean square displacement at 2 GPa and 40 °C

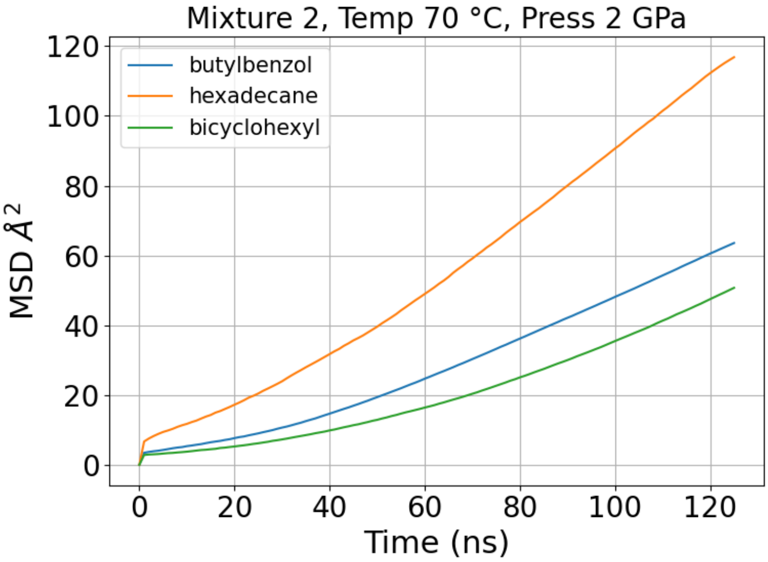

FIGURE B.20: Mixture 2 mean square displacement at 2 GPa and 70 °C

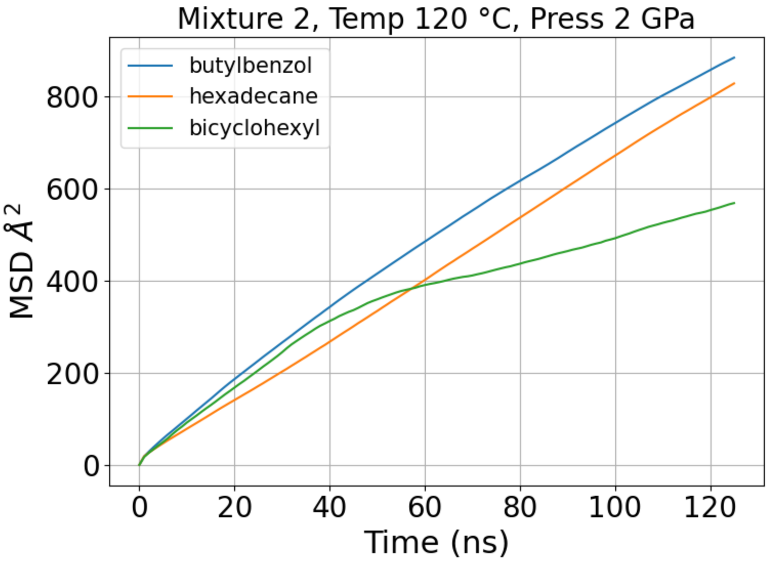

FIGURE B.21: Mixture 2 mean square displacement at 2 GPa and 120 °C

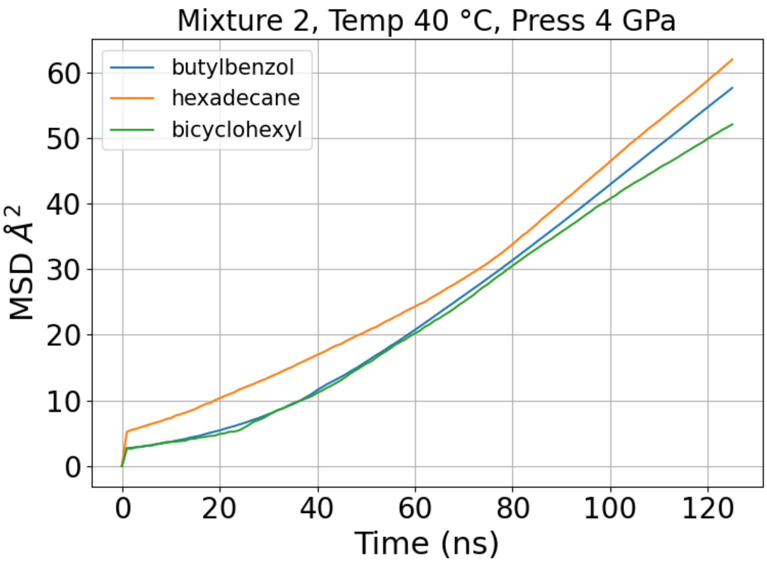

FIGURE B.22: Mixture 2 mean square displacement at 1 GPa and 40 °C

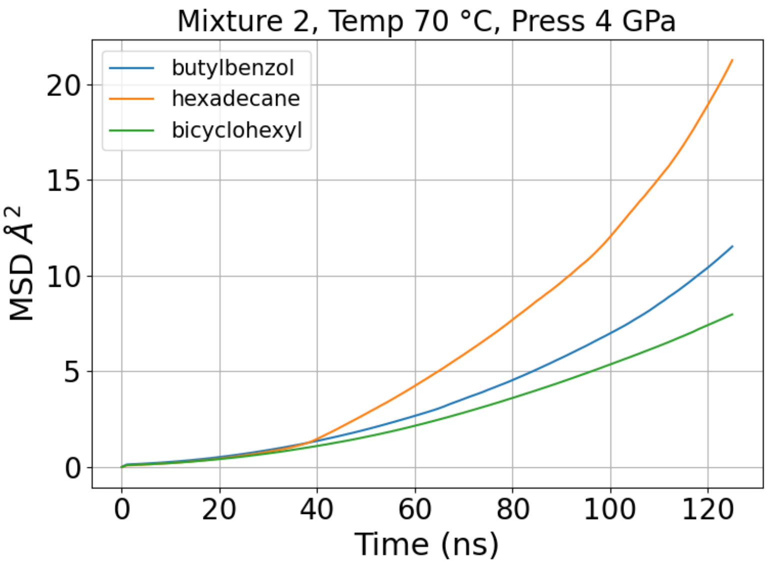

FIGURE B.23: Mixture 2 mean square displacement at 1 GPa and 70 °C

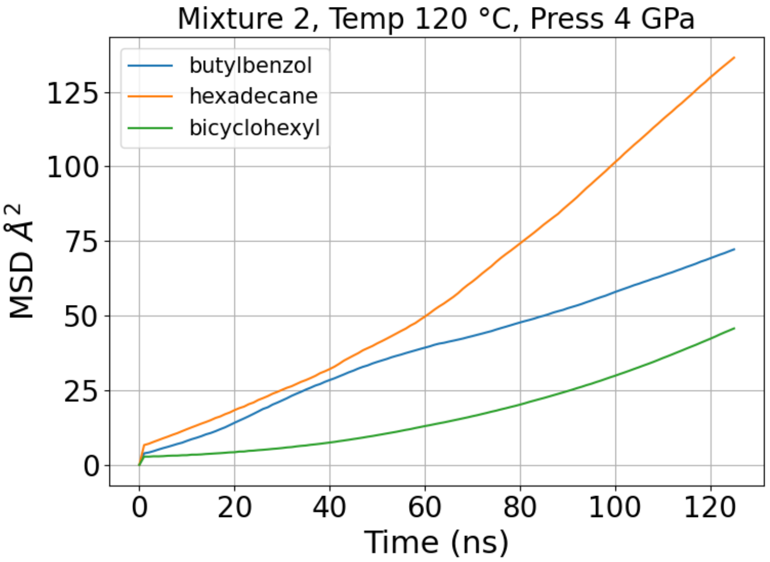

Figure B.24: Mixture 2 mean square displacement at 4 GPa and 120 °C

Appendix C

Non-ideal mixture radial distribution functions

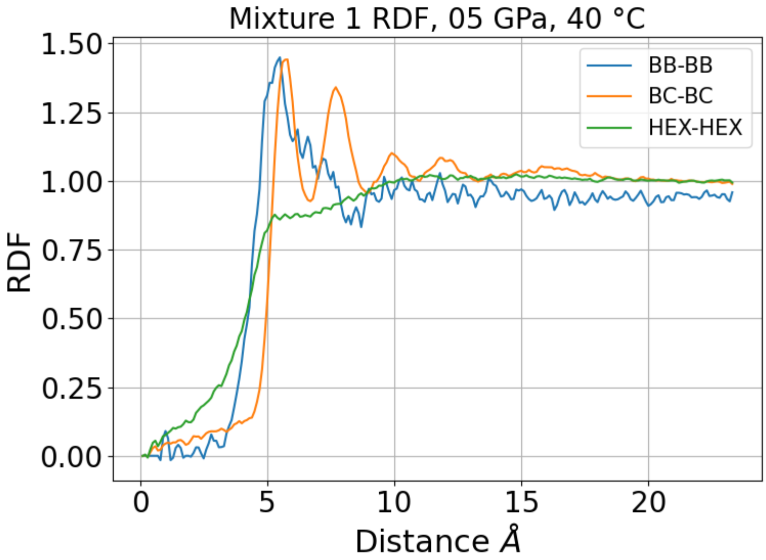

FIGURE C.1: Mixture 1 radial distribution function at 0.5 GPa and 40 °C

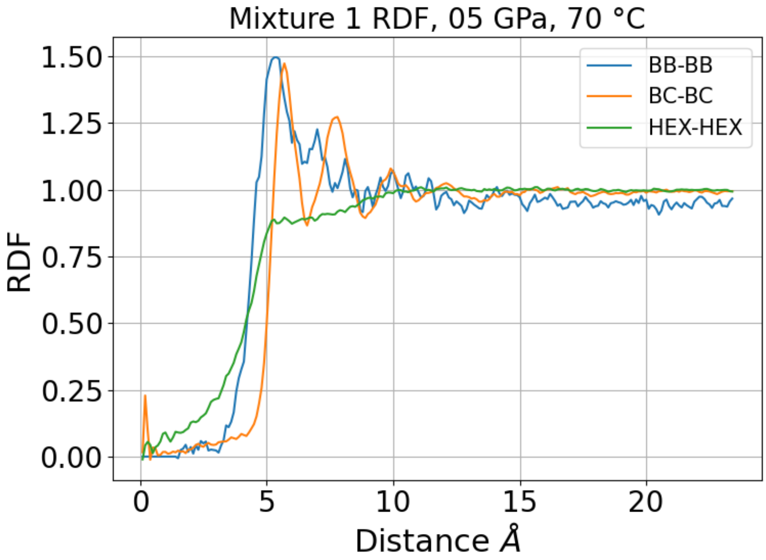

FIGURE C.2: Mixture 1 radial distribution function at 0.5 GPa and 70 °C

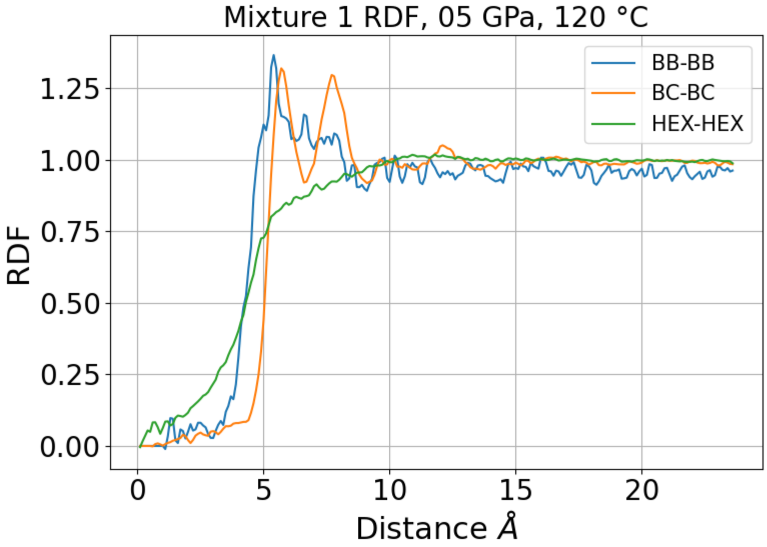

FIGURE C.3: Mixture 1 radial distribution function at 0.5 GPa and 120 °C

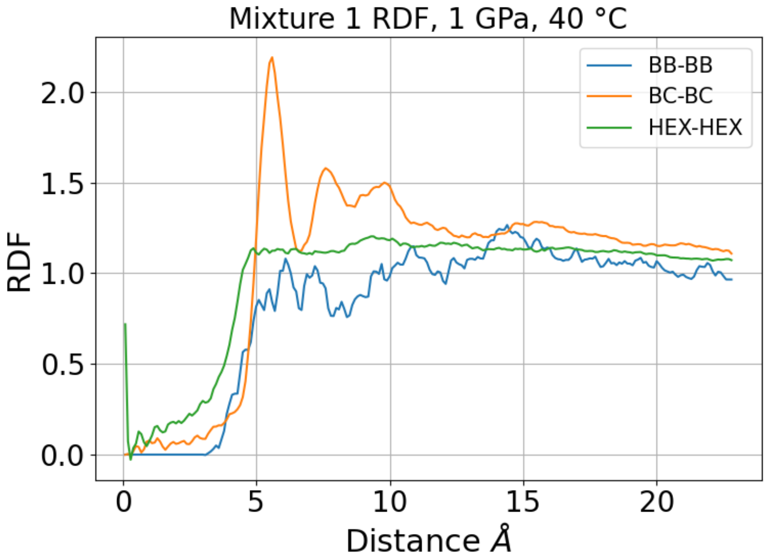

FIGURE C.4: Mixture 1 radial distribution function at 1 GPa and 40 °C

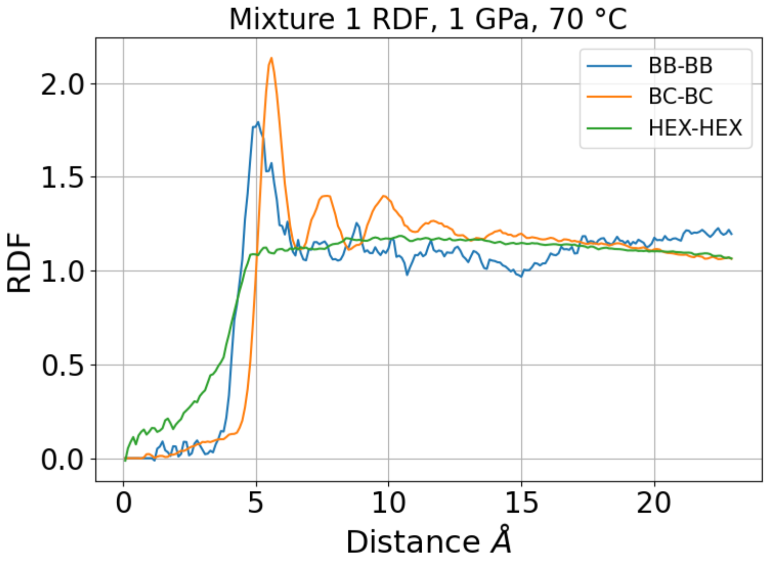

FIGURE C.5: Mixture 1 radial distribution function at 1 GPa and 70 °C

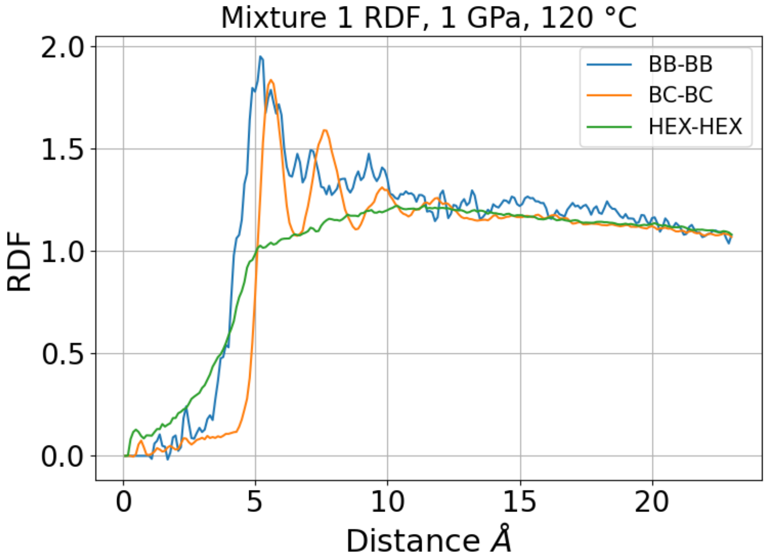

FIGURE C.6: Mixture 1 radial distribution function at 1 GPa and 120 °C

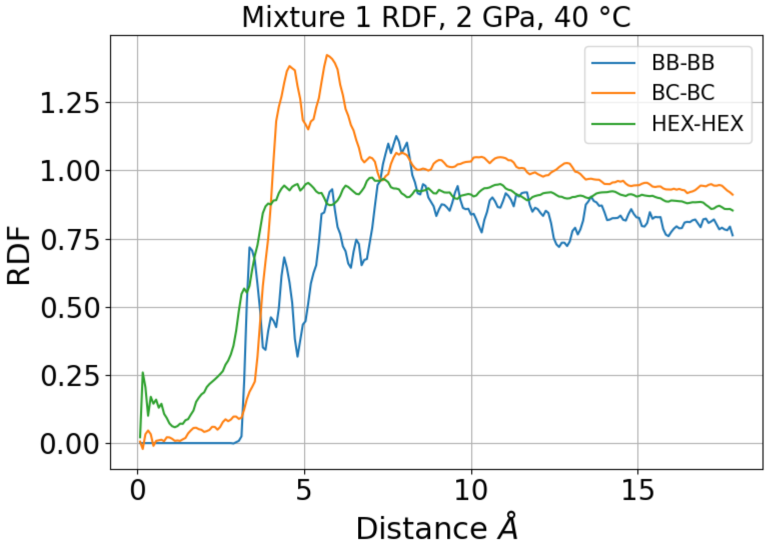

FIGURE C.7: Mixture 1 radial distribution function at 2 GPa and 40 °C

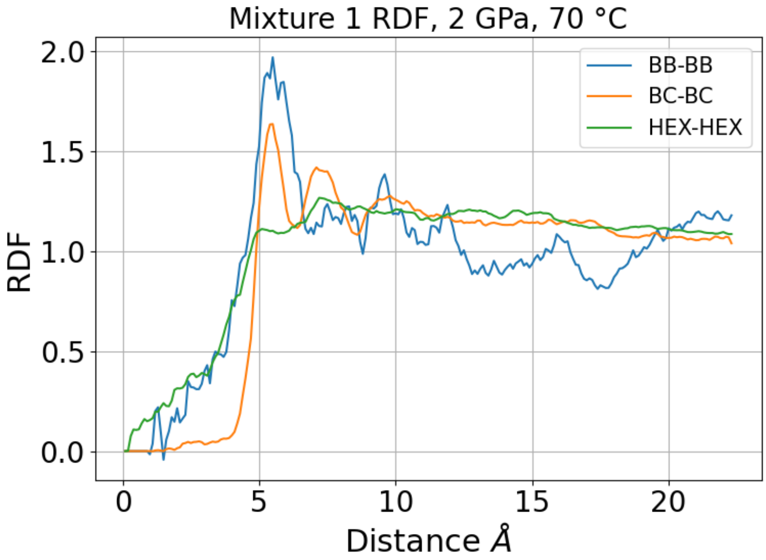

FIGURE C.8: Mixture 1 radial distribution function at 2 GPa and 70 °C

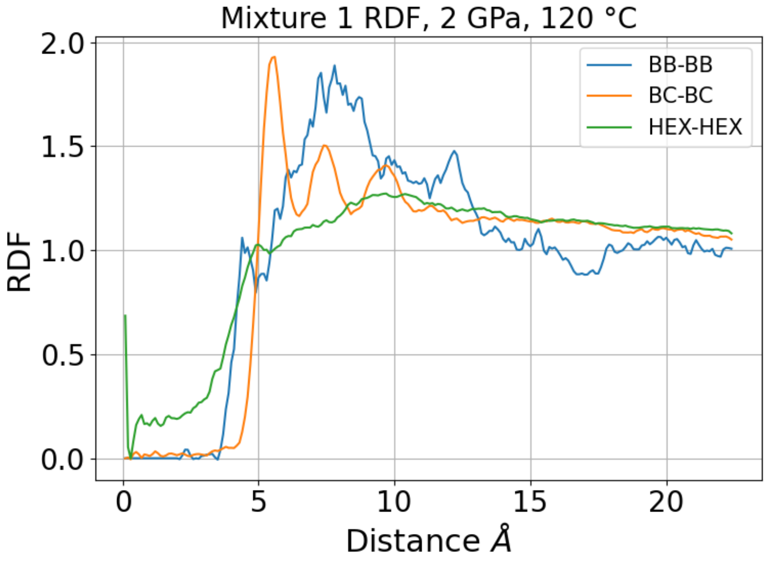

FIGURE C.9: Mixture 1 radial distribution function at 2 GPa and 120 °C

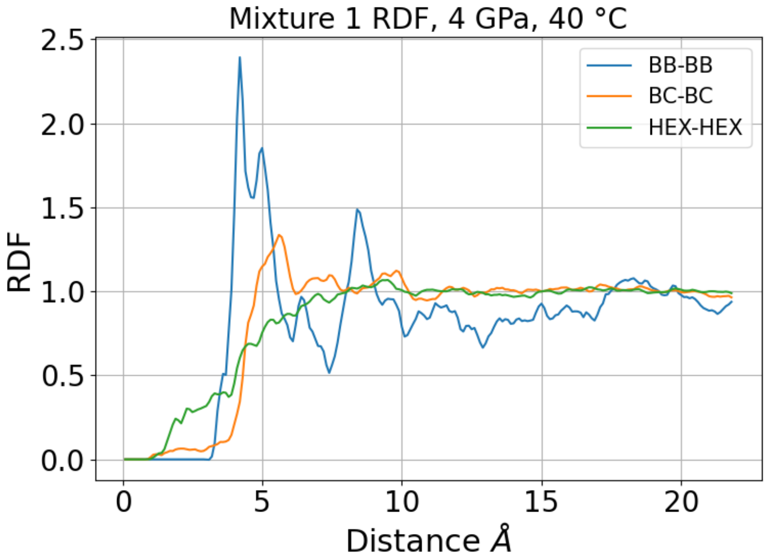

FIGURE C.10: Mixture 1 radial distribution function at 1 GPa and 40 °C

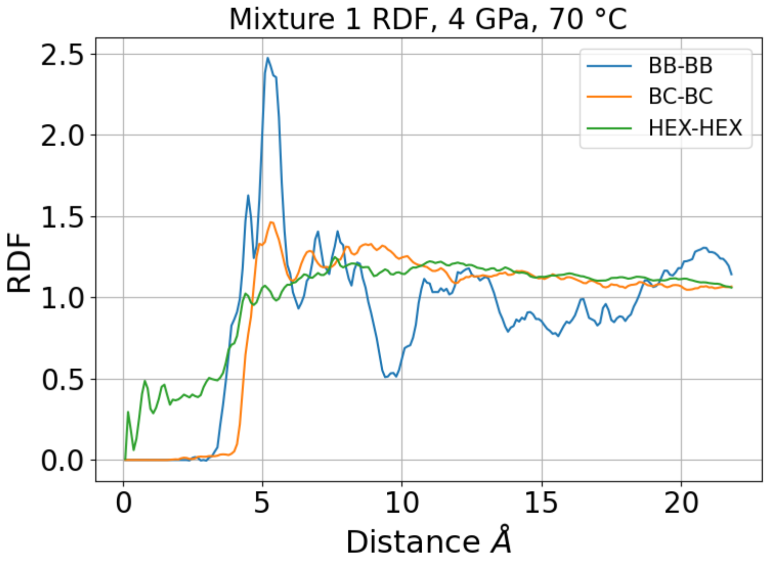

FIGURE C.11: Mixture 1 radial distribution function at 1 GPa and 70 °C

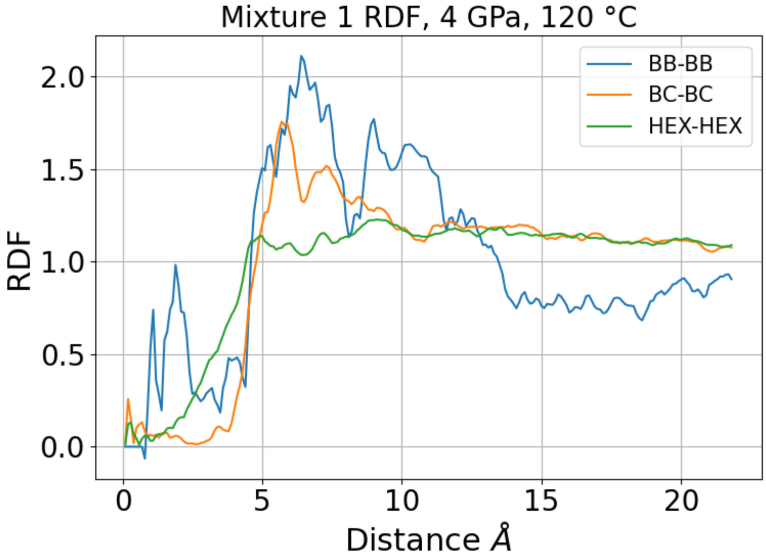

FIGURE C.12: Mixture 1 radial distribution function at 4 GPa and 120 °C

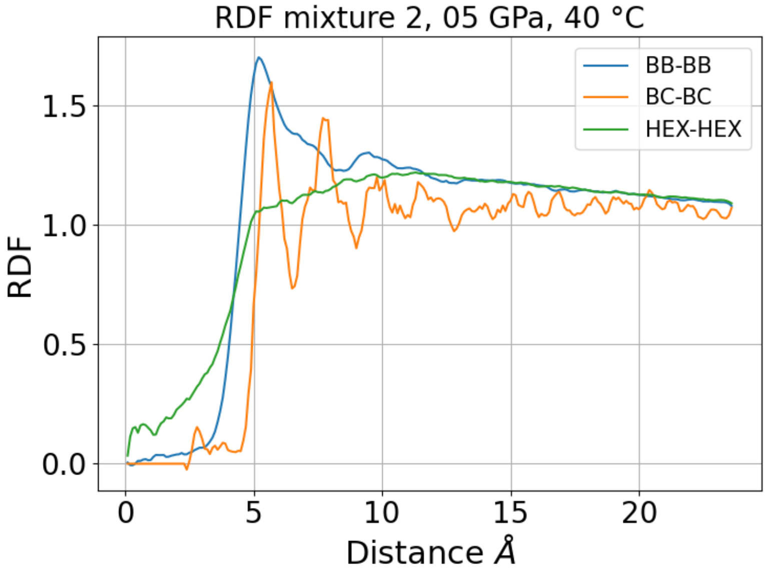

FIGURE C.13: Mixture 2 radial distribution function at 0.5 GPa and 40 °C

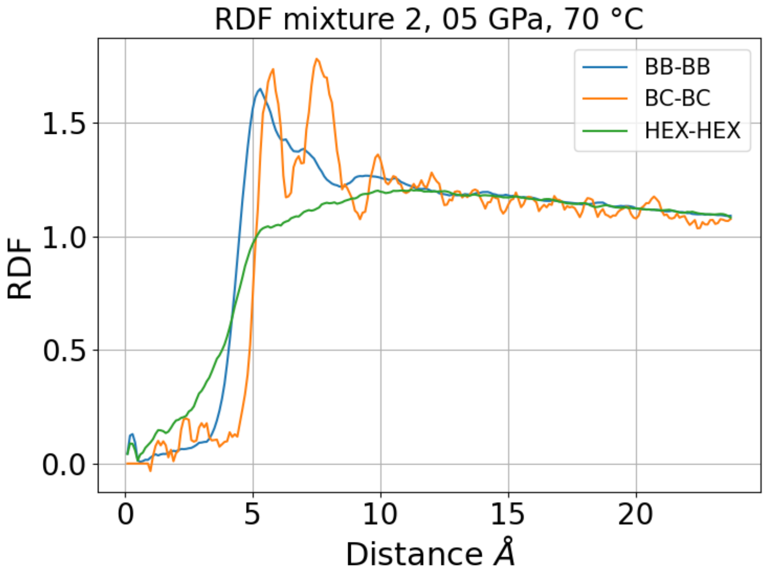

FIGURE C.14: Mixture 2 radial distribution function at 0.5 GPa and 70 °C

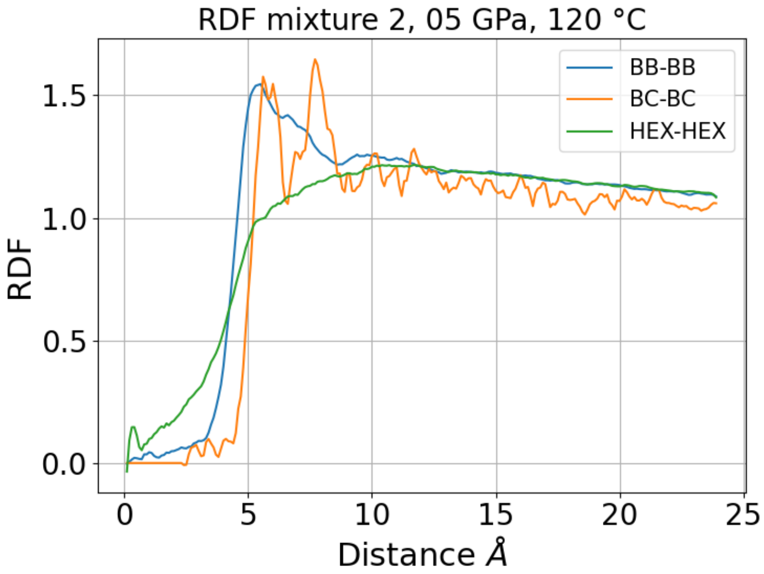

FIGURE C.15: Mixture 2 radial distribution function at 0.5 GPa and 120 °C

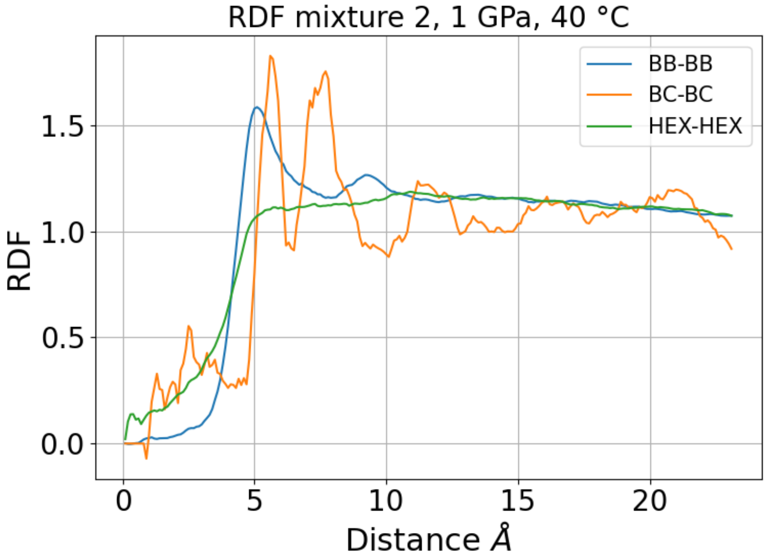

FIGURE C.16: Mixture 2 radial distribution function at 1 GPa and 40 °C

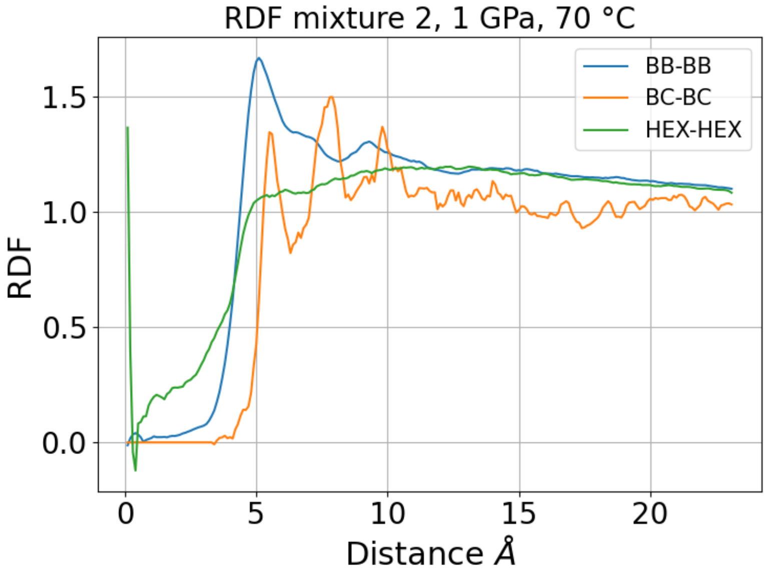

FIGURE C.17: Mixture 2 radial distribution function at 1 GPa and 70 °C

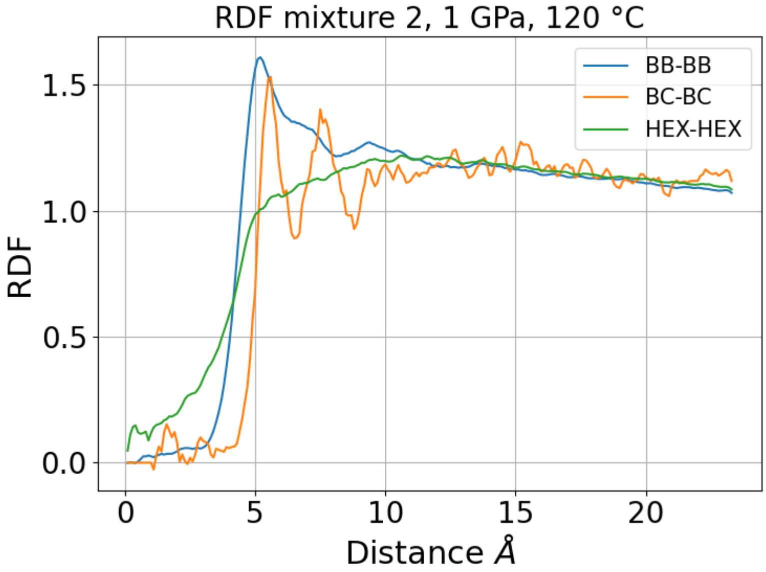

FIGURE C.18: Mixture 2 radial distribution function at 1 GPa and 120 °C

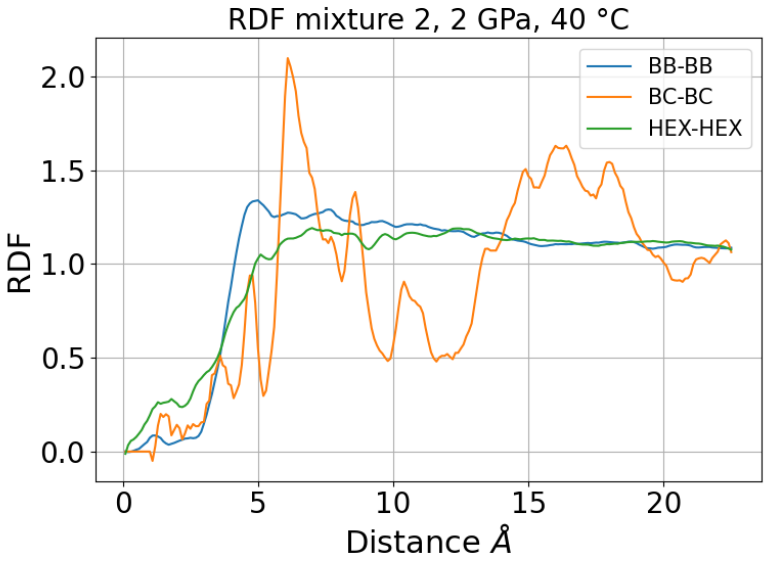

FIGURE C.19: Mixture 2 radial distribution function at 2 GPa and 40 °C

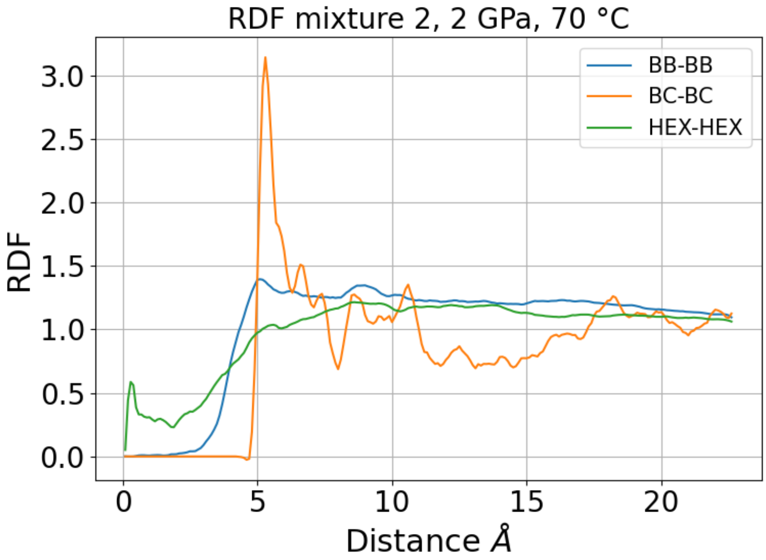

FIGURE C.20: Mixture 2 radial distribution function at 2 GPa and 70 °C

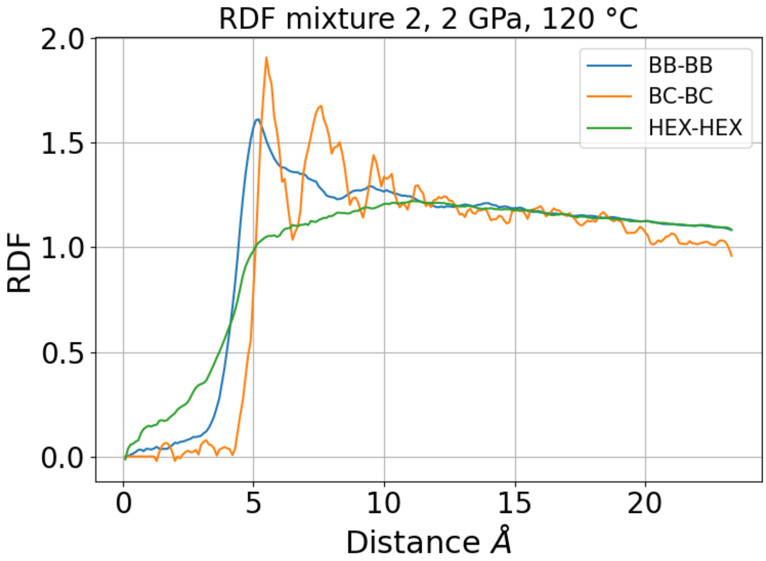

FIGURE C.21: Mixture 2 radial distribution function at 2 GPa and 120 °C

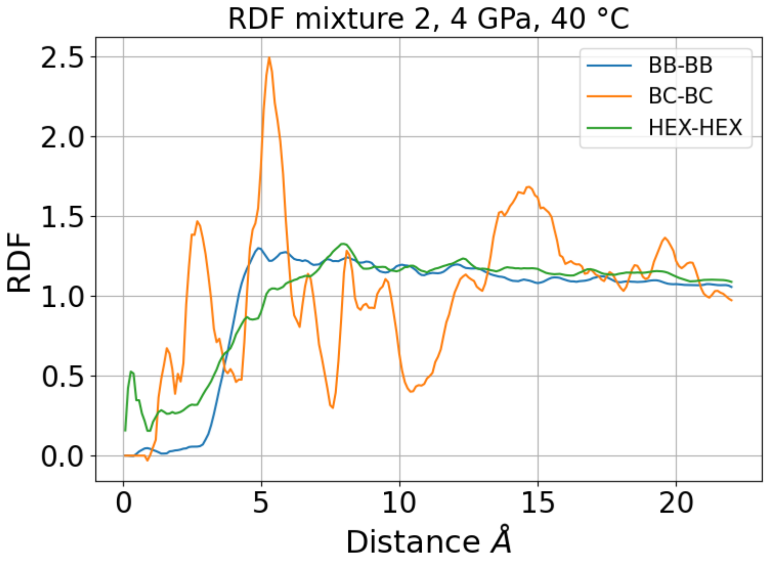

FIGURE C.22: Mixture 2 radial distribution function at 4 GPa and 40 °C

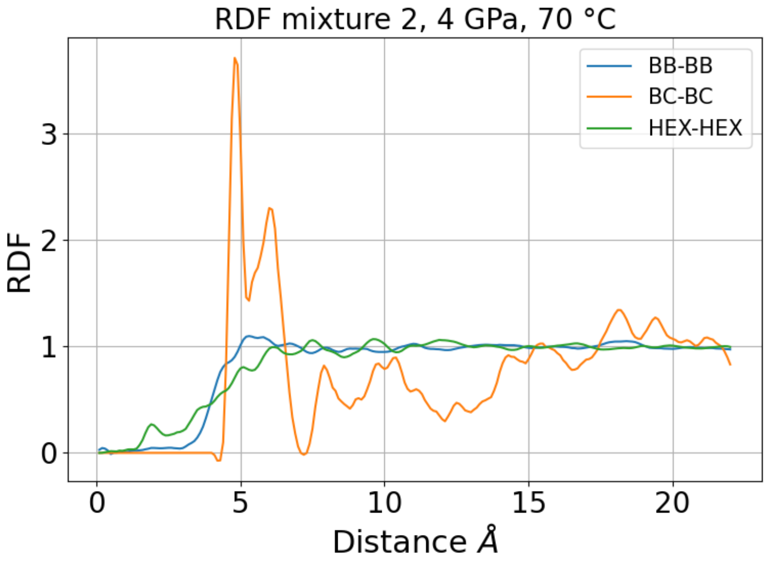

FIGURE C.23: Mixture 2 radial distribution function at 4 GPa and 70 °C

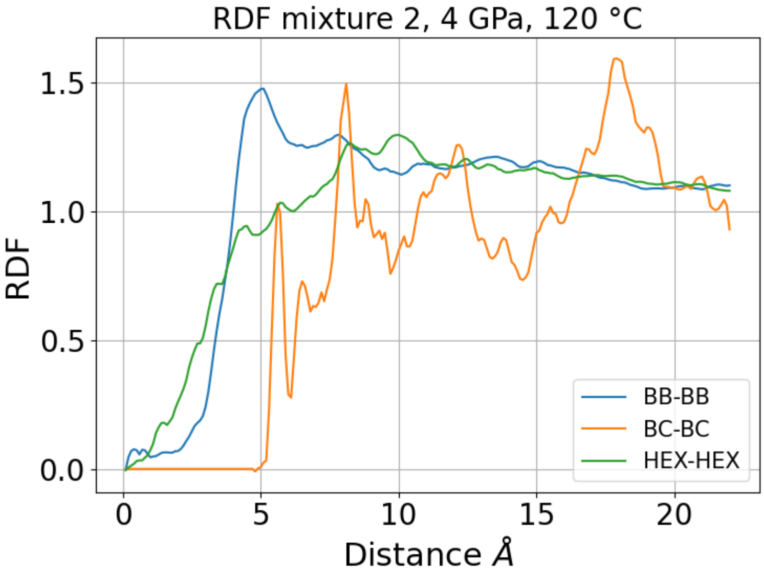

FIGURE C.24: Mixture 2 radial distribution function at 4 GPa and 120 °C

Appendix D

ZDDPs on Hematite surfaces

To resolve the issue of setting up the initial spin state, a finer grid is likely necessary to obtain a more accurate description of the pseudo-atom PES. We tested seven different values of kinetic energy cutoff: 1000, 1100, 1250, 1400, 1600, 1800, and 2000 eV. A higher cutoff value generates a finer integration grid. As shown in Fig. D.1, at 1000 eV, the total energy error per atom is still high, around 4 eV, but it decreases as we go to higher cutoff values. It's important to note how the band gap becomes nearly perfectly spin-independent, as expected in an antiferromagnetic system, and the DFT+U moment on each atom becomes very similar. To balance computational cost and accuracy, a kinetic energy cutoff of 1250 eV was chosen as an optimal trade-off.

The necessity to have such a high kinetic energy cutoff is due to the fact that the Fe norm-conserving pseudopotential includes semi-core electrons (3s and 3p) in the valence. The higher kinetic energy cutoff, as well as the initial guesses for NGWFs using the atomic solver, were essential to obtain a proper description of the antiferromagnetic state of hematite. Specifically, the higher energy cutoff helped in achieving the correct initial guess by using neutral projectors for iron and single negatively charged projectors for oxygen. These parameters will be employed for the rest of the simulations presented in this paper, alongside a U value of 6 eV.

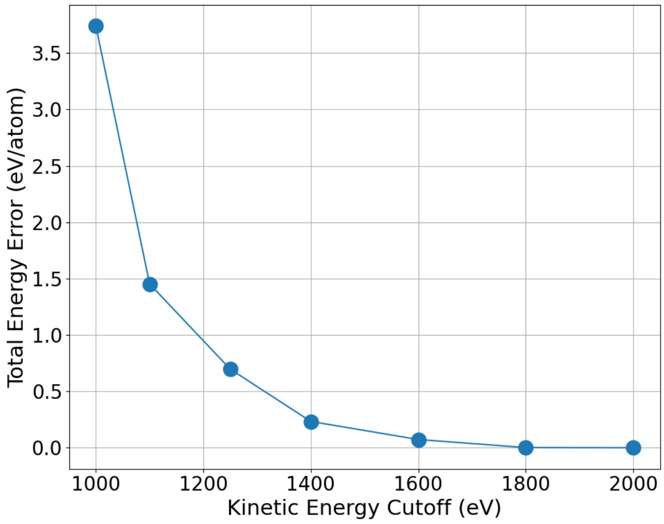

(A) Total energy error

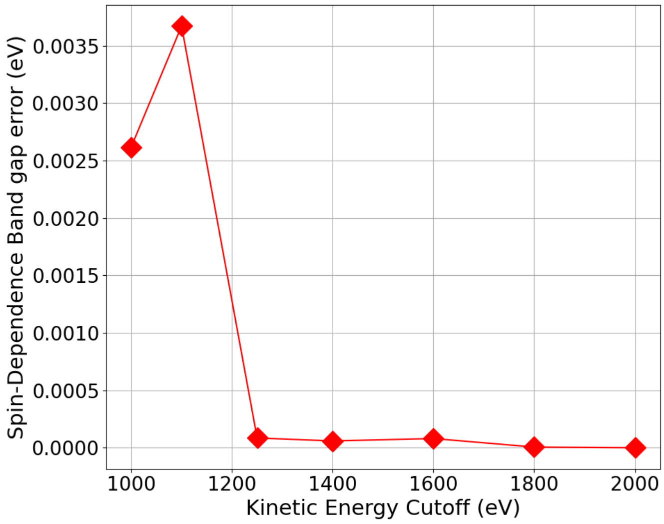

(B) Spin-dependence band gap error

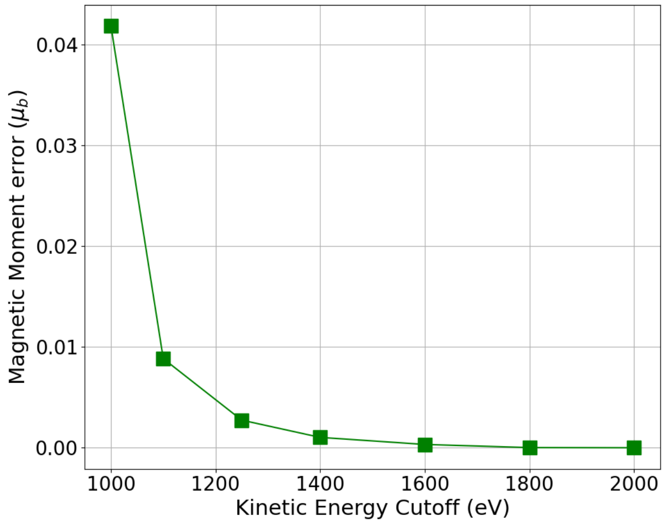

(C) Magnetic moment error

FIGURE D.1: Kinetic energy cutoff test. The value at 2000 eV was taken as the converged one and all the reported data are shown as an error compared to this value: (a) reports the total energy error per atom, (b) the spin-dependence band gap error, (c) the magnetic moment error

Bibliography

[1] Fuchs Petrolub, "Global Demand for Lubricants from 2000 to 2019 (in Million Metric Tons).," presented at the Statista, Statista Inc. May 13, 2020.

[2] "Lubricants and Their Composition," in *Engineering Tribology*. Elsevier, 2014, pp. 51–104. DOI: 10.1016/B978-0-12-397047-3.00003-5.

[3] N. D. Kondratyuk and M. A. Orekhov, "Shear viscosity of n-pentane from diffusivity based molecular dynamics methods," *J. Phys.: Conf. Ser.*, vol. 1556, p. 012 048, May 2020. DOI: 10.1088/1742-6596/1556/1/012048.

[4] N. D. Kondratyuk and V. V. Pisarev, "Calculation of viscosities of branched alkanes from 0.1 to 1000 MPa by molecular dynamics methods using COMPASS force field," *Fluid Phase Equilibria*, vol. 498, pp. 151–159, Oct. 15, 2019. DOI: 10.1016/j.fluid.2019.06.023.

[5] P. Liu, H. Yu, N. Ren, F. E. Lockwood, and Q. J. Wang, "Pressure–Viscosity Coefficient of Hydrocarbon Base Oil through Molecular Dynamics Simulations," *Tribol Lett*, vol. 60, no. 3, p. 34, 3 Oct. 30, 2015. DOI: 10.1007/s11249-015-0610-6.

[6] C. McCabe, S. Cui, and P. T. Cummings, "Characterizing the viscosity–temperature dependence of lubricants by molecular simulation," *Fluid Phase Equilibria*, Proceedings of the Fourteenth Symposium on Thermophysical Properties, vol. 183–184, pp. 363–370, Jul. 1, 2001. DOI: 10.1016/S0378-3812(01)00448-4.

[7] A. C. F. Mendonça, A. A. H. Pádua, and P. Malfreyt, "Nonequilibrium Molecular Simulations of New Ionic Lubricants at Metallic Surfaces: Prediction of the Friction," *J. Chem. Theory Comput.*, vol. 9, no. 3, pp. 1600–1610, 3 Mar. 12, 2013. DOI: 10.1021/ct3008827.

[8] O. Borodin, G. D. Smith, and H. Kim, "Viscosity of a Room Temperature Ionic Liquid: Predictions from Nonequilibrium and Equilibrium Molecular Dynamics Simulations," *J. Phys. Chem. B*, vol. 113, no. 14, pp. 4771–4774, 14 Apr. 9, 2009. DOI: 10.1021/jp810016e.

[9] L. Lin and M. A. Kedzierski, "Density and viscosity of a polyol ester lubricant: Measurement and molecular dynamics simulation," *International Journal of Refrigeration*, vol. 118, pp. 188–201, Oct. 1, 2020. DOI: 10.1016/j.ijrefrig.2020.07.004.

[10] T. D. Ta *et al.*, “Tribological Behavior of Aqueous Copolymer Lubricant in Mixed Lubrication Regime,” *ACS Appl. Mater. Interfaces*, vol. 8, no. 8, pp. 5641–5652, Mar. 2, 2016. DOI: `10.1021/acsami.5b10905`.

[11] N. Kondratyuk, D. Lenev, and V. Pisarev, “Transport coefficients of model lubricants up to 400 MPa from molecular dynamics,” *J. Chem. Phys.*, vol. 152, no. 19, p. 191 104, 19 May 21, 2020. DOI: `10.1063/5.0008907`.

[12] D. Mathas *et al.*, “Evaluation of methods for viscosity simulations of lubricants at different temperatures and pressures: A case study on PAO-2,” *Tribology Transactions*, vol. 0, no. ja, pp. 1–26, ja May 1, 2021. DOI: `10.1080/10402004.2021.1922790`.

[13] S. Echeverri Restrepo, M. C. P. van Eijk, and J. P. Ewen, “Behaviour of n-alkanes confined between iron oxide surfaces at high pressure and shear rate: A nonequilibrium molecular dynamics study,” *Tribology International*, vol. 137, pp. 420–432, Sep. 1, 2019. DOI: `10.1016/j.triboint.2019.05.008`.

[14] J. P. Ewen, D. M. Heyes, and D. Dini, “Advances in nonequilibrium molecular dynamics simulations of lubricants and additives,” *Friction*, vol. 6, no. 4, pp. 349–386, 4 Dec. 1, 2018. DOI: `10.1007/s40544-018-0207-9`.

[15] J. P. Ewen, C. Gattinoni, F. M. Thakkar, N. Morgan, H. A. Spikes, and D. Dini, “A Comparison of Classical Force-Fields for Molecular Dynamics Simulations of Lubricants,” *Materials*, vol. 9, no. 8, p. 651, 8 Aug. 2016. DOI: `10.3390/ma9080651`.

[16] T. D. Ta, H. D. Ta, K. A. Tieu, and B. H. Tran, “Impact of chosen force fields and applied load on thin film lubrication,” *Friction*, Jan. 7, 2021. DOI: `10.1007/s40544-020-0464-2`.

[17] T. D. Ta *et al.*, “Reactive Molecular Dynamics Study of Hierarchical Tribochemical Lubricant Films at Elevated Temperatures,” *ACS Appl. Nano Mater.*, vol. 3, no. 3, pp. 2687–2704, 3 Mar. 27, 2020. DOI: `10.1021/acsanm.0c00042`.

[18] A. Martini, S. J. Eder, and N. Dörr, “Tribochemistry: A Review of Reactive Molecular Dynamics Simulations,” *Lubricants*, vol. 8, no. 4, p. 44, 4 Apr. 2020. DOI: `10.3390/lubricants8040044`.

[19] E. J. Maginn, R. A. Messerly, D. J. Carlson, D. R. Roe, and J. R. Elliott, “Best Practices for Computing Transport Properties 1. Self-Diffusivity and Viscosity from Equilibrium Molecular Dynamics [Article v1.0],” *LiveCoMS*, vol. 1, no. 1, p. 6324, 1 Dec. 22, 2018. DOI: `10.33011/livecoms.1.1.6324`.

[20] Y. Zhang, A. Otani, and E. J. Maginn, “Reliable Viscosity Calculation from Equilibrium Molecular Dynamics Simulations: A Time Decomposition Method,” *J. Chem. Theory Comput.*, vol. 11, no. 8, pp. 3537–3546, 8 Aug. 11, 2015. DOI: `10.1021/acs.jctc.5b00351`.

[21] P. Santak and G. Conduit, "Enhancing NEMD with automatic shear rate sampling to model viscosity and correction of systematic errors in modeling density: Application to linear and light branched alkanes," *J. Chem. Phys.*, vol. 153, no. 1, p. 014 102, Jul. 7, 2020. DOI: 10.1063/5.0004377.

[22] U. Abdulfatai, A. Uzairu, S. Uba, and G. A. Shallangwa, "Molecular modelling and design of lubricant additives and their molecular dynamic simulations studies of Diamond-Like-Carbon (DLC) and steel surface coating," *Egyptian Journal of Petroleum*, vol. 28, no. 1, pp. 111–115, Mar. 1, 2019. DOI: 10.1016/j.ejpe.2018.12.004.

[23] L.-T. Kong, C. Denniston, and M. H. Müser, "The crucial role of chemical detail for slip-boundary conditions: Molecular dynamics simulations of linear oligomers between sliding aluminum surfaces," *Modelling Simul. Mater. Sci. Eng.*, vol. 18, no. 3, p. 034 004, Mar. 2010. DOI: 10.1088/0965-0393/18/3/034004.

[24] S. Loehlé *et al.*, "Mixed lubrication of steel by C18 fatty acids revisited. Part I: Toward the formation of carboxylate," *Tribology International*, vol. 82, pp. 218–227, Feb. 1, 2015. DOI: 10.1016/j.triboint.2014.10.020.

[25] Chen *et al.*, "Tribological performance of an ionic liquid as a lubricant for steel/aluminium contacts," *Journal of Synthetic Lubrication*, vol. 20, no. 3, pp. 217–225, 2003. DOI: 10.1002/jsl.3000200304.

[26] P. Iglesias, M. D. Bermúdez, F. J. Carrión, and G. Martínez-Nicolás, "Friction and wear of aluminium–steel contacts lubricated with ordered fluids-neutral and ionic liquid crystals as oil additives," *Wear*, vol. 256, no. 3, pp. 386–392, Feb. 1, 2004. DOI: 10.1016/S0043-1648(03)00442-3.

[27] H. Wang, Q. Lu, C. Ye, W. Liu, and Z. Cui, "Friction and wear behaviors of ionic liquid of alkylimidazolium hexafluorophosphates as lubricants for steel/steel contact," *Wear*, vol. 256, no. 1, pp. 44–48, Jan. 1, 2004. DOI: 10.1016/S0043-1648(03)00255-2.

[28] "Crystal Structure," in *The Iron Oxides*, John Wiley & Sons, Ltd, 2003, pp. 9–38. DOI: 10.1002/3527602097.ch2.

[29] G. S. Parkinson, "Iron oxide surfaces," *Surface Science Reports*, vol. 71, no. 1, pp. 272–365, 1 Mar. 1, 2016. DOI: 10.1016/j.surfrep.2016.02.001.

[30] "Introduction to the Iron Oxides," in *The Iron Oxides*, John Wiley & Sons, Ltd, 2003, pp. 1–7. DOI: 10.1002/3527602097.ch1.

[31] Y. Si, M. Li, Z. Zhou, M. Liu, and O. Prezhdo, "Improved description of hematite surfaces by the SCAN functional," *The Journal of Chemical Physics*, vol. 152, no. 2, p. 024 706, Jan. 10, 2020. DOI: 10.1063/1.5134951.

[32] S. Shousha, S. Khalil, and M. Youssef, "A complete ab initio thermodynamic and kinetic catalogue of the defect chemistry of hematite -Fe 2 O 3 , its cation diffusion, and sample donor dopants," *Physical Chemistry Chemical Physics*, vol. 23, no. 45, pp. 25 518–25 532, 2021. DOI: 10.1039/D1CP03394H.

[33] N. Naveas, R. Pulido, C. Marini, J. Hernández-Montelongo, and M. M. Silván, "First-principles calculations of hematite (-Fe2O3) by self-consistent DFT+U+V," *iScience*, vol. 26, no. 2, p. 106 033, Feb. 2023. DOI: 10.1016/j.isci.2023.106033.

[34] T. P. Trainor *et al.*, "Structure and reactivity of the hydrated hematite (0001) surface," *Surface Science*, vol. 573, no. 2, pp. 204–224, 2 Dec. 10, 2004. DOI: 10.1016/j.susc.2004.09.040.

[35] X.-G. Wang *et al.*, "The Hematite (0001) Surface: Evidence for Domains of Distinct Chemistry," *Phys. Rev. Lett.*, vol. 81, no. 5, pp. 1038–1041, 5 Aug. 3, 1998. DOI: 10.1103/PhysRevLett.81.1038.

[36] W. T. Ashurst and W. G. Hoover, "Argon Shear Viscosity via a Lennard-Jones Potential with Equilibrium and Nonequilibrium Molecular Dynamics," *Phys. Rev. Lett.*, vol. 31, no. 4, pp. 206–208, Jul. 23, 1973. DOI: 10.1103/PhysRevLett.31.206.

[37] W. G. Hoover, A. J. C. Ladd, R. B. Hickman, and B. L. Holian, "Bulk viscosity via nonequilibrium and equilibrium molecular dynamics," *Phys. Rev. A*, vol. 21, no. 5, pp. 1756–1760, May 1, 1980. DOI: 10.1103/PhysRevA.21.1756.

[38] M. Schoen and C. Hoheisel, "The shear viscosity of a Lennard-Jones fluid calculated by equilibrium molecular dynamics," *Molecular Physics*, vol. 56, no. 3, pp. 653–672, Oct. 20, 1985. DOI: 10.1080/00268978500102591.

[39] W. Allen and R. L. Rowley, "Predicting the viscosity of alkanes using nonequilibrium molecular dynamics: Evaluation of intermolecular potential models," *J. Chem. Phys.*, vol. 106, no. 24, pp. 10 273–10 281, Jun. 22, 1997. DOI: 10.1063/1.474052.

[40] S. T. Cui P. T. Cummings H. D. Cochran, "The calculation of viscosity of liquid n-decane and n-hexadecane by the Green-Kubo method," *Molecular Physics*, vol. 93, no. 1, pp. 117–122, Jan. 1, 1998. DOI: 10.1080/002689798169500.

[41] M. Mondello and G. S. Grest, "Viscosity calculations of n-alkanes by equilibrium molecular dynamics," *J. Chem. Phys.*, vol. 106, no. 22, pp. 9327–9336, Jun. 8, 1997. DOI: 10.1063/1.474002.

[42] L. I. Kioupis and E. J. Maginn, "Impact of Molecular Architecture on the High-Pressure Rheology of Hydrocarbon Fluids," *J. Phys. Chem. B*, vol. 104, no. 32, pp. 7774–7783, 32 Aug. 1, 2000. DOI: 10.1021/jp000966x.

[43] L. I. Kioupis and E. J. Maginn, "Molecular Simulation of Poly-α-olefin Synthetic Lubricants: Impact of Molecular Architecture on Performance Properties," *J. Phys. Chem. B*, vol. 103, no. 49, pp. 10 781–10 790, Dec. 1, 1999. DOI: 10.1021/jp992399n.

[44] C. McCabe, S. Cui, P. T. Cummings, P. A. Gordon, and R. B. Saeger, "Examining the rheology of 9-octylheptadecane to giga-pascal pressures," *The Journal of Chemical Physics*, vol. 114, no. 4, pp. 1887–1891, Jan. 22, 2001. DOI: `10.1063/1.1334676`.

[45] U. S. Ramasamy, S. Bair, and A. Martini, "Predicting Pressure–Viscosity Behavior from Ambient Viscosity and Compressibility: Challenges and Opportunities," *Tribol Lett*, vol. 57, no. 2, p. 11, Jan. 11, 2015. DOI: `10.1007/s11249-014-0454-5`.

[46] H.-C. Tseng, J.-S. Wu, and R.-Y. Chang, "Shear thinning and shear dilatancy of liquid n-hexadecane via equilibrium and nonequilibrium molecular dynamics simulations: Temperature, pressure, and density effects," *J. Chem. Phys.*, vol. 129, no. 1, p. 014 502, Jul. 7, 2008. DOI: `10.1063/1.2943314`.

[47] C. McCabe, C. W. Manke, and P. T. Cummings, "Predicting the Newtonian viscosity of complex fluids from high strain rate molecular simulations," *J. Chem. Phys.*, vol. 116, no. 8, pp. 3339–3342, 8 Feb. 12, 2002. DOI: `10.1063/1.1446045`.

[48] D. Nevins and F. J. Spera, "Accurate computation of shear viscosity from equilibrium molecular dynamics simulations," *Molecular Simulation*, vol. 33, no. 15, pp. 1261–1266, Dec. 1, 2007. DOI: `10.1080/08927020701675622`.

[49] K.-S. Kim, M. H. Han, C. Kim, Z. Li, G. E. Karniadakis, and E. K. Lee, "Nature of intrinsic uncertainties in equilibrium molecular dynamics estimation of shear viscosity for simple and complex fluids," *J. Chem. Phys.*, vol. 149, no. 4, p. 044 510, Jul. 28, 2018. DOI: `10.1063/1.5035119`.

[50] G. P. Morriss, P. J. Daivis, and D. J. Evans, "The rheology of n alkanes: Decane and eicosane," *J. Chem. Phys.*, vol. 94, no. 11, pp. 7420–7433, Jun. 1991. DOI: `10.1063/1.460174`.

[51] C. J. Mundy, S. Balasubramanian, K. Bagchi, J. I. Siepmann, and M. L. Klein, "Equilibrium and non-equilibrium simulation studies of fluid alkanes in bulk and at interfaces," *Faraday Discuss.*, vol. 104, no. 0, pp. 17–36, Jan. 1, 1996. DOI: `10.1039/FD9960400017`.

[52] R. Khare, J. de Pablo, and A. Yethiraj, "Molecular simulation and continuum mechanics study of simple fluids in non-isothermal planar couette flows," *J. Chem. Phys.*, vol. 107, no. 7, pp. 2589–2596, Aug. 15, 1997. DOI: `10.1063/1.474570`.

[53] M. J. Stevens, M. Mondello, G. S. Grest, S. T. Cui, H. D. Cochran, and P. T. Cummings, "Comparison of shear flow of hexadecane in a confined geometry and in bulk," *J. Chem. Phys.*, vol. 106, no. 17, pp. 7303–7314, May 1997. DOI: `10.1063/1.473692`.

[54] D. J. Lacks, "Energy Landscapes and the Non-Newtonian Viscosity of Liquids and Glasses," *Phys. Rev. Lett.*, vol. 87, no. 22, p. 225 502, Nov. 13, 2001. DOI: `10.1103/PhysRevLett.87.225502`.

[55] S. Bair, C. McCabe, and P. T. Cummings, “Comparison of Nonequilibrium Molecular Dynamics with Experimental Measurements in the Nonlinear Shear-Thinning Regime,” *Phys. Rev. Lett.*, vol. 88, no. 5, p. 058 302, Jan. 18, 2002. DOI: 10.1103/PhysRevLett.88.058302.

[56] A. Jabbarzadeh, J. D. Atkinson, and R. I. Tanner, “The effect of branching on slip and rheological properties of lubricants in molecular dynamics simulation of Couette shear flow,” *Tribology International*, vol. 35, no. 1, pp. 35–46, 1 Jan. 1, 2002. DOI: 10.1016/S0301-679X(01)00089-5.

[57] Y. Yang, T. A. Pakkanen, and R. L. Rowley, “NEMD Simulations of Viscosity and Viscosity Index for Lubricant-Size Model Molecules,” *International Journal of Thermophysics*, vol. 23, no. 6, pp. 1441–1454, Nov. 1, 2002. DOI: 10.1023/A:1020777514585.

[58] N. Galamba, C. A. Nieto de Castro, and J. F. Ely, “Shear viscosity of molten alkali halides from equilibrium and nonequilibrium molecular-dynamics simulations,” *J. Chem. Phys.*, vol. 122, no. 22, p. 224 501, 22 Jun. 8, 2005. DOI: 10.1063/1.1924706.

[59] Q. Guo, P. S. Chung, H. Chen, and M. S. Jhon, “Molecular rheology of perfluoropolyether lubricant via nonequilibrium molecular dynamics simulation,” *Journal of Applied Physics*, vol. 99, no. 8, 08N105, Apr. 15, 2006. DOI: 10.1063/1.2171937.

[60] V. Jadhao and M. O. Robbins, “Probing large viscosities in glass-formers with nonequilibrium simulations,” *Proceedings of the National Academy of Sciences*, vol. 114, no. 30, pp. 7952–7957, Jul. 25, 2017. DOI: 10.1073/pnas.1705978114.

[61] E. Sneha, A. Revikumar, J. Y. singh, A. D. Thampi, and S. Rani, “Viscosity prediction of Pongamia pinnata (Karanja) oil by molecular dynamics simulation using GAFF and OPLS force field,” *Journal of Molecular Graphics and Modelling*, vol. 101, p. 107 764, Dec. 1, 2020. DOI: 10.1016/j.jmgm.2020.107764.

[62] M. A. Galvani Cunha and M. O. Robbins, “Determination of pressure-viscosity relation of 2,2,4-trimethylhexane by all-atom molecular dynamics simulations,” *Fluid Phase Equilibria*, vol. 495, pp. 28–32, Sep. 1, 2019. DOI: 10.1016/j.fluid.2019.05.008.

[63] C. Braga and K. P. Travis, “Computer simulation of the role of torsional flexibility on mass and momentum transport for a series of linear alkanes,” *J. Chem. Phys.*, vol. 137, no. 6, p. 064 116, Aug. 14, 2012. DOI: 10.1063/1.4742187.

[64] J. Lu, Q. J. Wang, N. Ren, and F. E. Lockwood, “Correlation between pressure-viscosity coefficient and traction coefficient of the base stocks in traction lubricants: A molecular dynamic approach,” *Tribology International*, vol. 134, pp. 328–334, Jun. 1, 2019. DOI: 10.1016/j.triboint.2019.02.013.

[65] P. Liu, J. Lu, H. Yu, N. Ren, F. E. Lockwood, and Q. J. Wang, "Lubricant shear thinning behavior correlated with variation of radius of gyration via molecular dynamics simulations," *J. Chem. Phys.*, vol. 147, no. 8, p. 084 904, Aug. 28, 2017. DOI: `10.1063/1.4986552`.

[66] D. Valencia-Marquez, A. Flores-Tlacuahuac, A. J. García-Cuéllar, and L. Ricardez-Sandoval, "Computer aided molecular design coupled with molecular dynamics as a novel approach to design new lubricants," *Computers & Chemical Engineering*, vol. 156, p. 107 523, Jan. 1, 2022. DOI: `10.1016/j.compchemeng.2021.107523`.

[67] J. C. S. Kadupitiya and V. Jadhao, "Probing the Rheological Properties of Liquids Under Conditions of Elastohydrodynamic Lubrication Using Simulations and Machine Learning," *Tribol Lett*, vol. 69, no. 3, p. 82, May 27, 2021. DOI: `10.1007/s11249-021-01457-3`.

[68] L. Zhang, R. Balasundaram, S. H. Gehrke, and S. Jiang, "Nonequilibrium molecular dynamics simulations of confined fluids in contact with the bulk," *The Journal of Chemical Physics*, vol. 114, no. 15, pp. 6869–6877, Apr. 15, 2001. DOI: `10.1063/1.1359179`.

[69] E. Mangaud and B. Rotenberg, "Sampling mobility profiles of confined fluids with equilibrium molecular dynamics simulations," *The Journal of Chemical Physics*, vol. 153, no. 4, p. 044 125, Jul. 29, 2020. DOI: `10.1063/5.0013952`.

[70] G. Arya, H.-C. Chang, and E. J. Maginn, "A critical comparison of equilibrium, non-equilibrium and boundary-driven molecular dynamics techniques for studying transport in microporous materials," *The Journal of Chemical Physics*, vol. 115, no. 17, pp. 8112–8124, Nov. 1, 2001. DOI: `10.1063/1.1407002`.

[71] C. Gattinoni, D. M. Heyes, C. D. Lorenz, and D. Dini, "Traction and nonequilibrium phase behavior of confined sheared liquids at high pressure," *Phys. Rev. E*, vol. 88, no. 5, p. 052 406, Nov. 13, 2013. DOI: `10.1103/PhysRevE.88.052406`.

[72] B. Shan, W. Su, L. Gibelli, and Y. Zhang, "Molecular kinetic modelling of non-equilibrium transport of confined van der Waals fluids," *Journal of Fluid Mechanics*, vol. 976, A7, Dec. 2023. DOI: `10.1017/jfm.2023.893`.

[73] S. A. Somers and H. T. Davis, "Microscopic dynamics of fluids confined between smooth and atomically structured solid surfaces," *J. Chem. Phys.*, vol. 96, no. 7, pp. 5389–5407, Apr. 1992. DOI: `10.1063/1.462724`.

[74] Y. Zhu, Y. Zhang, Y. Shi, X. Lu, J. Li, and L. Lu, "Lubrication Behavior of Water Molecules Confined in TiO2 Nanoslits: A Molecular Dynamics Study," *J. Chem. Eng. Data*, vol. 61, no. 12, pp. 4023–4030, Dec. 8, 2016. DOI: `10.1021/acs.jced.6b00534`.

[75] X. Zheng, H. Zhu, B. Kosasih, and A. Kiet Tieu, “A molecular dynamics simulation of boundary lubrication: The effect of n-alkanes chain length and normal load,” *Wear*, Wear of Materials 2013, vol. 301, no. 1, pp. 62–69, Apr. 1, 2013. DOI: `10.1016/j.wear.2013.01.052`.

[76] X. Zheng, L. Su, G. Deng, J. Zhang, H. Zhu, and A. K. Tieu, “Study on Lubrication Characteristics of C4-Alkane and Nanoparticle during Boundary Friction by Molecular Dynamics Simulation,” *Metals*, vol. 11, no. 9, p. 1464, 9 Sep. 2021. DOI: `10.3390/met11091464`.

[77] R.-G. Xu and Y. Leng, “Squeezing and stick–slip friction behaviors of lubricants in boundary lubrication,” *Proc Natl Acad Sci USA*, vol. 115, no. 26, pp. 6560–6565, 26 Jun. 26, 2018. DOI: `10.1073/pnas.1805569115`.

[78] H. Berro, N. Fillot, and P. Vergne, “Hybrid Diffusion: An Efficient Method for Kinetic Temperature Calculation in Molecular Dynamics Simulations of Confined Lubricant Films,” *Tribol Lett*, vol. 37, no. 1, pp. 1–13, Jan. 1, 2010. DOI: `10.1007/s11249-009-9484-9`.

[79] J. L. Bradley-Shaw, P. J. Camp, P. J. Dowding, and K. Lewtas, “Molecular Dynamics Simulations of Glycerol Monooleate Confined between Mica Surfaces,” *Langmuir*, vol. 32, no. 31, pp. 7707–7718, Aug. 9, 2016. DOI: `10.1021/acs.langmuir.6b00091`.

[80] I. Yasuda *et al.*, “Combining Molecular Dynamics and Machine Learning to Analyze Shear Thinning for Alkane and Globular Lubricants in the Low Shear Regime,” *ACS Appl. Mater. Interfaces*, vol. 15, no. 6, pp. 8567–8578, Feb. 15, 2023. DOI: `10.1021/acsami.2c16366`.

[81] S. Tromp, L. Joly, M. Cobian, and N. Fillot, “Tribological Performance of the R1233zd Refrigerant in Extreme Confinement at the Nanoasperity Level: A Molecular Dynamics Study Using an ab Initio-Based Force Field,” *Tribol Lett*, vol. 67, no. 3, p. 67, May 15, 2019. DOI: `10.1007/s11249-019-1180-9`.

[82] H. Hoang and G. Galliero, “Shear behavior of a confined thin film: Influence of the molecular dynamics scheme employed,” *The Journal of Chemical Physics*, vol. 138, no. 5, p. 054 707, Feb. 5, 2013. DOI: `10.1063/1.4789582`.

[83] B. D. Todd and P. J. Daivis, “Homogeneous non-equilibrium molecular dynamics simulations of viscous flow: Techniques and applications,” *Molecular Simulation*, vol. 33, no. 3, pp. 189–229, Mar. 1, 2007. DOI: `10.1080/08927020601026629`.

[84] A. Jabbarzadeh and R. I. Tanner, “MOLECULAR DYNAMICS SIMULATION AND ITS APPLICATION TO NANO-RHEOLOGY,” p. 52, 2006.

[85] J. Shi, M. Zhang, J. Liu, G. Liu, and F. Zhou, “Molecular dynamics simulations of adsorption behavior of organic friction modifiers on hydrophilic silica surfaces under the effects of surface coverage and contact pressure,” *Tribology International*, vol. 156, p. 106 826, Apr. 1, 2021. DOI: `10.1016/j.triboint.2020.106826`.

[86] J. P. Ewen, C. Gattinoni, N. Morgan, H. A. Spikes, and D. Dini, "Nonequilibrium Molecular Dynamics Simulations of Organic Friction Modifiers Adsorbed on Iron Oxide Surfaces," *Langmuir*, vol. 32, no. 18, pp. 4450–4463, 18 May 10, 2016. DOI: `10.1021/acs.langmuir.6b00586`.

[87] A. M. Barnes, K. D. Bartle, and V. R. A. Thibon, "A review of zinc dialkyldithiophosphates (ZDDPS): Characterisation and role in the lubricating oil," *Tribology International*, vol. 34, no. 6, pp. 389–395, 6 Jun. 1, 2001. DOI: `10.1016/S0301-679X(01)00028-7`.

[88] H. Spikes, "The History and Mechanisms of ZDDP," *Tribology Letters*, vol. 17, no. 3, pp. 469–489, 3 Oct. 2004. DOI: `10.1023/B:TRIL.0000044495.26882.b5`.

[89] J. M. Martin, T. Onodera, C. Minfray, F. Dassenoy, and A. Miyamoto, "The origin of anti-wear chemistry of ZDDP," *Faraday Discuss.*, vol. 156, no. 0, pp. 311–323, 0 Jul. 2, 2012. DOI: `10.1039/C2FD00126H`.

[90] J. M. Martin, T. Onodera, M.-I. De Barros Bouchet, N. Hatakeyama, and A. Miyamoto, "Anti-wear Chemistry of ZDDP and Calcium Borate Nano-additive. Coupling Experiments, Chemical Hardness Predictions, and MD Calculations," *Tribol Lett*, vol. 50, no. 1, pp. 95–104, 1 Apr. 1, 2013. DOI: `10.1007/s11249-013-0108-z`.

[91] J. S. Tse, Y. Song, and Z. Liu, "Effects of Temperature and Pressure on ZDDP," *Tribol Lett*, vol. 28, no. 1, pp. 45–49, 1 Oct. 1, 2007. DOI: `10.1007/s11249-007-9246-5`.

[92] A. Pominov, J. Müller-Hillebrand, J. Träg, and D. Zahn, "Interaction Models and Molecular Simulation Systems of Steel–Organic Friction Modifier Interfaces," *Tribol Lett*, vol. 69, no. 1, p. 14, 1 Jan. 12, 2021. DOI: `10.1007/s11249-020-01384-9`.

[93] T. Onodera *et al.*, "A theoretical investigation on the abrasive wear prevention mechanism of ZDDP and ZP tribofilms," *Applied Surface Science*, 9th International Conference on Atomically Controlled Surfaces, Interfaces and Nanostructures 2007 (ASCIN-9), vol. 254, no. 23, pp. 7976–7979, Sep. 30, 2008. DOI: `10.1016/j.apsusc.2008.04.057`.

[94] H. Berro, N. Fillot, and P. Vergne, "Molecular dynamics simulation of surface energy and ZDDP effects on friction in nano-scale lubricated contacts," *Tribology International*, 36th Leeds–Lyon Symposium Special Issue: Multi-facets of Tribology, vol. 43, no. 10, pp. 1811–1822, 10 Oct. 1, 2010. DOI: `10.1016/j.triboint.2010.02.011`.

[95] C. Minfray *et al.*, "Experimental and Molecular Dynamics Simulations of Tribochemical Reactions with ZDDP: Zinc Phosphate–Iron Oxide Reaction," *Tribology Transactions*, vol. 51, no. 5, pp. 589–601, Sep. 22, 2008. DOI: `10.1080/10402000802011737`.

[96] N. J. Mosey and T. K. Woo, “Finite Temperature Structure and Dynamics of Zinc Dialkyldithiophosphate Wear Inhibitors: A Density Functional Theory and ab Initio Molecular Dynamics Study,” *J. Phys. Chem. A*, vol. 107, no. 25, pp. 5058–5070, Jun. 1, 2003. DOI: 10.1021/jp034085c.

[97] N. J. Mosey and T. K. Woo, “An ab Initio Molecular Dynamics and Density Functional Theory Study of the Formation of Phosphate Chains from Metathiophosphates,” *Inorg. Chem.*, vol. 45, no. 18, pp. 7464–7479, Sep. 1, 2006. DOI: 10.1021/ic0608391.

[98] T. Onodera, J. M. Martin, C. Minfray, F. Dassenoy, and A. Miyamoto, “Antiwear Chemistry of ZDDP: Coupling Classical MD and Tight-Binding Quantum Chemical MD Methods (TB-QCMD),” *Tribol Lett*, vol. 50, no. 1, pp. 31–39, 1 Apr. 1, 2013. DOI: 10.1007/s11249-012-0063-0.

[99] T. Onodera *et al.*, “Development of a quantum chemical molecular dynamics tribochemical simulator and its application to tribochemical reaction dynamics of lubricant additives,” *Modelling Simul. Mater. Sci. Eng.*, vol. 18, no. 3, p. 034 009, 3 Mar. 2010. DOI: 10.1088/0965-0393/18/3/034009.

[100] M. Koyama *et al.*, “Tribochemical Reaction Dynamics of Phosphoric Ester Lubricant Additive by Using a Hybrid Tight-Binding Quantum Chemical Molecular Dynamics Method,” *J. Phys. Chem. B*, vol. 110, no. 35, pp. 17 507–17 511, 35 Sep. 1, 2006. DOI: 10.1021/jp061210m.

[101] S. Peeters, A. Barlini, J. Jain, N. N. Gosvami, and M. C. Righi, “Adsorption and decomposition of ZDDP on lightweight metallic substrates: Ab initio and experimental insights,” *Applied Surface Science*, vol. 600, p. 153 947, Oct. 30, 2022. DOI: 10.1016/j.apsusc.2022.153947.

[102] W. Xue *et al.*, “Computational studies on the effects of substituents on the structure and property of zinc dialkyldithiophosphates,” *Computational and Theoretical Chemistry*, vol. 1099, pp. 195–202, Jan. 1, 2017. DOI: 10.1016/j.comptc.2016.11.027.

[103] T. Onodera *et al.*, “Influence of nanometer scale film structure of ZDDP tribofilm on Its mechanical properties: A computational chemistry study,” *Applied Surface Science*, VASSCAA-4, vol. 256, no. 4, pp. 976–979, 4 Nov. 30, 2009. DOI: 10.1016/j.apsusc.2009.04.205.

[104] N. J. Mosey and T. K. Woo, “A Quantum Chemical Study of the Unimolecular Decomposition Mechanisms of Zinc Dialkyldithiophosphate Antiwear Additives,” *J. Phys. Chem. A*, vol. 108, no. 28, pp. 6001–6016, Jul. 1, 2004. DOI: 10.1021/jp049371i.

[105] N. J. Mosey and T. K. Woo, “Insights into the chemical behavior of zinc dialkyldithiophosphate anti-wear additives in their isomeric and decomposed forms through molecular simulation,” *Tribology International*, vol. 39, no. 9, pp. 979–993, 9 Sep. 1, 2006. DOI: 10.1016/j.triboint.2005.07.041.

[106] F. Benini, P. Restuccia, and M. C. Righi, “Zinc dialkyldithiophosphates adsorption and dissociation on ferrous substrates: An ab initio study,” *Applied Surface Science*, vol. 642, p. 158 419, Jan. 2024. DOI: 10.1016/j.apsusc.2023.158419.

[107] P. Liao and E. A. Carter, “Testing variations of the GW approximation on strongly correlated transition metal oxides: Hematite (-Fe2O3) as a benchmark,” *Phys. Chem. Chem. Phys.*, vol. 13, no. 33, pp. 15 189–15 199, 33 Sep. 7, 2011. DOI: 10.1039/C1CP20829B.

[108] S. Piccinin, “The band structure and optical absorption of hematite (-Fe2O3): A first-principles GW-BSE study,” *Phys. Chem. Chem. Phys.*, vol. 21, no. 6, pp. 2957–2967, 6 Feb. 6, 2019. DOI: 10.1039/C8CP07132B.

[109] C. S. Lo, K. S. Tanwar, A. M. Chaka, and T. P. Trainor, “Density functional theory study of the clean and hydrated hematite $(1\overline{1}02)$ surfaces,” *Phys. Rev. B*, vol. 75, no. 7, p. 075 425, Feb. 27, 2007. DOI: 10.1103/PhysRevB.75.075425.

[110] T. Pabisiak and A. Kiejna, “Incipient adsorption of water and hydroxyl on hematite (0001) surface,” *J. Phys. Commun.*, vol. 3, no. 3, p. 035 023, Mar. 2019. DOI: 10.1088/2399-6528/ab0fa7.

[111] J. J. Gutierrez-Sevillano, A. Podsiadły-Paszkowska, B. M. Szyja, and S. Calero, “On the design of models for an accurate description of the water – hematite interface,” *Applied Surface Science*, vol. 560, p. 149 884, Sep. 15, 2021. DOI: 10.1016/j.apsusc.2021.149884.

[112] N. Snir, N. Yatom, and M. Caspary Toroker, “Progress in understanding hematite electrochemistry through computational modeling,” *Computational Materials Science*, vol. 160, pp. 411–419, Apr. 1, 2019. DOI: 10.1016/j.commatsci.2019.01.001.

[113] R. B. Wang and A. Hellman, “Surface terminations of hematite (-Fe2O3) exposed to oxygen, hydrogen, or water: Dependence on the density functional theory methodology,” *J. Phys.: Condens. Matter*, vol. 30, no. 27, p. 275 002, Jun. 2018. DOI: 10.1088/1361-648X/aac743.

[114] K. W. Corum, X. Huang, J. W. Bennett, and S. E. Mason, “Systematic density functional theory study of the structural and electronic properties of constrained and fully relaxed (0 0 1) surfaces of alumina and hematite,” *Molecular Simulation*, vol. 43, no. 5-6, pp. 406–419, Apr. 13, 2017. DOI: 10.1080/08927022.2017.1285402.

[115] F. Alvarez-Ramírez, J. M. Martínez-Magadán, J. R. B. Gomes, and F. Illas, "On the geometric structure of the (0001) hematite surface," *Surface Science*, vol. 558, no. 1, pp. 4–14, Jun. 1, 2004. DOI: 10.1016/j.susc.2004.04.009.

[116] H. Rong *et al.*, "Evaluation of DFT+U and HSE Frameworks for Strongly Correlated Iron Oxide," *ChemistrySelect*, vol. 8, no. 12, e202204450, 2023. DOI: 10.1002/slct.202204450.

[117] I. Lado-Touriño and F. Tsobnang, "Using computational approaches to model hematite surfaces," *Computational Materials Science*, vol. 17, no. 2, pp. 243–248, 2 Jun. 1, 2000. DOI: 10.1016/S0927-0256(00)00032-X.

[118] B. Iandolo and A. Hellman, "The Role of Surface States in the Oxygen Evolution Reaction on Hematite," *Angewandte Chemie*, vol. 126, no. 49, pp. 13 622–13 626, 2014. DOI: 10.1002/ange.201406800.

[119] X. Huang, S. K. Ramadugu, and S. E. Mason, "Surface-Specific DFT + U Approach Applied to -Fe2O3(0001)," *J. Phys. Chem. C*, vol. 120, no. 9, pp. 4919–4930, Mar. 10, 2016. DOI: 10.1021/acs.jpcc.5b12144.

[120] S. Bandaru, I. Scivetti, C.-Y. Yam, and G. Teobaldi, "The role of isotropic and anisotropic Hubbard corrections for the magnetic ordering and absolute band alignment of hematite -Fe2O3(0001) surfaces," *Progress in Natural Science: Materials International*, Special Issue of Computational Materials, vol. 29, no. 3, pp. 349–355, Jun. 1, 2019. DOI: 10.1016/j.pnsc.2019.05.010.

[121] A. Kiejna and T. Pabisiak, "Mixed Termination of Hematite (-Fe O)(0001) Surface," *J. Phys. Chem. C*, vol. 117, no. 46, pp. 24 339–24 344, Nov. 2013. DOI: 10.1021/jp406946s.

[122] H. Zhang, W. Sun, X. Xie, J. He, and C. Zhang, "Insights into the Fracture Nature of Hematite from First Principles DFT Calculations," *ACS Omega*, vol. 8, no. 9, pp. 8248–8255, Mar. 7, 2023. DOI: 10.1021/acsomega.2c06101.

[123] S. M. Souvi, M. Badawi, J.-F. Paul, S. Cristol, and L. Cantrel, "A DFT study of the hematite surface state in the presence of H2, H2O and O2," *Surface Science*, vol. 610, pp. 7–15, Apr. 2013. DOI: 10.1016/j.susc.2012.12.012.

[124] A. Rohrbach, J. Hafner, and G. Kresse, "Ab initio study of the (0001) surfaces of hematite and chromia: Influence of strong electronic correlations," *Phys. Rev. B*, vol. 70, no. 12, p. 125 426, 12 Sep. 28, 2004. DOI: 10.1103/PhysRevB.70.125426.

[125] W. Bergermayer, H. Schweiger, and E. Wimmer, "Ab initio thermodynamics of oxide surfaces: ${\Mathrm{O}}_{2}$ on ${\mathrm{Fe}}_{2}{\mathrm{O}}_{3}(0001)$," *Phys. Rev. B*, vol. 69, no. 19, p. 195 409, 19 May 20, 2004. DOI: 10.1103/PhysRevB.69.195409.

[126] T. D. Ta, A. K. Tieu, H. Zhu, and B. Kosasih, “Adsorption of Normal-Alkanes on Fe(110), FeO(110), and Fe2O3(0001): Influence of Iron Oxide Surfaces,” *J. Phys. Chem. C*, vol. 119, no. 23, pp. 12 999–13 010, Jun. 11, 2015. DOI: 10.1021/acs.jpcc.5b01847.

[127] A. Jaishankar, A. Jusufi, J. L. Vreeland, S. Deighton, J. Pellettiere, and A. M. Schilowitz, “Adsorption of Stearic Acid at the Iron Oxide/Oil Interface: Theory, Experiments, and Modeling,” *Langmuir*, vol. 35, no. 6, pp. 2033–2046, Feb. 12, 2019. DOI: 10.1021/acs.langmuir.8b03132.

[128] C. Gattinoni, J. P. Ewen, and D. Dini, “Adsorption of Surfactants on -Fe2O3(0001): A Density Functional Theory Study,” *J. Phys. Chem. C*, vol. 122, no. 36, pp. 20 817–20 826, 36 Sep. 13, 2018. DOI: 10.1021/acs.jpcc.8b05899.

[129] T. Stirner, D. Scholz, and J. Sun, “*Ab Initio* simulation of structure and surface energy of low-index surfaces of stoichiometric -Fe2O3,” *Surface Science*, vol. 671, pp. 11–16, May 2018. DOI: 10.1016/j.susc.2018.01.010.

[130] H. Guo and A. S. Barnard, “Thermodynamic modelling of nanomorphologies of hematite and goethite,” *Journal of Materials Chemistry*, vol. 21, no. 31, pp. 11 566–11 577, 2011. DOI: 10.1039/C1JM10381D.

[131] I. Newton, *Philosophiae naturalis principia mathematica*. J. Societatis Regiae ac Typis J. Streater, 1687, 534 pp.

[132] M. E. Tuckerman, *Statistical Mechanics: Theory and Molecular Simulation*. Oxford ; New York: Oxford University Press, 2010.

[133] B. J. Alder and T. E. Wainwright, “Phase Transition for a Hard Sphere System,” *J. Chem. Phys.*, vol. 27, no. 5, pp. 1208–1209, 5 Nov. 1, 1957. DOI: 10.1063/1.1743957.

[134] M. Allen and D. Tildesley, *Computer Simulation of Liquids: Second Edition*. Nov. 23, 2017, p. 626, 1 p. DOI: 10.1093/oso/9780198803195.001.0001.

[135] P. P. Ewald, “Die Berechnung optischer und elektrostatischer Gitterpotentiale,” *Annalen der Physik*, vol. 369, no. 3, pp. 253–287, 1921. DOI: 10.1002/andp.19213690304.

[136] R. W. Hockney and J. W. Eastwood, “Particle-Particle–Particle-Mesh (P3M) Algorithms,” in *Computer Simulation Using Particles*, CRC Press, 1988.

[137] L. Verlet, “Computer "Experiments" on Classical Fluids. I. Thermodynamical Properties of Lennard-Jones Molecules,” *Phys. Rev.*, vol. 159, no. 1, pp. 98–103, Jul. 5, 1967. DOI: 10.1103/PhysRev.159.98.

[138] G. S. Grest and K. Kremer, “Molecular dynamics simulation for polymers in the presence of a heat bath,” *Phys. Rev. A*, vol. 33, no. 5, pp. 3628–3631, May 1, 1986. DOI: 10.1103/PhysRevA.33.3628.

[139] T. Soddemann, B. Dünweg, and K. Kremer, "Dissipative particle dynamics: A useful thermostat for equilibrium and nonequilibrium molecular dynamics simulations," *Phys. Rev. E*, vol. 68, no. 4, p. 046 702, Oct. 8, 2003. DOI: 10.1103/PhysRevE.68.046702.

[140] H. C. Andersen, "Molecular dynamics simulations at constant pressure and/or temperature," *J. Chem. Phys.*, vol. 72, no. 4, pp. 2384–2393, Feb. 15, 1980. DOI: 10.1063/1.439486.

[141] H. J. C. Berendsen, J. P. M. Postma, W. F. van Gunsteren, A. DiNola, and J. R. Haak, "Molecular dynamics with coupling to an external bath," *J. Chem. Phys.*, vol. 81, no. 8, pp. 3684–3690, Oct. 15, 1984. DOI: 10.1063/1.448118.

[142] S. Nosé, "A molecular dynamics method for simulations in the canonical ensemble," *Molecular Physics*, vol. 52, no. 2, pp. 255–268, Jun. 10, 1984. DOI: 10.1080/00268978400101201.

[143] W. G. Hoover, "Canonical dynamics: Equilibrium phase-space distributions," *Phys. Rev. A*, vol. 31, no. 3, pp. 1695–1697, Mar. 1, 1985. DOI: 10.1103/PhysRevA.31.1695.

[144] G. J. Martyna, D. J. Tobias, and M. L. Klein, "Constant pressure molecular dynamics algorithms," *J. Chem. Phys.*, vol. 101, no. 5, pp. 4177–4189, Sep. 1994. DOI: 10.1063/1.467468.

[145] D. J. Evans and G. P. Morriss, "Nonlinear-response theory for steady planar couette flow," *Phys. Rev. A*, vol. 30, pp. 1528–1530, 3 Sep. 1984. DOI: 10.1103/PhysRevA.30.1528.

[146] B. D. Todd and P. J. Daivis, *Nonequilibrium Molecular Dynamics: Theory, Algorithms and Applications*. Cambridge: Cambridge University Press, 2017. DOI: 10.1017/9781139017848.

[147] E. Schrödinger, "An Undulatory Theory of the Mechanics of Atoms and Molecules," *Phys. Rev.*, vol. 28, no. 6, pp. 1049–1070, 6 Dec. 1, 1926. DOI: 10.1103/PhysRev.28.1049.

[148] R. G. Parr and Y. Weitao, *Density-Functional Theory of Atoms and Molecules*. Oxford University Press, May 26, 1994, 344 pp.

[149] W. Koch and M. C. Holthausen, "A Chemist's Guide to Density Functional Theory," Jun. 17, 2021.

[150] N. D. Mermin, "Thermal Properties of the Inhomogeneous Electron Gas," *Phys. Rev.*, vol. 137, no. 5A, A1441–A1443, 5A Mar. 1, 1965. DOI: 10.1103/PhysRev.137.A1441.

[151] P. D. Haynes, A. A. Mostof, C.-K. Skylaris, and M. C. Payne, "ONETEP: Linear-scaling density-functional theory with plane-waves," *J. Phys.: Conf. Ser.*, vol. 26, pp. 143–148, Feb. 22, 2006. DOI: 10.1088/1742-6596/26/1/034.

[152] C.-K. Skylaris, P. D. Haynes, A. A. Mostofi, and M. C. Payne, "Introducing ONETEP: Linear-scaling density functional simulations on parallel computers," *J. Chem. Phys.*, vol. 122, no. 8, p. 084 119, 8 Feb. 22, 2005. DOI: `10.1063/1.1839852`.

[153] V. I. Anisimov, F. Aryasetiawan, and A. I. Lichtenstein, "First-principles calculations of the electronic structure and spectra of strongly correlated systems: The LDA+ u method," *J. Phys.: Condens. Matter*, vol. 9, no. 4, p. 767, Jan. 1997. DOI: `10.1088/0953-8984/9/4/002`.

[154] B. Himmetoglu, A. Floris, S. de Gironcoli, and M. Cococcioni, "Hubbard-corrected DFT energy functionals: The LDA+U description of correlated systems," *International Journal of Quantum Chemistry*, vol. 114, no. 1, pp. 14–49, 2014. DOI: `10.1002/qua.24521`.

[155] M. Cococcioni and S. de Gironcoli, "Linear response approach to the calculation of the effective interaction parameters in the LDA + U method," *Phys. Rev. B*, vol. 71, p. 035 105, 3 Jan. 2005. DOI: `10.1103/PhysRevB.71.035105`.

[156] D. Sarpa *et al.*, "Computing Viscosities of Mixtures of Ester-Based Lubricants at Different Temperatures," *J. Phys. Chem. B*, vol. 127, no. 11, pp. 2587–2594, Mar. 2023. DOI: `10.1021/acs.jpcb.2c08553`.

[157] L. Martínez, R. Andrade, E. G. Birgin, and J. M. Martínez, "PACKMOL: A package for building initial configurations for molecular dynamics simulations," *Journal of Computational Chemistry*, vol. 30, no. 13, pp. 2157–2164, 2009. DOI: `10.1002/jcc.21224`.

[158] A. I. Jewett *et al.*, "Moltemplate: A Tool for Coarse-Grained Modeling of Complex Biological Matter and Soft Condensed Matter Physics," *Journal of Molecular Biology*, Computation Resources for Molecular Biology, vol. 433, no. 11, p. 166 841, May 28, 2021. DOI: `10.1016/j.jmb.2021.166841`.

[159] A. P. Thompson *et al.*, "LAMMPS - a flexible simulation tool for particle-based materials modeling at the atomic, meso, and continuum scales," *Computer Physics Communications*, vol. 271, p. 108 171, Feb. 1, 2022. DOI: `10.1016/j.cpc.2021.108171`.

[160] K. Pluhackova *et al.*, "Extension of the LOPLS-AA Force Field for Alcohols, Esters, and Monoolein Bilayers and its Validation by Neutron Scattering Experiments," *J. Phys. Chem. B*, vol. 119, no. 49, pp. 15 287–15 299, Dec. 10, 2015. DOI: `10.1021/acs.jpcb.5b08569`.

[161] K. Bernardino and M. C. Ribeiro, "Pressure and shear rate effects on viscosity and structure of imidazolium-based ionic liquids," *Fluid Phase Equilibria*, vol. 554, p. 113 345, 2022. DOI: `10.1016/j.fluid.2021.113345`.

[162] T. Mang and W. Dresel, *Lubricants and Lubrications*, 2nd completely revised and extended ed. Weinheim: Wiley-VCH, 2007.

[163] J. Zhang and H. Spikes, "Measurement of EHD Friction at Very High Contact Pressures," *Tribol Lett*, vol. 68, no. 1, p. 42, Feb. 2020. DOI: 10.1007/s11249-020-1281-5.

[164] N. D. Kondratyuk, V. V. Pisarev, and J. P. Ewen, "Probing the high-pressure viscosity of hydrocarbon mixtures using molecular dynamics simulations," *J. Chem. Phys.*, vol. 153, no. 15, p. 154 502, Oct. 21, 2020. DOI: 10.1063/5.0028393.

[165] H. Li *et al.*, "Extreme pressure and antiwear additives for lubricant: Academic insights and perspectives," *Int J Adv Manuf Technol*, vol. 120, no. 1, pp. 1–27, May 1, 2022. DOI: 10.1007/s00170-021-08614-x.

[166] S. Bair, L. Martinie, and P. Vergne, "Classical EHL Versus Quantitative EHL: A Perspective Part II—Super-Arrhenius Piezoviscosity, an Essential Component of Elastohydrodynamic Friction Missing from Classical EHL," *Tribology Letters*, vol. 63, no. 3, p. 37, Aug. 2, 2016. DOI: 10.1007/s11249-016-0725-4.

[167] D. Mathas *et al.*, "Calculating shear viscosity with confined non-equilibrium molecular dynamics: A case study on hematite – PAO-2 lubricant," *RSC Adv.*, vol. 13, no. 48, pp. 33 994–34 002, Nov. 2023. DOI: 10.1039/D3RA06929J.

[168] H. Hoang and G. Galliero, "Local viscosity of a fluid confined in a narrow pore," *Phys. Rev. E*, vol. 86, no. 2, p. 021 202, Aug. 20, 2012. DOI: 10.1103/PhysRevE.86.021202.

[169] P. Xu, T. Cagin, and W. A. Goddard, "Assessment of phenomenological models for viscosity of liquids based on nonequilibrium atomistic simulations of copper," *J. Chem. Phys.*, vol. 123, no. 10, p. 104 506, 2005. DOI: 10.1063/1.1881052.

[170] A. Porras-Vazquez, L. Martinie, P. Vergne, and N. Fillot, "Independence between friction and velocity distribution in fluids subjected to severe shearing and confinement," *Physical Chemistry Chemical Physics*, vol. 20, no. 43, pp. 27 280–27 293, 2018. DOI: 10.1039/C8CP04620D.

[171] M. Doig, C. P. Warrens, and P. J. Camp, "Structure and Friction of Stearic Acid and Oleic Acid Films Adsorbed on Iron Oxide Surfaces in Squalane," *Langmuir*, vol. 30, no. 1, pp. 186–195, 1 Jan. 14, 2014. DOI: 10.1021/la404024v.

[172] R. Zhou, C. Sun, and B. Bai, "Wall friction should be decoupled from fluid viscosity for the prediction of nanoscale flow," *J. Chem. Phys.*, vol. 154, no. 7, p. 074 709, 2021. DOI: 10.1063/5.0039228.

[173] E. Akhmatskaya, B. D. Todd, P. J. Daivis, D. J. Evans, K. E. Gubbins, and L. A. Pozhar, "A study of viscosity inhomogeneity in porous media," *J. Chem. Phys.*, vol. 106, no. 11, pp. 4684–4695, 1997. DOI: 10.1063/1.473505.

[174] J. P. Ewen, C. Gattinoni, J. Zhang, D. M. Heyes, H. A. Spikes, and D. Dini, "On the effect of confined fluid molecular structure on nonequilibrium phase behaviour and friction," *Physical Chemistry Chemical Physics*, vol. 19, no. 27, pp. 17 883–17 894, 2017. DOI: 10.1039/C7CP01895A.

[175] D. T. Ta, A. K. Tieu, H. T. Zhu, and B. Kosasih, "Thin film lubrication of hexadecane confined by iron and iron oxide surfaces: A crucial role of surface structure," *J. Chem. Phys.*, vol. 143, no. 16, p. 164 702, Oct. 28, 2015. DOI: 10.1063/1.4933203.

[176] X. Zheng, L. Su, G. Deng, J. Zhang, H. Zhu, and A. K. Tieu, "Study on Lubrication Characteristics of C4-Alkane and Nanoparticle during Boundary Friction by Molecular Dynamics Simulation," *Metals*, vol. 11, no. 1464, 9 2021. DOI: 10.3390/met11091464.

[177] R. Du, A. Zhang, Z. Du, and X. Zhang, "Molecular Dynamics Simulation on Thin-Film Lubrication of a Mixture of Three Alkanes," *Materials*, vol. 13, no. 3689, 17 2020. DOI: 10.3390/ma13173689.

[178] J. H. Irving and J. G. Kirkwood, "The Statistical Mechanical Theory of Transport Processes. IV. The Equations of Hydrodynamics," *J. Chem. Phys.*, vol. 18, no. 6, pp. 817–829, 1950. DOI: 10.1063/1.1747782.

[179] B. D. Todd, D. J. Evans, and P. J. Daivis, "Pressure tensor for inhomogeneous fluids," *Phys. Rev. E*, vol. 52, no. 2, pp. 1627–1638, 1995. DOI: 10.1103/PhysRevE.52.1627.

[180] A. Martini, Y. Liu, R. Snurr, and Q. J. Wang, "Molecular dynamics characterization of thin film viscosity for EHL simulation," *Tribol Lett*, vol. 21, no. 3, pp. 217–225, Mar. 1, 2006. DOI: 10.1007/s11249-006-9023-x.

[181] S. Plimpton, "Fast Parallel Algorithms for Short-Range Molecular Dynamics," *J. Comput. Phys.*, vol. 117, no. 1, pp. 1–19, 1995. DOI: 10.1006/jcph.1995.1039.

[182] J. Ewen and S. Echeverri Restrepo, *LAMMPS_builder, [Online]. Available: 10.5281/zenodo.1043867*, version master, Zenodo, 2017. DOI: 10.5281/zenodo.1043868.

[183] J. P. Ewen, S. Echeverri Restrepo, N. Morgan, and D. Dini, "Nonequilibrium molecular dynamics simulations of stearic acid adsorbed on iron surfaces with nanoscale roughness," *Tribology International*, vol. 107, pp. 264–273, Mar. 1, 2017. DOI: 10.1016/j.triboint.2016.11.039.

[184] S. W. I. Siu, K. Pluhackova, and R. A. Böckmann, "Optimization of the OPLS-AA Force Field for Long Hydrocarbons," *J. Chem. Theory Comput.*, vol. 8, no. 4, pp. 1459–1470, Apr. 10, 2012. DOI: 10.1021/ct200908r.

[185] M. Aryanpour, A. C. T. van Duin, and J. D. Kubicki, "Development of a Reactive Force Field for Iron-Oxyhydroxide Systems," *J. Phys. Chem. A*, vol. 114, no. 21, pp. 6298–6307, 2010. DOI: 10.1021/jp101332k.

[186] C. Zou, A. C. T. van Duin, and D. C. Sorescu, "Theoretical Investigation of Hydrogen Adsorption and Dissociation on Iron and Iron Carbide Surfaces Using the ReaxFF Reactive Force Field Method," *Top. Catal.*, vol. 55, no. 5, pp. 391–401, 2012. DOI: 10.1007/s11244-012-9796-0.

[187] J. P. Ewen *et al.*, "Substituent Effects on the Thermal Decomposition of Phosphate Esters on Ferrous Surfaces," *J. Phys. Chem. C*, vol. 124, no. 18, pp. 9852–9865, 18 May 7, 2020. DOI: `10.1021/acs.jpcc.9b11787`.

[188] D. Savio, N. Fillot, P. Vergne, and M. Zaccheddu, "A Model for Wall Slip Prediction of Confined n-Alkanes: Effect of Wall-Fluid Interaction Versus Fluid Resistance," *Tribol Lett*, vol. 46, no. 1, pp. 11–22, Apr. 1, 2012. DOI: `10.1007/s11249-011-9911-6`.

[189] T. Schneider and E. Stoll, "Molecular-dynamics study of a three-dimensional one-component model for distortive phase transitions," *Phys. Rev. B*, vol. 17, no. 3, pp. 1302–1322, 1978. DOI: `10.1103/PhysRevB.17.1302`.

[190] S. Bernardi, B. D. Todd, and D. J. Searles, "Thermostating highly confined fluids," *J. Chem. Phys.*, vol. 132, no. 24, p. 244 706, Jun. 28, 2010. DOI: `10.1063/1.3450302`.

[191] B. D. Jensen, K. E. Wise, and G. M. Odegard, "The effect of time step, thermostat, and strain rate on ReaxFF simulations of mechanical failure in diamond, graphene, and carbon nanotube," *J. Comput. Chem.*, vol. 36, no. 21, pp. 1587–1596, 2015. DOI: `10.1002/jcc.23970`.

[192] R. T. Bradshaw and J. W. Essex, "Evaluating parametrization protocols for hydration free energy calculations with the AMOEBA polarizable force field," *Journal of Chemical Theory and Computation*, vol. 12, no. 8, pp. 3871–3883, 2016. DOI: `10.1021/acs.jctc.6b00276`.

[193] S. Berkani *et al.*, "Model formation of ZDDP tribofilm from a mixture of zinc metaphosphate and goethite," *Tribology International*, vol. 79, pp. 197–203, Nov. 1, 2014. DOI: `10.1016/j.triboint.2014.06.013`.

[194] S. Zhang *et al.*, "Density Functional Studies on the Atomistic Structure and Properties of Iron Oxides: A Parametric Study," *Materials*, vol. 15, no. 23, p. 8316, Nov. 2022. DOI: `10.3390/ma15238316`.

[195] X. Xu and H. Spikes, "Study of zinc dialkyldithiophosphate in di-ethylhexyl sebacate using electrochemical techniques," *Tribol Lett*, vol. 25, no. 2, pp. 141–148, 2 Feb. 1, 2007. DOI: `10.1007/s11249-006-9132-6`.

[196] J. C. A. Prentice *et al.*, "The ONETEP linear-scaling density functional theory program," *The Journal of Chemical Physics*, vol. 152, no. 17, p. 174 111, May 2020. DOI: `10.1063/5.0004445`.

[197] J. Aarons, L. G. Verga, N. D. M. Hine, and C.-K. Skylaris, "Atom-projected and angular momentum resolved density of states in the ONETEP code," *Electron. Struct.*, vol. 1, no. 3, p. 035 002, Aug. 2019. DOI: `10.1088/2516-1075/ab34f5`.

[198] S. J. Clark *et al.*, "First principles methods using CASTEP," *Zeitschrift für Kristallographie - Crystalline Materials*, vol. 220, no. 5-6, pp. 567–570, May 2005. DOI: `10.1524/zkri.220.5.567.65075`.

[199] J. Redondo *et al.*, "Hematite -Fe2O3(0001) in Top and Side View: Resolving Long-Standing Controversies about Its Surface Structure," *Advanced Materials Interfaces*, vol. 10, no. 32, p. 2 300 602, 2023. DOI: 10.1002/admi.202300602.

[200] B. Klahr, S. Gimenez, F. Fabregat-Santiago, T. Hamann, and J. Bisquert, "Water Oxidation at Hematite Photoelectrodes: The Role of Surface States," *J. Am. Chem. Soc.*, vol. 134, no. 9, pp. 4294–4302, Mar. 7, 2012. DOI: 10.1021/ja210755h.

[201] E. B. Linscott, D. J. Cole, M. C. Payne, and D. D. O'Regan, "Role of spin in the calculation of Hubbard U and Hund's J parameters from first principles," *Phys. Rev. B*, vol. 98, no. 23, p. 235 157, Dec. 2018. DOI: 10.1103/PhysRevB.98.235157.

[202] B. Himmetoglu, R. M. Wentzcovitch, and M. Cococcioni, "First-principles study of electronic and structural properties of CuO," *Phys. Rev. B*, vol. 84, no. 11, p. 115 108, Sep. 2011. DOI: 10.1103/PhysRevB.84.115108.

[203] S. Rostami, N. Seriani, and R. Gebauer, "Hematite surfaces: Band bending and local electronic states," *Phys. Rev. Materials*, vol. 6, no. 10, p. 104 604, Oct. 2022. DOI: 10.1103/PhysRevMaterials.6.104604.

[204] S. Berman *et al.*, "Reconciling the theoretical and experimental electronic structure of NbO 2," *Phys. Rev. B*, vol. 108, no. 15, p. 155 141, Oct. 2023. DOI: 10.1103/PhysRevB.108.155141.

[205] D. R. Armstrong, E. S. Ferrari, K. J. Roberts, and D. Adams, "An examination of the reactivity of zinc di-alkyl-di-thiophosphate in relation to its use as an anti-wear and anti-corrosion additive in lubricating oils," *Wear*, vol. 217, no. 2, pp. 276–287, 2 May 15, 1998. DOI: 10.1016/S0043-1648(98)00150-1.

[206] M. Hacene, A. Anciaux-Sedrakian, X. Rozanska, D. Klahr, T. Guignon, and P. Fleurat-Lessard, "Accelerating vasp electronic structure calculations using graphic processing units," *Journal of Computational Chemistry*, vol. 33, no. 32, pp. 2581–2589, 2012. DOI: https://doi.org/10.1002/jcc.23096.

[207] C. Kutzner, S. Páll, M. Fechner, A. Esztermann, B. L. de Groot, and H. Grubmüller, "More bang for your buck: Improved use of gpu nodes for gromacs 2018," *Journal of Computational Chemistry*, vol. 40, no. 27, pp. 2418–2431, 2019. DOI: https://doi.org/10.1002/jcc.26011.

[208] A. W. Götz, T. Wölfle, and R. C. Walker, "Chapter 2 - quantum chemistry on graphics processing units," in ser. Annual Reports in Computational Chemistry, R. A. Wheeler, Ed., vol. 6, Elsevier, 2010, pp. 21–35. DOI: https://doi.org/10.1016/S1574-1400(10)06002-0.

[209] J. A. Keith *et al.*, "Combining machine learning and computational chemistry for predictive insights into chemical systems," *Chemical Reviews*, vol. 121, no. 16, pp. 9816–9872, 2021, PMID: 34232033. DOI: 10.1021/acs.chemrev.1c00107.

[210] O. T. Unke *et al.*, “Machine learning force fields,” *Chemical Reviews*, vol. 121, no. 16, pp. 10 142–10 186, 2021, PMID: 33705118. DOI: 10.1021/acs.chemrev.0c01111.

[211] S. Wu *et al.*, “Applications and advances in machine learning force fields,” *Journal of Chemical Information and Modeling*, vol. 63, no. 22, pp. 6972–6985, 2023, PMID: 37751546. DOI: 10.1021/acs.jcim.3c00889.

[212] I. Poltavsky and A. Tkatchenko, “Machine learning force fields: Recent advances and remaining challenges,” *The Journal of Physical Chemistry Letters*, vol. 12, no. 28, pp. 6551–6564, 2021, PMID: 34242032. DOI: 10.1021/acs.jpclett.1c01204.

[213] J. Westermayr, M. Gastegger, K. T. Schütt, and R. J. Maurer, “Perspective on integrating machine learning into computational chemistry and materials science,” *The Journal of Chemical Physics*, vol. 154, no. 23, p. 230 903, Jun. 2021. DOI: 10.1063/5.0047760.